

**ASSESSMENT OF THE FACTORS AFFECTING PROTECTIVE ALUMINA
FORMATION UNDER HOT CORROSION CONDITIONS**

by

Michael Nathan Task

Bachelor of Science, University of Pittsburgh, 2007

Master of Science, University of Pittsburgh, 2009

Submitted to the Graduate Faculty of
The Swanson School of Engineering in partial fulfillment
of the requirements for the degree of
Doctor of Philosophy

University of Pittsburgh

2012

UNIVERSITY OF PITTSBURGH
SWANSON SCHOOL OF ENGINEERING

This dissertation was presented

by

Michael N. Task

It was defended on

April 24, 2012

and approved by

Ian Nettleship, PhD., Associate Professor, Department of Mechanical Engineering and
Materials Science

Brian Gleeson, PhD., Harry S. Tack Chair in Materials Science, Department of Mechanical
Engineering and Materials Science

Sridhar Seetharaman, PhD., POSCO Professor, Department of Materials Science and
Engineering, Carnegie Mellon University

Dissertation Co-Advisor: Frederick S. Pettit, PhD., Emeritus Professor, Department of
Mechanical Engineering and Materials Science

Dissertation Co-Advisor: Gerald H. Meier, PhD., William Kepler Whiteford Professor,
Department of Mechanical Engineering and Materials Science

Copyright © by Michael N. Task

2012

ASSESSMENT OF THE FACTORS AFFECTING PROTECTIVE ALUMINA FORMATION UNDER HOT CORROSION CONDITIONS

Michael N. Task, PhD

University of Pittsburgh, 2012

In this study, the influence of microstructure, composition, and phase constitution on the Type I (900°C) and Type II (700°C) hot corrosion resistance of MCrAlY and β -NiAl base alloys was investigated. The Type II hot corrosion resistance of MCrAlY alloys is generally enhanced by microstructural refinement. This can be attributed to the more rapid establishment of a protective Al_2O_3 -rich scale due to the higher density of short-circuit diffusion paths for Al (phase boundaries). However, it was shown that for a given bulk composition, the compositions of the individual phases is also extremely important. If one phase is lean in an element which is highly beneficial from a hot corrosion standpoint, e.g., Cr, Type II hot corrosion resistance is quite poor, regardless of the microstructural scale. In addition, coarse reactive-element-rich phases, which are commonly found in MCrAlY alloys, can be incorporated into the thermally grown Al_2O_3 scale and act as initiation sites for Type II attack. This stresses the importance of reactive element content and distribution in MCrAlY coatings.

During Type I hot corrosion exposure of β -Ni-36Al (at. %) base alloys, the incubation stage is greatly extended by the addition of 5% Pt, Co, or Cr. In each case, the beneficial effects can be linked to an enhanced ability to rapidly form a protective Al_2O_3 scale, and to heal this scale when it sustains damage during exposure. With regard to Type II hot corrosion, individual additions of 5 at. % Pt or Cr are beneficial, largely for the same reason; however, additions of 5

at. % Co and co-additions of 5 at. % Pt + 5 at. % Cr result in a decrease in the duration of the incubation stage. Subsurface phase transformations that occur in the latter systems prevent the alloy from maintaining the growth of the Al_2O_3 scale. This mechanism is discussed in detail.

Finally, the influence of alloy composition and exposure environment on the kinetics of the $\theta \rightarrow \alpha$ Al_2O_3 transformation in scales grown on β -NiAl alloys at 900°C was thoroughly investigated. The relative importance of the kinetics of this transformation during Type I hot corrosion exposure is discussed.

TABLE OF CONTENTS

ACKNOWLEDGEMENTS	xiv
1.0 INTRODUCTION.....	1
2.0 BACKGROUND	5
2.1 FORMATION OF SALT DEPOSITS ON GAS TURBINE HARDWARE... 	5
2.2 Na₂SO₄ – INDUCED HOT CORROSION.....	8
2.2.1 The Stages of Hot Corrosion.....	9
2.2.1.1 Initiation Stage.....	10
2.2.1.2 Propagation Stage.....	13
2.2.2 High Temperature (Type I) Hot Corrosion.....	22
2.2.2.1 Basic Fluxing.....	23
2.2.2.2 Alloy-Induced Acidic Fluxing.....	35
2.2.3 Low Temperature (Type II) Hot Corrosion	38
2.2.3.1 Gas Phase-Induced Acidic Fluxing.....	39
2.3 (Ni,Pt)Al DIFFUSION COATINGS.....	48
2.3.1 Phase Equilibria in the Ni-Al-Pt System.....	48
2.3.1.1 The Equilibrium Ni-Al-Pt Phase Diagram.....	48
2.3.1.2 The B2 ↔ L10 Martensitic Transformation in the NiAl system.....	50

2.3.2	Deposition and Resulting Microstructures of (Ni,Pt)Al Diffusion Coatings.....	52
2.3.3	Oxidation Behavior of (Ni,Pt)Al Diffusion Coatings.....	54
2.3.4	Hot Corrosion Behavior of (Ni,Pt)Al Diffusion Coatings.....	57
2.4	MCrAlY OVERLAY COATINGS.....	61
2.4.1	Phase Equilibria in the Ni-Cr-Al System.....	61
2.4.2	Deposition and Resulting Microstructures of MCrAlY Overlay Coatings.....	65
2.4.3	Oxidation Behavior of MCrAlY Overlay Coatings.....	69
2.4.3.1	Early-Stage (Transient) Oxidation Behavior.....	69
2.4.3.2	Steady-State Scale Growth Kinetics.....	72
2.4.3.3	Coating Durability During Thermal Cycling.....	73
2.4.4	Hot Corrosion Behavior of MCrAlY Overlay Coatings.....	76
3.0	DEFICIENCIES IN THE CURRENT BODY OF KNOWLEDGE AND MOTIVATION FOR CURRENT WORK.....	79
4.0	THE EFFECT OF MICROSTRUCTURE ON THE TYPE II HOT CORROSION OF Ni-BASE MCrAlY ALLOYS.....	81
4.1	EXPERIMENTAL PROCEDURE	81
4.1.1	Alloy Preparation.....	81
4.1.2	Type II Hot Corrosion Exposures.....	82
4.1.3	Analytical Methods.....	84
4.2	RESULTS	85
4.2.1	Starting Microstructures.....	85

4.2.2	Type II Hot Corrosion.....	92
4.2.3	Type II Hot Corrosion of a Pre-Oxidized NiCoCrAlY Alloy and the Use of a Na ₂ SO ₄ - NiSO ₄ Deposit.....	104
4.3	DISCUSSION.....	108
4.3.1	The Influence of Microstructural Scale, Phase Constitution, and Phase Composition on Type II Hot Corrosion Resistance.....	108
4.3.2	The Influence of Pre-Oxidation.....	112
4.4	CONCLUSIONS.....	114
5.0	COMPOSITIONAL EFFECTS ON THE TYPE I HOT CORROSION OF β -NiAl ALLOYS	116
5.1	EXPERIMENTAL PROCEDURE	117
5.1.1	Alloy Preparation.....	117
5.1.2	Type I Hot Corrosion Exposures.....	118
5.2	RESULTS	121
5.3	DISCUSSION.....	128
5.3.1	The Influence of Co on Type I Hot Corrosion Resistance.....	128
5.3.2	The Influence of Cr and Pt on Type I Hot Corrosion Resistance.....	140
5.3.3	Relationship Between Type I Hot Corrosion Resistance and Al ₂ O ₃ Scale Healing.....	141
5.4	CONCLUSIONS.....	145
6.0	COMPOSITIONAL EFFECTS ON THE TYPE II HOT CORROSION OF β -NiAl ALLOYS.....	147
6.1	EXPERIMENTAL PROCEDURE.....	148

6.1.1	Alloy Preparation.....	148
6.1.2	Type II Hot Corrosion Exposures.....	148
6.1.3	Oxidation Exposures.....	148
6.1.4	Analytical Techniques.....	149
6.2	RESULTS	149
6.2.1	Type II Hot Corrosion	149
6.2.2	700°C Oxidation in O ₂ + 1000 ppm SO ₂	153
6.3	DISCUSSION.....	167
6.4	CONCLUSIONS	178
7.0	ENVIRONMENTAL AND COMPOSITIONAL EFFECTS ON THE Al ₂ O ₃ STABILITY AND ASSOCIATED HOT CORROSION BEHAVIOR OF β-NiAl ALLOYS.....	179
7.1	EXPERIMENTAL PROCEDURE	181
7.1.1	Alloy Preparation.....	181
7.1.2	Exposures.....	182
7.2	RESULTS	184
7.2.1	Compositional Effects on the θ → α Al ₂ O ₃ Transformation Kinetics ..	184
7.2.1.1	Isothermal Oxidation Kinetics and Scale Microstructure	184
7.2.1.2	PSLS Analysis.....	190
7.2.2	Environmental Effects on the θ → α Al ₂ O ₃ Transformation Kinetics.....	193

7.3	DISCUSSION.....	200
7.3.1	Compositional Effects on the $\theta \rightarrow \alpha$ Al₂O₃ Transformation Kinetics ...	200
7.3.1.1	The Template Effect.....	203
7.3.1.2	Ionic Size Effects.....	205
7.3.1.3	The Influence of Co and the Importance of Defect Structure.....	206
7.3.1.4	The Influence of Preventing Sulfur Segregation.....	208
7.3.2	The Influence of S on the $\theta \rightarrow \alpha$ Al₂O₃ Transformation Kinetics.....	209
7.3.3	Influence of the $\theta \rightarrow \alpha$ Al₂O₃ Transformation on Type I Hot Corrosion Resistance.....	210
7.4	CONCLUSIONS	216
8.0	CONCLUDING REMARKS	218
	APPENDIX A.....	222
	BIBLIOGRAPHY	230

LIST OF TABLES

Table 1.	Approximate sea salt composition.....	5
Table 2.	Cast alloy compositions (wt. %), measured by ICP-OES.....	81
Table 3.	Phase boundary intersections per unit line length for the as-processed MCrAlYs	91
Table 4.	SEM-EDS-measured phase compositions in the IC and LPPS NiCrAlY, along with the predicted equilibrium phase compositions at 1100°C	111
Table 5.	Nominal alloy compositions	117
Table 6.	Correlation between Type II resistance and duration of transient oxidation stage...	171
Table 7.	Nominal alloy compositions	181
Table 8.	Instantaneous parabolic rate constants as a function of time at 900°C.....	185
Table 9.	Summary of the estimated interaction parameters ε_{AlAl} , ε_{CoAl} , ε_{AlPt} , and ε_{CoCo}	226

LIST OF FIGURES

Figure 1.	Plot of weight change per unit area vs. time for a Ni-8Cr-6Al (wt%) alloy exposed to Type I hot corrosion conditions, demonstrating the initiation and propagation stages of hot corrosion.....	9
Figure 2.	Schematic phase stability diagram for the Na-S-O system, showing schematically the compositional changes that can lead to corrosive conditions in the salt.....	11
Figure 3.	Thermodynamic stability diagram for the Cr-S-O system superimposed onto the Na ₂ SO ₄ portion of the Na-S-O stability diagram at T = 1200K.....	15
Figure 4.	Solubilities of various oxides in Na ₂ SO ₄ as a function of melt basicity at = 1 atm and T = 1200°K.....	17
Figure 5.	Schematic of the Rapp-Goto negative solubility gradient criterion	21
Figure 6.	1000°C Al-S-O phase stability diagram, demonstrating the compositional changes which lead to the basic fluxing of Ni-Al alloys	33
Figure 7.	The CoSO ₄ -Na ₂ SO ₄ pseudo-binary phase diagram.....	40
Figure 8.	pSO ₃ required to form solid CoSO ₄ and a liquid eutectic mixture from pure Co ₃ O ₄ at pO ₂ =1atm	42
Figure 9.	Phase equilibria in the Ni-Al-Pt systems as determined by Bätzner [52] at 1060°C and by Gleeson et. al. [54] at 1150°C.....	49

Figure 10.	Equilibrium phase diagram in the Ni-Cr-Al system at 1150°C [78].	62
Figure 11.	Thermocalc-calculated phase fractions in a Ni-31Cr-11.25Al-0.6Y (wt. %) alloy and corresponding SEM micrographs at various temperatures [79].	64
Figure 12.	Optical micrograph of an EB-PVD NiCrAlY coating [3].	66
Figure 13.	SEM micrograph of a VPS NiCoCrAlY coating.	68
Figure 14.	Type II hot corrosion apparatus schematic	83
Figure 15.	Starting microstructures of the drop cast a) NiCoCrAlY and b) NiCrAlY	85
Figure 16.	Starting microstructures of the injection cast a) NiCrAlY and b) NiCoCrAlY	87
Figure 17.	Starting microstructures of the LPPS a) NiCrAlY and b) NiCoCrAlY	89
Figure 18.	Microstructure of the as-coated LPPS NiCrAlY prior to surface grinding	90
Figure 19.	As coated LPPS NiCoCrAlY, demonstrating the lines that were used to quantify the scale of the microstructure	91
Figure 20.	Microstructure of the DC NiCrAlY after a 10 h Type II hot corrosion exposure	93
Figure 21.	SEM micrograph and associated X-ray maps of the DC NiCrAlY after a 10 h Type II hot corrosion exposure	94
Figure 22.	SEM micrograph of the DC NiCrAlY after a 10 h Type II hot corrosion exposure, showing the internal attack along the interphase boundaries surrounding the α phase.	95
Figure 23.	SEM micrographs of the IC NiCrAlY after a 10 h Type II hot corrosion exposure	96
Figure 24.	SEM micrograph and associated X-ray maps of the IC NiCrAlY after a 10 h Type II hot corrosion exposure	97

Figure 25.	SEM micrograph of the IC NiCrAlY after a 10 h Type II hot corrosion exposure, showing the internal attack along the interphase boundaries surrounding the α phase.....	98
Figure 26.	SEM micrograph of the LPPS NiCrAlY after surface grinding/polishing followed by a 10 h Type II hot corrosion exposure	99
Figure 27.	SEM micrographs of the DC NiCoCrAlY after a 10 h Type II hot corrosion exposure	100
Figure 28.	SEM micrograph and associated X-ray maps of the DC NiCoCrAlY after a 10 h Type II hot corrosion exposure	101
Figure 29.	SEM micrographs of the IC NiCoCrAlY after a 10 h Type II hot corrosion exposure.....	102
Figure 30.	SEM micrographs of the LPPS NiCoCrAlY after a 10 h Type II hot corrosion exposure	103
Figure 31.	SEM micrograph of the as-cast NiCoCrAlY-2	104
Figure 32.	SEM micrograph of the NiCoCrAlY-2 after pre-oxidation at 1100°C for 1 h.....	105
Figure 33.	SEM micrographs of the pre-oxidized NiCoCrAlY-2 after a 10 h Type II hot corrosion exposure in the presence of a Na ₂ SO ₄ - 40 mol % NiSO ₄	106
Figure 34.	SEM micrographs of the NiCoCrAlY-2 exposed to Type II conditions for 10 h with no pre-oxidation treatment	106
Figure 35.	SEM micrographs of the pre-oxidized NiCoCrAlY-2 after a 5 h Type II hot corrosion exposure in the presence of a Na ₂ SO ₄ - 40 mol % NiSO ₄	107
Figure 36.	Schematic of the Type I hot corrosion apparatus	119
Figure 37.	Plots of weight change vs. time for the Type I hot corrosion of the β systems.....	122

Figure 38.	Cross-sectional SEM micrographs of the a) Ni-36Al and b) Ni-36Al-5Co after 60 h Type I hot corrosion exposures	123
Figure 39.	SEM micrographs of the a-c) Ni-36Al-5Pt, d-f) Ni-36Al-5Pt-5Co, and g-i) Ni-36Al-5Cr after 100 h Type I hot corrosion exposures.....	126
Figure 40.	Plots of IOZ and IOZ + MCZ depth for the Ni-3Al and Ni-3Al-5Co after a 170 h exposure at 900°C in air + 10% H ₂ O	131
Figure 41.	Optical micrograph of the Ni-3Al-5Co after 170 h exposure at 900°C in air + 10% H ₂ O.....	132
Figure 42.	Optical micrograph of the Ni-3Al-5Co after 170 h exposure at 900°C showing the difference in internal Al ₂ O ₃ precipitate morphology between grains	134
Figure 43.	TGA curves for the oxidation of Ni-36Al and Ni-36Al-5Co at 900°C.....	136
Figure 44.	SEM micrographs of the a) Ni-36Al-5Pt and b) Ni-36Al-5Pt-5Co after 180 h and 320 h, respectively, of Type I hot corrosion exposure.....	137
Figure 45.	SEM micrograph of the internal corrosion product in the Ni-36Al-5Pt after 180 h of Type I hot corrosion exposure, showing the formation of Ni ₃ S ₂	138
Figure 46.	Surface SEM micrographs of the a) Ni-36Al-5Pt, b) Ni-36Al-5Pt-5Co, and c) Ni-36Al-5Cr after 100 h of Type I hot corrosion exposure followed by 20 min of ultrasonic cleaning in water	142
Figure 47.	SEM micrographs of spalled areas on the a) Ni-36Al-5Pt and b) Ni-36Al-5Pt-5Co	143
Figure 48.	Surface SEM micrographs of the spalled regions on the a) Ni-36Al-5Pt, b) Ni-36Al-5Pt-5Co, and c) Ni-36Al-5Cr after an additional 100 h exposure at 900°C in air with no salt deposit.....	144

Figure 49.	Plots of weight change per cm^2 of the β systems after 100 h of Type II hot corrosion exposure	150
Figure 50.	Cross sectional SEM micrographs of the a) Ni-36Al, b) Ni-36Al-5Pt, c) Ni-36Al-5Pt-5Co, d) Ni-36Al-5Cr, and e) Ni-36Al-5Pt-5Cr after a 100 h Type II hot corrosion exposure	151
Figure 51.	Cross sectional SEM micrograph of the Ni-36Al-5Pt-5Cr after a 100 h Type II hot corrosion exposure	152
Figure 52.	XPS depth profiles of the scale formed on the Ni-36Al alloy after 700°C oxidation for 100 h in $\text{O}_2 + 1000 \text{ ppm SO}_2$	154
Figure 53.	XPS depth profiles of the scale formed on the Ni-36Al-5Pt alloy after 700°C oxidation for 100 h in $\text{O}_2 + 1000 \text{ ppm SO}_2$	155
Figure 54.	XPS depth profiles of the scale formed on the Ni-36Al-5Pt-5Co alloy after 700°C oxidation for 100 h in $\text{O}_2 + 1000 \text{ ppm SO}_2$	156
Figure 55.	XPS depth profiles of the scale formed on the Ni-36Al-5Cr alloy after 700°C oxidation for 100 h in $\text{O}_2 + 1000 \text{ ppm SO}_2$	157
Figure 56.	XPS depth profiles of the scale formed on the Ni-36Al-5Pt-5Cr alloy after 700°C oxidation for 100 h in $\text{O}_2 + 1000 \text{ ppm SO}_2$	158
Figure 57.	XPS depth profiles of the scale formed on the Ni-36Al alloy after 700°C oxidation for 100 h in $\text{O}_2 + 1000 \text{ ppm SO}_2$, showing the Si contamination in the scale.....	159
Figure 58.	Lateral TOF-SIMS images of the Ni-36Al alloy showing the Ni distribution within the scale formed during 100 h oxidation at 700°C in $\text{O}_2 + 1000 \text{ ppm SO}_2$ at a depth of 5 nm and 10 nm	162

Figure 59.	Cross-sectional TOF-SIMS images showing the Ni and Cr distributions within the scale formed on the Ni-36Al-5Cr alloy during 100 h oxidation at 700°C in O ₂ + 1000 ppm SO ₂	164
Figure 60.	Lateral TOF-SIMS images showing the Ni and Co distributions within the scale formed on the Ni-36Al-5Pt-5Co alloy during 100 h oxidation at 700°C in O ₂ + 1000 ppm SO ₂ at a depth of 5 nm and 10 nm	165
Figure 61.	Cross-sectional TOF-SIMS image showing the Cr distribution within the scale formed on the Ni-36Al-5Pt-5Cr alloy during 100 h oxidation at 700°C in O ₂ + 1000 ppm SO ₂	166
Figure 62.	XPS depth profiles of the scale formed on the a) Ni-36Al-5Cr and b) Ni-36Al-5Pt alloys after 700°C oxidation for 20 h in O ₂ + 1000 ppm SO ₂	170
Figure 63.	Cross sectional SEM micrograph of the Ni-36Al-5Pt-5Cr alloy after a 100 h Type II hot corrosion exposure	172
Figure 64.	Cross-sectional SEM micrographs of the Ni-36Al-5Pt-5Cr after a 10 h Type II hot corrosion exposure	173
Figure 65.	Cross-sectional SEM micrographs of the Ni-36Al-5Pt-5Cr after a 2 h Type II exposure, showing the precipitation of γ -Pt beneath the Al ₂ O ₃ scale	174
Figure 66.	Schematic representation of the layered corrosion product formed during Type II hot corrosion attack of the Ni-36Al-5Pt-5Cr	175
Figure 67.	Parabolic weight changes plots for the oxidation of the β systems at 900°C	186
Figure 68.	Surface SEM micrographs of the β systems after 100 h isothermal oxidation at 900°C: a) Ni-36Al, b) Ni-36Al-5Co, c) Ni-36Al-5Cr, d) Ni-46Al, and e) Ni-46Al-5Pt	188

Figure 69.	Cross sectional SEM micrograph of the Ni-36Al after 100 h isothermal oxidation at 900°C.....	189
Figure 70.	PSLS spectra from the scales formed during isothermal oxidation at 900°C for 50 and 100 h	191
Figure 71.	Surface SEM micrographs of the a) Ni-36Al, b) Ni-36Al-5Co, c) Ni-36Al-5Cr, d) Ni-46Al, and e) Ni-46Al-5Pt after 10 h of Type I hot corrosion exposure followed by ultrasonic cleaning in water. Select regions of adherent Al ₂ O ₃ are identified with arrows.	194
Figure 72.	PSLS spectra from the remaining adherent Al ₂ O ₃ after a 10 h Type I hot corrosion exposure followed by ultrasonic cleaning in water for 10 h: a) Ni-36Al, b) Ni-36Al-5Co, c) Ni-36Al-5Cr, d) Ni-46Al, and e) Ni-46Al-5Pt	196
Figure 73.	Surface SEM micrograph of the Ni-46Al-5Pt after a 100 h isothermal oxidation exposure in O ₂ + 1000 ppm SO ₂	198
Figure 74.	PSLS spectrum from the oxide formed on the Ni-46Al-5Pt after 100 h isothermal oxidation at 900°C in O ₂ + 1000 ppm SO ₂	199
Figure 75.	Schematic of the nucleation of α - Al ₂ O ₃ from θ	201
Figure 76.	Schematic representation of the heterogeneous nucleation of α -Al ₂ O ₃ on transient Cr ₂ O ₃	204
Figure 77.	Surface SEM micrograph of an Al ₂ O ₃ scale grown on a Zr-modified NiAl alloy, showing tensile cracks that form as a result of the volume decrease that occurs upon transformation from θ to α (from ref. [121])	211
Figure 78.	Surface SEM micrograph of the partially-transformed scale grown on the Ni-36Al-5Co specimen after 100 h oxidation at 900°C	214

Figure 79.	Plot of $\ln\gamma_{Al}$ vs. X_{Co} used to estimate ε_{CoAl}	225
Figure 80.	Plots of a) X_{Al}/X_{Pt} vs. $-\ln\gamma_{Al}$ and b) X_{Ni}/X_{Pt} vs. $-\ln\gamma_{Ni}$ which were numerically integrated in order to solve Equation (54). The relevant areas are indicated by red lines.	228

ACKNOWLEDGEMENTS

Firstly, I owe an enormous debt of gratitude to my mentors, Profs. Gerald H. Meier, Frederick S. Pettit, and Brian Gleeson, from whom I have learned an immeasurable amount about materials science, scientific research, and what it means to be a professional.

To my mother Karen, my brother Keith, my uncle Mark, and my beautiful fiancé Jessica, I haven't the words to describe what you mean to me. Your love, patience, and encouragement have contributed more to my success than any number of study sessions or late nights in the lab.

Finally, thanks are due to the Office of Naval Research for providing the funding for this research under project number N00014-10-1-0661.

I would like to dedicate this work to the memory of my father, Allen.

1.0 INTRODUCTION

Materials used in industrial, marine, and aero gas turbine engines must be able to withstand a host of harsh conditions, including large cyclic stresses in the presence of a high-temperature oxidizing environment. The strength requirements are typically met by Ni-base superalloys, which form the structural base of turbine vanes and blades. At relatively low temperatures, these materials may also have sufficient oxidation-resistance to require no further protection. Often, however, an aluminum-rich coating is applied to the superalloy surface in order to impart oxidation-resistance, which is achieved by the formation of a thermally grown $\alpha\text{-Al}_2\text{O}_3$ surface scale. A number of materials have been studied extensively and put into practice for this purpose. For operation at the most extreme temperatures, ceramic thermal barrier coatings (TBCs) are applied on the surface of the above-mentioned coatings in order to lower the temperature to which these metallic components are exposed.

A further complication commonly arises during the operation of gas turbines, which involves the formation of fused salt deposits on the surface of the turbine hardware. The principal salt that tends to deposit is Na_2SO_4 . It is commonly believed that this salt forms as a result of sulfur impurities in the fuel oxidizing and reacting at high temperatures with NaCl which has been ingested via the intake air or fuel contamination, although other mechanisms are also conceivable [1]. This is a considerable problem when engines operate in coastal regions

where NaCl may be a significant source of contamination, particularly in marine and industrial applications where low-grade fuel oils with high S-contents are routinely burned. These salt deposits can result in highly accelerated degradation at elevated temperatures. This severe and sometimes catastrophic degradation process has been termed “hot corrosion”.

Much of the work that has been done in the area of Na₂SO₄-induced hot corrosion has focused on identifying the mechanisms that are active during the very rapid period of attack known as the “propagation stage”. From a practical standpoint, however, we are more concerned with extending the “incubation stage”, i.e., the period during which the alloy or coating is able to resist extensive degradation by the salt. Very little work has been done to determine the factors that influence the duration of the incubation stage; such knowledge is vital for the successful design of hot corrosion-resistant coatings.

Modern coatings are based largely on either the MCrAlY (M = Ni and/or Co) or Pt-modified NiAl systems. MCrAlY overlay coatings are multi-phase alloys rich in Al and Cr, with minor additions of reactive elements such as Y or Hf for improved oxide-scale adhesion [2]. These coatings are typically applied via a low-pressure plasma spray process. Pt-modified β -NiAl coatings are typically applied by a pack cementation or CVD process, preceded by the electrodeposition of a thin layer of Pt [3]. These so-called “diffusion coatings” are very widely used and form adherent, slowly-growing α -Al₂O₃ scales during high-temperature oxidation.

Previous work has demonstrated the very strong dependence of the hot corrosion performance of MCrAlY alloys on alloy composition [4]. The results of this study also suggest a significant correlation between alloy microstructure and resistance to Type II hot corrosion. Therefore, in the current study, a systematic investigation of the effect of microstructure on the hot corrosion resistance of MCrAlY alloys was undertaken. Attention was paid primarily to the

effects of microstructural scale and phase composition. In some cases, specimens were also tested after a pre-oxidation treatment, and the effect of this pre-formed scale on hot corrosion resistance was evaluated.

β - (Ni, Pt)Al alloys, by the nature of the deposition process, have a strong compositional dependence on the substrate alloy. During high-temperature exposure, Al is removed from the coating at the coating/oxide interface due to oxide formation, and also at the base of the coating due to coating/substrate interdiffusion. This interdiffusion occurs as a result of an Al activity mismatch between the coating and substrate. Similarly, elements from the superalloy substrate, such as Co, Cr, and various refractory elements, diffuse into the coating during deposition and high temperature exposure. This coating/substrate interdiffusion has a negative impact on the oxidation resistance as Al is depleted from the coating, and also on the mechanical integrity of the coating due to the formation of an interdiffusion zone which contains refractory-element rich topologically close-packed (TCP) phases [5].

Lesser known is the effect of this depletion and interdiffusion on the hot corrosion behavior of these coatings. Consequently, another goal of the current research was to assess the hot corrosion behavior of β - NiAl base alloys and how it depends on alloy composition. The primary focus was to characterize the effects of composition on the duration of the incubation stage, i.e., on the ability of these alloy systems to form protective Al_2O_3 scales under hot corrosion conditions, to maintain the growth of these scales throughout the exposure, and to reform them if they sustain damage. The nature of the Al_2O_3 scales that form, i.e., scale composition and phase stability, were characterized using advanced techniques. Model alloys were evaluated so that specimen composition could be carefully controlled. The results of this

study serve to elucidate the mechanisms by which various alloying additions influence the hot corrosion behavior of β - (Ni, Pt)Al coatings, thus guiding coating development.

2.0 BACKGROUND

2.1 FORMATION OF SALT DEPOSITS ON GAS TURBINE HARDWARE

In gas turbine engines, particularly those used in coastal regions or for marine propulsion, Na_2SO_4 -rich salt deposits commonly develop on turbine vanes and blades. When the environment is such that these salts are molten, conditions can develop for severe hot corrosion. In order to understand and combat hot corrosion in these systems, an appreciation of the origin of these corrosive salts is necessary.

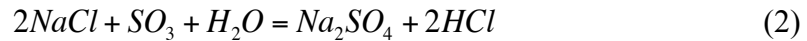
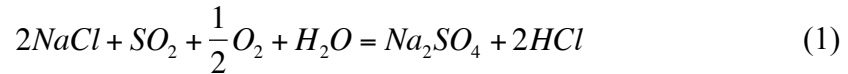
The approximate composition of sea salt is presented in [1].

Table 1. Approximate sea salt composition

Ion	Concentration (wt%)	Concentration (mole%)
Na^+	30.3	42.04
K^+	0.52	0.35
Mg^{2+}	3.69	4.85
Ca^{2+}	1.26	1.02
Cl^-	54.78	49.25
SO_4^{2-}	7.44	2.49

It is generally believed that the Na_2SO_4 found in the hot sections of a gas turbine can either be directly deposited due to impact of ingested sea salt particles, or condensed from the vapor phase [6]. In order for vapor phase condensation to occur, sulfur, which is commonly present as a fuel impurity, must be oxidized to SO_2 and/or SO_3 in the combustor section of the engine. These species then react with oxygen and gaseous NaCl , which has been introduced via sea salt impurities in either the intake air or the fuel. If the surface temperature of the turbine hardware is below the dew point of Na_2SO_4 , which is determined by the concentration of ingested salt and the level of sulfur in the fuel, then a condensed sulfate deposit will be formed.

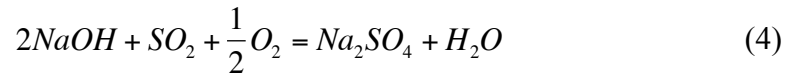
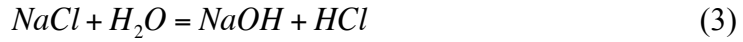
DeCrescente and Bornstein [7] studied this process using basic thermodynamic considerations, assuming 1 ppm NaCl (v) and 0.4 wt% S in the fuel. The following two reactions were considered.



All species in Equations (1) and (2) are present in the vapor phase. It was found that the reaction between NaCl and SO_2 , Equation (1), proceeded to 75% completion at 1000°C and 1 atm total pressure. Consideration of Le Chatelier's Principle reveals that an increase in total pressure would result in an increase in the degree of $\text{NaCl} \rightarrow \text{Na}_2\text{SO}_4$ conversion. The investigators therefore concluded that the high pressure ratios present in a gas turbine engine should cause complete conversion to gaseous sulfate.

The gaseous phases present after combustion in a gas turbine engine were further studied by Hanby and Beer [8] who suggested that at significantly high temperatures, NaCl vapor may

be converted to Na_2SO_4 with NaOH as an intermediate species according to the following series of reactions:



In addition, these investigators determined, using a controlled mixing history combustor, that the degree of gas phase sulfation of NaCl to Na_2SO_4 changes very little with sulfur concentration in the fuel (from 0.1 – 1 wt%) and NaCl concentration in the intake air (from 10 – 50 ppm).

Noteworthy temperature dependence does exist, with the degree of sulfation increasing as the gas temperature is increased from 1190°C to 1350°C.

As mentioned above, direct impact of ingested sea salt particles with turbine hardware can also result in the formation of a Na_2SO_4 deposit. Bornstein and Allen [1] investigated the exact mechanism of salt deposition on turbine airfoils. Salts deposited on the compressor as well as the inner and outer surfaces of internally cooled vanes and blades from an industrial turbine were evaluated using Inductively Coupled Plasma, ion chromatography, and Electron Probe Micro Analysis. Two key observations were made. Firstly, the salts taken from the first three turbine stages were equivalent in both amount and composition. In addition, the compositions of the salts sampled from the internal and external surfaces of the first and second stage airfoils were comparable. The surface temperature of the turbine hardware would be expected to decrease in the latter stages of the engine. Also, the temperature of the internal surfaces would clearly be lower than the external surfaces. If gas-phase condensation were the dominant salt deposition mechanism, these temperature differences would result in differences in the amount and composition of salt deposited in various regions. Such differences were not observed, and

therefore it was concluded that impact deposition of salt particles on turbine airfoils is likely the central mechanism.

The results of earlier work by McCreath [6] support this conclusion under certain conditions. This research demonstrated that at a constant engine load, nearly 96 wt. % of the salt ingested into a naval gas turbine engine through the air intake was filtered out in the compressor section. During acceleration from idle conditions to full power, considerable salt shedding from the compressor was observed. Thus, sulfate deposits found downstream from the compressor can conceivably be the result of salt shedding from the compressor, but this was found to be significant only during transient engine conditions.

2.2 Na_2SO_4 – INDUCED HOT CORROSION

Regardless of the manner in which the Na_2SO_4 is deposited, it can be highly corrosive if present as a molten film. If the temperature of the environment is above the melting point of Na_2SO_4 ($T_m=884^\circ\text{C}$ [9]), the resulting degradation is typically termed Type I, or high temperature hot corrosion. As discussed in Section 2.2.3, a corrosive Na_2SO_4 -based molten salt can also form below 884°C as a result of a chemical interaction with the combustion gas and underlying alloy. This highly accelerated, self-sustaining form of corrosion has been termed Type II, or low temperature hot corrosion. These two forms of hot corrosion are quite distinct mechanistically and occur under significantly different environmental conditions. Together they constitute the primary modes of degradation considered in this study; therefore a comprehensive review of the available hot corrosion literature is presented below.

2.2.1 The Stages of Hot Corrosion

Hot corrosion can be considered to occur in two distinct stages, initiation and propagation [3]. These two stages are demonstrated , in which the weight change per unit area for a Ni-8Cr-6Al (wt%) alloy exposed to Type I hot corrosion conditions is plotted as a function time. The specimen was coated with $2\text{--}3\text{ mg cm}^{-2}$ Na_2SO_4 every 20 hours and exposed at 900°C .

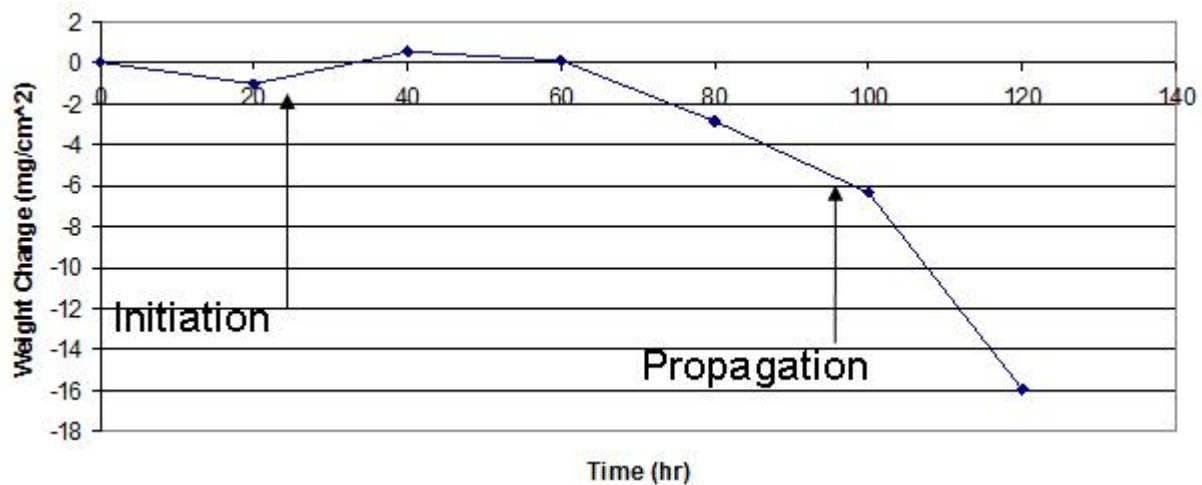


Figure 1. Plot of weight change per unit area vs. time for a Ni-8Cr-6Al (wt%) alloy exposed to Type I hot corrosion conditions, demonstrating the initiation and propagation stages of hot corrosion

In , the existence of two distinct stages is demonstrated. During the initiation stage, i.e. up to approximately 60 hours of exposure, weight changes are relatively small and no catastrophic degradation occurs. During the propagation stage, beginning at roughly 60 hours, severe degradation commences and large weight losses are observed as a result of rapid oxidation and scale spallation. It is important to note that shows the behavior of an

alloy which is known to be quite susceptible to this type of hot corrosion; thus, the initiation stage is relatively short. The duration of the initiation stage can vary considerably for different alloys exposed under the same conditions. For example, CoCrAlY alloys can typically be exposed for well over 1000 hours under the above conditions before the propagation stage commences. In fact, it has been established that the length of the initiation stage is highly dependent on a number of variables related to alloy composition and exposure conditions.

2.2.1.1 Initiation Stage During the initiation stage of the hot corrosion of metals and alloys, the chemical processes that take place are quite similar to those that occur during simple oxidation. Specifically, metallic elements are oxidized and some other species, typically oxygen, is reduced to form an external scale [3]. One important difference between this process and simple oxidation is that during hot corrosion, the reducible species can originate from the salt deposit. This alloy-salt interaction can ultimately result in the local development of extremely corrosive conditions due to a gradual shift to highly basic or acidic salt compositions. In time, the deposit becomes sufficiently corrosive to cause the breakdown of the protective scale, and the propagation stage commences.

In Fig 2, a schematic phase stability diagram for the Na-S-O system is shown. The large dot in the Na_2SO_4 phase field indicates the composition of the initially-deposited salt, as defined by the parameters $\log p_{\text{O}_2}$ and $-\log a_{\text{Na}_2\text{O}}$ (see section 2.2.1.2 for a more thorough explanation of these compositional parameters and phase stability diagrams in general)

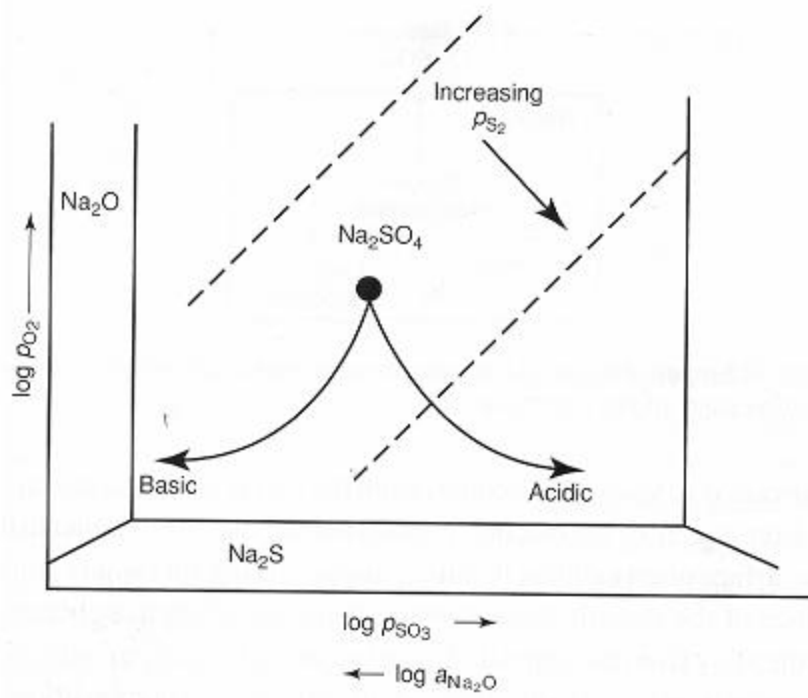


Figure 2. Schematic phase stability diagram for the Na-S-O system, showing schematically the compositional changes that can lead to corrosive conditions in the salt.

This diagram roughly illustrates the compositional changes that can occur in the Na_2SO_4 deposit during the initiation stage. It is seen that locally the salt can become more basic (higher $a_{\text{Na}_2\text{O}}$) or more acidic (lower $a_{\text{Na}_2\text{O}}$) as a result of interaction with the underlying alloy. In certain situations, interaction with the gas can also be important.

Some of the factors that have been shown to influence the processes which occur during the initiation stage as well as its duration, as outlined in detail in reference [10], are summarized below. As will be discussed subsequently, the available hot corrosion literature is generally lacking in detailed studies of the processes occurring during the incubation stage; this is the main driving force for the current work.

Alloy Composition: As noted above, Co-base materials generally exhibit extended initiation stages relative to Ni-base alloys during Type I hot corrosion; however, under Type II conditions, the behavior of the two alloys systems is reversed. For example, Deodeshmukh and Gleeson [11] found that the addition of Co to β -(Ni,Pt)Al coatings greatly decreased the resistance of these materials to Type II hot corrosion attack. In Sections 2.2.2 and 2.2.3, the mechanisms of hot corrosion propagation, in addition to the effect of composition on these processes, will be discussed in more detail. A more thorough determination of the influence of alloy composition on the duration of the incubation stage, and the mechanisms by which various species exert this influence, is one of the major goals of the current research.

Alloy Condition: The condition of the material, i.e., as-cast vs. homogenized vs. vapor deposited, can have a large effect on hot corrosion resistance. For example, the first metal to solidify in an as-cast material would, in many cases, be expected to be solute-lean (there are exceptions to this in, for example, peritectic alloy systems). The incubation period can be extremely short in these localized Cr- and Al- depleted regions resulting in an overall reduction in corrosion resistance. The influence of microstructure and phase composition is also addressed in the current work in the case of MCrAlY alloy systems.

Gas Composition: The composition of the gas has a large impact on the duration of the initiation stage, particularly at temperatures below the melting point of Na_2SO_4 . At these relatively low temperatures, commonly those considered during Type II hot corrosion, the initiation stage may persist indefinitely when SO_2/SO_3 are not present in the atmosphere. These gaseous species have a pronounced effect on the physical and chemical state of the salt deposit, the exact nature of which will be described subsequently.

Amount of Salt Deposit: It has been generally accepted that the greater the amount of salt deposited on a specimen, the more severe the hot corrosion. However, it has been observed in Ref. [11] that in most cases this is only true up to some limiting deposit thickness. The Type I hot corrosion resistance of (Ni,Pt)Al diffusion coatings was decreased when the salt deposition rate increased from 1 to 8 mg/cm². When the sample was buried in salt, no discernable hot corrosion attack was observed. Similarly, minimal Type II hot corrosion attack was observed when a Ni-base superalloy was buried in salt, while severe attack occurred when deposits of 1 to 8 mg/cm² were applied.

Temperature: The exposure temperature has a marked effect on the observed hot corrosion processes. As previously mentioned, it is well accepted that a molten salt deposit is required to initiate severe hot corrosion. At temperatures above the melting temperature of Na₂SO₄, the salt will clearly be molten and conditions may develop which are conducive to Type I attack. Below this temperature, severe corrosion will typically not occur in the absence of SO₂/SO₃ gas mixtures or other salt deposits which may form eutectics with Na₂SO₄.

2.2.1.2 Propagation Stage Three commonly encountered propagation modes have been mechanistically developed in the literature: basic fluxing, alloy-induced acidic fluxing, and gas phase-induced acidic fluxing. The first two occur at relatively high temperatures (~900°C - 1000°C) and thus fall into the category of high temperature (Type I) hot corrosion. Gas phase-induced acidic fluxing occurs at lower temperatures (~650°C - 750°C) and is, therefore, termed low temperature (Type II) hot corrosion. Which of these propagation modes occurs is largely dependent on the way in which the alloy and salt are preconditioned during the initiation stage; all of the variables discussed in section 2.2.1.1 are therefore extremely influential.

Na_2SO_4 is an oxyanion salt which displays an acid-base character with $\text{SO}_3(\text{g})$ being the acidic component and oxide ions, present as Na_2O , the Lewis base [12]. With this convenient definition, one can describe the composition of a Na_2SO_4 melt by specifying the oxygen potential, p_{O_2} and the basicity, $a_{\text{Na}_2\text{O}}$. Equivalently, the salt chemistry can be expressed by considering the SO_3 potential in the melt, since this is linked to the Na_2O activity via the equilibrium represented in Equation (5) [3]:



An underlined chemical formula indicates that the species is in solution.

Thermodynamic stability diagrams are very useful in describing the phases that are expected to be stable during hot corrosion. Figure 3 shows such a diagram for the Cr-S-O system superimposed onto the Na_2SO_4 portion of the Na-S-O stability diagram for $T = 1200\text{K}$ [13]. In these isothermal diagrams, p_{O_2} is plotted vs. $-\log a_{\text{Na}_2\text{O}}$, and the thermodynamically stable phase under a given set of conditions can be clearly ascertained. The dashed lines in this plot indicate lines of constant solute activity.

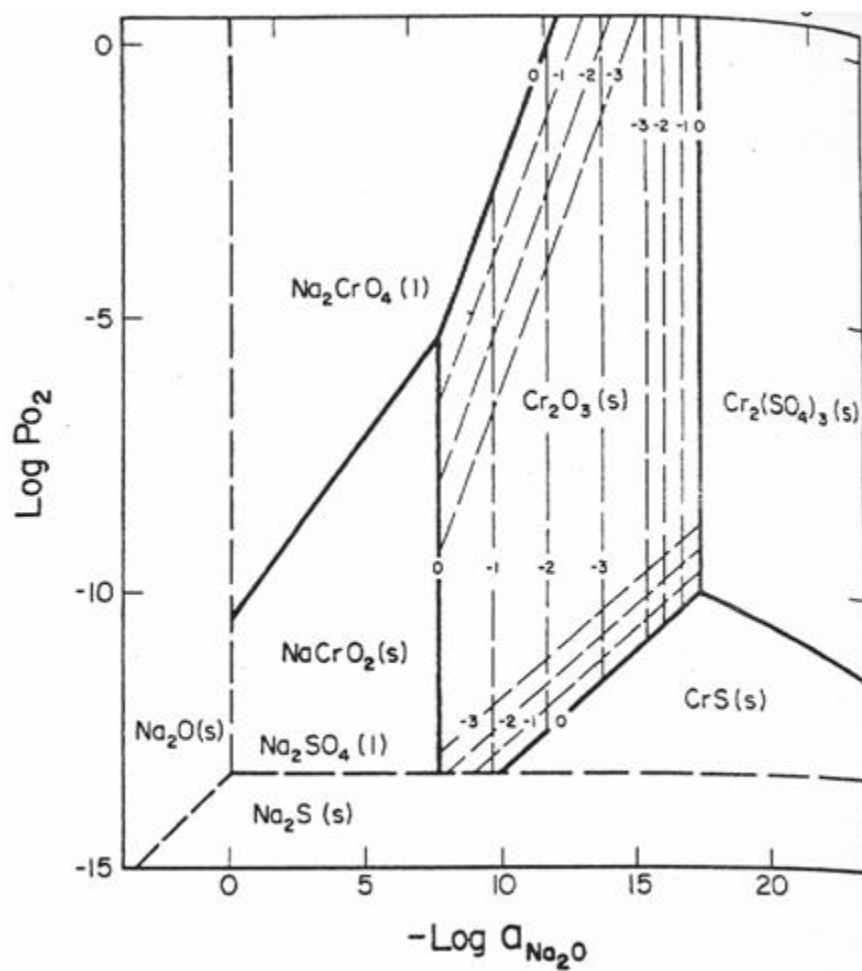


Figure 3. Thermodynamic stability diagram for the Cr-S-O system superimposed onto the Na_2SO_4 portion of the Na-S-O stability diagram at $T = 1200\text{K}$

Such compound phase stability diagrams are extremely useful when one is attempting to determine if a given protective oxide, Cr_2O_3 in this example, will dissolve in the presence of a molten salt, and if so, what solutes will be expected. According to Fig 3, Cr (s) is never stable in the presence of molten Na_2SO_4 at 1200K. Also, we see that at this temperature there are four possible solute species that can form, two basic solutes and two acidic solutes. Cr_2O_3 dissolves as one of the basic solutes, Na_2CrO_4 or NaCrO_2 , in moderately basic salts. Conversely, if acidic conditions are developed in the salt, chromia can dissolve as either $\text{Cr}_2(\text{SO}_4)_3$ or CrS , depending on the oxygen potential. Similar diagrams for the other pertinent oxides have been developed in references [14-17].

It is of great engineering importance not only to know the identities of the stable phases as a function of salt composition, but also the degree to which a given oxide will dissolve in the melt. Using high temperature reference electrodes, the solubilities of NiO , Co_3O_4 , and Al_2O_3 in Na_2SO_4 melts have been measured as a function of melt basicity at $p_{\text{O}_2} = 1 \text{ atm}$ and $T = 1200^\circ\text{K}$ [14-17]. A compilation of the results, combined with similar curves for Fe_2O_3 and Cr_2O_3 , is presented in Fig 4 [13]:

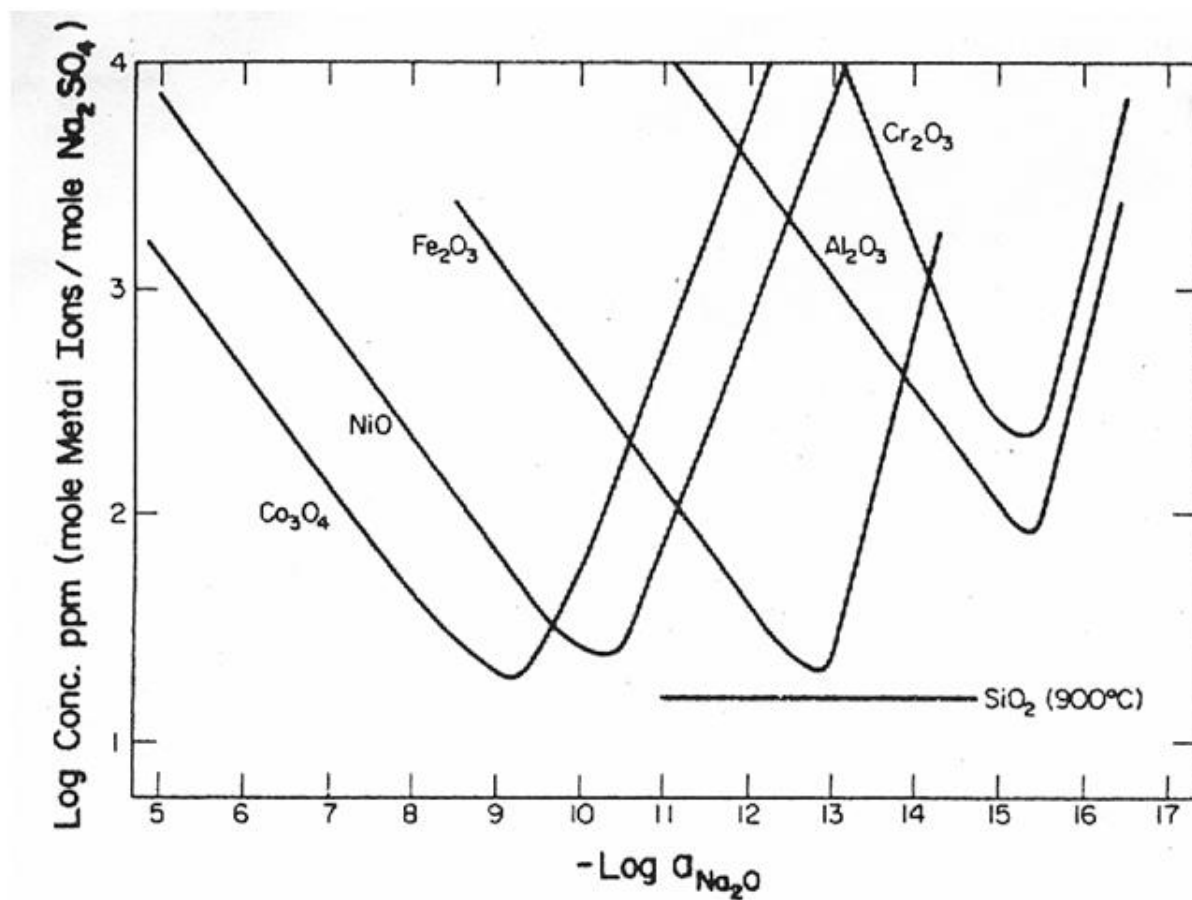
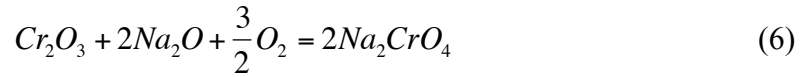


Figure 4. Solubilities of various oxides in Na_2SO_4 as a function of melt basicity at $p_{\text{O}_2} = 1$ atm and $T = 1200^\circ\text{K}$

It is observed that the solubility minima for these oxides occur over a range of approximately 6 orders of magnitude with respect to salt basicity, which clearly demonstrates the importance of local salt chemistry on the hot corrosion process.

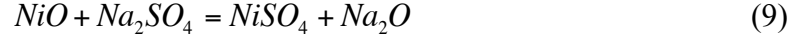
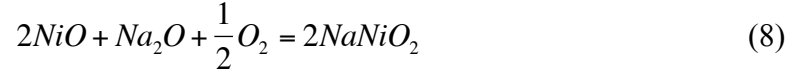
It is also worthwhile to note that the above solubility plots are constructed at a constant p_{O_2} . In general, these oxide solubilities will be a function of oxygen potential. Consider the basic dissolution of Cr_2O_3 and Al_2O_3 in Na_2SO_4 [3]:



According to Equations (6) and (7), the Cr ion is oxidized from Cr^{3+} to Cr^{6+} during basic dissolution, while no such change in valence occurs for the Al^{3+} ion. As a result, the solubility of Cr_2O_3 in Na_2SO_4 is expected to increase with p_{O_2} , while the solubility of Al_2O_3 should exhibit no such dependence. Rapp and Otsuka [18] use this fact in an attempt to explain why Cr has such a positive effect on the hot corrosion resistance of most alloys. The p_{O_2} , and thus the solubility of Cr_2O_3 in the salt deposit, increases with increasing distance from the salt/oxide interface, and so the “negative oxide solubility gradient” criteria for continued hot corrosion (discussed below) cannot be met. The dependencies of oxide solubility on p_{O_2} have been measured for Cr_2O_3 [19], Fe_2O_3 [20], and Fe_3O_4 [20], for which very good agreement with thermodynamic prediction has been observed.

The shapes of these solubility curves can be predicted with remarkably good accuracy by simple thermodynamic calculations. Nickel oxide will be considered as an example. The

reactions for the basic and acidic dissolution of NiO are shown in Equations (8) and (9), respectively:



Assuming unit NiO activity, the equilibrium constant for the basic dissolution of NiO can be expressed as

$$K = \frac{a_{NaNiO_2}^2}{a_{Na_2O} p_{O_2}^{1/2}} \quad (10)$$

Taking the logarithm of both sides, solving for a_{NaNiO_2} , and differentiating with respect to $-\log a_{Na_2O}$, one finds

$$\left[\frac{\partial \log a_{NaNiO_2}}{\partial (-\log a_{Na_2O})} \right] = -\frac{1}{2} \quad (11)$$

This is the slope of the leftmost portion of the NiO dissolution curve in Fig 4, i.e., the portion representing the basic dissolution of NiO. Similarly for the acidic dissolution reaction, Equation (9):

$$K = a_{NiSO_4} a_{Na_2O} \quad (12)$$

$$\left[\frac{\partial \log a_{NiSO_4}}{\partial (-\log a_{Na_2O})} \right] = 1 \quad (13)$$

Equation (13) gives the slope of the rightmost portion of the NiO dissolution curve in Fig 4, i.e. the portion representing the acidic dissolution of NiO.

Rapp and Goto [21] proposed a general criterion which must be fulfilled in order for self-sustained hot corrosion attack to occur. This useful criterion can be most simply expressed as

$$\left[\frac{d[\text{oxide solubility}]}{dx} \right]_{x=0} < 0 \quad (14)$$

where x is the distance into the molten salt film from the oxide/salt interface. According to this proposed model, a negative gradient in the oxide solubility at the oxide/salt interface will result in the dissolution of the protective oxide at this interface and reprecipitation of the oxide as discrete, non-protective particles in regions of the salt where the solubility is lower.

The oxide solubility that is addressed in Equation (14) is a function of melt basicity (Fig 4) and in some cases p_{O_2} . Therefore, at a constant p_{O_2} , a basicity gradient must develop in the salt such that the oxide solubility gradient is negative at the oxide/salt interface. The sign of this basicity gradient will depend on whether the oxide is dissolving as an acidic or basic solute. Figure 5 schematically shows conditions in the salt which would satisfy the Rapp-Goto criterion and allow the hot corrosion of a material with a hypothetical surface oxide to occur [21]:

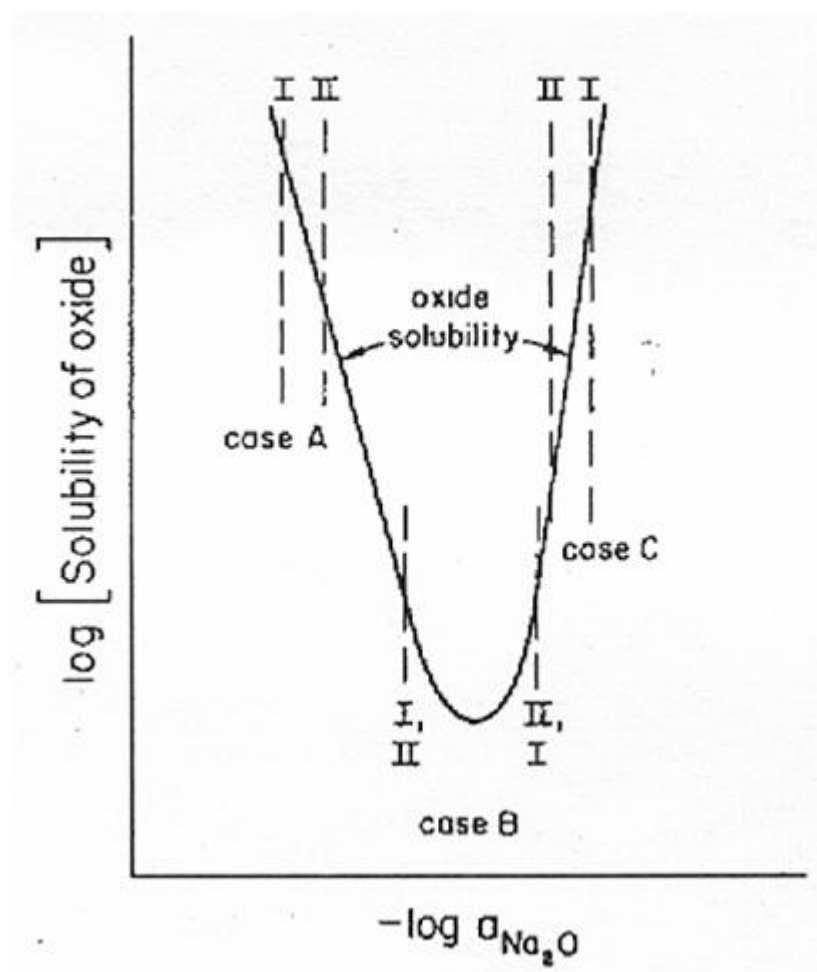
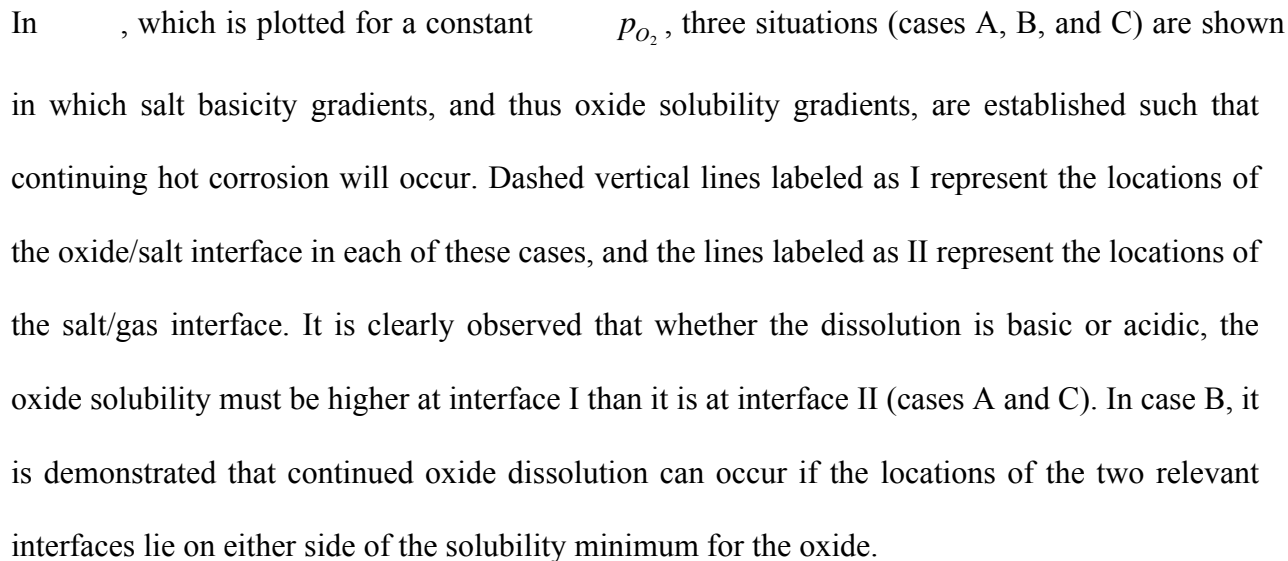


Figure 5. Schematic of the Rapp-Goto negative solubility gradient criterion

In , which is plotted for a constant p_{O_2} , three situations (cases A, B, and C) are shown in which salt basicity gradients, and thus oxide solubility gradients, are established such that continuing hot corrosion will occur. Dashed vertical lines labeled as I represent the locations of the oxide/salt interface in each of these cases, and the lines labeled as II represent the locations of the salt/gas interface. It is clearly observed that whether the dissolution is basic or acidic, the oxide solubility must be higher at interface I than it is at interface II (cases A and C). In case B, it is demonstrated that continued oxide dissolution can occur if the locations of the two relevant interfaces lie on either side of the solubility minimum for the oxide.

The discussion has thus far been concerned with hot corrosion in general and the thermodynamic tools which can be used to predict how it will proceed under various environmental conditions. In the following two sections, the exact processes that occur during the propagation stage of Na_2SO_4 – induced hot corrosion will be described in detail.

2.2.2 High Temperature (Type I) Hot Corrosion

Type I hot corrosion is known to occur at relatively high temperatures, approximately 900°C - 1000°C . There are generally two forms of this high temperature attack that can occur. One involves the dissolution of the protective oxide scale due to the formation of a highly basic melt (high $a_{\text{Na}_2\text{O}}$) and the other results from the development of a highly acidic melt (high p_{SO_3}). In spite of the obvious differences that exist between these two propagation modes, they have in common the characteristic that the local corrosive conditions in the salt arise from the interaction between the salt and the underlying material. Dissolution of oxides into a basic melt, henceforth

referred to as basic fluxing, was the first hot corrosion mechanism to be studied and characterized mechanistically.

2.2.2.1 Basic Fluxing In the early stages of hot corrosion research, it was quickly recognized that a salt deposit composed principally of Na_2SO_4 was responsible for the observed accelerated oxidation, however there were a number of schools of thought concerning the operative degradation mechanism. The first of these was primarily focused on the oxidation of sulfides that were commonly observed in hot corrosion (a.k.a. “sulfidation”) microstructures. Simons et al [22] were among the first to suggest that sulfidation attack was the result of rapid oxidation of sulfide phases which form when a reducing agent in the alloy reacts with the salt deposit. Quets and Drescher [23] were also advocates of the sulfidation/oxidation mechanism. They suggested, however, that the formation of alkali compounds such as NaAlO_2 and Na_2CrO_4 were necessary to achieve sulfur potentials that were sufficient to form sulfides within the alloy.

An alternative stance was that taken by Danek [24] and Seybolt [25]. These investigators concluded that the decreased oxidation resistance observed in the presence of Na_2SO_4 films was attributable to Cr-depletion in the substrate alloy. Seybolt [25] studied ternary Ni-Cr-X alloys as well as various commercial Ni-base superalloys and determined that the decrease in oxidation resistance in the presence of the salt is the result of Cr-depletion which results from the precipitation of Cr_xS_y particles within the alloy. This hypothesis was tested by oxidizing a Udimet 500 specimen which was modified such that the Cr content was reduced to levels found in the regions adjacent to chromium sulfides in previously hot corroded specimens. This modified superalloy did indeed demonstrate reduced oxidation resistance. The author also

concluded that the oxidation of chromium sulfides perpetuates the reaction by releasing sulfur according to the following reaction:



This sulfur can then diffuse into the alloy resulting in further chromium sulfide formation. When the oxidation front reaches these new sulfides, they will be oxidized, releasing sulfur, and the process will continue.

The first step towards the currently-accepted basic fluxing mechanism was taken by Bornstein and DeCrescente [26]. These investigators studied the oxidation of three superalloys, B-1900, U-700 (both Al_2O_3 -formers), and Waspaloy (Cr_2O_3 -former) at $900^\circ C$ with and without deposits of Na_2SO_4 and $NaNO_3$. A sulfur impregnation was also performed prior to oxidation both with and without a $NaNO_3$ deposit. The experiments were designed principally to test the importance of sulfur in the hot corrosion process. The results showed that both salts resulted in the same amount of degradation, which was greatly accelerated in the case of the alumina-formers and not in the case of Waspaloy. The only microstructural difference was the formation of sulfides when Na_2SO_4 deposits were applied; sulfides were clearly absent when $NaNO_3$ was deposited. All salt-induced corrosion produced microstructures consisting of a porous external oxide and an alloy-depleted zone beneath the scale. Importantly, sulfur impregnation did not accelerate the oxidation of any specimen with or without a $NaNO_3$ deposit. The authors concluded that the formation and/or oxidation of sulfides does not directly cause the observed accelerated oxidation during hot corrosion. Rather, it is an interaction between oxide ions in the salt and the substrate which renders the scale non-protective and results in accelerated rates of

degradation. When Na_2SO_4 is applied, the removal of sulfur from the salt via chromium-rich sulfide formation in the substrate produces oxide ions in the melt. These accrued oxide ions (present as Na_2O) somehow interact with the substrate resulting in accelerated oxidation.

Goebel and Pettit [27] conducted a series of experiments with pure Ni in order to test and further develop this theory. It was first determined that a condensed salt is necessary for hot corrosion attack of pure Ni to occur; gaseous Na_2SO_4 did not result in the accelerated oxidation that is observed when the sulfate is condensed. The condensed salt has the same composition as the vapor from which it condensed. Therefore, a concentration gradient must develop across the molten salt, which is unable to form in the gaseous phase due to rapid transport rates.

Specimens of Ni oxidized at 1000°C in the presence of a molten Na_2SO_4 deposit generally displayed accelerated oxidation kinetics during the early stages of exposure which slowed to normal parabolic growth kinetics after approximately 6 minutes [27]. The microstructure consisted of an internal layer of NiS below a dense layer of NiO, above which a porous, nonprotective NiO layer was present. These observations led the authors to the following mechanism for the hot corrosion of Ni at 1000°C .

By constructing a phase stability diagram for the Na-Ni-S-O system, it was determined that in the presence of laboratory grade Na_2SO_4 at 1000°C , NiO should be stable on the surface of Ni [27]. The oxygen required for NiO formation must be supplied either by gaseous oxygen dissolved in the molten salt or by the decomposition of sulfate ions, Equation 16:



As oxygen is consumed at the NiO/salt interface, a p_{O_2} gradient will develop across the salt if molecular oxygen is unable to diffuse to the interface from the atmosphere. It has been shown that the solubility of oxygen in Na_2SO_4 is in fact quite low, and the oxidant with significant solubility in the salt is SO_3 (as $S_2O_7^{2-}$) [28-31]. Therefore, a positive oxygen potential gradient will develop at the NiO/ Na_2SO_4 interface, resulting in a locally high sulfur potential according to the Reaction 17:



In the presence of two oxidants, S_2 and O_2 in this case, both at sufficient activities to form their respective phases (sulfide and oxide) in the absence of the other oxidant, phase stability at the metal surface will be determined by the ratio $\frac{p_{O_2}}{p_{S_2}}$ according to Equation 18:

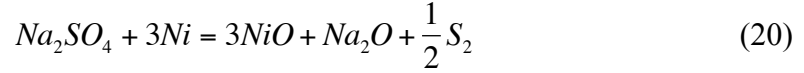


Therefore, at the surface of the NiO, NiS will likely be unstable unless very significant amounts of oxygen are removed from the salt. However, if sulfur can diffuse through the oxide to the region of low p_{O_2} at its base, it has been demonstrated that a subscale of NiS can form beneath NiO [32], which was indeed observed. As sulfur is removed from the Na_2SO_4 adjacent to the

substrate by diffusing through the NiO scale to form internal NiS, oxide ions are produced in this region according to Equation 19:



Thus, the net effect of sulfur removal is an increase in the oxide ion activity at the salt/scale interface, described by the following overall reaction:



When the oxide ion activity in the melt adjacent to the NiO scale reaches sufficiently high values, the following reaction can occur:



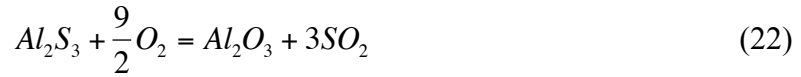
i.e. NiO reacts with oxide ions in the melt to form nickelate ions, NiO_2^{2-} , which are soluble in molten Na_2SO_4 . The high oxide ion activity that is achieved is localized at the salt/scale interface, and therefore as the nickelate ions diffuse out into the salt, they encounter regions of lower oxide ion activity and precipitate out as discontinuous, nonprotective oxide particles according to the reverse of Equation 21. This, the researchers proposed, is the source of the porous NiO scale observed on hot corroded pure Ni.

As mentioned above, the accelerated oxidation of Ni seems to come to a halt after approximately 6 hours at 1000°C [27]. To explain this, it is noted that eventually very high oxide ion activities will result in very low sulfur potentials, NiS will cease to be formed and the oxide ion concentration will stabilize at some higher level. When this occurs, a continuous, protective layer of NiO will form below the porous outer scale and the accelerated oxidation will stop.

It is instructive to evaluate this mechanism in terms of the Rapp-Goto criterion, which is concisely stated in Equation 14 [21]. During the propagation stage, the oxide ion activity is higher at the NiO/salt interface than it is in regions of the salt further from this interface. According to Equation 21, this is equivalent to stating that the NiO solubility is greater at the NiO/salt interface than it is further out in the salt, i.e. there is a negative gradient in the oxide solubility at this interface (see Fig 5, Case A). According to Equation 14, accelerated oxidation should occur, as observed. When NiS formation ceases and the oxide ion activity stabilizes throughout the salt, the NiO solubility gradient flattens and accelerated oxidation stops, in accord with Eq. 14.

Further tests were conducted by Goebel and Pettit to determine the effect of sulfur on the hot corrosion of Ni-base alloys [33]. Pure Cr, Ni-Cr, Ni-Al, and various chromia- and alumina-forming superalloys were oxidized in pure O_2 at 1000°C after a presulfidizing treatment in an H_2/H_2S environment in order to observe the effect of sulfur on the subsequent oxidation behavior of these materials. In the case of pure Cr, the presulfidation treatment had no effect on the oxidation behavior; a protective layer of Cr_2O_3 formed over the preformed layer of CrS. During the oxidation of the Ni-Cr alloys, it was observed that presulfidation increased the rate of oxidation only if NiS was formed, which is liquid at 1000°C. If this occurs, the external Cr_2O_3 layer is permeated with NiS, which provides rapid diffusion paths for oxygen, and oxidation is

accelerated. Al₂O₃-forming Ni-Al alloys oxidized at an accelerated rate only if the Al activity in the alloy was high enough to form Al₂S₃. The subsequent oxidation of these sulfides resulted in a release of SO₂ per Equation 22

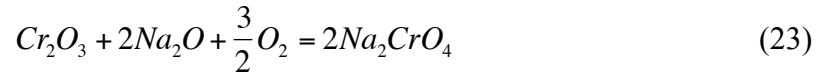


which prevented the formation of a protective Al₂O₃ layer. If the Al activity was insufficient to form Al₂S₃, only NiS was formed, and during oxidation Al was selectively oxidized to form a protective external Al₂O₃ scale. The chromia forming superalloys behaved similarly to the Ni-Cr alloys during oxidation, while the alumina forming superalloys behaved similarly to the Ni-Al alloys which did not form Al₂S₃. These results showed that hot corrosion mechanisms which depend on oxidation of sulfides at temperatures ~1000°C are only feasible for non-Al₂O₃-forming superalloys and high activity Ni-Al alloys.

Bornstein and DeCrescente [34] oxidized samples of B-1900, Waspaloy, and various binary Ni-Cr and Ni-Al alloys at 800°C - 1000°C with deposits of Na₂SO₄ and Na₂CO₃ to further understand the effect of deposit composition on the hot corrosion process. It was observed that the oxidation of the Al₂O₃-forming B-1900 alloy was accelerated equally by both salts. The kinetics of the oxidation in the presence of each salt could be described by a modified parabolic relationship, suggesting that diffusion through the scale was the rate limiting process. However, removal of the scale during the test resulted in no change in the oxidation rate. Arrhenius plots were used to determine that the activation energies for both processes were approximately equal. Oxidation of the Cr₂O₃ - forming Waspaloy was not accelerated by either salt and displayed parabolic scale-growth kinetics. Ni-5Cr, Ni-8Cr, Ni-13Cr, and Ni-17Cr alloys did not oxidize in

an accelerated manner at 900°C or 1000°C, but the two higher-Cr alloys showed steady weight losses after approximately 100 minutes at 1000°C in the presence of both deposits. Soluble chromium was found in the wash water after exposure of the binary Ni-Cr alloys. Finally, Na₂CO₃ deposits did not cause accelerated degradation of pure Ni, however Ni-1Al was oxidized at a rate similar to that observed for B-1900 with this same deposit. It had previously been shown that the oxidation of pure Ni is greatly enhanced by Na₂SO₄ [27].

A number of conclusions were drawn from this work [34]. Firstly, the lack of degradation of the Ni-Cr alloys suggested that Cr is beneficial for hot corrosion resistance due to the formation and dissolution of Cr₂O₃, which lowers oxide ion levels at the oxide/salt interface according to the following reaction:

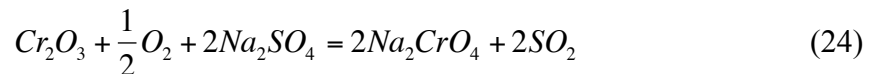


The chemical analysis of the wash water did indeed contain soluble Cr ions, however no further substantiation of this mechanism was provided. The authors also concluded that the weight losses observed in the case of the Ni-13Cr and Ni-17Cr at 1000°C were due to the evaporation of Na₂CrO₄.

It has been observed that the equilibrium oxide ion content of Na₂CO₃ is at least as high as that of Na₂SO₄ at 1000°C [24]. Therefore, to explain the observation that Na₂CO₃ did not result in rapid oxidation of pure Ni, while Na₂SO₄ did result in such attack, it was mentioned that while NiS formation results in an increase in oxide ion activity in the presence of a sulfate deposit, there is no analogous reaction for a carbonate deposit [34]. It was asserted that Na₂CO₃

accelerates the oxidation of Ni-1Al because the formation of NaAlO₂ promotes the formation of oxide ions. The proposed reaction was not, however, explained in detail.

Goebel et al [35] performed a number of oxidation experiments on various commercial and model alloys containing elements such as Cr, Al, Mo, W, and V in order to clearly determine the effect of alloy composition on Na₂SO₄-induced hot corrosion. It was concluded that there are generally two types of high temperature hot corrosion: Na₂SO₄-induced accelerated oxidation and Na₂SO₄-induced catastrophic oxidation. The latter has since been termed “alloy-induced acidic fluxing” and will be discussed in more detail in Section 2.2.2.2. The former, Na₂SO₄-induced accelerated oxidation, is a basic fluxing mechanism which was found to occur when the alloy contained no molybdenum (catastrophic oxidation, as will be seen, occurs when elements typified by Mo are present in the alloy). Ni-1Al and Ni-31Al alloys showed slightly accelerated oxidation in the presence of 0.5 mg/cm² Na₂SO₄, and in the presence of thicker deposits a very rapid, breakaway oxidation was observed for the Ni-31Al. Sulfur entered the alloy from the beginning of the exposure, and water soluble NaAlO₂ was formed via reaction between Na₂SO₄ and Al₂O₃. Ni-5Cr and Ni-30Cr alloys formed protective external NiO and Cr₂O₃ scales, respectively, and the Na₂SO₄ turned yellow during exposure because of the dissolution of chromate ions, which were detected in the wash water. SO₂ was detected in the effluent gas, indicating that the following reaction was taking place:



Finally, Ni-30Cr-6Al and Ni-11Cr-22Al each gained less weight than in simple oxidation, while Ni-8Cr-6Al (a marginal Al₂O₃-former) was severely degraded. It seemed that the first two Ni-Cr-

Al alloys are able to form a protective Al_2O_3 scale as transient Cr_2O_3 lowers the oxide ion content of the salt via Equation 24, while the Cr-depletion resulting from this reaction is enough to prevent protective Al_2O_3 scale formation on Ni-8Cr-6Al (the presence of Cr in Ni-Cr-Al alloys produces a third element effect, i.e., it allows the selective oxidation of Al to occur at lower Al activities than in binary Ni-Al alloys [36]).

A mechanism for the hot corrosion of Ni-31Al was developed from these experimental results [35]. It can be discussed with reference to the 1000°C Al-S-O phase stability diagram, presented in Fig 6.

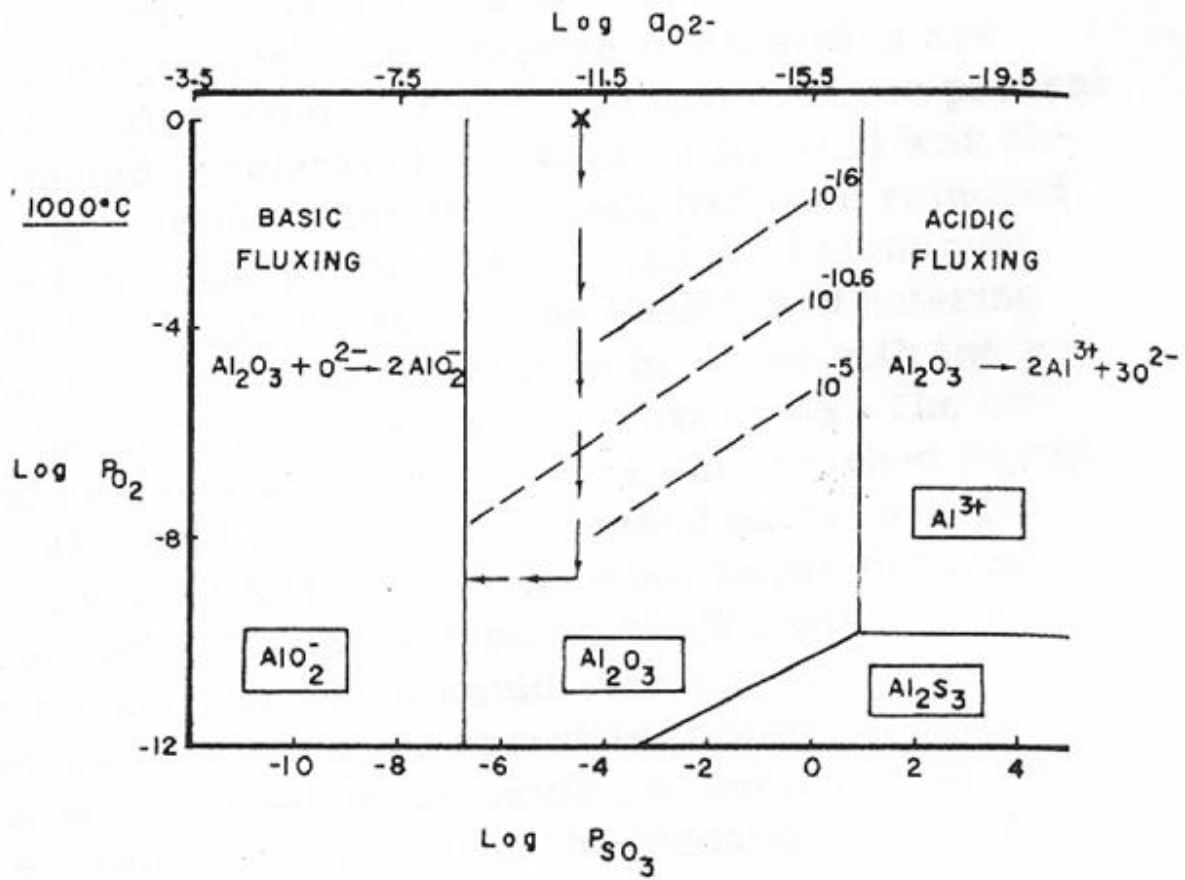
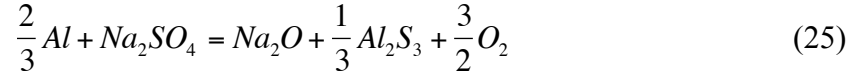


Figure 6. 1000°C Al-S-O phase stability diagram, demonstrating the compositional changes which lead to the basic fluxing of Ni-Al alloys

In Fig 6, the composition of the as-deposited Na_2SO_4 is indicated by an x. At this composition, Al_2O_3 is stable, and therefore an alumina scale initially forms at the surface of the alloy. As oxygen from the salt is consumed, the p_{O_2} drops at the oxide/salt interface with a concomitant increase in the p_{S_2} in this region (indicated by the downward-pointing arrow in Fig 6). At a sufficiently high activity, sulfur diffuses through the Al_2O_3 scale and forms

aluminum sulfides in the alloy. This results in a net increase in the oxide ion activity in the Na_2SO_4 at the oxide/salt interface according to the overall reaction:



When sufficient oxide ion activities are achieved, the protective Al_2O_3 dissolves in accordance with Equation 7. This entire process is shown in Fig 6, where the broken diagonal lines represent sulfur isobars. In this schematic, the composition of the sulfate begins to move left to more basic compositions when the p_{S_2} reaches approximately 10^{-5} atm, which is presumably high enough to form Al_2S_3 at the scale/alloy interface. When the composition crosses the $\text{AlO}_2^-/\text{Al}_2\text{O}_3$ boundary, Al_2O_3 is no longer stable and will react rapidly with oxide ions, degrading by a so-called basic fluxing mechanism.

The Ni-5Cr and Ni-30Cr specimens did not degrade at an accelerated rate because, as suggested by Bornstein and DeCrescente [34], chromia, present either as a continuous scale or a transient oxide, dissolves in the salt according to Equation 23 and prevents the development of high oxide ion activities [35]. The Ni-5Cr was actually observed to oxidize at a slower rate with a Na_2SO_4 deposit compared with simple oxidation, and this was attributed to a possible doping effect. Doping NiO with Na would result in a decrease in the cation vacancy concentration and thus a slower outward migration of Ni^{2+} , i.e. a slower scale growth rate.

Like Cr_2O_3 , Al_2O_3 reacts with oxide ions to form a soluble species, AlO_2^- , however the beneficial effects of Cr_2O_3 are not observed with Al_2O_3 . This was investigated by heating pure Al_2O_3 and pure Cr_2O_3 with reagent grade Na_2SO_4 ; a reaction between Cr_2O_3 and the salt was

evident while there was no such reaction with Al_2O_3 . Therefore, Cr_2O_3 has a stronger affinity for oxide ions than Al_2O_3 and consequently it is a better hot corrosion inhibitor.

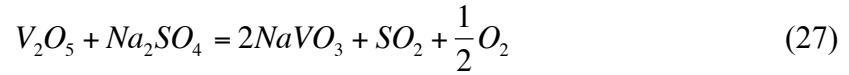
Rapp and Goto [21] point out that while the removal of sulfur from the Na_2SO_4 to form sulfides does in fact increase the local melt basicity, an electrochemical reduction reaction will have the same result. For example, they propose that, in a highly basic melt, the reduction of peroxide ions:



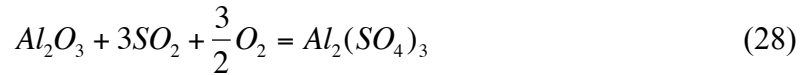
at the oxide/salt interface will result in an increase in basicity. Therefore, while sulfide formation may contribute to the establishment of basic fluxing conditions in the salt film, it is not the only factor to be considered.

2.2.2.2 Alloy-Induced Acidic Fluxing It has been shown in section 2.2.2.1 that scale fluxing conditions can be established as a result of locally basic conditions at the salt/scale interface. This results in accelerated rates of degradation in many engineering alloys, however the attack is not self-sustaining. The oxide solubility plots of Fig. 4 demonstrate that acidic melts (those with a low $a_{\text{Na}_2\text{O}}$) can also effectively dissolve protective oxide scales. Acidic conditions can generally be established in a Na_2SO_4 melt either by SO_3 in the gas or by the dissolution of acidic transient oxides of W, Mo, or V, which are added to superalloys as solid-solution strengtheners [37]. The first process will be discussed in section 2.2.3; the latter, referred to as alloy-induced acidic fluxing, is the topic of this section.

Bornstein, DeCrescente, and Roth [38] studied the effects of various elements on the Na₂SO₄-induced accelerated oxidation of Ni-base alloys at temperatures of 800-1000°C. The hot corrosion rates of Al₂O₃-forming alloys were greatly enhanced when Mo or V was present in the alloys, or when Na₂SO₄ was co-deposited with MoO₃ or V₂O₅. The first possible explanation for this is that these acidic oxides react with oxide ions, liberating SO₂ according to, for example, Equation 27:



The SO₂ released from this reaction can then dissolve the Al₂O₃ scale, forming soluble sulfate:

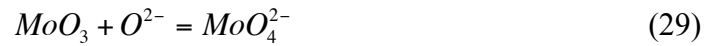


The authors assert, however, that in order for sufficiently high SO₂ potentials to be developed for reaction 28 to be feasible, the activity of SO₄²⁻ would have to deviate significantly from unity. In other words, the reaction between V₂O₅ and Na₂SO₄ (Equation (27)) would have to be very rapid, which was not observed when the two substances were liquefied in a quartz tube.

Bornstein et al [38] therefore concluded that the accelerated attack is a result of the fact that MoO₃ and V₂O₅ are molten at the test temperatures. These molten, corrosive oxides flux the Al₂O₃ scale, resulting in rapid degradation of the Al₂O₃-forming alloys. No such degradation was observed in the presence of W because WO₃ is solid at the temperatures considered.

Goebel et al oxidized a number of Ni-Al and Ni-Cr-Al alloys containing W, Mo, and V in air with thin Na₂SO₄ deposits [35]. All alloys degraded catastrophically. It was observed that the refractory elements were enriched in the scale adjacent to the alloy/scale interface and that the attack initiated at refractory-element rich phases, e.g. α -Mo or Mo-carbide. In addition, oxides of W, Mo, V, and Cr were mixed with Na₂SO₄ and heated in an alumina crucible to 1000°C. In the cases of WO₃, MoO₃, and V₂O₅, the crucible lost weight and Al was detected in the salt after the test; no such effect was seen with Cr₂O₃. It was concluded that the first three aforementioned oxides lower the oxide ion content sufficiently for reaction 28 to occur; Cr₂O₃ reacts with oxide ions (Equation 24), however not to as great of an extent. Based on these observations, the following mechanism for alloy-induced acidic fluxing of Ni-Al-Mo alloys was developed. The analysis is applicable to any refractory element-containing alloy.

During the transient oxidation period, the oxides Al₂O₃, NiO, and MoO₃ form at the alloy surface. MoO₃ reacts with oxide ions in the salt according to Equation (29)



which prevents basic fluxing from occurring. The activity of oxide ions in the melt adjacent to the scale can be lowered by this reaction until reaction 28 becomes possible, i.e. the Al₂O₃ scale dissolves as an acidic solute. This attack is found to initiate near Mo-rich particles because the activity of MoO₃ is highest in the salt adjacent to these regions. Al³⁺ and MoO₄²⁻ ions diffuse out through the salt, where Al₂O₃ precipitates out as a porous, nonprotective scale and MoO₃ evaporates. Unlike basic fluxing, this attack is self-sustaining due to the continued formation of MoO₃ at the alloy/salt interface and its evaporation at the salt/gas interface. In terms of the Rapp-

Goto criterion [21], a negative solubility gradient is maintained in the salt at the salt/alloy interface.

2.2.3 Low Temperature (Type II) Hot Corrosion

An interesting characteristic of hot corrosion is that it tends to occur in perhaps its most severe form when the temperature is fairly low, approximately 650°C - 750°C. Na₂SO₄ is solid in this temperature regime, and thus one would expect negligible corrosion. Conde and Wareham [39], who demonstrated pitting corrosion of a Nimonic 105 blade after operating in a marine environment at a turbine inlet temperature of approximately 750°C, were among the first to prove the occurrence of hot corrosion at these low temperatures. From that point, numerous examples of this so-called Type II hot corrosion were shown and a number of mechanistic studies were performed. Mechanisms have been developed which seem to be consistent with commonly encountered hot corrosion microstructures, however none of the mechanisms have achieved ubiquitous acceptance. It is generally agreed upon that accelerated degradation at these low temperatures is made possible by the formation of a Na₂SO₄/MSO₄ eutectic which has a melting point well below that of pure Na₂SO₄ [40]. It has been shown that a p_{SO_3} of approximately 10⁻⁵ atm is required to stabilize this eutectic melt [41]; these SO₃ pressures are not uncommon in the gas stream of an industrial or marine gas turbine. As first observed by Wortman et al [42], CoCrAlY coatings tend to be very susceptible to this form of hot corrosion, and thus the bulk of the work on Type II hot corrosion has centered on Co-base materials.

2.2.3.1 Gas Phase-Induced Acidic Fluxing Numerous publications have documented the typical Type II corrosion morphologies, particularly in Co-base materials [41, 43-45]. Generally, Co-Cr-Al alloys exhibit severe localized attack in the form of deep pits containing mixtures of porous, nonprotective Cr_2O_3 , Al_2O_3 , CoCr_2O_4 , and CoAl_2O_4 with a band at the base of the pit enriched in Al and S. Near the corrosion product/gas interface, a layer of Co_3O_4 and/or CoSO_4 is commonly observed, depending on p_{SO_3} . At high p_{SO_3} , CoSO_4 will tend to be the stable phase at the sample surface, while Co_3O_4 is stable at lower SO_3 potentials [43].

Binary Co-Cr alloys tend to have similar Type II corrosion morphologies, with the obvious exception that only Cr- and Co- rich corrosion products are present. Binary Co-Al alloys commonly experience a more frontal attack, however the elemental distributions are quite similar to Co-Cr and Co-Cr-Al alloys [43]. Again, there is the trivial exception that only Al- and Co- rich corrosion products are present in these alloys.

It has been well established that a liquid Na_2SO_4 film is required for hot corrosion to occur, regardless of the temperature or active corrosion mechanism. In the case of low temperature hot corrosion, liquid deposits form at temperatures well below the melting point of pure Na_2SO_4 ($T_m = 884^\circ\text{C}$). The CoSO_4 - Na_2SO_4 phase diagram is shown in Fig. 7 [46]:

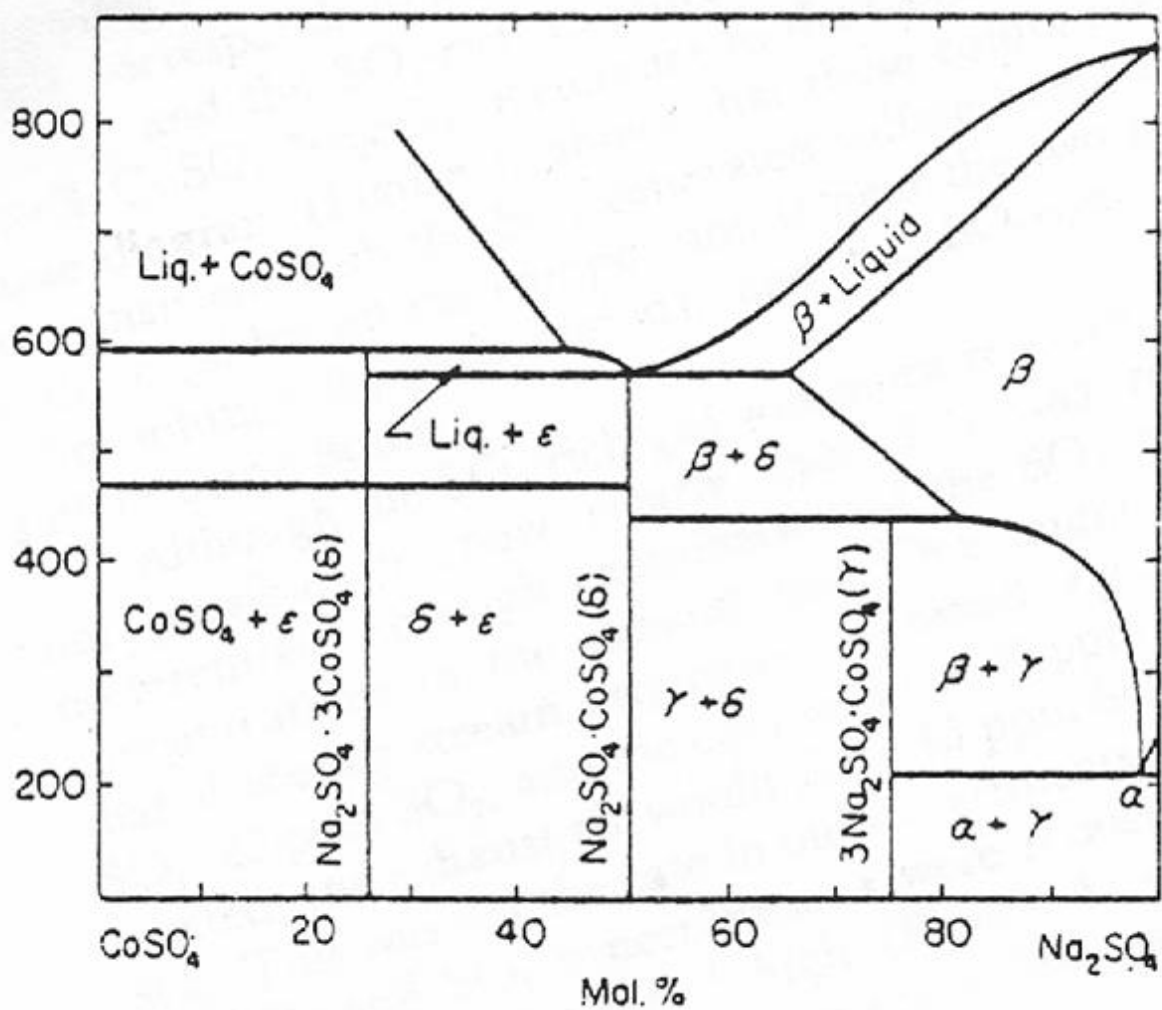
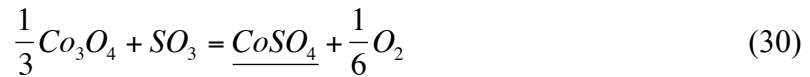


Figure 7. The CoSO_4 - Na_2SO_4 pseudo-binary phase diagram

A eutectic is observed in this pseudo-binary system at approximately 50 mol% Na₂SO₄ and 560°C. Therefore, if a sufficient activity of CoSO₄ can be established in the Na₂SO₄ film, liquid formation is expected at temperatures in the 650°C - 750°C range.

When an engineering alloy such as CoCrAlY is exposed to elevated temperatures in an oxidizing environment, it is commonly protected from this environment by a slow-growing external scale of α -Al₂O₃ during steady state oxidation. However, during the initial stages of exposure, oxides of all other elements in the alloy will form at the surface, provided that the free energy changes for their formations are negative under the given conditions. This process is known as transient oxidation [3]. Therefore, when a CoCrAlY alloy is covered with a solid Na₂SO₄ deposit and exposed at elevated temperatures, regions of relatively fast-growing Co₃O₄ and/or CoO (depending on temperature and p_{O_2}) are expected to nucleate. These transient oxides can be sulfidized according to Reactions 30 and 31:



In these reactions, CoSO₄ is underlined, meaning that it is dissolved in Na₂SO₄ at less than unit activity. If a high enough SO₃ potential is present in the combustion gas, the activity of CoSO₄ in the salt can reach levels sufficient for eutectic formation.

Based on available thermodynamic data, Luthra and Shores [47] generated a plot showing the SO₃ potential required to form solid CoSO₄ and a liquid eutectic mixture from pure Co₃O₄ at $p_{O_2} = 1\text{atm}$, shown in Fig.8:

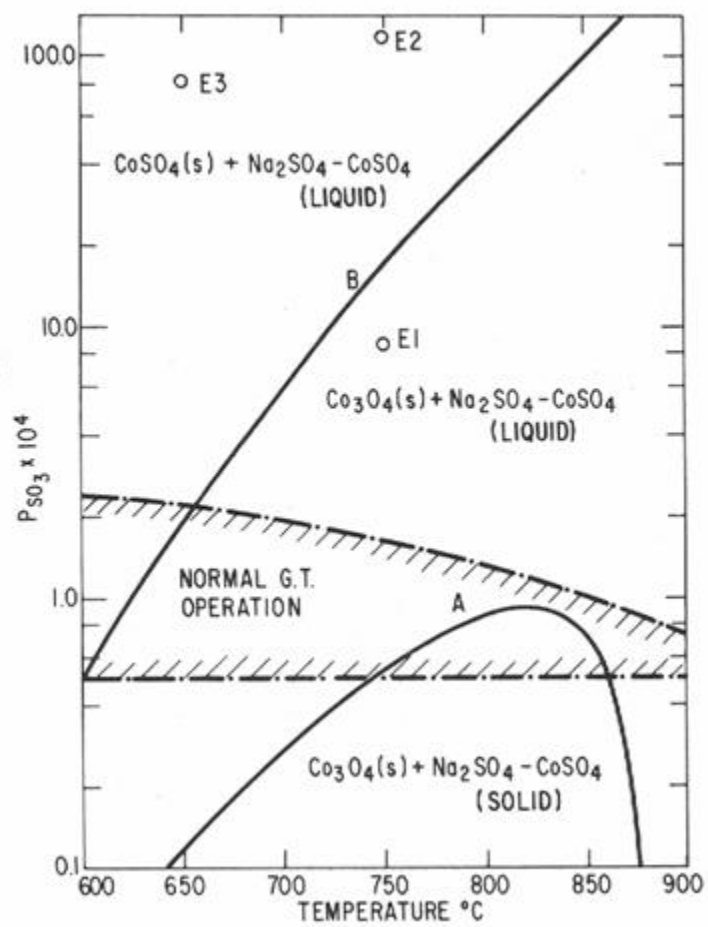


Figure 8. p_{SO_3} required to form solid CoSO_4 and a liquid eutectic mixture from pure Co_3O_4 at $p_{\text{O}_2} = 1 \text{ atm}$

A $\text{Na}_2\text{SO}_4\text{-CoSO}_4$ liquid is stable above line A. It can be seen that the eutectic is stable over a wide range of SO_3 potentials that can typically be achieved in a gas turbine engine (common gas turbine operating conditions are contained within the dashed lines). The authors note that this plot is generated only for $p_{\text{O}_2} = 1 \text{ atm}$, and that the location of the curves will change with p_{O_2} per Reaction 30. Assume that a turbine is operating at a total pressure of 10 atm, corresponding to a p_{O_2} of approximately 1.6 atm. The result of this increase in oxygen potential would be a 7% increase in the p_{SO_3} levels required for eutectic formation (curve A). This fairly small change does not render the given plot ineffective for application to real gas turbine systems.

Jones [46] further elucidated the nature of the interaction between Co_3O_4 and SO_2/SO_3 mixtures. Mixtures of Co_3O_4 and Na_2SO_4 were exposed to gas mixtures rich in SO_2 and/or SO_3 and monitored via weight gain measurements, observation of the physical state of the mixture, measurement of the amount of SO_2 consumed from the incident gas stream, and measurement of SO_3/SO_2 ratios in the exiting gas. It was determined that indeed SO_3 and not SO_2 is the important species in converting cobalt oxide to sulfate. However, it was found that Co_3O_4 is a catalyst for the typically sluggish reaction



Therefore, even if the inlet and exit gases consist solely of SO_2 , significant eutectic formation can occur due to locally high SO_3 .

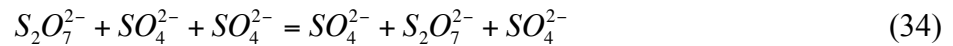
Luthra [48] proposed an interesting mechanism for low temperature hot corrosion attack of Co- base alloys. He pointed out that at the SO_3 potentials required for this type of attack,

alumina and chromia will dissolve as sulfates, i.e. basic fluxing cannot occur. Further, the p_{SO_3} will be higher at the salt/gas interface than at the salt/alloy interface, and thus a positive acidic solubility gradient will exist in the salt. In addition, over the range of experimental conditions (p_{SO_3} and p_{O_2}) examined in his study, Al_2O_3 and Cr_2O_3 should be stable and form a protective layer, which was not observed. Therefore, the concept of scale fluxing as it was developed for Type I hot corrosion does not seem to be applicable for Type II degradation.

Transport rates of SO_2 and SO_3 through molten Na_2SO_4 in ionic and molecular form were calculated and it was found that only SO_3 , present as dissolved $S_2O_7^{2-}$ ions, was capable of providing a large enough flux of oxidant to the salt/alloy interface to account for the observed weight gains during corrosion [48]. At the salt gas interface, the reaction



incorporates SO_3 into the salt. It is then transported towards the salt/alloy interface by the $SO_4^{2-}/S_2O_7^{2-}$ exchange reaction shown schematically in Reaction 34:



At the salt/alloy interface, SO_3 is the primary oxidant. Very low p_{O_2} levels will develop at this interface, resulting in a high p_{SO_2} if $O_2/SO_2/SO_3$ equilibrium is assumed. Thus, SO_2 will likely migrate out through the salt.

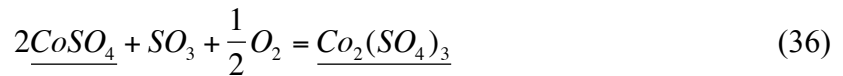
Cobalt is very commonly observed in the outer regions of the corrosion product as Co_3O_4 , meaning that it must somehow migrate out through the salt. Co is a transition metal that

can exist in the 2+ or 3+ valence states. In order for Co migration to occur, there must be some coupled ionic migration as a result of electrical neutrality requirements. Luthra determined three possibilities for such migration [48]. The first involves the outward migration of Co^{2+} and SO_4^{2-} , which would require that the activity of $CoSO_4$ is greatest at the scale/alloy interface. At high SO_3 pressures, $CoSO_4$ is observed at unit activity at the surface of the corrosion product formed on CoCrAlY specimens, and so this cannot be the mechanism. The second possibility is a coupled outward migration of Co^{2+} and SO_3^{2-} . There should be a negative gradient in the activity of SO_3^{2-} at the scale/alloy interface, where the p_{O_2} is low, per Reaction (35):



However, Fick's 1st Law considerations showed that the flux of Co provided by this mechanism is much less than that observed experimentally, and so this is also unlikely. The final mechanism for Co transport, that which was proposed to be operative during Type II hot corrosion, involves a $3Co^{2+}/2Co^{3+}$ exchange reaction.

According to Reaction (36), the Co^{3+}/Co^{2+} ratio will be higher at the salt/gas interface than it is at the salt/alloy interface:



This results in a net outward transport of Co due to an inward migration of Co^{3+} , which is reduced at the salt/alloy interface, and an outward transport of Co^{2+} , which forms Co_3O_4 and/or CoSO_4 toward the salt/gas interface.

Thus, a reaction sequence was developed for the Type II hot corrosion of Co- base alloys which is based on the acidic fluxing of Co and its oxides [48]. Binary Co-Cr alloys will be used as an example. Initially, during transient oxidation, oxides of Co and Cr form on the alloy surface. Co_3O_4 reacts with SO_3 to form CoSO_4 , which dissolves in the solid Na_2SO_4 . If sufficient SO_3 is present, a liquid Na_2SO_4 - CoSO_4 eutectic forms, and porous, nonprotective Cr_2O_3 is left behind. The reaction is perpetuated by the inward migration of SO_3 (as $\text{S}_2\text{O}_7^{2-}$) and the outward migration of Co^{2+} . SO_3 oxidizes Cr at the salt/alloy interface, releasing SO_2 , which can penetrate the alloy and form sulfides. This accounts for the S-rich band commonly observed at the base of the corrosion pit. These sulfides can be oxidized as the corrosion front progresses, releasing sulfur, which can form sulfides deeper in the alloy. Therefore, the boundary between the alloy and the sulfur-rich band, as well as that between the sulfur-rich band and the rest of the pit, advance further into the sample. Eventually, the maximum CoSO_4 activity is reached at the salt/gas interface, and solid Co_3O_4 precipitates in this region.

Luthra emphasizes that this reaction is unlikely for Ni-base alloy systems because there are no known compounds of Ni^{3+} ; however, Ni has been observed in the outer regions of the corrosion product during Type II attack [4], which generates some uncertainty concerning the validity of the Luthra mechanism for Ni-base alloys.

Chiang et al [45] studied the low temperature hot corrosion of binary and ternary Ni- and Co- base alloys at 700°C and 750°C. All binary (Ni,Co)-Cr and ternary (Ni,Co)-Cr-Al alloys exhibited the degradation microstructure typical for Co-Cr-Al, as described at the beginning of

this section, however some additional observations were made. Sulfides of Cr were prevalent beneath the corrosion pits in the Ni-base alloys, and NiS was present within the corrosion product. Also, higher SO₃ pressures were required to produce significant degradation in the Ni-base systems relative to the Co-base systems. Preferential attack of Co-18Cr-6Al occurred along the β-CoAl phase.

The following reaction mechanism for Type II hot corrosion was proposed [45]. Initially, a molten eutectic phase is formed at the alloy surface as a result of the sulfation of transient NiO or Co₃O₄. High SO₂ and S₂ potentials are achieved at the scale/salt interface due to the low oxygen potential in this region. For the Co-Cr-Al alloys, the following acidic fluxing reaction occurs at the scale/salt interface:



The aluminum sulfite diffuses out into the salt and reprecipitates as nonprotective Al₂O₃ at regions of higher p_{O_2} . Cr either experiences an analogous reaction or oxidizes *in situ*. The base metal dissolves in the acidic salt, diffuses out to the salt gas interface, and precipitates as Co₃O₄. Note that this mechanism is consistent with the preferential attack of the Al-rich β phase. For Ni-Cr-Al alloys, the important reaction at the salt/alloy interface is the sulfidation of Al and Cr, and the subsequent oxidation of these sulfides, as evidenced by the presence of numerous internal sulfides in these alloys. The S₂ released from the oxidation of these phases is apparently enough to form NiS, which can dissolve in the salt, allowing Ni to diffuse to the surface and form NiO.

2.3 (Ni,Pt)Al DIFFUSION COATINGS

Diffusion coatings based on the β -NiAl system are used extensively in the gas-turbine industry to impart high temperature oxidation and corrosion resistance to the Ni-base superalloys that form the structural basis of turbine blades and vanes [49]. Of utmost importance for this application is the formation and maintenance of a slowly growing and adherent α -Al₂O₃ scale, which serves to slow the ingress of oxidant and thus prevent rapid degradation of the turbine hardware. Platinum is commonly incorporated into β coatings by an electroplating step prior to aluminizing. The addition of Pt to β has been found to be extremely beneficial in terms of oxidation and hot corrosion resistance [50]. In the following sections, aspects of the oxidation and hot corrosion behavior of these coatings is reviewed, with an emphasis placed on the influence of Pt. Prior to this discussion, a brief review of the phase equilibria in the Ni-Al-Pt system and the methods by which these coatings are produced is presented.

2.3.1 Phase Equilibria in the Ni-Al-Pt System

2.3.1.1 The Equilibrium Ni-Al-Pt Phase Diagram Among the first attempts to determine a ternary phase diagram for the Ni-Al-Pt system was that of Bätzner [51]. The diagram is based on the results obtained by Jackson and Rairden [52] who studied the aluminization of Pt-coated IN-738 superalloy. Later experimental work by Gleeson and colleagues [53, 54] further elucidated the phase equilibria over the majority of the Gibbs triangle in the Ni-Al-Pt system, including the compositional regimes of interest for high temperature Pt-modified bond coats.

Gleeson et. al. [53] determined a 1150°C Ni-Al-Pt isotherm using experimental techniques. This phase diagram is compared with the 1060°C diagram generated by Bätzner [51] in Fig. 9.

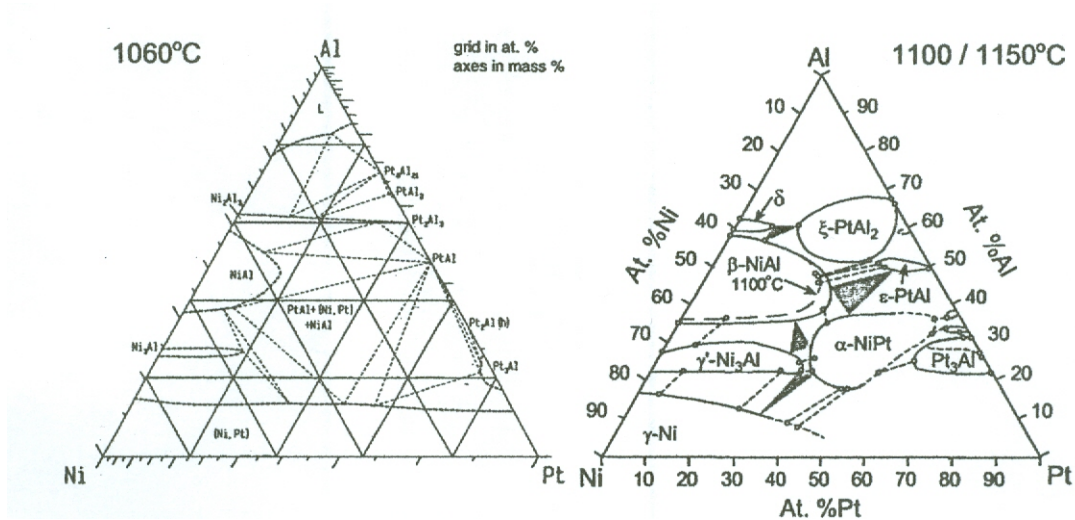


Figure 9. Phase equilibria in the Ni-Al-Pt systems as determined by Bätzner [52] at 1060°C and by Gleeson et. al. [54] at 1150°C

Two significant corrections were made in the work by Gleeson et. al. Firstly, it was found that the ternary α -NiPt(Al) phase has a significant field of stability at 1150°C. This was the first report of such a high temperature phase; the binary α -NiPt phase is only stable up to about 645°C. Secondly, the solubility of Pt in the β and γ' phases was found to be significantly greater than previously thought: approximately 35 at. % in each phase [53].

In light of these results, further work by the Gleeson group was conducted in order to carefully determine the phase equilibria associated with the α -NiPt(Al) phase [54]. Prior to this work, the equilibria involving this phase were largely speculative, as indicated by the dashed phase boundary line in the vicinity of the Pt-Al binary side of the phase diagram in Fig. 9. In

order to address this, diffusion couples were constructed, exposed at 1150°C for 50 h, and quenched into water. The resulting diffusion paths were determined using SEM and EPMA, from which interfacial compositions, i.e., phase boundaries, and a number of tie lines through the relevant two-phase fields were constructed. From this work, it was determined that the solubility of Pt in the α -NiPt(Al) phase ranges from 33-60 at. %. Further, the solubilities of Pt in γ' and β were determined to be around 32 and 42 at. %, respectively. In addition, the phase fields of the Pt₃Al, Pt₃Al₅, and Pt₂Al phases were measured.

2.3.1.2 The B2 \leftrightarrow L10 Martensitic Transformation in the NiAl System It has been known for a number of decades that in Ni-rich β -NiAl alloys, a martensitic transformation occurs upon cooling from the B2 (primitive cubic, CsCl-type) to the L10 (face-centered tetragonal) structure [55]. Due to the widespread use of β -NiAl base coatings, numerous studies have since been dedicated to understanding the kinetics of this transformation and the repercussions during service in thermal barrier coating systems.

Smialek and Hehemann [55] utilized resistivity measurements to determine the transformation temperature (upon both heating and cooling) of cast binary NiAl alloys as a function of composition from approximately 60-70 at. % Ni. It was found that the transformation temperature increased approximately linearly with Ni content, and a simple empirical equation for the M_s temperature as a function of composition was developed.

Kainuma et. al. were interested in the effects of various ternary alloying additions on the M_s temperature of β -NiAl alloys because of the potential for use of these materials in shape-memory devices [56]. This work is very much of interest in the high-temperature oxidation community, because various elements other than Ni and Al are always found in β coatings due to

interdiffusion with the substrate alloy. These investigators prepared numerous alloys based on the $\text{Ni}_{64}\text{Al}_{36}$ composition, and found that the following elements stabilize the B2 structure, i.e., lower the M_s temperature: Ti, V, Cr, Mn, Fe, Zr, Nb, Mo, Ta, W, and Si. Cobalt, Cu, and Ag, however, destabilize the B2 structure, thereby increasing the M_s temperature. An empirical equation was developed which related the M_s temperature to the composition of the alloy; the validity of this equation has not been verified.

Pan et. al. performed a very elegant study in order to determine the evolution of the microstructure and mechanical properties of diffusion aluminide bond coats as a function of thermal cycling in an actual TBC system [57]. This study verified that the as-deposited bond coat has the B2 structure, and the L10 martensite phase appears with thermal cycling. Interestingly, it was found that the yield and creep strength of the coating at intermediate temperatures (~600-800°C) increased with thermal cycling, and this was attributed to the formation of martensite. At higher temperatures, this effect disappeared due to the transformation of the martensite to β .

To follow up on this study, Chen et. al. [58] investigated the morphological evolution of Pt-modified aluminide coatings as a function of thermal cycling time using SEM, XRD, EPMA, and TEM. It was confirmed that, due to the increase in Ni content of the coating with thermal cycling at 1125°C, the bond coats eventually transformed to L10 martensite upon cooling. Using TEM, it was determined that the martensite lamellae, which were approximately 50 nm in width, were twin related. Micro-twinning was also observed within the lamellae using high resolution TEM. The twinning which was observed in these systems accounted for the increase in intermediate temperature strength of the coatings with thermal cycling which was observed in ref. [57], i.e., the twin boundaries helped to prevent dislocation motion in the coatings. Finally, hot stage TEM revealed that indeed the transformation to martensite was fully reversible on

heating; at elevated temperatures (over $\sim 800^{\circ}\text{C}$ in this study) the martensite transformed back to the parent B2 structure.

Chen et. al. [59] further studied the martensitic transformation in β coatings and its potential consequences in TBC systems using high temperature XRD and finite element analysis (FEA). XRD measurements led to the conclusion that the molar volume of the martensite phase is approximately 2% less than that of the β phase; this leads to transformation strains of $\sim 0.7\%$ upon thermal cycling. FEA modeling indicated that the importance of this transformation strain in determining TBC lifetime is directly dependent on the transformation temperature (which depends strongly on composition) relative to the creep strength of the bond coat.

Finally, Sordélet et. al. [60] used high energy XRD and differential scanning calorimetry to carefully characterize the kinetics of the martensitic transformation in model (Ni,Pt)Al alloys. It was determined that in these systems the transformation is indeed isothermal in nature, following C-curve kinetics and displaying a single activation energy barrier. Further, it was determined that increasing the Pt content in the alloys decreased the M_s temperature, increased the range of temperatures over which the transformation to martensite occurred during cooling at a given rate, and decreased the degree of thermal expansion upon heating. These effects were attributed to a lowering of the shear moduli and increase in the bulk modulus with Pt addition.

2.3.2 Deposition and Resulting Microstructures of (Ni,Pt)Al Diffusion Coatings

Overviews of the aluminizing process used to produce NiAl and (Ni,Pt)Al coatings have been provided by a number of authors [61-63]. A succinct review of the deposition of diffusion aluminide coatings on Ni-base alloys was given by Birks, Meier, and Pettit [3].

Pack cementation is the most common method used to deposit aluminide coatings [3]. During pack cementation, the parts to be coated (commonly gas turbine blades) are buried within a powder mixture containing three constituents: a source (Al or an Al-containing alloy), an activator (a halide, e.g., NaCl), and a filler (an inert substance, typically Al₂O₃, used essentially for support). Upon heating, the volatilized activator reacts with the source to form volatile Al-halides, which are transported through the porous pack to the surface of the part to be coated. At this surface, deposition of Al occurs by chemical reaction, e.g.,



where the underline indicates a species in solid solution.

The growth direction of the coating is determined by the activity of Al in the pack and by temperature [3]. Inward growing coatings are produced at relatively low temperatures using high Al activity packs, while outward growing coatings are produced at higher temperature with low Al activity packs. If it is undesirable to have the part in contact with the pack, aluminide coatings can also be produced by keeping the parts isolated from the powder mixture, generating the Al-containing gaseous species, and allowing these gases to flow to the surface of the component (this is commonly referred to as CVD aluminizing).

To produce Pt-modified β -NiAl coatings, the component to be aluminized is first electroplated with Pt and annealed to diffuse the Pt into the substrate. Following this treatment, aluminizing is carried out as discussed above. After an appropriate heat treatment, the component is generally coated with a β -NiAl layer containing Pt in solution. However,

depending on the amount of Pt deposited prior to aluminizing, the coating may contain PtAl_2 either as discrete particles within the β phase or as a complete layer above it [64].

2.3.3 Oxidation Behavior of (Ni, Pt)Al Diffusion Coatings

The beneficial effect of Pt on the oxidation behavior of Al_2O_3 -forming alloys was recognized as early as 1976. Felten and Pettit [65] studied the oxidation of Pt-Al alloys with up to 6 wt. % Al. During cyclic oxidation, it was found that alloys containing 2 and 6 wt. % Al formed protective Al_2O_3 scales which remained adherent up to approximately 5000 h of exposure at 1200°C. The scale adherence was comparable to a FeCrAlY alloy, which is known to form scales with excellent adherence due to the addition of Y, a so-called “reactive element”. It was inferred that Pt addition could be used as a means to increase oxide adherence on alloys of commercial interest. Although the mechanism by which Pt improved scale adherence was not entirely clear, the authors hypothesized that the irregular oxide/alloy interface that developed during oxidation of the Pt-Al alloys resulted in a mechanical keying effect.

Schaeffer et. al. [66] studied the isothermal and cyclic oxidation behavior of straight (Pt-free) and Pt-modified NiAl diffusion coatings on various superalloy substrates. These investigators found that the pronounced beneficial effect of Pt incorporation into the coatings could not be fully attributed to an increase in Al_2O_3 scale adherence. This was supported by the observation that scale spallation occurred during exposure of both straight and Pt-modified coatings during the fairly early stages of cyclic oxidation exposure. Furthermore, acoustic emission studies indicated that, upon cooling from 1100°C, the scales formed on the Pt-modified coatings underwent as much damage as those formed on straight aluminides. As a result, the

improved cyclic oxidation behavior in the presence of Pt was attributed to the promotion of the selective oxidation of Al in the presence of a Pt-rich coating. This allowed the coating to reform a pure Al_2O_3 scale when spallation occurred.

Zhang et. al. [67] deposited low-S CVD Pt-modified and Pt-free diffusion coatings on a single crystal Ni-base superalloy, and exposed the coatings to isothermal oxidation exposures at 1150°C . No differences in scale growth kinetics or coating refractory element content were observed between the Pt-modified and Pt-free coatings. However, Pt greatly enhanced the Al_2O_3 scale adhesion during oxidation exposure. It was noted that the Pt-free coatings developed large voids at the scale/coating interface during exposure and exhibited scale spallation after 100 h at 1150°C ; no scale spallation, and importantly, no interfacial void formation was observed on the Pt-modified coatings after 200 h at 1150°C . These investigators concluded that the major beneficial effect of Pt is enhanced oxide scale adhesion due to the suppression of void growth at the oxide/coating interface.

The influence of S, Pt, and Hf on the cyclic and isothermal oxidation of aluminide coatings on Ni-base superalloy substrates was investigated by Haynes et. al. [68]. High S levels in the coatings, which were present due to the high S level in the underlying superalloy, resulted in void growth at the scale/coating interface and subsequent oxide spallation on the Pt-free coatings. When the S level of the coating was decreased, oxide adherence became much stronger. The addition of Pt to the coating greatly reduced this S effect, resulting in adherent scales regardless of the S level of the coating. Interfacial voids were not present on the Pt-modified coatings, in agreement with previous studies conducted in this group [67].

Svensson et. al. [69] studied interfacial void formation in cast β -NiAl alloys during the early stages of oxidation exposure at 1050°C . It was found that in Pt-free and Pt-containing

alloys, voids formed during the early stages (~ 1 h) of oxidation due to vacancy injection caused by the outward growth of transition (primarily θ) Al_2O_3 and the Kirkendall effect. According to these investigators, these voids disappear with time due to oxide filling both from the inward growth of α - Al_2O_3 , which eventually nucleates and grows at the expense of the outward-growing θ - Al_2O_3 , and, interestingly, from the outward growth of Al_2O_3 from the void surface. Pt additions were found to greatly accelerate this void filling. Hence, in addition to the suppression of void growth demonstrated in, e.g., refs. [67] and [68], this work demonstrated that the voids that do form will heal more quickly, resulting in enhanced scale adhesion. This rapid void filling was attributed to an enhanced rate of Al diffusion in the alloy. This of course relies on the assumption that the growth rate of the Al_2O_3 at the surface of the void is dependent on the rate of diffusion in the alloy, which has been found to be true for transient Al_2O_3 by Rivoaland et. al. [70]. However, if this were the case, then it would have to be shown that the oxides that form at the void surface are indeed transient (γ or θ Al_2O_3); since this was not shown unequivocally, the mechanism is still in question.

More recent work on the Pt effect has been done by Gleeson et. al. [71]. The work published by this group was focused primarily on γ' - Ni_3Al – base alloys, but it is likely that the mechanisms discussed also apply to β - NiAl systems. These researchers found that Pt additions favor the exclusive formation of a pure Al_2O_3 scale, excluding the formation of rapidly growing Ni-rich transient oxides. Two major reasons for this phenomenon were proposed. Firstly, as a result of the strong preference for Pt to occupy Ni sites in the γ' lattice (L12 structure), there is an effective enrichment of Al on any surface plane containing both Ni and Al (this structural consideration also holds true in the B2 structure of β - NiAl [72]). This Al enrichment kinetically favors alumina formation. The second reason is thermodynamic in nature. During oxidation of

(Ni, Pt)₃Al – base alloys, Pt tends to enrich in the subsurface. Pt has a negative thermodynamic interaction with Al, i.e., Pt decreases the chemical activity of Al. This decrease in Al activity at the alloy/scale interface results in an increase in the subsurface Al activity gradient, and thus an increased flux of Al to this interface. This too aids in the rapid establishment of a pure Al₂O₃ scale. Furthermore, first-principles calculations indicate that in the β -(Ni,Pt)Al system, Pt reduces the activation energy for Al diffusion, further enhancing the flux of Al to the scale/alloy interface [73].

Finally, internal oxidation studies conducted on dilute Ni-Al – base alloys showed that, for a given exposure time at 1150°C, the internal oxidation zone (IOZ) depth was reduced by a factor of approximately 2 by the addition of 20 at. % Pt [53]. This implies that Pt decreases the oxygen permeability (product of solubility and diffusivity), which aids in the selective oxidation of Al. These experiments were, out of necessity, performed on single phase γ -Ni alloys; however, due to the similarity between the crystal structures of the γ and γ' -Ni₃Al phases, it was concluded that this influence of Pt is also in effect during the oxidation of $\gamma + \gamma'$ bond coats. It is likely also valid in the case of β -(Ni,Pt)Al coatings, particularly when considering the ability of the coating to heal a damaged/spalled scale when a subsurface γ' layer has developed due to alloy depletion during the selective oxidation of Al.

2.3.4 Hot Corrosion Behavior of (Ni,Pt)Al Diffusion Coatings

As discussed by Tatlock et. al. in their 1987 review of the effect of Pt in high temperature oxidation and corrosion [50], researchers have known that Pt can have a beneficial effect on hot corrosion resistance nearly as long as hot corrosion has been a well-established problem. The

mechanism by which Pt enhances hot corrosion resistance is still not well known; however, there have been a few notable attempts to demonstrate the effect and propose an explanation [66, 74, 75].

Wu et. al. [75] studied the 900°C hot corrosion of diffusion aluminide coatings with and without Pt on the superalloy IN738 LC using electrochemical techniques. It was found that Pt greatly enhanced the hot corrosion resistance of the coating in basic melts, however no significant improvement was noted in acidic melts. In the acidity regime where both coatings exhibited passive behavior, the Pt-containing coating oxidized at a significantly lower rate. The beneficial effect of Pt was attributed to the development of a corrosion-resistant Pt-rich subsurface layer, and to an increase in the Al content in the scale formed on the Pt-containing coating.

Schaeffer et. al. [66] studied the Type I and Type II hot corrosion behavior of Pt-modified and Pt-free aluminide coatings on various superalloy substrates. Pt was found to increase both the Type I and Type II hot corrosion resistance. In Type I, the improvement in behavior with Pt addition was linked to an improvement in selective oxidation. As mentioned above, these authors observed an enhancement in the ability of the coating to reform an Al_2O_3 scale upon spallation in the presence of Pt, which also resulted in improved hot corrosion behavior. Interestingly, the substrate upon which the coating was applied was eventually found to have an impact on the extent of degradation of the coatings. The coatings deposited on substrates that contained high concentrations of refractory elements such as W and Mo underwent severe hot corrosion attack at shorter times than those deposited on superalloys with lower refractory metal content. This was attributed to the diffusion of these refractory elements,

which are known to negatively impact Type I hot corrosion resistance [35], from the substrate into the coating.

At lower temperatures (Type II), the reason for the beneficial effect of Pt was not as clear [66]. It was proposed that the incorporation of Pt into the coating at the expense of Ni should help to reduce the amount of acidic fluxing of NiO. In addition, it was suggested that the presence of Pt somehow inhibits the incorporation of refractory metals into the coating at the relatively low temperatures encountered during Type II hot corrosion.

Gleeson et. al. [76] developed a method to co-deposit Cr-modified NiAl coatings on superalloy René 80H using a pack cementation technique. The resulting coatings had a β -NiAl + α -Cr constitution, the microstructure of which could be controlled by the coating parameters. It was found that Cr resulted in a drastic improvement in Type I (900°C) hot corrosion resistance, and that the degree of improvement was highly dependent on the amount and distribution of α -Cr precipitates in the microstructure. Specifically, hot corrosion resistance increased with increasing Cr content, and a homogeneous distribution of spheroidal α -Cr precipitates was preferable to a lamellar distribution.

More recently, Leyens et. al. [74] studied the effect of Cr and various Pt group metals on the oxidation and hot corrosion behavior of cast NiAl alloys. Of interest for the current discussion is the influence of Pt. While proving to be rather beneficial during 1150°C cyclic oxidation, Pt was determined to have very little effect on 950°C Type I hot corrosion resistance. Only Cr was found to positively influence hot corrosion performance. This negligible effect of Pt is in poor agreement with most other studies (see above). The reasons for this are not currently clear.

Murakami et. al. [77] deposited Pt+Ir-modified aluminide coatings on superalloy TMS-82+ and exposed coatings with various Ir content to 900°C hot corrosion conditions with a Na₂SO₄-10%NaCl deposit. These investigators found, contrary to the results of Leyens et. al. [74], that Ir additions resulted in enhanced hot corrosion resistance relative to coatings containing Pt additions alone. A Pt+Ir aluminide containing 46 at.% Ir resulted in optimized hot corrosion resistance. The beneficial effect of Ir was attributed to the expansion to lower Al content of the β phase field in the presence of Ir. This effect on the phase equilibria prevented the $\beta \rightarrow \gamma'$ phase transformation from occurring at the scale/alloy interface, allowing for the formation of a protective Al₂O₃ scale while minimizing the scale cracking that normally can occur due to the volume contraction which occurs during the transformation from β to γ' .

2.4 MCrAlY OVERLAY COATINGS

MCrAlY (M = Ni, Co, and/or Fe) overlay coatings are the second major class of coatings used for high temperature oxidation and corrosion protection. They are extremely important in the gas turbine industry, as they too are capable of forming α -Al₂O₃ scales upon thermal exposure. As discussed below, there are significant differences between the oxidation and hot corrosion behavior of these coatings and that of (Ni,Pt)Al diffusion coatings. These differences in behavior arise from differences in composition and microstructure, particularly the higher Cr content, presence of reactive elements (e.g., Y, Zr, and/or Hf), and multiphase microstructures of MCrAlY coatings. In the following literature review of MCrAlY coatings, focus is placed on systems in which M = Ni and/or Co, as these are the systems that are relevant to the current study.

2.4.1 Phase Equilibria in the Ni-Cr-Al System

An isothermal section through the Ni-Cr-Al phase diagram at 1150°C is shown in Fig. 10 [78]:

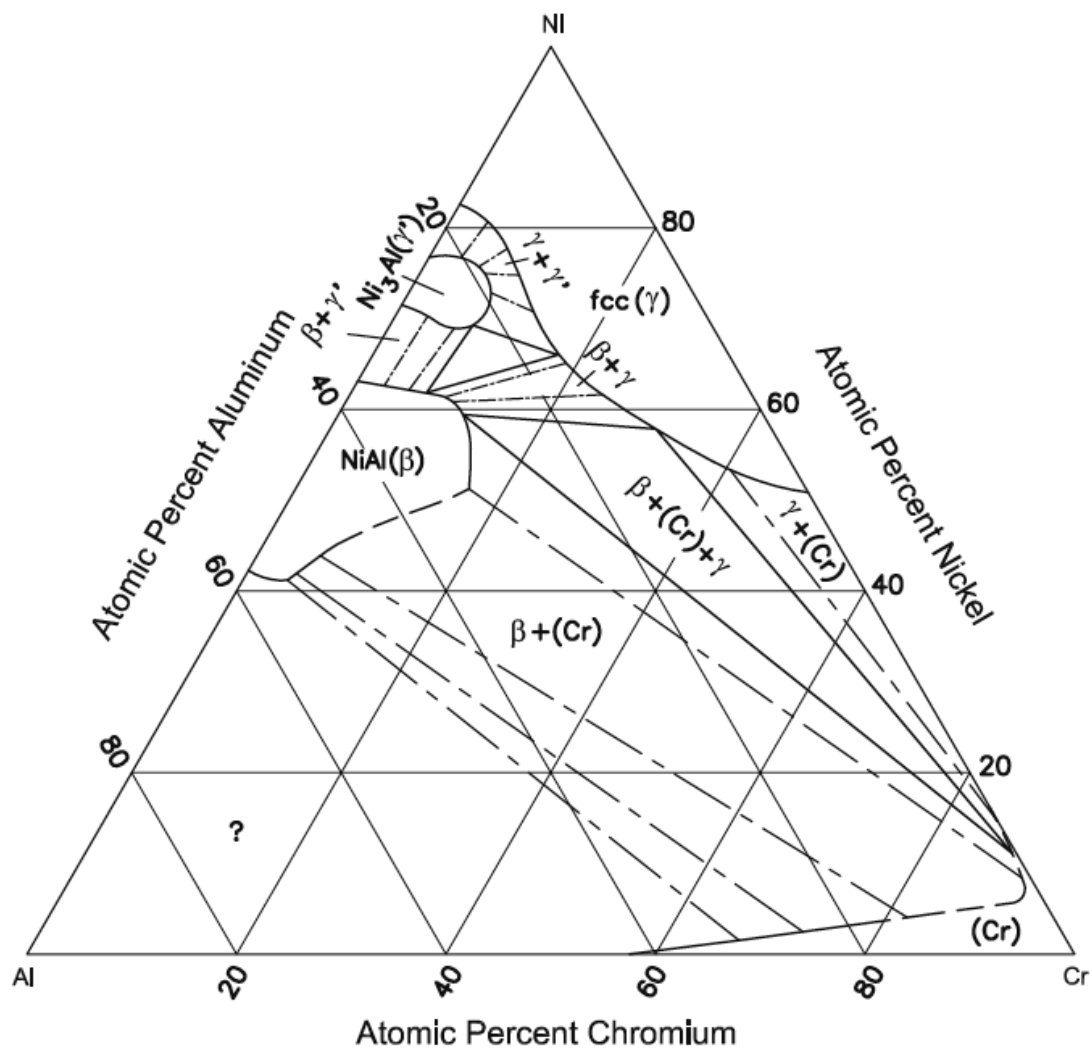


Figure 10. Equilibrium phase diagram in the Ni-Cr-Al system at 1150°C [78].

Of particular interest for high temperature coatings is the Ni-rich corner of the diagram. There are essentially four important phases: γ (FCC Ni solid solution), γ' (ordered L12 Ni₃Al), β (ordered B2 NiAl), and α (BCC Cr solid solution).

As demonstrated in the following sections, most MCrAlY coatings have $\gamma + \beta$ phase constitutions. The phase equilibria in this system are, however, rather complex. Task et. al. [79] conducted a study which coupled experimental techniques with thermodynamic calculation using ThermoCalc© software in order to study the phase stability in the Ni-Cr-Al system as a function of temperature, and subsequent effects on cyclic oxidation performance. An alloy of composition Ni-31Cr-11.25Al-0.6Y (wt. %) was equilibrated at 700°C, 900°C, and 1100°C and the resulting phase constitutions were probed using SEM and XRD. In addition, calculations were done to determine the expected phases as a function of temperature and their amounts. The results are summarized in Fig. 11 [79]:

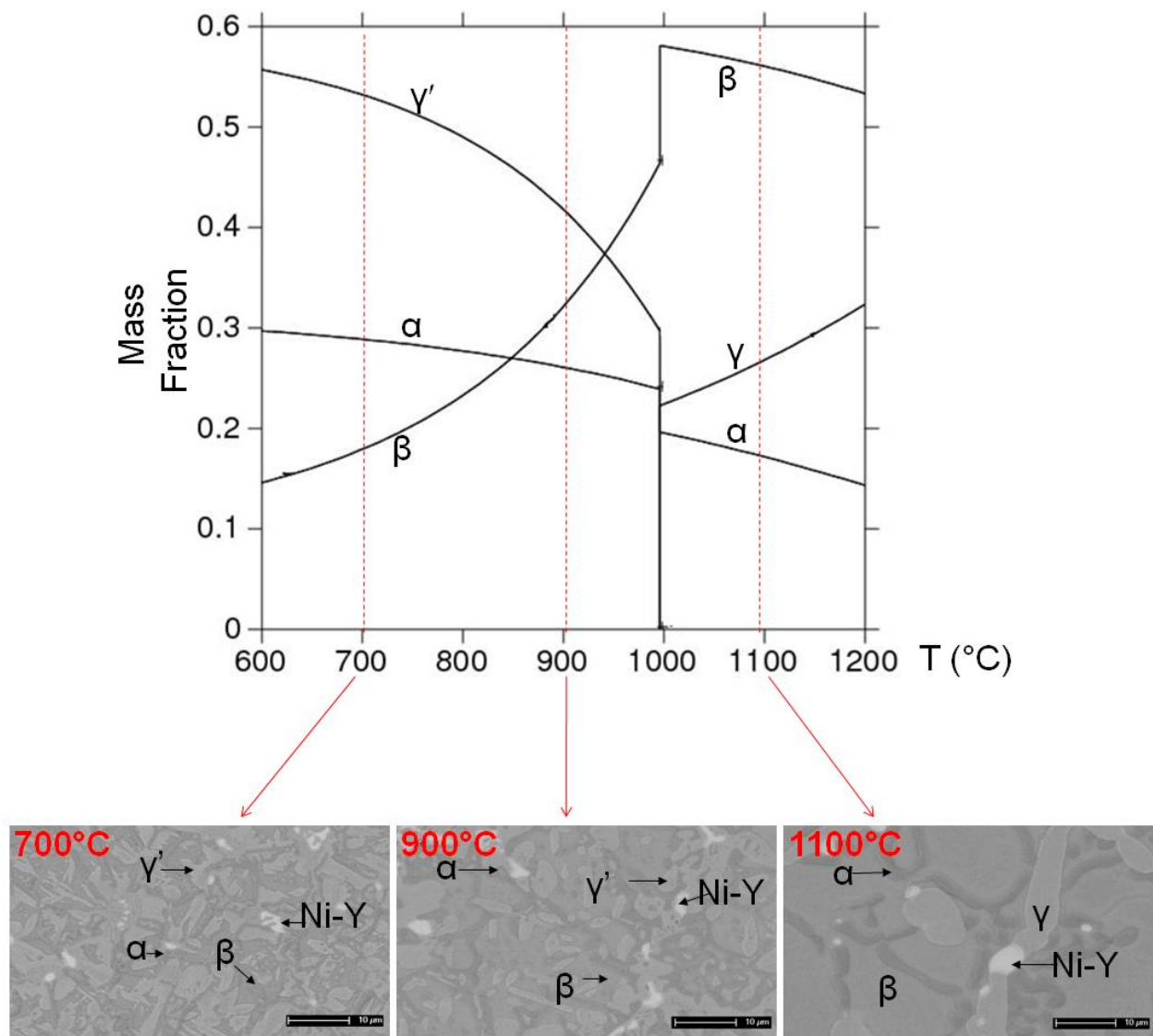


Figure 11. Thermocalc-calculated phase fractions in a Ni-31Cr-11.25Al-0.6Y (wt. %) alloy and corresponding SEM micrographs at various temperatures [79].

There was excellent agreement between experiment and calculation, both in terms of phases present (Fig. 11) and volume fractions of each phase (not shown). At low temperatures (below $\sim 996^{\circ}\text{C}$), the microstructure consists of γ' , β , and α . At approximately 996°C , a four phase equilibrium $\gamma' + \alpha \rightarrow \beta + \gamma$ exists, and above this temperature the alloy consists of the γ , β , and α phases. There is a significant volume change associated with this phase transformation, and the consequences of this for cyclic oxidation performance are discussed in section 2.4.3.

It is also to be noted that, due to the very small solubility of Y in these coatings, the Y is generally present as discrete Ni-Y particles, which can be seen in Fig. 11.

2.4.2 Deposition and Resulting Microstructures of MCrAlY Overlay Coatings

Three major processing routes used to manufacture MCrAlY overlay coatings are electron beam physical vapor deposition (EB-PVD), low-pressure or vacuum plasma spraying (VPS), and cathodic arc deposition (CAD). The EB-PVD process [3] utilizes an electron beam to heat a metal/alloy target sufficiently to produce a molten pool. The vapor exiting from this pool travels towards a substrate (commonly a gas turbine blade), which is rotating and/or spinning such that the entire surface to be coated is exposed to the incident vapor. At the surface of the substrate, a dense coating with a columnar grain structure is deposited. Upon subsequent heat treatment, a very fine microstructure is produced. If a single master alloy is used as a target, its composition will generally differ significantly from that of the coating due to differences in the evaporation rates of the constituent elements. As a result, either the composition of the master alloy must be appropriately adjusted, or multiple targets consisting of elemental metals must be used. An optical micrograph of an EB-PVD NiCrAlY coating is shown in Fig. 12 [3].

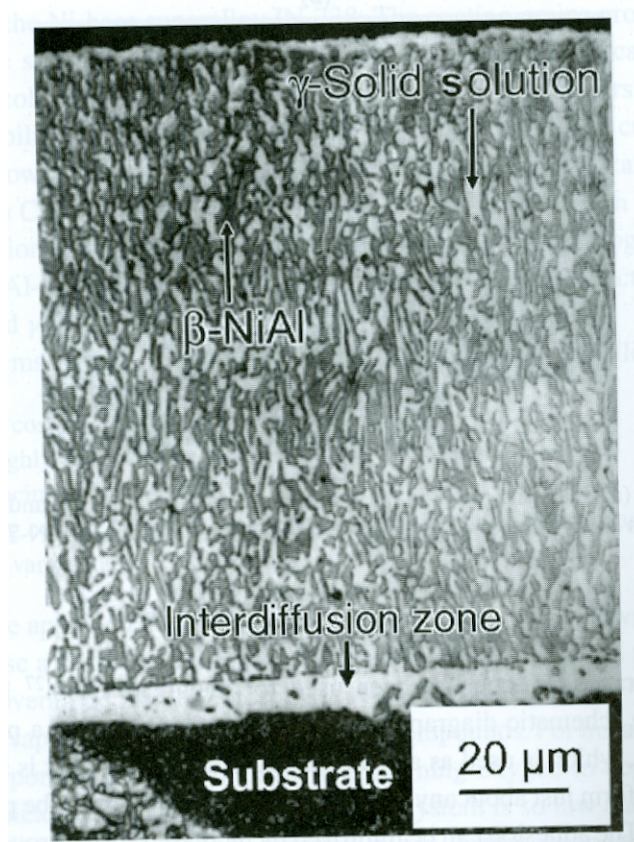


Figure 12. Optical micrograph of an EB-PVD NiCrAlY coating [3]

During the deposition of VPS MCrAlY coatings, a powder of the desired composition is fed into a plasma torch and is abruptly melted and sprayed towards a substrate, where it rapidly solidifies to form a fine-grained coating [3]. Although this can be done in air, the process is generally carried out under vacuum so that the highly reactive elements in the coating (Al, Cr, Y, etc.) do not oxidize during deposition. Coatings deposited using this technique tend to be significantly less dense than those produced by EB-PVD. An example of a VPS NiCoCrAlY coating in the as-sprayed condition is shown in Fig. 13, in which the γ (light gray phase) and β (dark gray phase) can be seen, in addition to numerous pores (black regions).

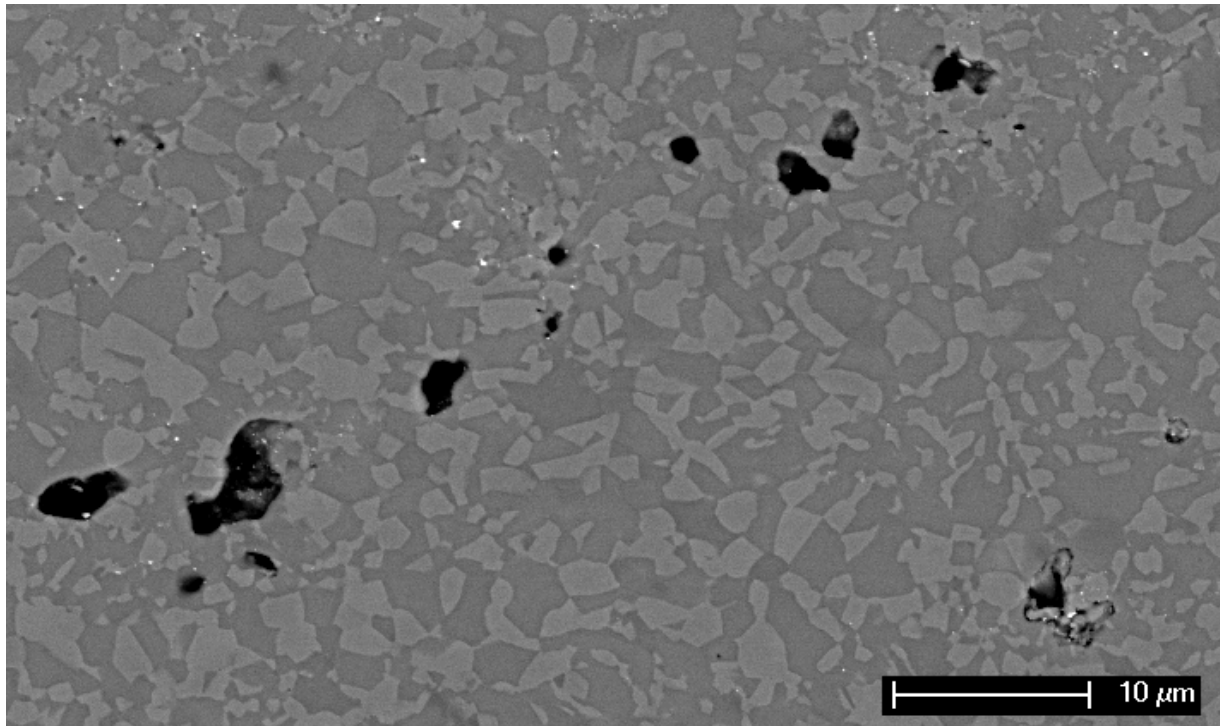


Figure 13. SEM micrograph of a VPS NiCoCrAlY coating.

CAD is, like EB-PVD, an evaporative process. In the case of CAD, however, the source material is evaporated by means of an electric arc which is struck between the source (cathode) and some anode [80]. This offers significant advantages, including high deposition rates, low substrate temperatures, and elimination of the problems associated with differing evaporation rates amongst the various components of a source alloy.

2.4.3 Oxidation Behavior of MCrAlY Overlay Coatings

The oxidation behavior of MCrAlY overlay coatings has been studied extensively, and a fairly recent review of the topic effectively summarizes much of the work that has been done to date [2]. In the current review, no attempt is made to discuss exhaustively the extensive body of literature in this area; however, some of the most important studies concerning the effects of microstructure and composition on the oxidation behavior of this important class of coating are touched upon.

2.4.3.1 Early-Stage (Transient) Oxidation Behavior The occurrence of a transient oxidation stage, during which the oxides of various elements, as well as the metastable forms of the desired Al_2O_3 corrosion product, form at the surface of alloys and coatings, is rather well known [3]. In the case of multi-phase alloy oxidation, the situation during the early stages of oxidation exposure is rather interesting, as the difference in composition of the various phases can result in significant heterogeneities in the scale. Nijdam et. al. [81] conducted a thorough study on the effect of exposure atmosphere on the transient oxidation of a dual phase ($\gamma\text{-Ni} + \beta\text{-NiAl}$) NiCoCrAlY coating. These investigators studied the effects of the atmospheric conditions upon heating, the p_{O_2} during exposure, and the presence or absence of a native (grown at room temperature prior to exposure) oxide on the initially grown scales. Concerning oxide phase constitution, it was found that the suppression of NiAl_2O_4 in favor of pure $\alpha\text{-Al}_2\text{O}_3$ was promoted during low p_{O_2} exposure. Further, decreasing the β -phase fraction in the coating suppressed the formation of metastable $\theta\text{-Al}_2\text{O}_3$, again in favor of the $\alpha\text{-Al}_2\text{O}_3$ phase, as does the segregation of a large amount of Y to the coating surface prior to oxidation exposure. This Y segregation was

promoted by the removal of the native oxide by sputtering prior to exposure, and also by heating in an inert atmosphere. The segregated Y is incorporated into the inward-growing alumina scale during oxidation, forming Y-rich oxide “pegs” which penetrate further into the alloy than does the rest of the pure Al_2O_3 scale.

The influence of microstructural scale on the transient oxidation of NiCoCrAlY alloys was investigated by Nijdam, Kwakernaak, and Sloof [82]. The NiCoCrAlY alloy of interest was prepared by conventional casting (coarse structure), laser-surface melting (LSM, intermediate structure), and electron beam physical vapor deposition (EB-PVD, greatly refined structure). It was found that the homogeneity of the scale after oxidation for 1 h at 1100°C was greatly increased as the microstructure was refined. The cast alloy formed a dual-layer scale, consisting of an inner layer of $\alpha\text{-Al}_2\text{O}_3$ and an outer layer of Co-containing $\text{Ni}(\text{Al},\text{Cr})_2\text{O}_4$ spinel oxides. The thickness of the outer spinel layer was much greater over the γ phase than over the β phase, i.e., the scales were laterally inhomogeneous. The thickness of these scales and the associated subsurface Al depletion were much greater than what was observed in the case of the LSM and EB-PVD alloys. The latter alloys also formed dual layer scales, with an inner $\alpha\text{-Al}_2\text{O}_3$ and an outer layer of Co-containing $\text{Ni}(\text{Al},\text{Cr})_2\text{O}_4$ spinel oxides. However, the outer spinel layers were much thinner than those grown on the cast alloy, and the lateral inhomogeneity observed during oxidation of the cast alloy was not present, i.e., the scales formed over the γ and β phases on the LSM and EB-PVD alloys were very similar.

The difference in the distribution of Y in the cast, LSM, and EB-PVD alloys also contributed to differences in short-term oxidation performance at 1100°C [82]. In all cases, the Y was present in the as-processed alloys as discrete NiY intermetallic particles, present primarily at phase boundaries, as a result of the low solubility of Y in the alloy. The yttride particles in the

LSM and EB-PVD alloys were very fine and homogeneously distributed. In the cast alloy, however, these particles were very coarse. During oxidation exposure of the cast alloy, very thick Ni-rich oxides formed over these coarse precipitates as a result of their low Al content. No such oxides formed over the NiY precipitates in the LSM and EB-PVD alloys.

Goedjen and Shores [83] studied the effect of alloy grain size on transient and long-term oxidation behavior of a NiCrAlY(Fe, Si) alloy at 1150°C. The alloy was prepared by plasma spraying followed by various heat treatments that were designed to establish various grain sizes, ranging from 1.4 to 32 μm . It was found that decreasing the alloy grain size resulted in a decrease in the growth rate during the transient oxidation stage. However, the effect of grain size ceased once an Al_2O_3 scale had been established. The early-stage oxidation behavior is greatly influenced by the supply of Al from the underlying alloy. Microstructural refinement resulted in an increased number of short-circuit diffusion paths (phase boundaries) which allowed for the rapid supply of Al to the scale/alloy interface and a subsequent decrease in the amount of transient oxidation. Once an Al_2O_3 scale had been established, growth was controlled purely by transport through this scale; hence the lack of importance of alloy grain size during oxidation after extended times.

During the deposition of ceramic thermal barrier coatings (TBCs) onto MCrAlY (or (Ni,Pt)Al) bond coats, a thermally grown oxide forms on the bond coat. As a result, when these systems are put into use, a pre-formed oxide scale is already present. Levi et. al. [84] investigated the growth rate, morphology, and chemical composition of the TGO formed on a NiCrAlY alloy during deposition of a ZrO_2 -1.5 mol. % $\text{YO}_{1.5}$ TBC. These investigators discovered that, absent a TBC, the γ/γ' and β phases formed oxides which were significantly different after short exposures at 1100°C. Each phase grew a dual-layer scale, with the underlying layer being α -

Al_2O_3 ; however, the upper layer consisted of $\text{Ni}(\text{Al,Cr})_2\text{O}_4$ spinels in the oxides grown over the γ/γ' phases, while over the β phase, the outer oxide consisted of a thicker layer of $\theta\text{-Al}_2\text{O}_3$. Interestingly, at low p_{O_2} , the $\theta\text{-Al}_2\text{O}_3$ formation was suppressed, and the oxide grown over the β phase was in fact thinner than that grown over the γ/γ' phases. When the oxide was grown during TBC deposition under a low p_{O_2} , the “high p_{O_2} ” behavior was once again observed, i.e., the oxide grown over the β phase was thicker than that grown over the γ/γ' phases and consisted of an inner layer of $\alpha\text{-Al}_2\text{O}_3$ with a thick external $\theta\text{-Al}_2\text{O}_3$ layer. It was determined that the presence of ZrO_2 delays the transformation to $\alpha\text{-Al}_2\text{O}_3$ by dissolving into and subsequently stabilizing the $\theta\text{-Al}_2\text{O}_3$.

2.4.3.2 Steady-State Scale Growth Kinetics As with most high temperature alloys and coatings, after a transient oxidation stage, MCrAlY alloys enter a period of steady-state oxidation during which, theoretically, the oxidation kinetics can be described by a single rate constant. In the case of pure scale (e.g., Al_2O_3) growth, we expect that the parabolic rate constant should be sufficient. However, in actual MCrAlY systems, the situation is quite complex and the parabolic rate law generally fails to adequately describe the reaction kinetics [2]. This is largely due to the presence of NiY precipitates in the microstructures of these coatings. The two factors of importance in determining the oxide growth kinetics are the distribution of the Y in the microstructure and the Y reservoir (product of Y content and coating thickness).

Using experimental and modeling techniques, Nijdam and Sloof [85] studied the effect of Y distribution on the isothermal oxidation kinetics of a NiCoCrAlY alloy. Cast alloys and free-standing EB-PVD coatings were prepared in order to produce microstructures which had Ni_5Y precipitates which were large and small, respectively. Upon oxidation, the Y in the alloy was

incorporated into the Al_2O_3 scale as YAlO_3 pegs. These pegs were few in number and rather large in the case of the cast alloy, and numerous and small in the scale grown on the EB-PVD coating. It was shown that scales containing these pegs grew faster than pure Al_2O_3 scales, and also that the presence of a high density of small pegs (EB-PVD coating) resulted in more rapid growth kinetics than the presence of a low density of large pegs (cast alloy). These investigators also demonstrated that, upon exhaustion of the Y supply in a thin coating, the pegs attain a maximum size, followed by a decrease in the oxidation kinetics. Thus, this work demonstrated the influence of both the Y distribution and reservoir.

Quadakkers et. al. [86] demonstrated the effect of specimen thickness on the oxide growth rate and microstructure for various Al_2O_3 - and Cr_2O_3 -forming alloys. Of interest for the current review are the results gathered from a freestanding CoNiCrAlY coating that was sectioned and ground to two different thicknesses, 0.15 mm and 2 mm. After 120 h of oxidation at 1100°C, metallographic examination revealed that the scale grown on the 2 mm thick specimen was approximately twice as thick as that grown on the thinner specimen. In addition, the extent of Y-rich oxide inclusion into the Al_2O_3 scale was much greater in the thicker specimen. These observations demonstrated the strong dependence of oxide growth kinetics on Y reservoir in the coating. For a given bulk composition, thicker coatings tend to form more rapidly growing, heavily included scales during oxidation exposure as a result of the higher reactive element reservoir.

2.4.3.3 Coating Durability During Thermal Cycling During service of a MCrAlY coating, thermal cycling conditions are generally encountered as a result of engine shutdown and start-up. It is extremely important for the coating to form a scale that is not only slow growing, but also

remains adherent during these thermal cycles. Elastic strain energy is stored in the thermally grown oxide during thermal cycling as a result of the coefficient of thermal expansion (CTE) mismatch between the oxide and the coating, and it is this strain energy which is the driving force for scale spallation [87]. Numerous studies have been conducted to elucidate the factors influencing the durability of MCrAlY coatings during thermal cycling conditions [2, 88-92]; presented below is a summary of a small number of these studies, which serves to illustrate the important factors governing coating durability during thermal cycling.

Meier et. al. [88] studied the effect of Y content and surface condition on the 1100°C cyclic oxidation behavior of an Ar-shrouded plasma sprayed NiCoCrAlY coating. Coatings with 0.5 wt. % Y developed oxide protrusions during exposure, which penetrated deep into the coating. It was shown that these protrusions likely initiated as a result of the preferential oxidation of Y in the concave regions of the coating, where Y enrichment is commonly observed [93]. Either fine polishing or reducing the Y content to 0.1 wt. % prevented the occurrence of these protrusions. These methods were effective because both resulted in a decrease in the amount of Y-rich regions at the coating surface.

Sloof and Nijdam [2] demonstrated the effect of phase constitution and distribution on the cyclic oxidation performance of various MCrAlY alloys. Firstly, these investigators exposed three MCrAlY alloys, one single phase γ , one single phase β , and one two-phase $\gamma+\beta$ to cyclic oxidation conditions, and found that the single phase β outperformed the other MCrAlYs. The scale grown on the single phase γ alloy began to spall profusely after relatively short times, while the two phase alloy demonstrated intermediate behavior. The fact that the CTE mismatch between β and $\alpha\text{-Al}_2\text{O}_3$ is less than that between γ and $\alpha\text{-Al}_2\text{O}_3$ was offered as a potential

explanation for this behavior; however, it should be noted that as the compositions of these alloys were significantly different, there may be numerous other influential factors.

In order to study the influence of Y distribution on cyclic oxidation behavior, a NiCoCrAlY was prepared by casting, casting followed by laser surface melting, and EB-PVD, which resulted in successively refined microstructures with smaller, more evenly-distributed Ni₅Y precipitates [2]. Microstructural refinement resulted in increased spallation resistance during thermal cycling; it was concluded that for a given Y content, a relatively homogeneous distribution of fine Ni₅Y precipitates was more effective at promoting oxide adhesion than a heterogeneous distribution of coarse precipitates. Again, there are other factors to consider when a microstructure is refined, such as the promotion of exclusive Al₂O₃ formation resulting from an increased density of short circuit diffusion paths (see Section 2.4.3.3), but it seems likely that the Ni₅Y distribution is also an important factor.

Toscano et. al. [89] demonstrated the importance of Y depletion on cyclic oxidation behavior. As discussed above, Y is incorporated into the growing oxide scale as Y-rich oxide inclusions, which increase the scaling rate. As this occurs, Y is being depleted from the coating. It was shown that after extended oxidation times, the Y in the coating can be depleted to such a level that its beneficial effects on scale adhesion are lost, and scale spallation follows. Again, it is important to consider not only the Y content of the coating, but also the Y reservoir, which is dependent on coating thickness. For a given composition, a thinner coating (i.e., coating with a smaller Y reservoir) will become depleted below this critical Y level more rapidly, and thus potentially fail at a shorter time than a thicker coating (i.e., coating with a greater Y reservoir).

Task et. al. [79] provided an interesting example of the influence of phase stability on the cyclic oxidation performance of MCrAlY alloys. As mentioned in Section 2.4.1, these

investigators studied the phase stability and cyclic oxidation behavior of a cast Ni-31Cr-11.25Al-0.6Y (wt. %) alloy and found that the phase transformation $\gamma' + \alpha \rightarrow \beta + \gamma$ occurred around 996°C during heating. Using ThermoCalc© - predicted phase fractions and density measurements made by Lowell et. al. [94], it was determined that a 1% volume change occurred as a result of this phase transformation. When cyclic oxidation was performed at 1100°C, profuse scale spallation occurred after approximately 40 1 – h cycles, which was attributed partially to transformation strains due to this volume change. When samples were cycled below the transformation temperature (900°C), scale spallation did not occur over the exposure times studied. It was acknowledged by the authors that other factors are at play, including the decrease in CTE mismatch stresses with decreasing exposure temperature, however the volume change was concluded to be a contributing factor to the poor 1100°C cyclic oxidation behavior of the NiCrAlY alloy.

2.4.4 Hot Corrosion Behavior of MCrAlY Overlay Coatings

Much attention has been paid to the mechanistic aspects of the hot corrosion of MCrAlY alloys, including coatings, bulk model alloys, and superalloys, in Sections 2.2.2 and 2.2.3. Most of the studies that were reviewed in these sections were carried out a number of decades ago; interestingly, very little progress has been made in this field since that time. As a result, this section will briefly review only two studies which have been conducted fairly recently which were aimed at identifying hot corrosion-resistant coatings.

Gurrappa [95] studied the 900°C hot corrosion behavior of various coatings on a Ni-base superalloy in the presence of Na₂SO₄ deposits with small amounts of NaCl and/or V₂O₅. It was

found that, out of the coatings studied, a NiCoCrAlY containing 18% Cr, 22% Co, 12% Al, and 0.5% Y by weight exhibited the best resistance to hot corrosion degradation. The addition of Hf and Si to the coating degraded the hot corrosion resistance, and this was attributed to the rapid reaction of Hf- and Si- containing compounds with the salt deposit. While giving useful insight into the hot corrosion of MCrAlY alloys, this study also demonstrates the main weakness of many of the hot corrosion studies that have been conducted. The issue that arises is the absence of a systematic study of the effects of individual variables on hot corrosion behavior. For example, in ref. [95], NiCoCrAlY alloys of the same compositions except for the presence of Hf and/or Si were tested. This is desirable, as the only variable changing from coating to coating is the Hf or Si content. However, the NiCrAlY and CoCrAlY alloys that were prepared differed from the NiCoCrAlY coatings with regard to Ni, Co, Cr, and Al content. As a result, it is difficult to ascertain why the NiCoCrAlY alloy exhibited the best hot corrosion resistance.

Task et. al. [4] investigated the behavior of a number of bulk MCrAlY alloys under Type I, Type II, and intermittent Type I/cyclic oxidation conditions. Intermittent Type I/cyclic oxidation tests consisted of a 20 h Type I hot corrosion exposure followed by 100 h of cyclic oxidation (1 h cycles) at 1100°C. It was found that Ni-31Cr-11.25Al-0.65Y, Co-23Cr-13Al-0.65Y, Ni-20Co-18Cr-12.5Al-0.6Y-0.4Hf-0.25Si (wt. %) alloys all performed rather well in Type I. Type II hot corrosion was, however, much more severe. The NiCrAlY alloy was relatively resistant, while the CoCrAlY and NiCoCrAlY were degraded very rapidly. Increasing the Ni content at the expense of Co in the NiCoCrAlY alloy did not result in an increase in Type II resistance; some improvement in behavior was realized when the decreased Co content was instead balanced by Cr addition. The intermittent Type I exposures revealed that, for the alloys studied, a brief Type I hot corrosion exposure prior to cyclic oxidation had no effect on oxidation

performance. Once again, this study revealed a number of very interesting aspects of the hot corrosion of MCrAlY alloys, however studies which are more systematic in the variation of coating composition are still required.

3.0 DEFICIENCIES IN THE CURRENT BODY OF KNOWLEDGE AND MOTIVATION FOR CURRENT WORK

Upon review of the existing hot corrosion literature, one observes that the majority of the research that has been dedicated to the subject has been primarily focused on developing an understanding of the modes of *propagation*. These studies have been rather fruitful; however, from an engineering standpoint, what is of interest is a thorough understanding of the *incubation stage* and what factors determine its duration. The incubation stage essentially defines the useful lifetime of a gas turbine component, and as it is desirable to extend the lifetime of a given component for reasons both economical and safety-related, it is consequently desirable to extend the incubation stage.

Five factors that influence the duration of the incubation stage were discussed in section 2.2.1.1. Three of these, gas composition, amount of deposit, and temperature, are generally defined for a particular application and thus are not within the control of the engineer. Alloy composition and alloy condition (i.e., microstructure) are two variables that can be controlled to an extent; therefore, it is of vital importance to develop a thorough understanding of how these two factors can be optimized for improved hot corrosion resistance. In addition, the influence of phase constitution on hot corrosion behavior is an issue that has been largely ignored, however it is reasonable to hypothesize that the phases present and their individual compositions, as well as

any phase transformations which may occur during service, should be as important as bulk composition.

In the current study, the various factors that influence the hot corrosion behavior of modern coating compositions are explored, with special attention being paid to the incubation stage and how these factors affect its duration. The results are presented and discussed over the course of four chapters, with each chapter covering a different factor, be it compositional, microstructural, environmental, etc., for a given alloy system and exposure condition (Type I or Type II hot corrosion). When necessary, a given chapter will begin with a brief review of the literature that is pertinent to the results presented in said chapter.

In chapter 4, the effect of microstructural scale on the Type II hot corrosion resistance of MCrAlY alloys is explored by observing the behavior of MCrAlY alloys and coatings prepared by a number of different processing routes. Compositional effects on the Type I and Type II hot corrosion behavior of β -NiAl alloys are investigated in chapters 5 and 6, respectively. Focus will be placed on the effects of Co, Cr, and Pt, three elements that are commonly found in actual diffusion aluminide coatings. Finally, in chapter 7, the results of a thorough investigation of the phase stability in scales grown on β -NiAl alloys, i.e., the kinetics of the θ to α -Al₂O₃ transformation, the importance (or lack thereof) of this transformation during Type I hot corrosion, and the effects of alloy composition and exposure environment on the kinetics of the transformation are presented.

4.0 THE EFFECT OF MICROSTRUCTURE ON THE TYPE II HOT CORROSION OF NI-BASE MCrAlY ALLOYS

4.1 EXPERIMENTAL PROCEDURE

4.1.1 Alloy Preparation

The compositions of the cast alloys used in this study, measured by inductively coupled plasma optical emission spectroscopy, are shown in Table 2.

Table 2. Cast alloy compositions (wt. %), measured by ICP-OES

	Ni	Co	Cr	Al	Y	Hf	Si
NiCrAlY	Balance	-	31.5	11.5	0.6	-	-
NiCoCrAlY	Balance	20.9	19.2	12.5	0.5	0.3	0.4

All alloy castings were prepared by the Materials Preparation Center at Ames Laboratory [96]. They were received as drop-cast (DC) bars which were homogenized at 1000°C for 24 h in Ar, and were tested in this condition. The bars were cut into coupon specimens approximately 3mm thick and 18mm in diameter, diamond polished to a 3μm finish, cleaned in soap and water, degreased in acetone, dried and weighed immediately prior to testing. 3mm diameter injection cast (IC) pins of nominally the same compositions as the DC NiCrAlY and NiCoCrAlY were

also tested after a 24 h homogenizing heat treatment at 1000°C. Injection casting is a rapid solidification technique that resulted in microstructures that were significantly refined relative to the DC materials (see Section 4.2.1). The surface preparation procedure of the IC materials was the same as that mentioned above. Finally, the NiCrAlY and NiCoCrAlY were sprayed via a low-pressure plasma spray (LPPS) process onto a René N5 substrate, approximately 30 mm in diameter.

4.1.2 Type II Hot Corrosion Exposures

A 2-3mg/cm² deposit of Na₂SO₄ was applied to one of the broad surfaces of the hot corrosion specimens by heating with a heat gun to approximately 200°C and spraying with a saturated solution of laboratory grade Na₂SO₄ in distilled water. Specimens were weighed periodically to ensure that the proper amount of salt was deposited.

Figure 14 is a schematic depiction of the Type II hot corrosion apparatus used in this study.

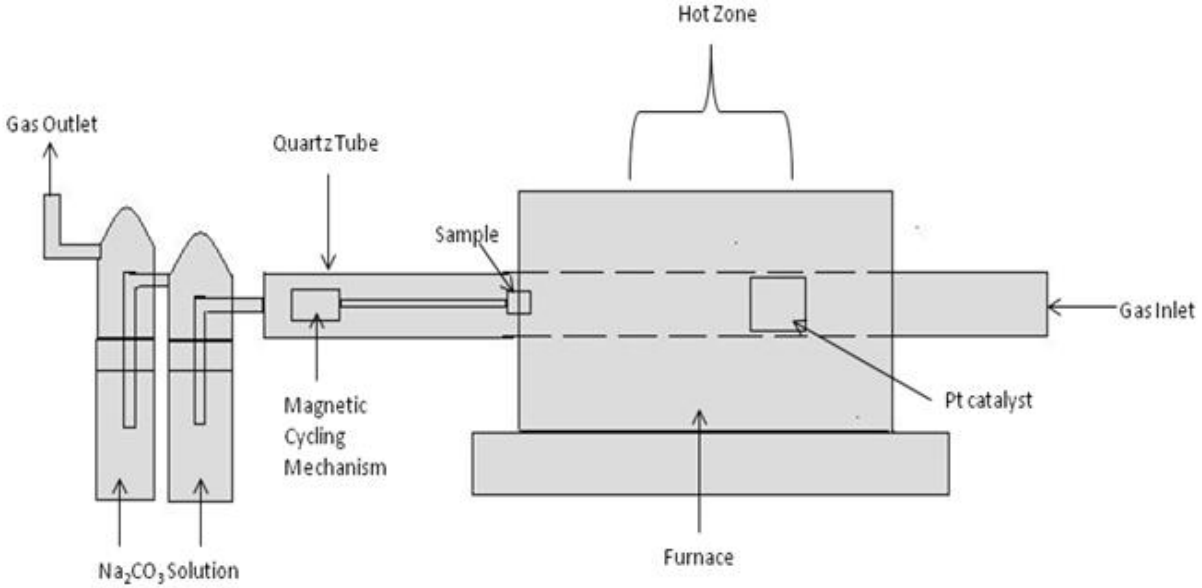
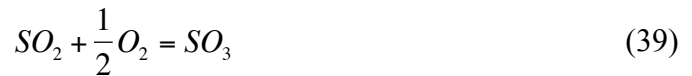


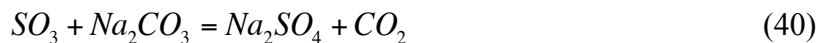
Figure 14. Type II hot corrosion apparatus schematic

The furnace was cycled manually by using a magnet to push the rod from which the specimen holder was attached into the furnace until the specimens were in the hot zone, which was maintained at $700^{\circ}\text{C} \pm 3^{\circ}\text{C}$. The specimens were laid flat on the holder, with the salt-deposited side facing up. A gas containing $\text{O}_2 + 1000\text{ppm SO}_2$ flowed into the tube at a constant volumetric flow rate of $\sim 15 \text{ cm}^3/\text{min}$. This gas mixture was passed over a Pt honeycomb catalyst which was placed at the end of the hot zone just upstream of the specimens in order to establish an equilibrium p_{SO_3} in the atmosphere according to Reaction 39:



Assuming thermodynamic equilibrium, the p_{SO_3} under these conditions was $\sim 7.0 \times 10^{-4}$ atm. The total pressure was 1 atm. Upon exiting the furnace, the gases were bubbled through a

solution of Na_2CO_3 in water prior to being released into a fume hood. The purpose of this step was to remove SO_3 from the gas according to Reaction 40:



Sodium sulfate is formed and the majority species exiting the apparatus are O_2 and CO_2 .

After a 10 h isothermal exposure, specimens were metallographically prepared in the absence of water or water-based solutions in order to preserve any water-soluble corrosion products that may have formed during the corrosion process.

4.1.3 Analytical Methods

The extent of Type II degradation was primarily investigated via cross-sectional analysis of the exposed specimens using a Philips XL-30 Field Emission Gun Scanning Electron Microscope (FEG-SEM) capable of performing energy dispersive spectroscopic analysis (EDS). X-ray diffraction (XRD) was used in order to determine the phases present in the starting microstructures.

4.2 RESULTS

4.2.1 Starting Microstructures

The microstructures of the drop cast NiCrAlY and NiCoCrAlY are shown in Fig. 15. The NiCrAlY was four-phase, consisting of β -NiAl (primitive cubic intermetallic), γ -Ni (FCC Ni-base solid solution), α -Cr (BCC Cr-base solid solution), and a Ni-rich yttride, as determined by EDS in conjunction with XRD. The stoichiometry of the yttride could not be unambiguously determined, but based on another study, it may be Ni₉Y [97]. It was unclear based on XRD whether γ' -Ni₃Al (primitive cubic intermetallic) was present in addition to γ . The DC NiCoCrAlY contained γ , β , and the yttride phase.

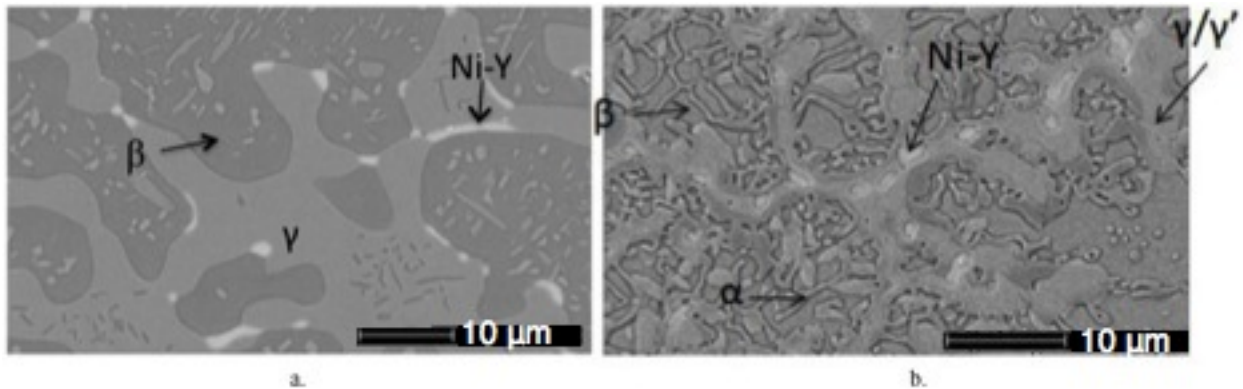
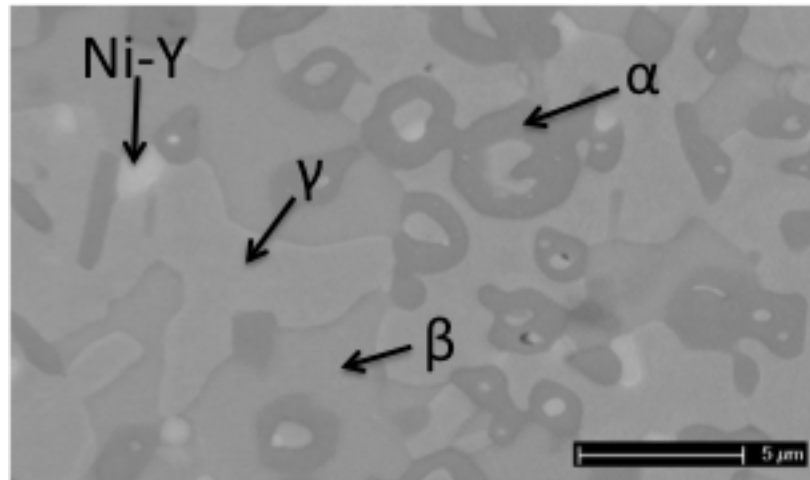
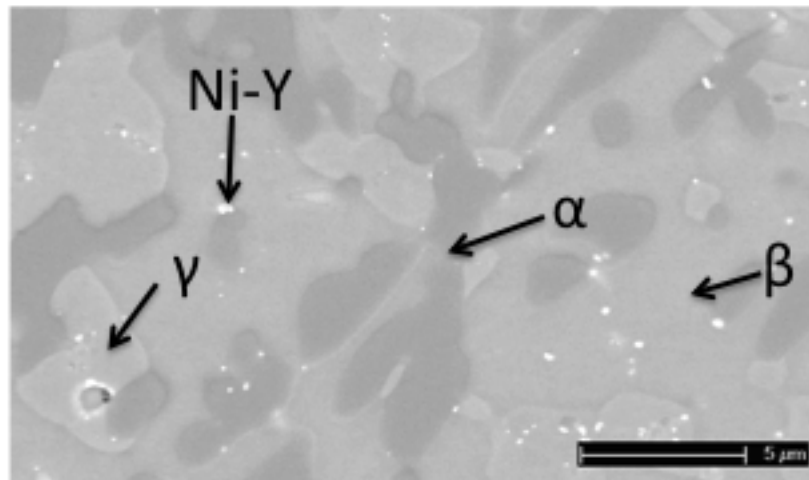


Figure 15. Starting microstructures of the drop cast a) NiCoCrAlY and b) NiCrAlY

The NiCrAlY microstructure was greatly refined when prepared via the injection casting process, as indicated by the images in Fig. 16. Similar to the DC NiCrAlY, the IC alloy had a four-phase $\beta + \gamma + \alpha + \text{Ni-rich yttride}$ microstructure. Interestingly, while injection casting did significantly refine the microstructure of the NiCoCrAlY, the phase constitution differed from the DC alloy. Specifically, plate-like Cr-rich precipitates, presumably $\alpha\text{-Cr}$, were observed in the IC NiCoCrAlY microstructure (Fig. 16). Apparently, during the IC process, the solidification path of the NiCoCrAlY was such that a significant amount of $\alpha\text{-Cr}$ was precipitated. The details of this were not further investigated.



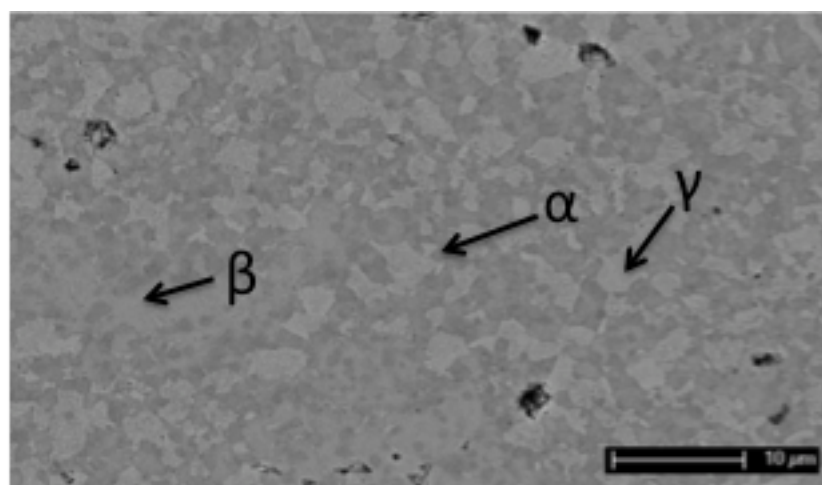
a.



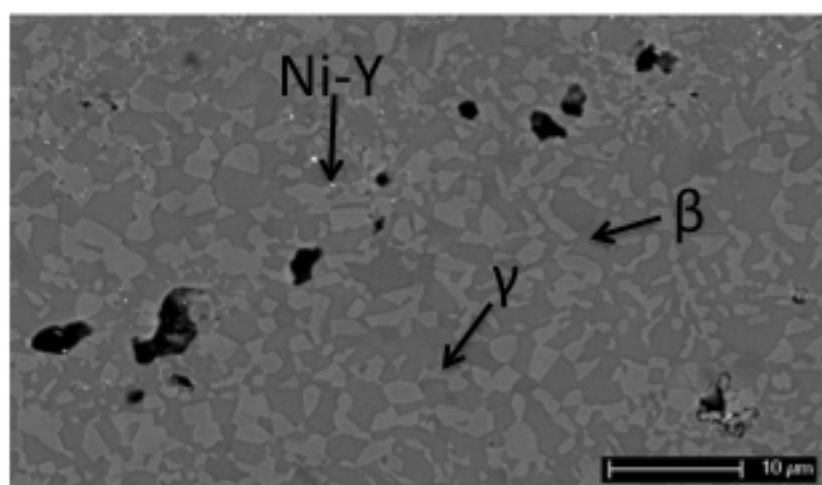
b.

Figure 16. Starting microstructures of the injection cast a) NiCrAlY and b) NiCoCrAlY

The LPPS NiCrAlY and NiCoCrAlY coating microstructures are shown in Fig. 17. The phases present in each microstructure were the same as those present in the DC specimens, with the one exception that very little of the yttride phase was observed in the LPPS NiCrAlY.



a.



b.

Figure 17. Starting microstructures of the LPPS a) NiCrAlY and b) NiCoCrAlY

The LPPS NiCoCrAlY was tested in the as-coated condition, with no further surface modifications made. However, the surface of the LPPS NiCrAlY was ground to a depth of approximately 50 μm and polished to a 3 μm finish prior to testing. Grinding of the LPPS NiCrAlY was necessary because after spraying, a 2-3 μm layer of α -Cr was observed at the surface, underneath which was a 5-10 μm layer of β -NiAl, followed by an Al-depleted zone, as shown in Fig. 18. The bulk $\gamma + \beta + \alpha + \text{yttride}$ phase constitution was observed only beneath these layers, for reasons currently unknown. Hot corrosion testing in the as-coated condition would, therefore, potentially lead to misleading results.

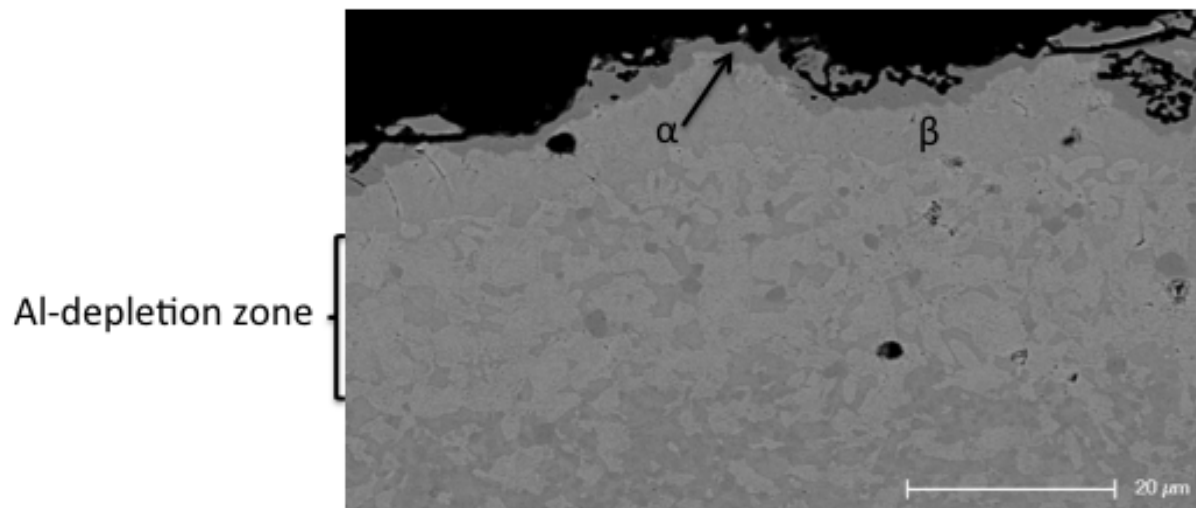


Figure 18. Microstructure of the as-coated LPPS NiCrAlY prior to surface grinding

In order to quantify the scales of the microstructures, lines were drawn over a number of as-processed micrographs, and the number of intersections between these lines and phase boundaries was counted. As an example, a micrograph of the LPPS NiCoCrAlY with these lines

drawn is shown in Fig. 19. The micrographs of the DC alloys were analyzed at a lower magnification (1000X) than those of the IC and LPPS structures (2000X). The number of micrographs analyzed was adjusted such that the same line length was evaluated for each specimen. The results of these measurements, reported as phase boundary intersections per mm of line length, are shown in Table 3. In this table, a higher number indicates a finer microstructure. Thus, the NiCrAlY microstructure became coarser in the order IC < LPPS < DC, while the NiCoCrAlY became coarser in the order LPPS < IC < DC.

Table 3. Phase boundary intersections per unit line length for the as-processed MCrAlYs

Phase Boundary Intersections per mm line length		
	NiCrAlY	NiCoCrAlY
DC	89	138
IC	489	280
LPPS	352	484

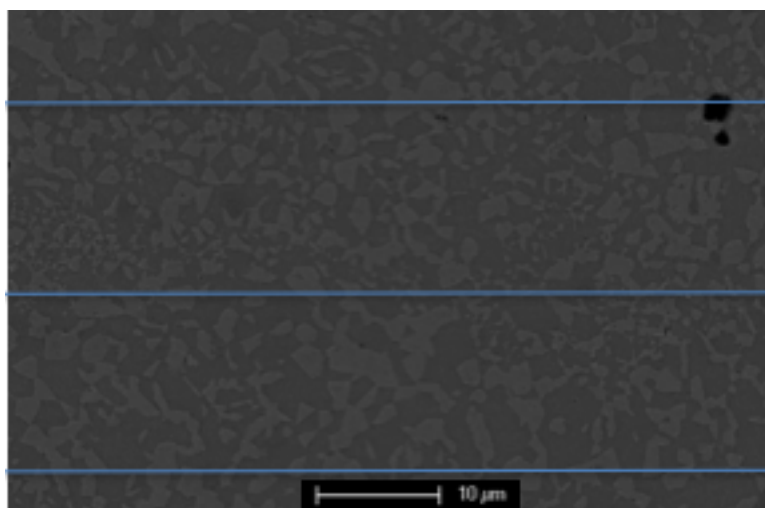


Figure 19. As coated LPPS NiCoCrAlY, demonstrating the lines that were used to quantify the scale of the microstructure

4.2.2 Type II Hot Corrosion

The microstructure of the DC NiCrAlY alloy after a 10 h Type II hot corrosion exposure and corresponding X-ray maps of the relevant elements are presented in Figs. 20 and 21, respectively:

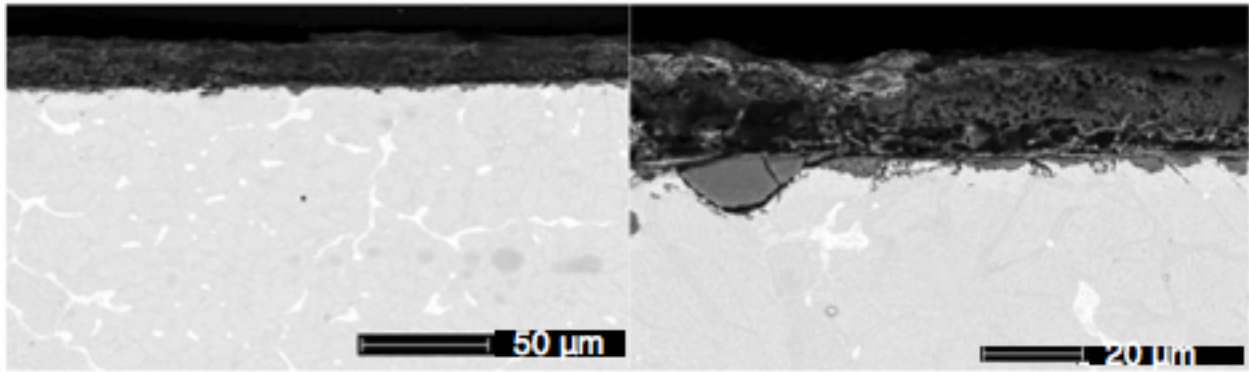


Figure 20. Microstructure of the DC NiCrAlY after a 10 h Type II hot corrosion exposure

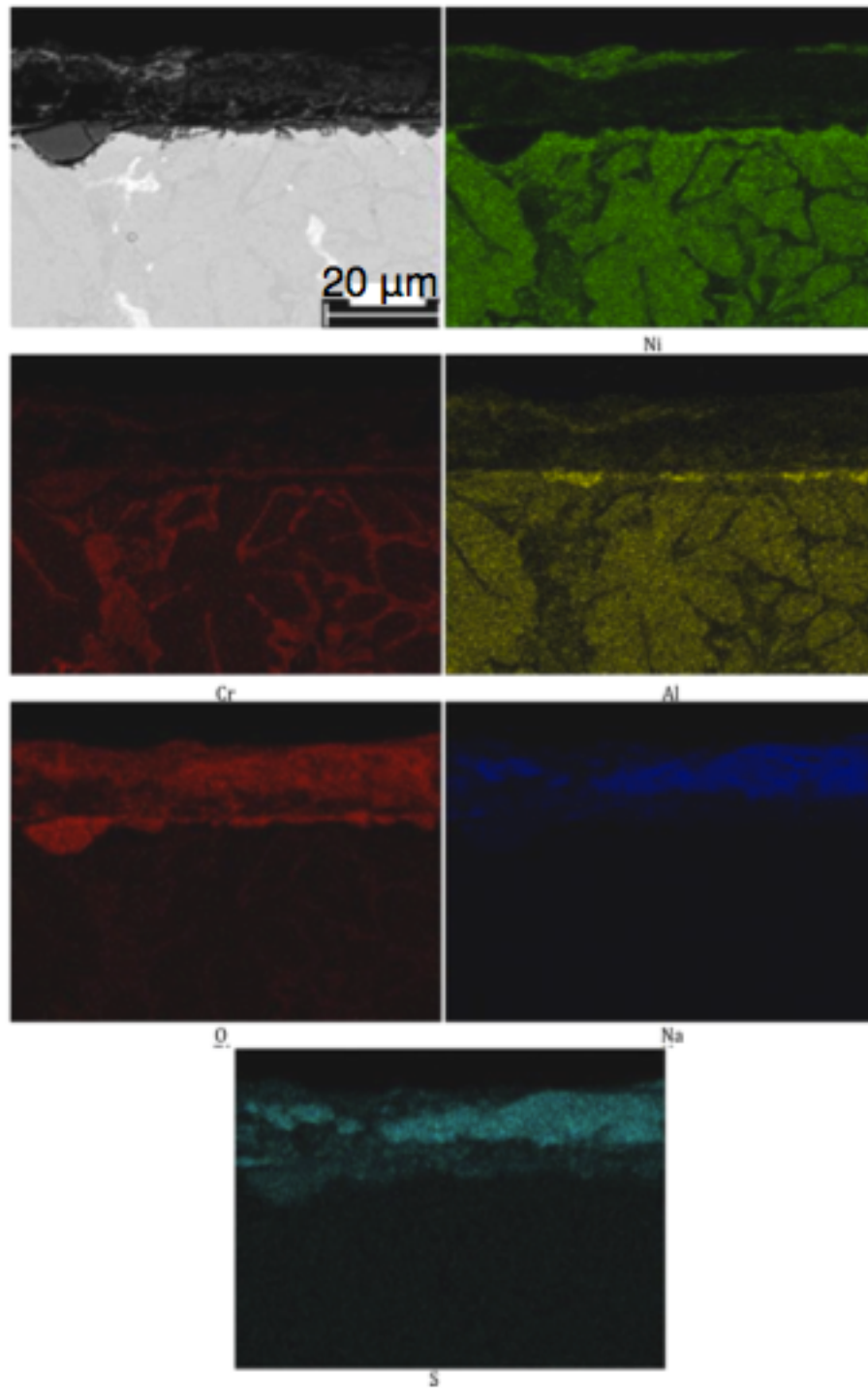


Figure 21. SEM micrograph and associated X-ray maps of the DC NiCrAlY after a 10 h Type II hot corrosion exposure

The DC NiCrAlY underwent only minor Type II attack. A solidified Na_2SO_4 layer was observed on the surface of the specimen with NiO precipitates near the salt/gas interface. Relatively small corrosion pits, rich in Cr, Al, S, and O, were found in the specimen. These pits were very shallow compared to those formed on many other MCrAlY alloys [44]. Preferential oxidation/sulfidation attack was found to occur along phase boundaries surrounding the α -Cr phase, as is shown more clearly in Fig. 22.

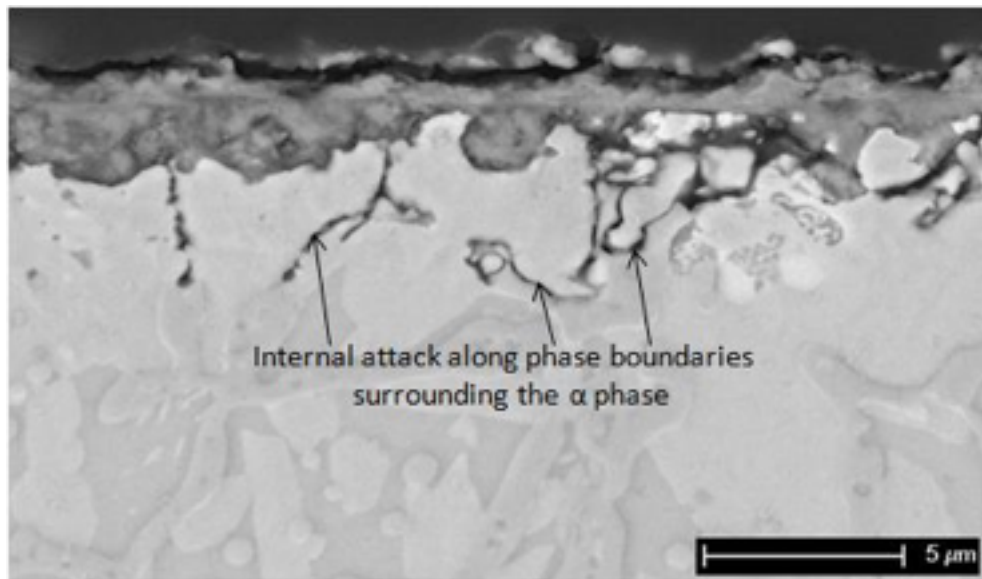


Figure 22. SEM micrograph of the DC NiCrAlY after a 10 h Type II hot corrosion exposure, showing the internal attack along the interphase boundaries surrounding the α phase

The microstructure of the IC NiCrAlY after a 10 h Type II hot corrosion exposure and the associated X-ray maps are shown in Figs. 23 and 24, respectively.

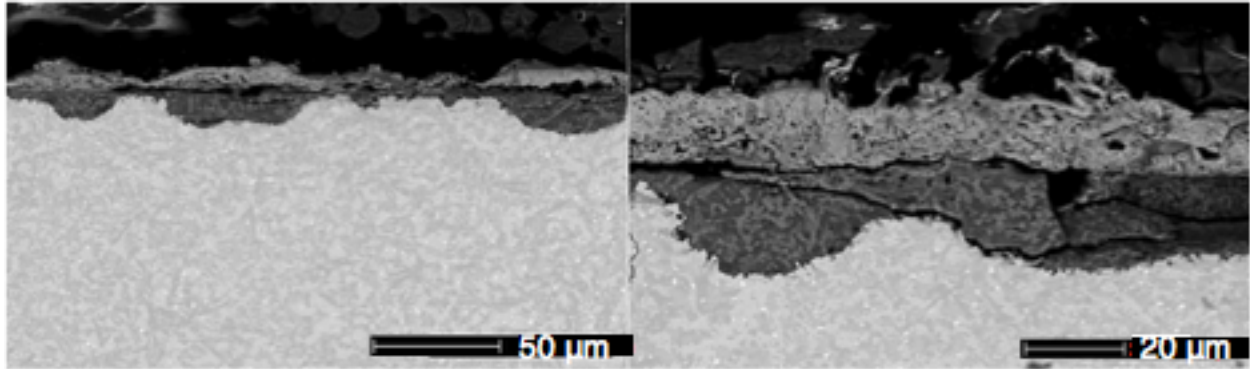


Figure 23. SEM micrographs of the IC NiCrAlY after a 10 h Type II hot corrosion exposure

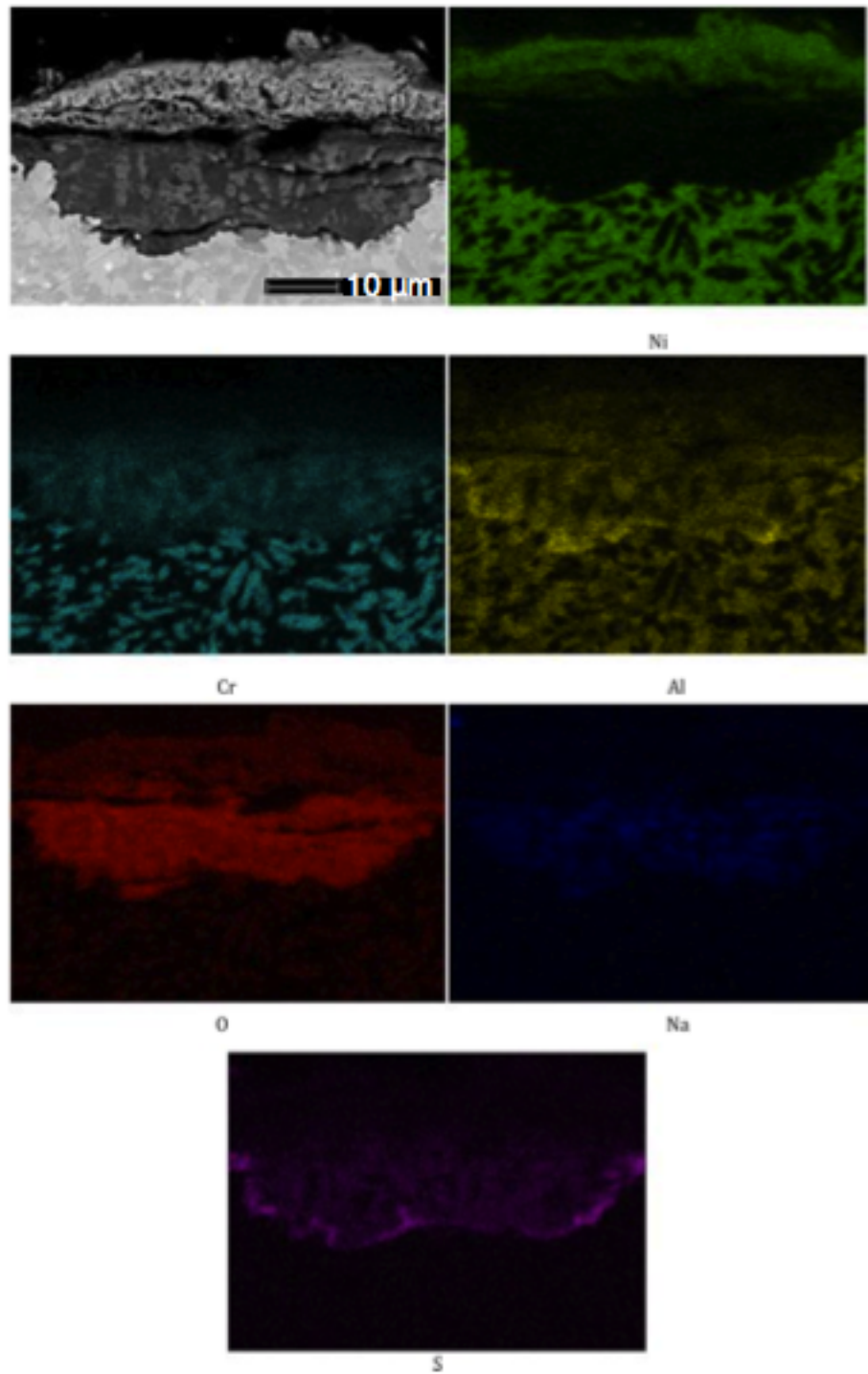


Figure 24. SEM micrograph and associated X-ray maps of the IC NiCrAlY after a 10 h Type II hot corrosion exposure

Microstructural refinement via injection casting resulted in much more severe hot corrosion attack (compare Fig. 20 and Fig. 23). Pits greater than 20 μm in depth were regularly observed in the IC alloy. Such features were absent in the DC specimen. A small amount of internal oxidation/sulfidation at the inter-phase boundaries surrounding the α phase was also found in the IC alloy, as indicated by the arrows in Fig. 25.

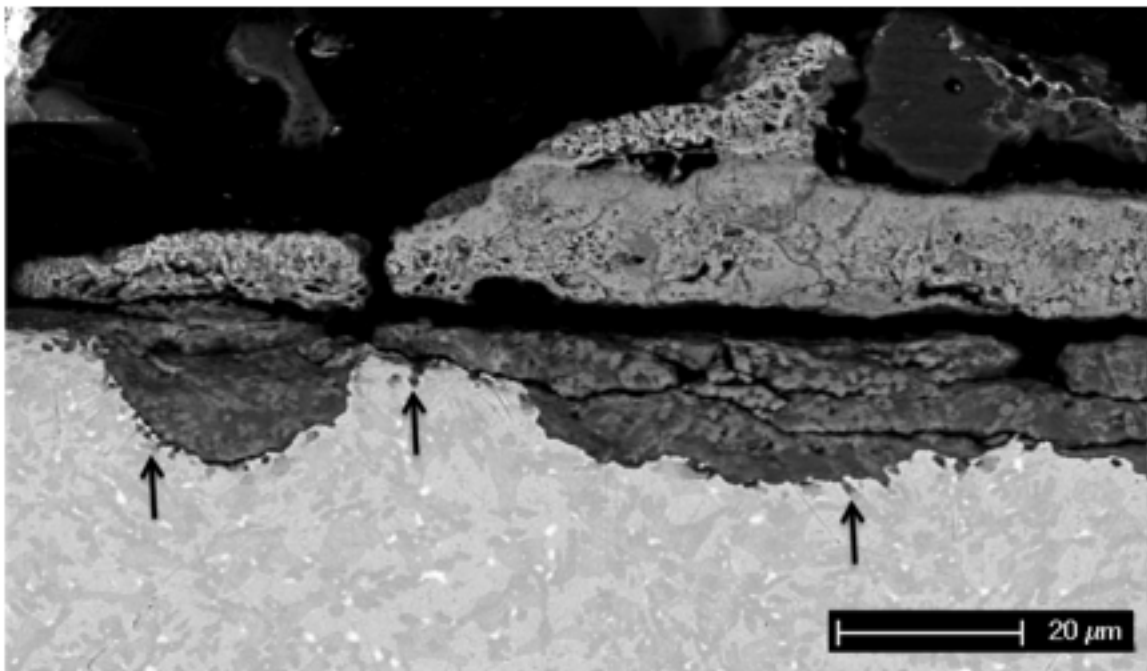


Figure 25. SEM micrograph of the IC NiCrAlY after a 10 h Type II hot corrosion exposure, showing the internal attack along the interphase boundaries surrounding the α phase

The microstructure of the LPPS NiCrAlY, tested after the above-mentioned surface treatment, is shown in Fig. 26. It was found that LPPS deposition of the NiCrAlY resulted in the best hot corrosion resistance of the NiCrAlY specimens studied; the attack was negligible after the 10 h exposure.

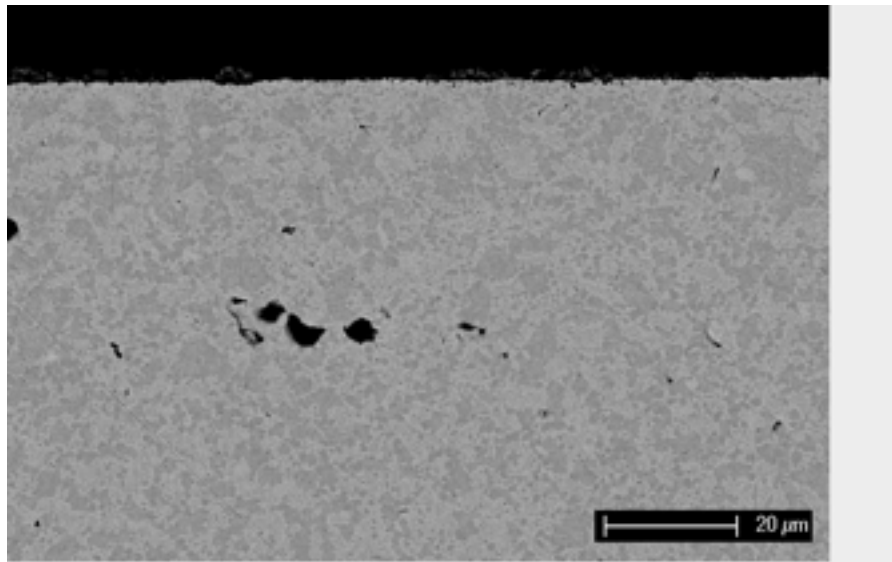


Figure 26. SEM micrograph of the LPPS NiCrAlY after surface grinding/polishing followed by a 10 h Type II hot corrosion exposure

The microstructure and associated X-ray maps of the DC NiCoCrAlY alloy after a 10 h Type II hot corrosion exposure are shown in Figs. 27 and 28, respectively. Degradation of the DC NiCoCrAlY was found to be quite severe. Very broad, nearly uniform hot corrosion attack was observed. An approximately 20 μm layer of single-phase γ -Ni formed beneath the scale as a result of extensive Al depletion during hot corrosion. Internal Cr-rich sulfide precipitates were observed within this depletion zone. Oxides of Ni and Co precipitated near the salt/gas interface.

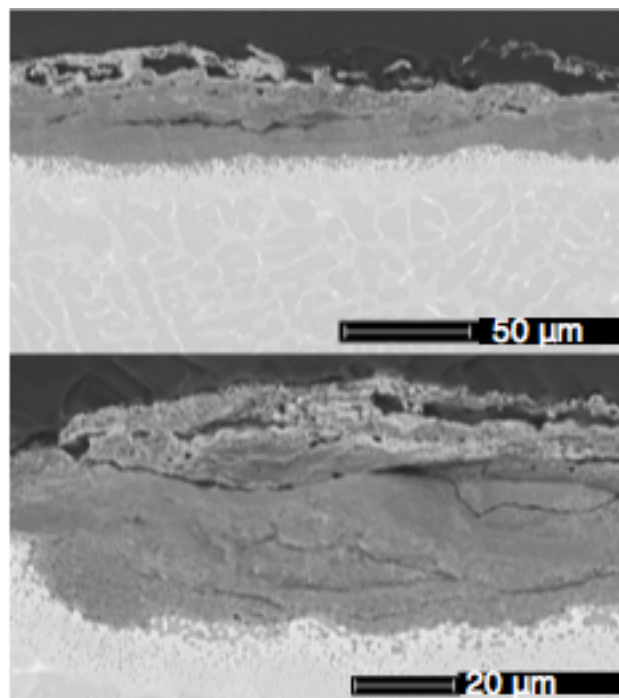


Figure 27. SEM micrographs of the DC NiCoCrAlY after a 10 h Type II hot corrosion exposure

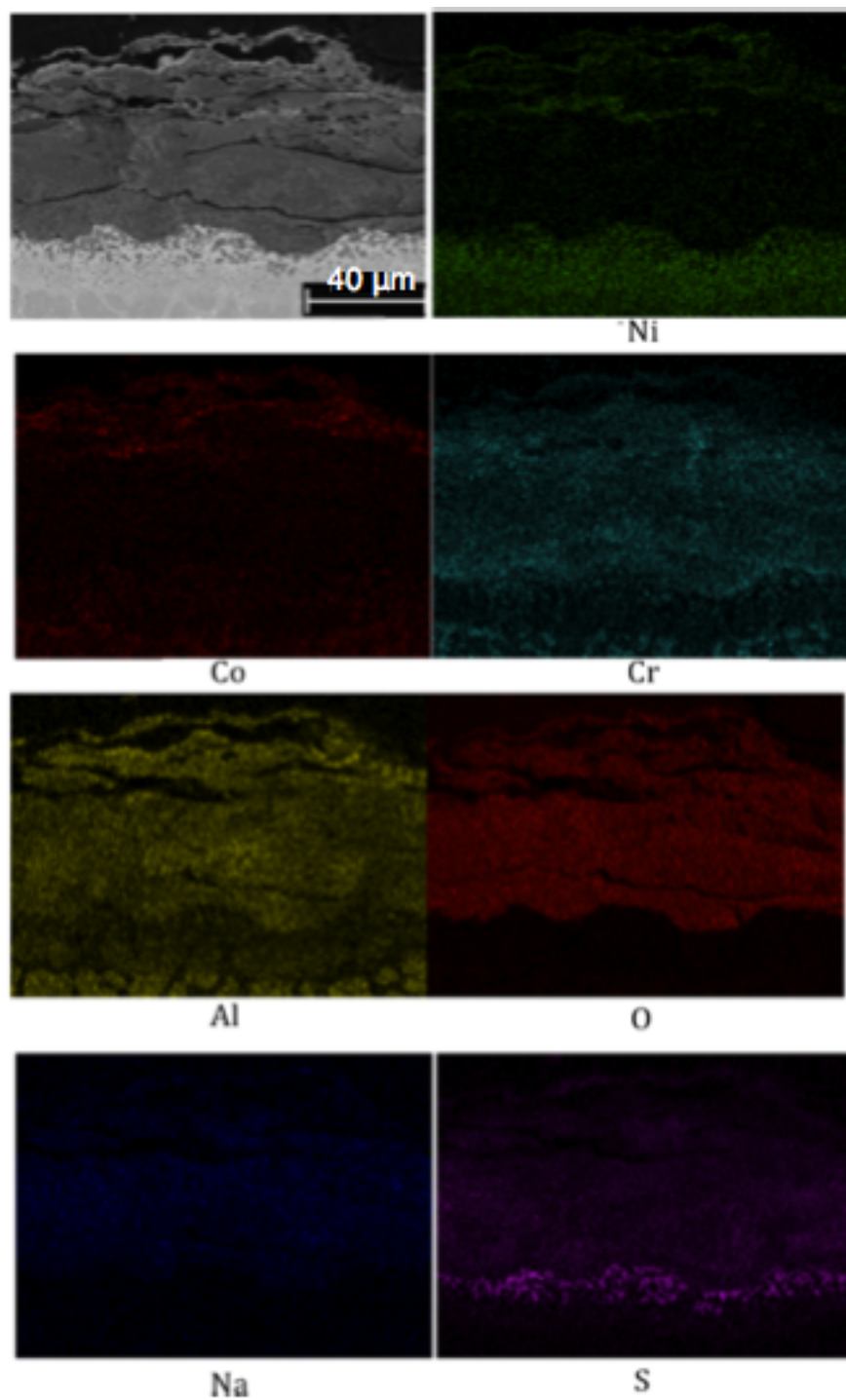


Figure 28. SEM micrograph and associated X-ray maps of the DC NiCoCrAlY after a 10 h Type II hot corrosion exposure

Injection casting of the NiCoCrAlY resulted in significantly improved resistance to Type II attack (Fig. 29). The depth of attack decreased from 60-80 μm in the DC NiCoCrAlY to $\sim 20\text{ }\mu\text{m}$ in the IC specimen. Notably, the amount of subsurface Al depletion was significantly less (indicated by the lack of an observable continuous γ -Ni layer at the scale/alloy interface), and the internal sulfidation observed in the DC specimen was absent in the IC specimen.

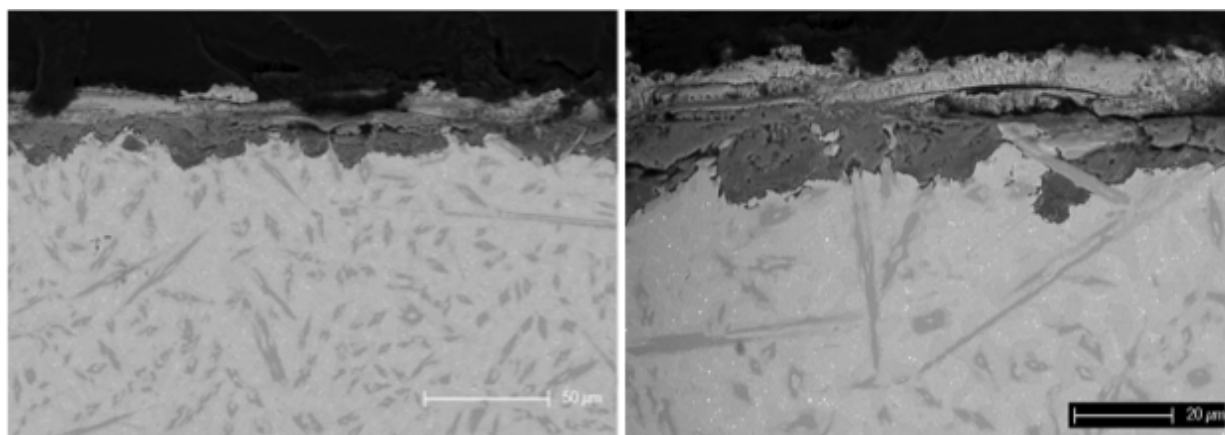


Figure 29. SEM micrographs of the IC NiCoCrAlY after a 10 h Type II hot corrosion exposure

The LPPS NiCoCrAlY generally displayed excellent resistance to Type II hot corrosion, as shown in Fig. 30. Only very localized accelerated corrosion was observed, with the depth of attack in these regions being only $\sim 5\text{ }\mu\text{m}$. Aluminum depletion resulted in the development of a 4-5 μm layer of single-phase γ -Ni beneath the largely protective Al-rich scale. Locally, a small amount of internal Cr-rich sulfide was precipitated within this depletion zone (not shown in Fig. 30), but this was not observed over the majority of the cross section. Microstructural

refinement was found to be extremely beneficial in terms of the Type II hot corrosion behavior of the NiCoCrAlY alloy.

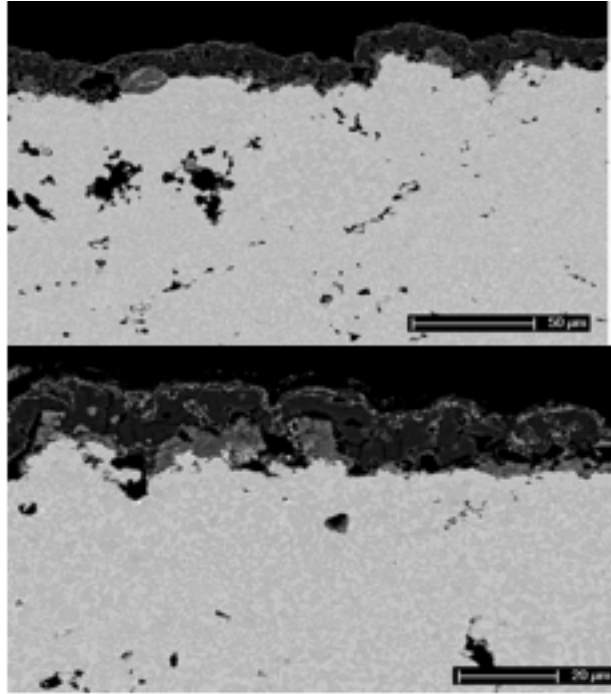


Figure 30. SEM micrographs of the LPPS NiCoCrAlY after a 10 h Type II hot corrosion exposure

4.2.3 Type II Hot Corrosion of a Pre-oxidized NiCoCrAlY Alloy and the Use of a $\text{Na}_2\text{SO}_4 - \text{NiSO}_4$ Deposit

In order to investigate the influence of pre-oxidation on Type II hot corrosion behavior, an alloy of composition Ni-10Co-18Cr-12.5Al-0.6Y-0.3Hf-0.4Si (wt.%), referred to henceforth as “NiCoCrAlY-2”, was drop cast and prepared as described in Section 4.1.1. The microstructure of the as-cast NiCoCrAlY-2 alloy is shown in Fig. 31.

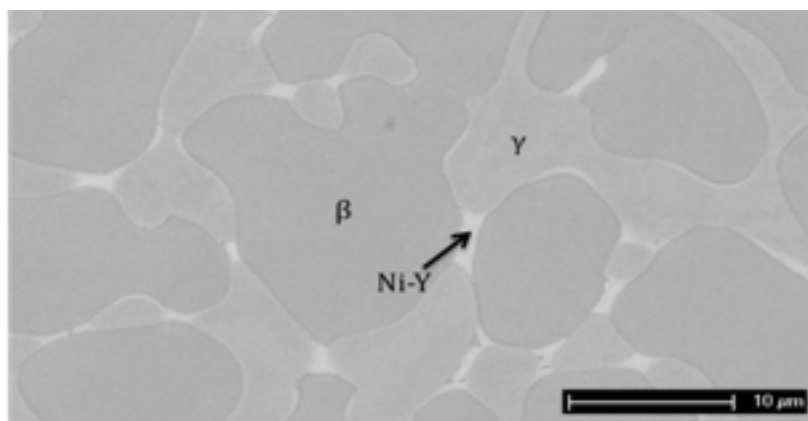


Figure 31. SEM micrograph of the as-cast NiCoCrAlY-2

Specimens of this alloy were pre-oxidized at 1100°C for 1 h prior to Type II hot corrosion exposure. A cross-section of the specimen after pre-oxidation is shown in Fig. 32. The alloy formed a thin ($\sim 1\mu\text{m}$) $\alpha\text{-Al}_2\text{O}_3$ scale (as confirmed by glancing angle XRD) with numerous reactive-element-rich inclusions. The pre-oxidized specimen was then exposed to Type II conditions for 10 h using the procedure described in Section 4.1.2, however a Na_2SO_4 - 40 mol % NiSO_4 salt mixture was used as the deposit. This salt is at the eutectic composition in the $\text{Na}_2\text{SO}_4 - \text{NiSO}_4$ system and is molten at 700°C without any need for NiO formation,

sulfation, and subsequent incorporation into the Na_2SO_4 . The use of this eutectic salt mixture is necessary because Type II exposure of the pre-oxidized NiCoCrAlY-2 with a pure Na_2SO_4 deposit resulted in negligible attack, presumably because insufficient transient NiO was present following pre-oxidation to subsequently stabilize the eutectic melt. This itself is noteworthy, as pre-oxidation clearly inhibits pure Na_2SO_4 -induced Type II hot corrosion of this alloy. Nonetheless, the eutectic mixture was applied for subsequent testing in order to investigate the efficacy of pre-oxidation in providing resistance to Type II hot corrosion in the presence of a molten salt deposit.

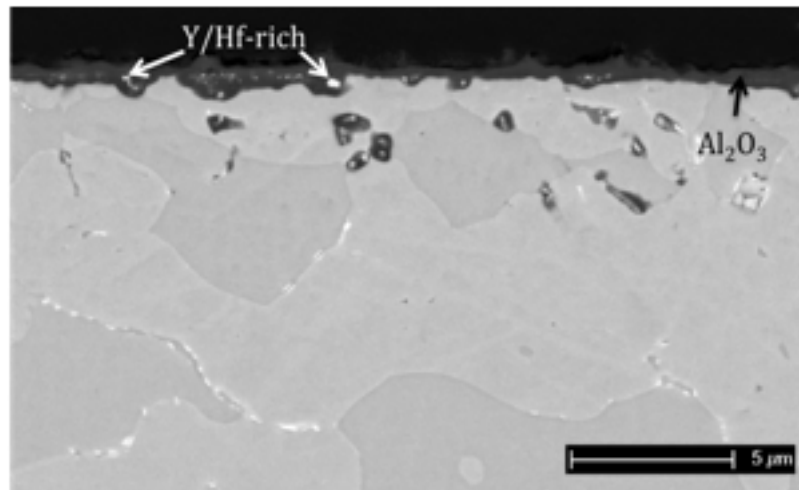


Figure 32. SEM micrograph of the NiCoCrAlY-2 after pre-oxidation at 1100°C for 1 h

The microstructure of the pre-oxidized NiCoCrAlY-2 after a 10 h Type II hot corrosion exposure in the presence of a Na_2SO_4 - 40 mol % NiSO_4 deposit is shown in Fig. 33. Localized penetration of the pre-formed Al_2O_3 scale was found to occur, resulting in infiltration of the salt and very rapid corrosion in these regions. For comparison, the microstructure of the NiCoCrAlY-2 exposed to Type II conditions for 10 h with no pre-oxidation treatment is shown in Fig. 34.

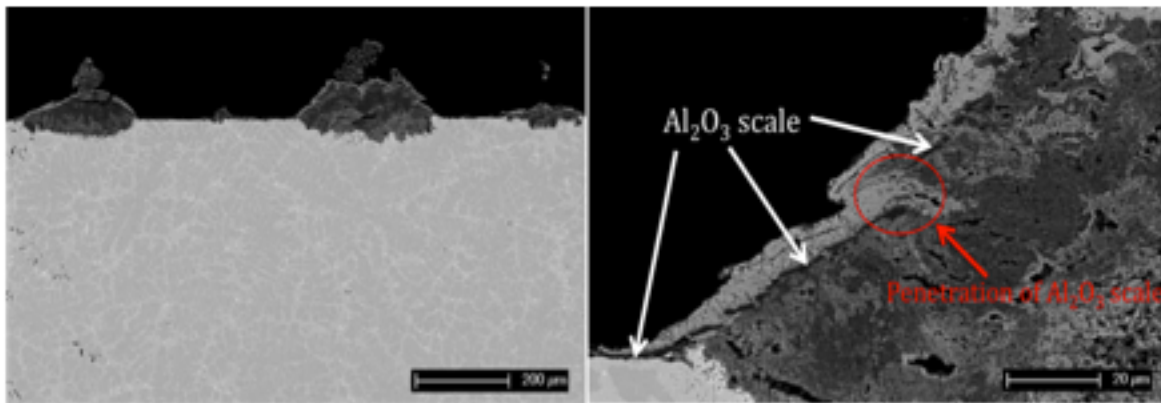


Figure 33. SEM micrographs of the pre-oxidized NiCoCrAlY-2 after a 10 h Type II hot corrosion exposure in the presence of Na_2SO_4 - 40 mol % NiSO_4

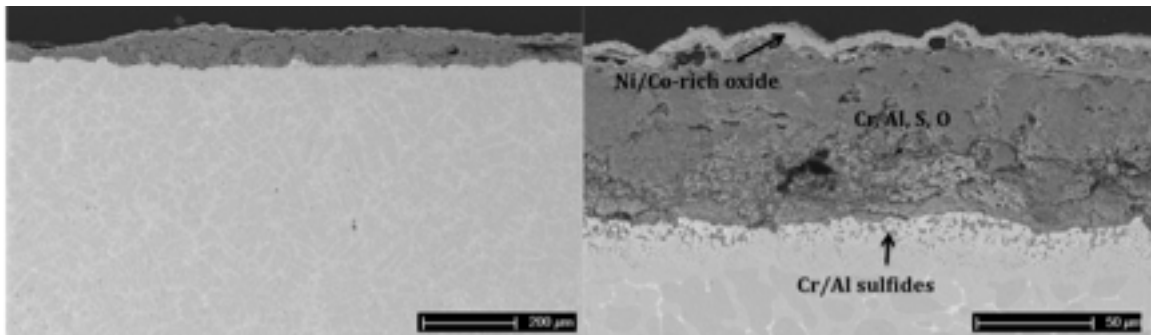


Figure 34. SEM micrographs of the NiCoCrAlY-2 exposed to Type II conditions for 10 h with no pre-oxidation treatment

Without pre-oxidation, the NiCoCrAlY-2 with a $\text{Na}_2\text{SO}_4 - \text{NiSO}_4$ deposit experienced very broad attack with an extensive amount of internal sulfidation, rather similar to the DC NiCoCrAlY specimen. It is clear that a pre-oxidation treatment greatly enhanced the corrosion resistance of the alloy, allowing for only localized pitting attack at locations of scale penetration rather than the very severe attack observed across the entire surface of the specimen with no pre-oxidation.

In order to determine the cause of the local scale breakdown observed with the pre-oxidized NiCoCrAlY-2, a 5 h Type II hot corrosion exposure with the eutectic salt mixture was carried out on the alloy after the same pre-oxidation treatment. The microstructure of this specimen is shown in Fig. 35. Scale penetration and subsequent pit formation was found to initiate at the Y/Hf-rich regions in the pre-formed Al_2O_3 scale.

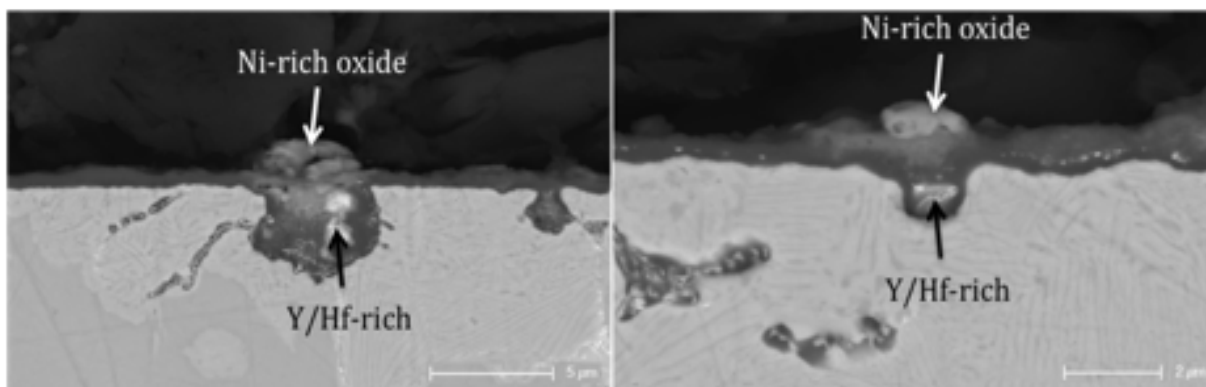


Figure 35. SEM micrographs of the pre-oxidized NiCoCrAlY-2 after a 5 h Type II hot corrosion exposure in the presence of a $\text{Na}_2\text{SO}_4 - 40 \text{ mol } \% \text{ NiSO}_4$

4.3 DISCUSSION

4.3.1 The Influence of Microstructural Scale, Phase Constitution, and Phase Composition on Type II Hot Corrosion Resistance

Two different trends were observed for the NiCrAlY and NiCoCrAlY alloys in this study. The Type II hot corrosion resistance of the NiCrAlY alloy increased relative to the DC alloy when the microstructure was refined via LPPS; however the IC specimen, which had the finest microstructure of all of the NiCrAlYs, underwent very rapid hot corrosion attack. By contrast, the NiCoCrAlY consistently displayed improved hot corrosion resistance with increasing microstructural refinement. It is apparent that hot corrosion resistance depends not only on bulk composition, but also on microstructure and phase constitution.

There are two factors that must be considered when discussing the ability of an alloy to display protective scaling behavior at elevated temperatures [98]: 1) the ability of the alloy to supply a sufficient flux of the element to be selectively oxidized to the alloy surface, such that the formation of a continuous external oxide is favored over internal attack and oxidation of the more noble metal, and 2) an adequate reservoir and sufficiently rapid supply of this element to the oxide/alloy interface to maintain the growth of the scale during subsequent exposure. These principals have traditionally been applied to gas-phase oxidation; however, they should also hold true during hot corrosion. Under hot corrosion conditions, the rapid formation of an oxide scale is still required for protection and, if this scale is compromised, it is of utmost importance for the

alloy to be able to heal the damaged oxide. Thus, when microstructural refinement of an alloy leads to improved hot corrosion resistance, it strongly indicates that the ability of the alloy to rapidly form and maintain a protective oxide scale has been enhanced.

Goedjen and Shores [83] showed quantitatively that a reduction in grain size results in an increase in the flux of solute to the alloy surface during oxidation of plasma sprayed NiCrAlY at 1150°C. Using a mathematical model of solute diffusion in polycrystalline materials developed by Gilmer and Farrel [99], these former investigators found that the total flux of solute to the alloy surface increased by up to an order of magnitude when the grain size was reduced from 100 to 0.1 μm . This calculation was in agreement with the experimental observation that as the grain size of the NiCrAlY was increased via annealing heat treatments, the instantaneous oxidation rate during the transient stage increased, corresponding to an increase in the amount of base-metal oxide formed on the alloy.

The results presented by Goedjen and Shores [83] for oxidation at 1150°C should be equally valid at 700°C, the temperature of interest for this study. It is therefore inferred that the increase in Type II hot corrosion resistance of the NiCoCrAlY alloy with decreasing grain size is due to an enhanced flux of solute to the surface, allowing for the rapid formation of an Al-rich scale early in the exposure. This scale provides protection from the salt and, if it is able to form quickly, an effective barrier between the alloy and the salt will be present from the early stages of exposure.

The rapid establishment of an Al-rich scale, and the consequent prevention of a significant amount of base-metal oxidation, is likely to have an additional effect on Type II hot corrosion resistance. As discussed in Section 2.2.3.1, in order for Type II hot corrosion to occur, the base-metal oxide must be converted to a sulfate and dissolved into the solid Na_2SO_4 until it is

present at a high enough activity to form an $\text{MSO}_4\text{-Na}_2\text{SO}_4$ eutectic melt. Therefore, it would seem that the amount of base-metal oxide that forms during the transient stage is important in determining the Type II hot corrosion resistance of a given alloy. If the transient oxidation stage is extremely brief, very little MSO_4 will be created and an appreciable melt may not be stabilized. This is significant since rapid hot corrosion attack of these alloys will typically only occur in the presence of a molten salt deposit. Thus, the observation of Goedjen and Shores [83] that fewer transient base-metal oxides formed as the grain size of a NiCrAlY alloy was decreased implies that under Type II conditions, a coarse-grained MCrAlY should form a liquid deposit more readily than a fine-grained material of the same bulk composition, and thus experience more severe hot corrosion attack. This trend was indeed observed with the NiCoCrAlY alloy in the current study.

A more complicated trend was observed in the case of the NiCrAlY. The Type II hot corrosion resistance of the DC alloy, and particularly the LPPS coating, were found to be much greater than that of the IC specimen, which had the finest microstructure of all of the NiCrAlYs. The DC and LPPS NiCrAlY formed continuous Al/Cr-rich corrosion products that resulted in rather protective behavior, while no such corrosion product formed on the IC alloy (Fig. 24). Internal oxidation/sulfidation occurred in the NiCrAlY alloy and initiated primarily at phase boundaries surrounding the α phase (Figs. 22 and 25). Due to the intergranular nature of this attack, microstructural refinement increases its severity because of the increased phase boundary density. The consumption of Cr and consequent blocking of its transport to the scale/alloy interface resulting from this internal oxidation/sulfidation could potentially make the IC alloy more susceptible to hot corrosion than the DC alloy. However, the internal attack observed in the IC alloy does not appear to be extensive enough to account for the large

difference between the hot corrosion resistance of the DC and IC NiCrAlY. In addition, if the internal attack were the cause of the rapid degradation of the IC NiCrAlY, one would expect similar degradation of the LPPS coating, which was not observed.

In order to better elucidate these observations, the compositions of the β and γ phases in the IC and LPPS NiCrAlYs were measured using FEG-SEM/EDS, the results from which are summarized in Table 4. The Calphad-predicted equilibrium compositions of these phases at 1100°C are included for comparison:

Table 4. SEM-EDS-measured phase compositions in the IC and LPPS NiCrAlY, along with the predicted equilibrium phase compositions at 1100°C

	γ			β		
	at.% Ni	at.% Cr	at.% Al	at.% Ni	at.% Cr	at.% Al
IC	67	3	30	58	4	38
LPPS	56	30	14	52	20	28
1100°C Equil.	55	32	13	58	12	30

It can be seen in Table 4 that the compositions of the γ and β phases were reasonably close to the equilibrium values in the LPPS coating. In the IC alloy, however, the Cr content in both of these phases was far below the equilibrium value due to the precipitation of a large amount of α -Cr. Chromium is known to be a very beneficial alloying element from a hot corrosion standpoint [3] (the reasons for this will be explored in subsequent chapters), and so the low levels of Cr in the γ and β phases in the IC alloy were the primary cause of its poor Type II

hot corrosion performance. This was true even though a fairly large volume fraction of α -Cr was present in the IC microstructure, demonstrating that the overall hot corrosion resistance of a given alloy can depend on the corrosion resistance of the matrix phase, even if a finely dispersed phase containing a large reservoir of a protective scale-forming element is present. Specifically, it is the *distribution* of the protective element (i.e., Cr in this case) that is important, not only its overall *content*. This is an important aspect of multiphase alloy oxidation and corrosion [100].

Thus, in the NiCrAlY system, refining the microstructure via LPPS resulted in enhanced hot corrosion resistance relative to the DC specimen, although even the latter specimen formed a rather protective scale after the 10 h exposure. The small improvement in performance observed in the LPPS specimen can be explained by the same arguments made above for the NiCoCrAlY system. However, in order to explain the poor Type II hot corrosion resistance of the IC NiCrAlY, close attention must be paid to its phase constitution and corresponding phase compositions. Although the IC specimen had the same bulk composition as the DC and LPPS specimens and had the finest microstructure, it degraded very rapidly under Type II hot corrosion conditions as a result of the low Cr-content in the γ and β phases. Hence, in addition to bulk composition, microstructural scale, phase constitution and corresponding phase compositions are very important factors to consider when evaluating Type II hot corrosion resistance.

4.3.2 The Influence of Pre-Oxidation

During service, the surface of an MCrAlY coating is likely to have a thermally-grown oxide scale present when a salt is deposited. This scale will help protect the underlying coating from hot corrosion attack, but if local failure of the scale occurs, the salt will penetrate and rapid localized degradation of the coating may occur. This is observed in Figure 33 and Figure 35, where local penetration occurs at Y/Hf-rich regions of the Al_2O_3 scale.

Over-doping of MCrAlY coatings has been shown to have negative effects on their oxidation behavior (e.g., ref. [88]). The results of this study indicate excessive amounts of a reactive element can also have negative effects on hot corrosion behavior. As shown in Figure 15 and Figure 31, the low solubility of Y and Hf in these alloys causes the precipitation of reactive element-rich phases in the microstructure which are incorporated into the scale upon oxidation (Figure 32). These regions of the scale are highly reactive with the salt deposit and act as defects at which scale penetration and subsequent rapid attack can initiate.

4.4 CONCLUSIONS

Microstructure was found to have a profound effect on the Type II hot corrosion resistance of MCrAlY alloys. The NiCoCrAlY alloy used in this study demonstrated an increase in hot corrosion resistance with increasing microstructural refinement. This can be attributed to the rapid establishment of a protective Al-rich scale conferred by an increased density of short-circuit diffusion paths in the IC and particularly in the LPPS specimens. This rapidly-established scale provided an effective barrier between the salt and the underlying alloy, and also prevented a significant amount of transient oxidation, and hence liquid salt formation, from occurring.

The NiCrAlY alloy showed a more complicated trend. The LPPS NiCrAlY coating had excellent hot corrosion resistance, slightly better than the DC alloy. However, the IC specimen, which had the finest microstructure of all of the NiCrAlYs, degraded very rapidly under Type II hot corrosion conditions. This was attributed to the low Cr content in the γ and β phases in the IC specimen, which was presumably due to the primary precipitation of a large amount of α -Cr in the microstructure during rapid solidification. These results demonstrate the importance of microstructure and both phase constitution and phase composition on oxidation and hot corrosion resistance.

The cast NiCoCrAlY-2 alloy, while severely degraded after 10 h of Type II exposure without a pre-oxidation treatment, showed much improved corrosion resistance in the presence of a pre-formed α -Al₂O₃ scale. Local pit-formation in the pre-oxidized specimen was observed to occur at sites of local scale penetration. Shorter hot corrosion exposures revealed that this local

scale failure occurred at reactive element-rich regions of the scale, further demonstrating the potential negative effects of the over-doping of MCrAlY coatings.

5.0 COMPOSITIONAL EFFECTS ON THE TYPE I HOT CORROSION OF β -NiAl ALLOYS

Much of the work that has been done to evaluate the oxidation and hot corrosion performance of β -NiAl coatings was reviewed in sections 2.3.3 and 2.3.4. It is observed upon review of the existing literature that a systematic study of the influence of composition on the hot corrosion behavior of these alloys is lacking. Thus, over the course of the next two chapters, the influence of the elements Co, Cr, and Pt on the Type I and Type II hot corrosion resistance of cast β -NiAl base alloys is thoroughly discussed. As mentioned in section 3.0, these elements are of interest because they are commonly present in diffusion coatings as a result of either intentional addition or coating/substrate interdiffusion during deposition and service. In this work, particular attention was paid to the manner by which several alloying additions influence the protective properties of the corrosion products that form during exposure, because it is the nature of these corrosion products which determine the duration of the incubation stage during both Type I and Type II hot corrosion.

5.1 EXPERIMENTAL PROCEDURES

5.1.1 Alloy Preparation

The nominal compositions of the alloys used in this study are shown in Table 5. The base alloy was Ni-36Al, to which various additions of Co, Cr, and/or Pt were made in order to systematically determine their effects on Type I hot-corrosion resistance. Circular coupons approximately 1 cm in diameter and 1.5 mm thick were cut from the alloy castings, which were processed by the Materials Preparation Center at the Ames Laboratory [96]. The castings were homogenized at 1200°C for 6 h followed by 1150°C for 48 h in a vacuum furnace. The coupons were polished to a 1200-grit finish on all sides, cleaned ultrasonically in soap and water, and then degreased in acetone.

Table 5. Nominal alloy compositions

Designation	Ni-36Al	Ni-36Al-5Co	Ni-36Al-5Cr	Ni-36Al-5Pt	Ni-36Al-5Co-5Pt
Ni	Balance	Balance	Balance	Balance	Balance
Al	36	36	36	36	36
Co	-	5	-	-	5
Cr	-	-	5	-	-
Pt	-	-	-	5	5

5.1.2 Type I Hot Corrosion Exposures

The specimens were deposited with salt as described in section 4.1.2 and placed in a crucible with the salt-deposited side facing upward. This crucible was fastened to the end of a rod that was connected to a pneumatic piston/cylinder mechanism suspended above a vertical tube furnace (Fig. 36). This mechanism was powered by a compressed air source and wired into a controller, which allowed the samples to be cycled into the hot zone of the furnace, held there for 20 h, and then automatically removed to air cool. After each 20 h cycle, the specimens were weighed, re-deposited with 2-3 mg/cm² Na₂SO₄, and then placed back into the furnace for another 20 h cycle.

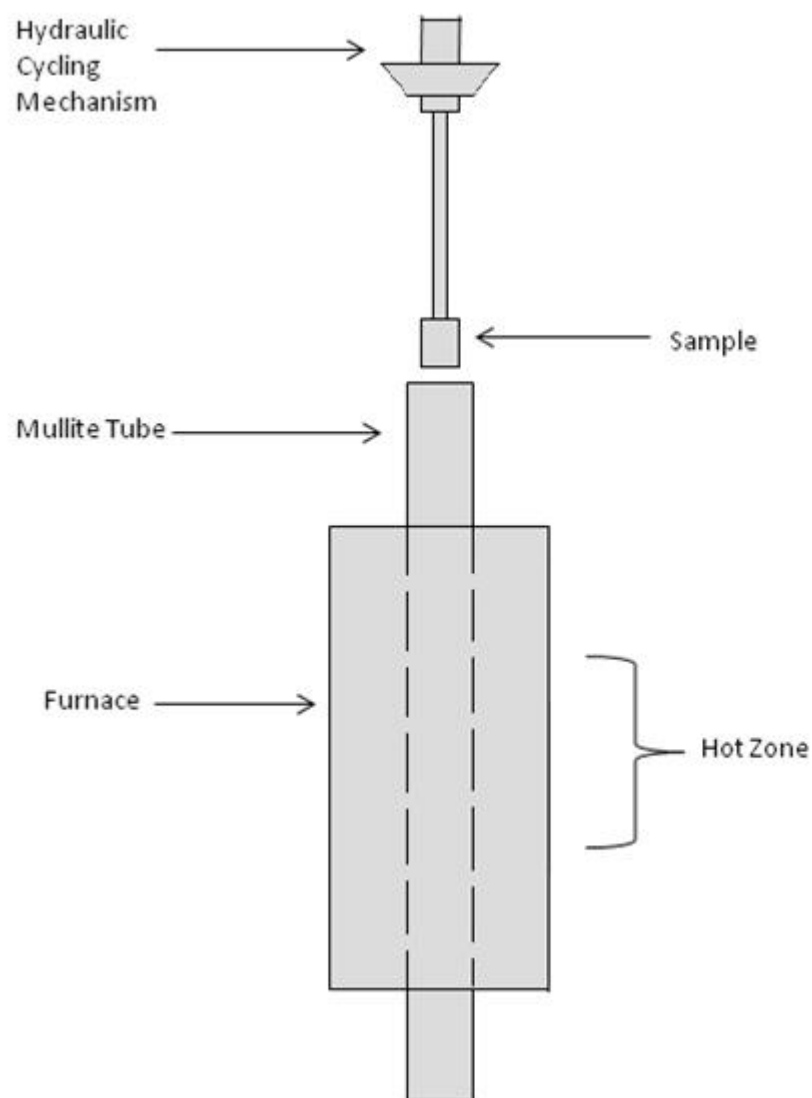


Figure 36. Schematic of the Type I hot corrosion apparatus

Samples were characterized using SEM/EDS. These tools were used in conjunction with weight-change data in order to determine the effects of the various alloying additions on Type I hot corrosion resistance.

5.2 RESULTS

Plots of weight change vs. time for the Type I hot-corrosion exposures are presented in Fig.

37. Each specimen was removed from the test either when the weight change became relatively large, indicating rapid degradation of the alloy, or after 320 h of testing. There was no observable period of protective scaling for the binary Ni-36Al alloy. The Ni-36Al-5Co specimen was also rapidly attacked during the first 20 h hot corrosion cycle, however the rate of corrosion was reduced relative to Ni-36Al. Corresponding cross-sectional micrographs of these specimens are shown in Fig. 38.

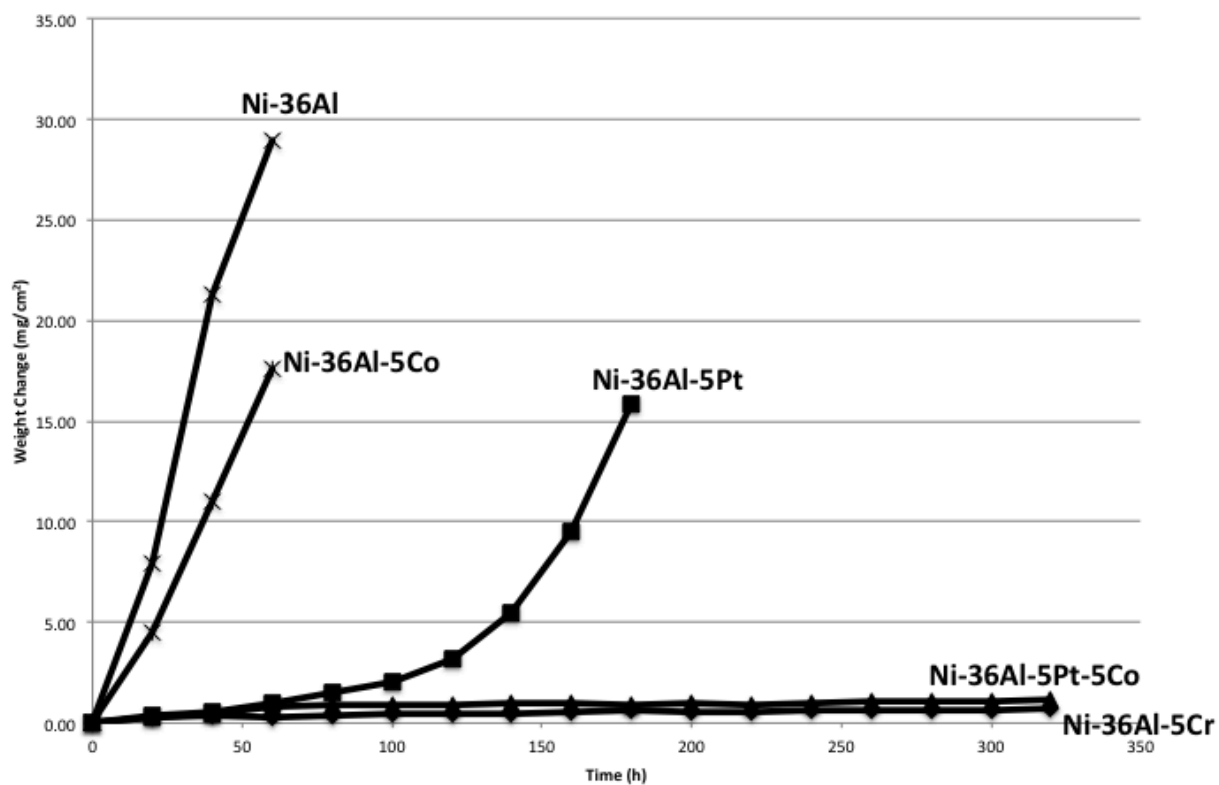


Figure 37. Plots of weight change vs. time for the Type I hot corrosion of the β systems

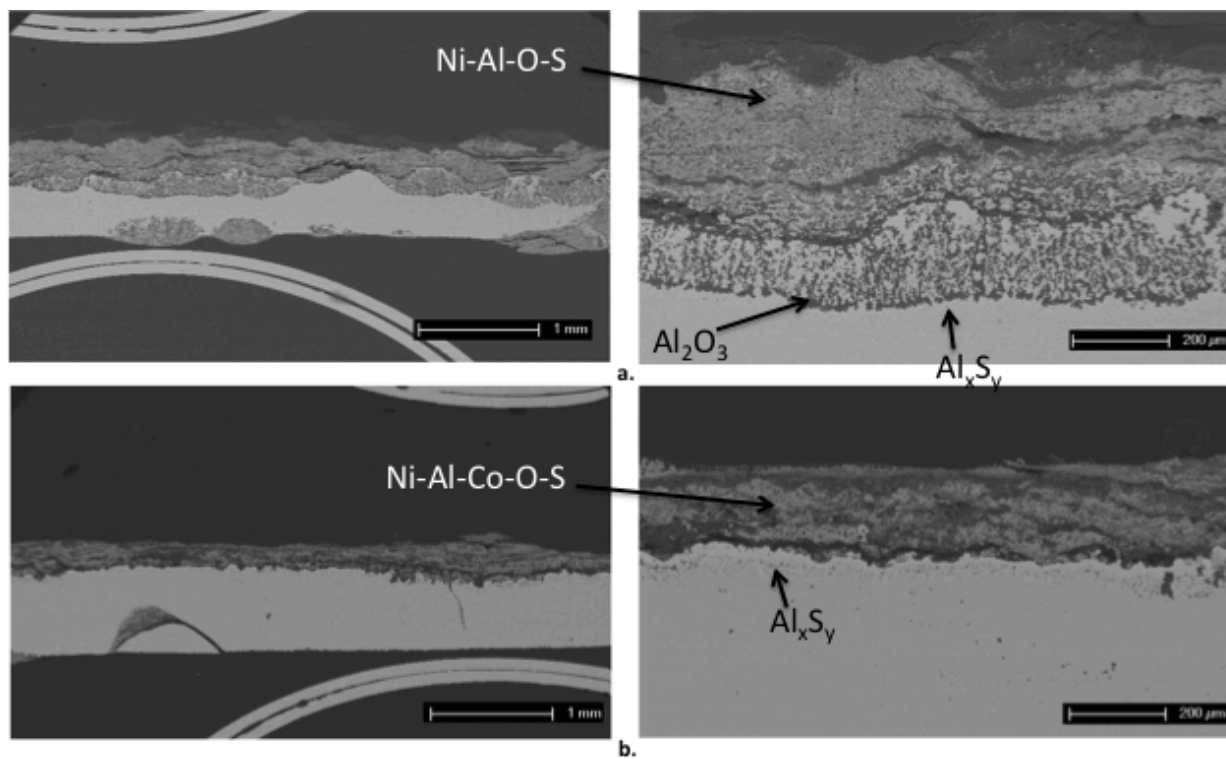


Figure 38. Cross-sectional SEM micrographs of the a) Ni-36Al and b) Ni-36Al-5Co after 60 h Type I hot corrosion exposures

Both specimens were degraded significantly; however, the beneficial effect of Co is apparent. The binary Ni-36Al specimen grew a thick, non-protective Ni and Al-rich oxide scale, underneath of which there was an extensive internal oxidation zone. The scale was slightly thinner on the Ni-36Al-5Co specimen, no internal Al_2O_3 formed, and a subsurface layer of Al-rich sulfide precipitates was observed. On the basis of EDS analysis, very small Al-rich sulfide precipitates, inferred to be Al_2S_3 , were also detected near the base of the internal oxidation zone in the Ni-36Al, but they were very few in number. This was likely a result of the rapid ingress of oxygen in this specimen causing the conversion of the sulfide to non-protective Al_2O_3 . A more detailed description of this process will be discussed presently. EDS measurements of the matrix phase within the internal sulfidation zone of the Ni-36Al-5Co indicated that the alloy contained approximately 24 at. % Al, and so it is inferred that this is the γ' - Ni_3Al phase. A similar analysis was not done on the Ni-36Al specimen because the closely-spaced internal Al_2O_3 precipitates resulted in an overestimation of the Al content, and thus rendered the results unreliable.

The addition of 5 % Pt to the Ni-36Al alloy improved the Type I resistance dramatically; protective scaling was observed for the Ni-36Al-5Pt specimen to approximately 130 h, after which rapid hot-corrosion degradation occurred. A further addition of 5 % Co resulted in very good hot corrosion resistance for the Ni-36Al-5Co-5Pt specimen, which reacted in a protective manner to around 220 h. The Ni-36Al-5Cr alloy was the most resistant to Type I hot corrosion of the materials studied. The weight change data indicated that an adherent, protective scale was maintained for 320 h, at which time the test was stopped.

Cross-sectional micrographs of the Ni-36Al-5Pt, Ni-36Al-5Co-5Pt, and Ni-36Al-5Cr specimens after 100 h of Type I exposure are shown in Fig. 39. For each specimen, one low

magnification micrograph and two slightly higher magnification micrographs are shown. This is done because the corrosion product was generally not completely uniform across the entire surface of a given specimen, and so multiple micrographs were necessary to give a representative depiction of the extent of degradation.

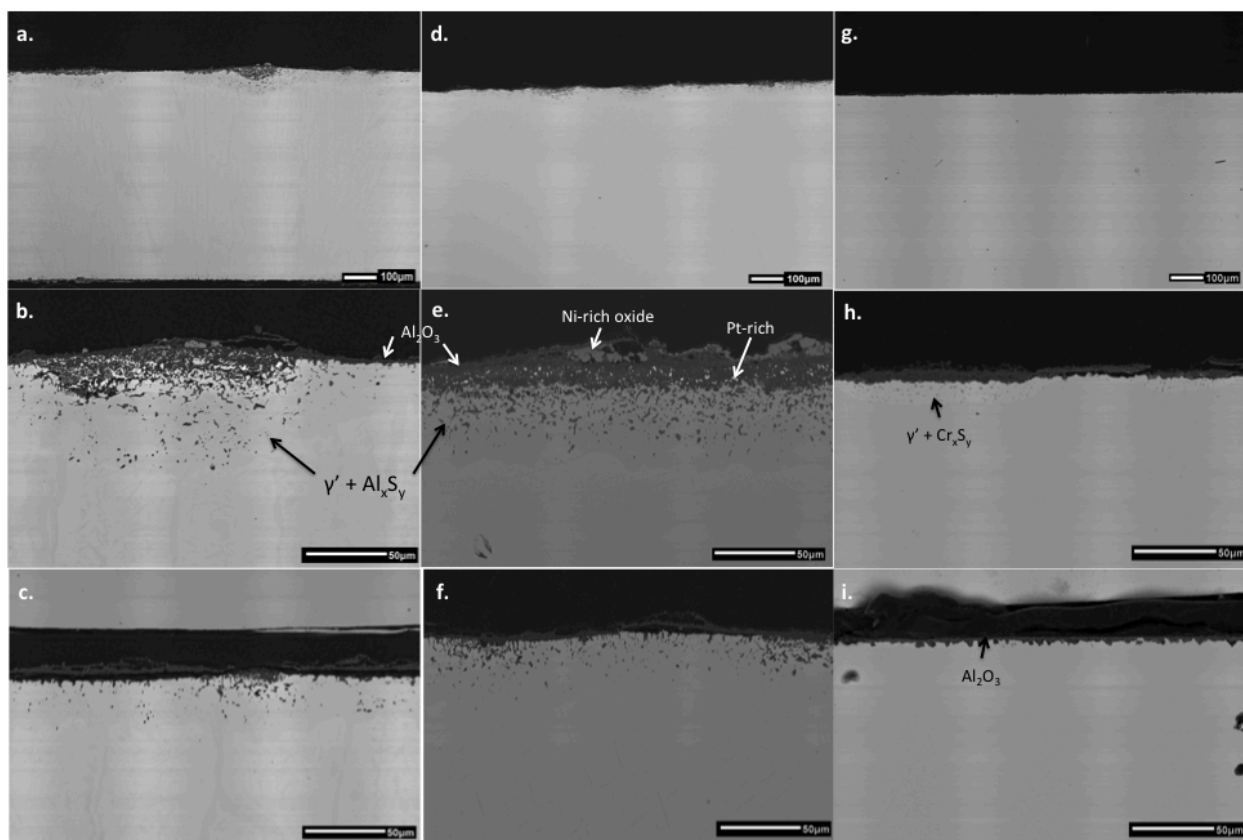


Figure 39. SEM micrographs of the a-c) Ni-36Al-5Pt, d-f) Ni-36Al-5Pt-5Co, and g-i) Ni-36Al-5Cr after 100 h Type I hot corrosion exposures

After 100 h, there were only subtle differences between the Ni-36Al-5Pt and Ni-36Al-5Pt-5Co degradation microstructures. An Al₂O₃ - rich scale had formed, which was not entirely protective and allowed for the internal sulfidation of Al. This internal sulfidation was rather severe locally, and was observed to occur within a region that had transformed to γ' -Ni₃Al as a result of Al depletion. In the regions of severe internal sulfidation, the external scale was relatively thick and Ni/Co-rich oxides were observed near the surface. Some Pt had been incorporated into the scale and was present as small Pt-rich metallic particles.

Close observation of the corrosion product revealed that many of the internal precipitates closest to the alloy/scale interface were converted to Al₂O₃, particularly in the Ni-36Al-5Pt. Thus, the primary mode of attack seems to be internal sulfidation/oxidation. This attack has been previously observed during high temperature exposure in an oxidizing/sulfidizing gas mixture and can be explained in the following manner [101]. The surface scale formed on the Ni-36Al-5Pt alloy was not completely protective, and internal precipitates of Al₂O₃ began to form as oxygen dissolved into and diffused through the alloy. Sulfur also dissolved and diffused into the alloy; however, since Al₂O₃ is much more stable than Al₂S₃, only the oxide was observed in the upper regions of the internal precipitation zone. Specifically, the solubility product for Al₂S₃ formation could not be exceeded in the internal oxidation zone near the alloy surface. Accordingly, S continued to diffuse through this internal oxidation zone until it reached a point where the oxygen activity was low and the sulfur activity was sufficiently high for Reaction (41) to be thermodynamically feasible:



Underlined species in reaction (41) are present in solution. At this location, internal Al_2S_3 began to precipitate. As oxygen continued to arrive at the $\text{Al}_2\text{O}_3/\text{Al}_2\text{S}_3$ interface, the oxygen activity increased such that the reverse of reaction (41) became energetically favorable, and consequently the sulfide at this interface was converted to oxide. Based on the observed sequence of corrosion products, i.e., internal Al_2O_3 near the surface and Al_2S_3 deeper into the alloy, it is inferred that the S that was released from this reaction diffused further into the alloy to form more sulfide and deepen the internal sulfidation zone.

The Ni-36Al-5Cr alloy formed a thin, protective Al_2O_3 scale after 100 h of Type I exposure. Locally, Al depletion resulted in the formation of a subsurface γ' region in which Cr-rich sulfides precipitated (Fig. 39 h.), however only the β phase was detected over most of the cross section with no internal sulfidation.

5.3 DISCUSSION

5.3.1 The Influence of Co on Type I Hot Corrosion Resistance

The addition of 5 % Co to Ni-36Al and Ni-36Al-5Pt resulted in improved Type I hot corrosion resistance. To begin to explain this, one must consider the subsurface degradation of the alloys after hot corrosion exposure. Subsurface degradation is extremely important in high temperature oxidation, and includes phenomena such as the depletion of an alloying element and subsequent phase changes (dissolution or precipitation) that occur as a result of external scaling or interdiffusion between a coating and the substrate [102]. If a scale is compromised in some way

(cracking, erosion, fluxing, etc.) the extent of subsurface degradation determines the ability of the alloy to reform a protective oxide layer. The importance of this scale healing is particularly crucial during hot corrosion; if the molten salt is able to penetrate the scale and make contact with a greatly depleted alloy that is unable to reform a protective scale, catastrophic attack will ensue.

As mentioned above, internal oxidation of Al accounted for a large amount of the attack observed during Type I hot corrosion of the Ni-36Al alloy. The formation of internal Al_2O_3 was completely inhibited by 5 % Co addition. Only internal Al-sulfides were observed in the Ni-36Al-5Co alloy, and these did not penetrate nearly as deeply as the Al_2O_3 precipitates in the Ni-36Al. It is possible that the addition of Co reduced the oxygen permeability in the alloy or that the external scale formed on the Ni-36Al-5Co alloy was intrinsically more protective, resulting in a lower oxygen activity in the alloy at the scale/alloy interface. The same can be said to explain the enhanced Type I resistance of the Ni-36Al-5Pt-5Co compared with the Ni-36Al-5Pt.

In order to determine if the oxygen permeability was indeed decreased by the addition of Co, internal oxidation experiments were performed. Ni-3Al and Ni-3Al-5Co (at. %) alloys were exposed at 900°C for 170 h in air + 10% H_2O and the internal oxidation zone (IOZ) depth was measured using optical microscopy. A decrease in the internal oxidation zone depth with Co addition would strongly suggest that Co does indeed lower the oxygen permeability in the alloy. A plot of the IOZ depth for each alloy is shown in Fig. 40. The depth of both the IOZ and the IOZ + MCZ (metal consumption zone) are plotted. The IOZ and MCZ are defined in Fig. 41, which is an optical micrograph of the Ni-3Al-5Co after 170 h exposure at 900°C. An external NiO scale had formed, as expected, and the MCZ is defined as the portion of this NiO scale that

grows inward, commonly containing numerous pores [103]. The IOZ is the zone beneath the MCZ, which contains internal Al_2O_3 precipitates in a γ -Ni matrix.

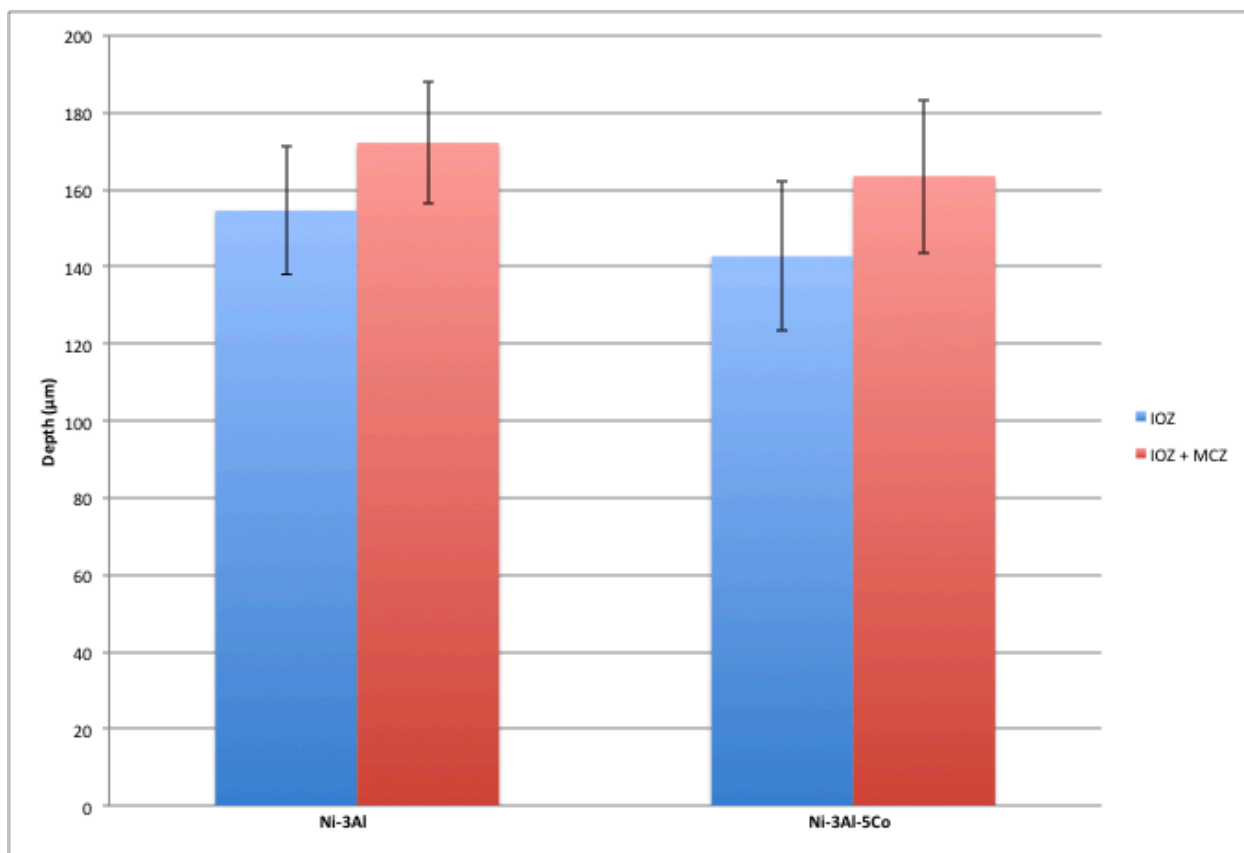


Figure 40. Plots of IOZ and IOZ + MCZ depth for the Ni-3Al and Ni-3Al-5Co after a 170 h exposure at 900°C in air + 10% H₂O

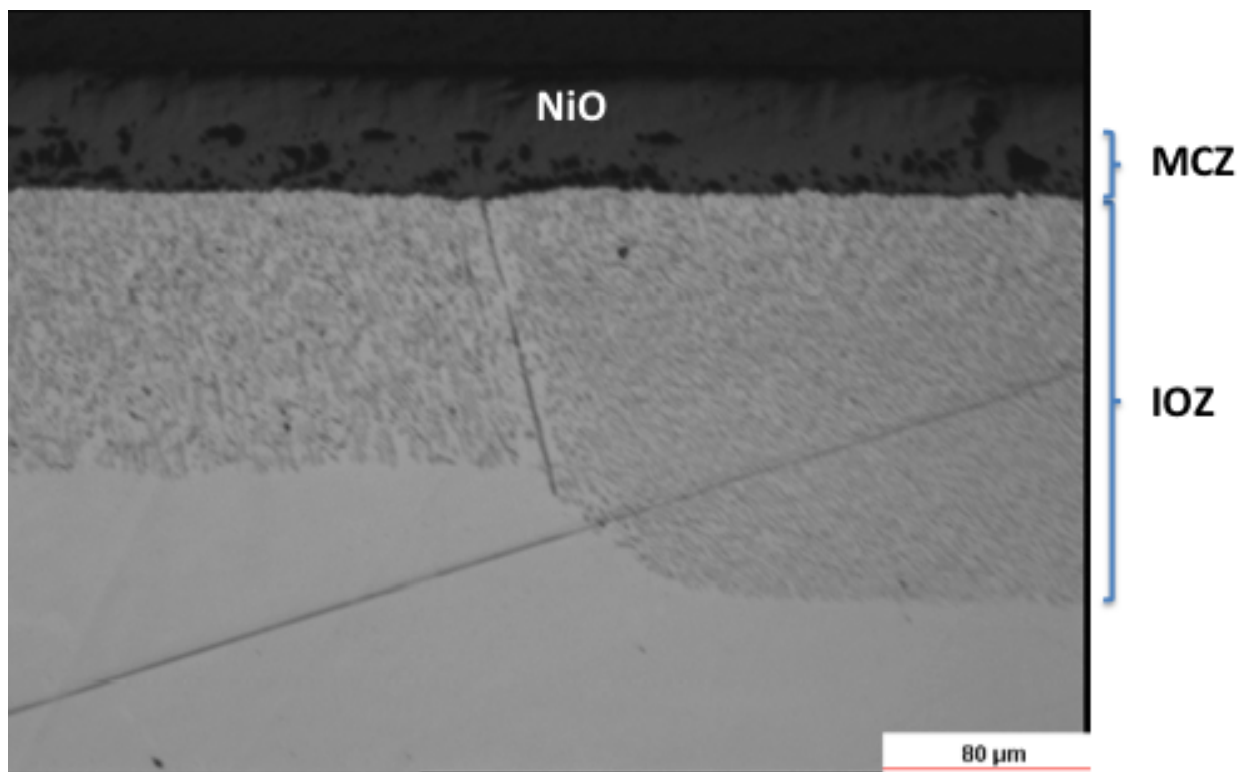


Figure 41. Optical micrograph of the Ni-3Al-5Co after 170 h exposure at 900°C in air + 10% H₂O

Based on these measurements, the IOZ and IOZ+MCZ depths are slightly decreased by the presence of Co, indicating a decrease in oxygen permeability with Co addition; however, the statistical significance of these measurements is questionable due to the large deviation in the measurements. The reason for this large deviation is obvious upon observation of Fig. 41. In the middle of the image, an alloy grain boundary is clearly visible as a result of intergranular oxidation. The depth of the IOZ differs by $\sim 70\text{ }\mu\text{m}$ in the adjacent grains, indicating a strong influence of crystallographic orientation on the depth of internal oxidation. This could be due to a dependence of either oxygen permeability or internal Al_2O_3 morphology on grain orientation. Internal Al_2O_3 tends to form as rod-shaped oxide precipitates which extend from the external NiO/alloy interface to the IOZ front, and as a result of this morphology, enhanced oxygen diffusion along the internal oxide/matrix interface often leads to rapid internal oxidation kinetics [104]. Some apparent differences in internal oxide morphology are indeed observed from grain to grain, e.g., Fig. 42:

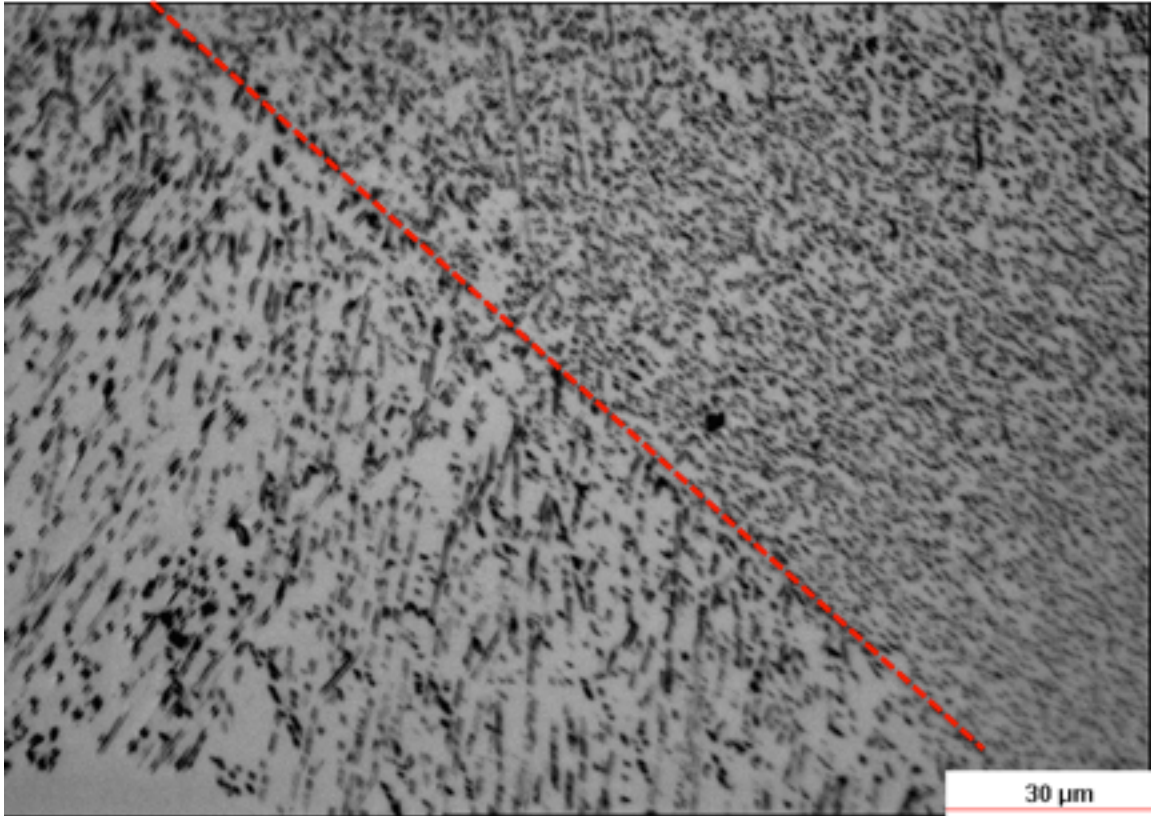


Figure 42. Optical micrograph of the Ni-3Al-5Co after 170 h exposure at 900°C showing the difference in internal Al_2O_3 precipitate morphology between grains

In this optical micrograph, the location of a grain boundary is highlighted by a red line. The morphology of the internal oxide precipitates seems to be different, with more equiaxed precipitates in the grain on the right and the expected rod-shaped precipitates on the left. However, it could indeed be the case that the precipitates are rod-shaped in each grain, but the axes of the rods in the adjacent grains are oriented differently relative to the plane of the image. Whatever the cause for the apparent difference in oxide morphology, there is no systematic correlation between the morphology observed within a given grain and IOZ depth.

In Fig. 43, weight change squared vs. time curves for the Ni-36Al and Ni-36Al-5Co during 900°C isothermal oxidation in dry air with no salt deposit are shown. The Ni-36Al is observed to undergo a period of accelerated oxidation during the first ~1.5 h of exposure. This likely correlates with the formation of transient Ni-rich oxides, prior to the establishment of a complete Al₂O₃ layer, indicated by the change of the plot from a curved line during the transient stage to a straight line once the Al₂O₃ is fully established (see Chapter 7 for a more complete discussion of the interpretation of these plots). In the case of the Ni-36Al-5Co, however, no transient stage is observed. The line is straight from the onset of the exposure, indicating that the Al₂O₃ scale is very rapidly established. This result is consistent with the decrease in the extent of conversion of sulfide to oxide during Type I exposure when Co is present. The presence of Co enhances the rate at which a pure Al₂O₃ scale is established, resulting in a decrease in the extent of internal oxidation of sulfides, and more protective behavior during Type I exposure. In order for the sulfidation/oxidation mechanism by which these alloys degrade to operate, the internal sulfides must be converted to oxide in order to drive the sulfur further into the alloy. If internal oxidation is prevented or slowed, then the entire degradation process will also be slow comparatively, which was observed when 5 % Co was added to either the Ni-36Al or Ni-36Al-5Pt. The slight decrease in IOZ depth in the Ni-3Al-5Co relative to the Ni-3Al seems to indicate that the reason for the enhanced selective oxidation of Al may be a decrease in oxygen permeability with Co addition; however, further experimentation is required in order to verify this mechanism.

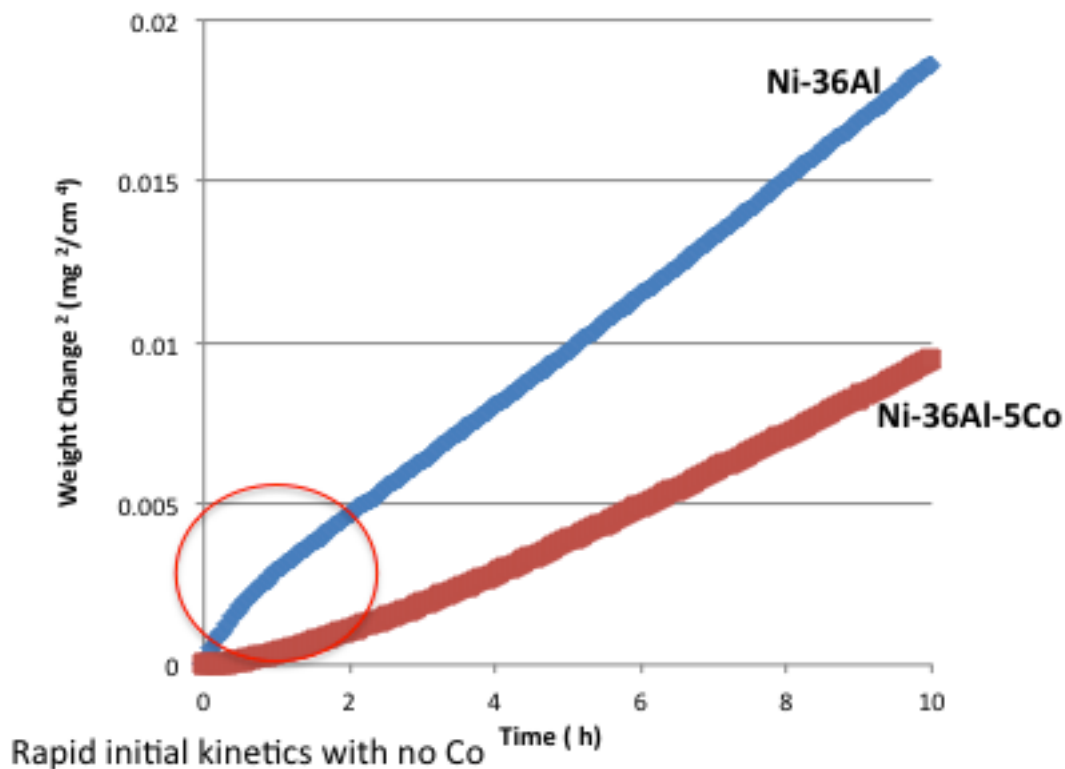


Figure 43. TGA curves for the oxidation of Ni-36Al and Ni-36Al-5Co at 900°C

Micrographs of the Ni-36Al-5Pt and Ni-36Al-5Pt-5Co specimens after removal from the test (180 h and 320 h, respectively) are shown in Fig. 44. Here, it is clearly observed that the addition of 5% Co was greatly beneficial and significantly slowed the sulfidation/oxidation attack. The Ni-36Al-5Pt developed a deep (up to ~400 μm) internal oxidation zone, below which a band of Al-rich sulfides had precipitated. Primarily sulfides were observed in the subsurface of the Ni-36Al-5Pt-5Co, with no extensive internal oxidation zone.

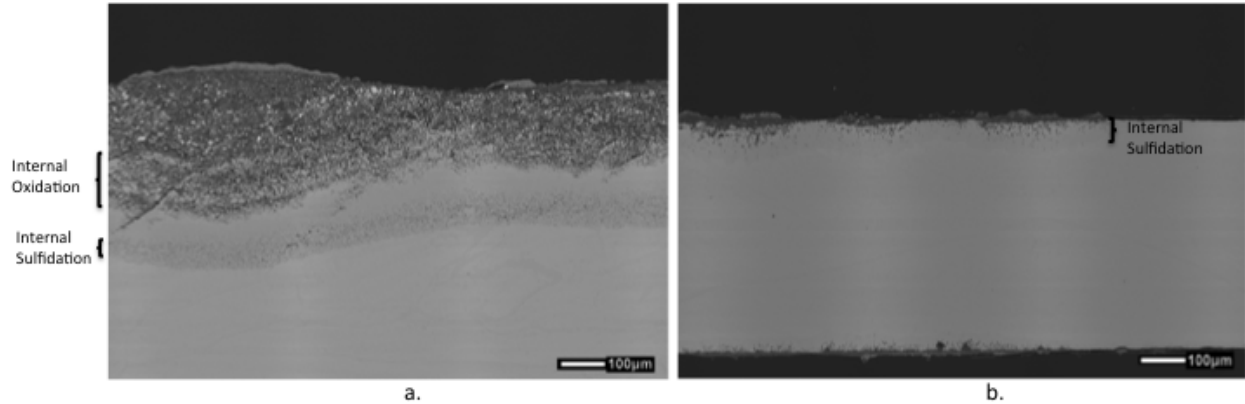


Figure 44. SEM micrographs of the a) Ni-36Al-5Pt and b) Ni-36Al-5Pt-5Co after 180 h and 320 h, respectively, of Type I hot corrosion exposure

It has been demonstrated (e.g., ref. [105]) that the formation of Ni_3S_2 during Type I hot corrosion exposure is generally associated with very rapid attack, largely because this product is molten at 900°C . Figure 45 shows a higher magnification SEM micrograph of the region of the Ni-36Al-5Pt specimen labeled “internal oxidation” in Fig. 44. In this image, the light gray Ni_3S_2 phase can clearly be seen. Based on the microstructure, it is inferred that internal molten Ni_3S_2 with Al in solution has formed and rapidly penetrated the alloy, largely wetting the grain boundaries, and has been mostly converted to Al_2O_3 in a process analogous to what was described above (see Eq. 41).

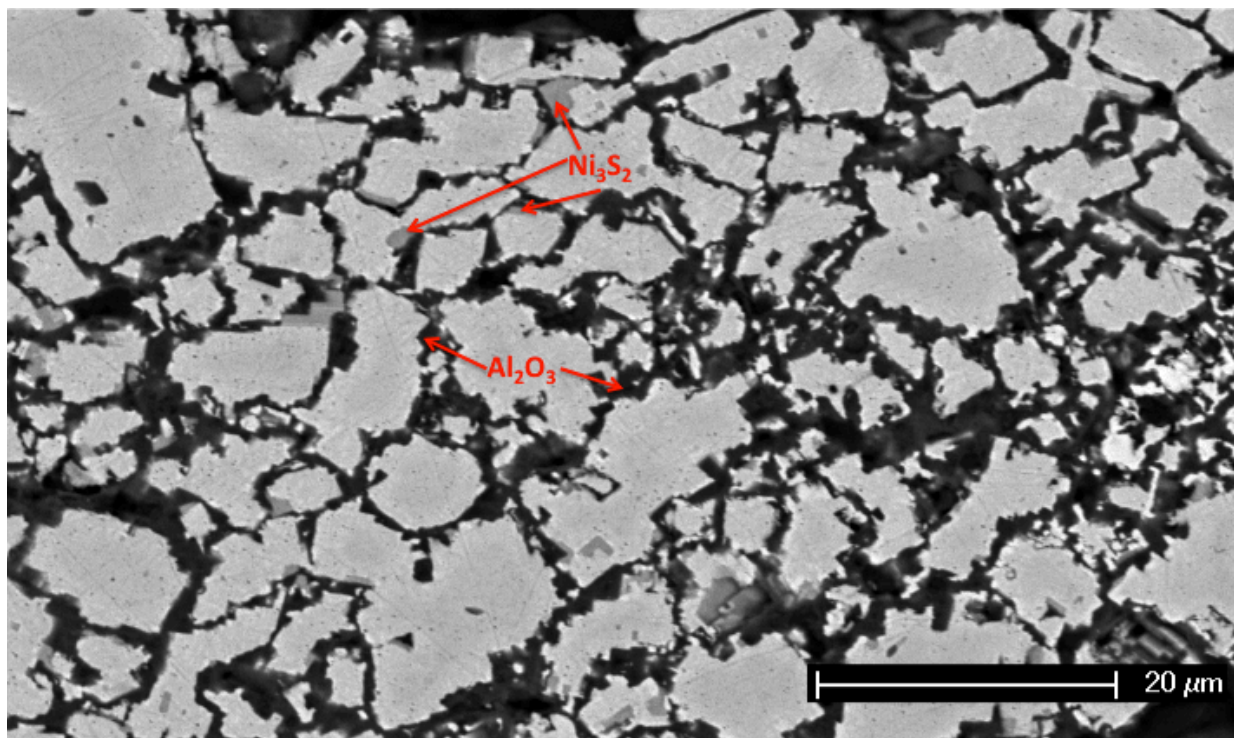


Figure 45. SEM micrograph of the internal corrosion product in the Ni-36Al-5Pt after 180 h of Type I hot corrosion exposure, showing the formation of Ni_3S_2

This internal Ni_3S_2 was not observed over the majority of the cross section of the Ni-36Al-5Pt-5Co during the 320 h exposure. In order to explain this, the following reaction was considered:



Investigation of the effect of Co on the thermodynamic activities of the various components in the alloy can, in theory, determine whether the addition of 5 at. % Co will decrease the tendency to form Ni_3S_2 . This is a relevant reaction because upon observation of the microstructure of the Ni-36Al-5Pt before and after rapid degradation (Figs. 39 and 44, respectively), the

internal sulfides directly beneath the external scale change from Al_2S_3 during the incubation stage to Ni_3S_2 during the propagation stage.

A calculation was carried out based on the modified interaction parameter analysis proposed by Pelton and Bale [106] and activity measurements made in the γ' -(Ni,Co)₃Al [107] and γ' -(Ni,Pt)₃Al [108] systems. This calculation is presented in detail in Appendix A. Although not exact, this calculation suggested that Co addition can markedly decrease the tendency to form Ni_3S_2 due to an increase in a_{Al} and decrease in a_{Ni} with Co addition. A limitation of the calculation method used is that although the method of Pelton and Bale allows for the use of tabulated interaction parameters ($\frac{\partial \log \gamma_i}{\partial X_j}$, where γ is the activity coefficient, X is mole fraction, and i and j represent components in the solution) at finite concentrations, rather than only at infinite dilution as first proposed by Wagner [109], the interaction parameters themselves must still be measured at infinite dilution. Based on the data of Copland [108] and Albers et. al. [107], “interaction parameters” could only be estimated from activity coefficient data measured at significant concentrations, often with only two data points being available, necessitating the approximation of a linear relationship between $\log \gamma_i$ and X_j . These approximations were determined to yield significant errors.

However, it is true that Ni_3S_2 was only observed in the Ni-36Al-5Pt specimen, and also that Co does indeed increase the activity of Al and decrease the activity of Ni [107], thus favoring Reaction (42) to the left. Thus, it is likely that the destabilization of Ni_3S_2 is also a contributing factor when considering the beneficial effect of Co on Type I hot corrosion resistance.

5.3.2 The Influence of Cr and Pt on Type I Hot Corrosion Resistance

It has been proposed [18] that Cr can act as a chemical buffer, preventing the development of the highly basic conditions in the salt at the salt/scale interface that cause basic fluxing to occur.

Considering the basic fluxing mechanism [27], if this were in fact the role of Cr during Type I hot corrosion of Ni-36Al-5Cr, one would still expect to see Cr-rich sulfides beneath the oxide. Sulfide formation is a prerequisite for the development of basic conditions in the salt, and thus only after internal sulfidation occurs would the benefit of Cr as a buffer begin to come into play. Chromium-rich sulfides were occasionally observed in the Ni-36Al-5Cr alloy after Type I exposure (see Fig. 39 h), but certainly not with any regularity (see, for example, the absence of sulfides in Fig. 39 i, which shows a region that is representative of the majority of the cross section). Therefore, the ability of Cr to aid in both the rapid establishment of an Al_2O_3 scale at the beginning of the exposure and the healing of the scale after it sustains damage are proposed to be the primary reasons for its beneficial effect. The exact reason for this enhanced scale formation is likely related to the role of Cr in the “third element effect”. The presence of Cr in solid solution allows an external scale of Al_2O_3 to form at significantly lower Al contents than would be required in the absence of Cr [3]. This proposed explanation will be demonstrated experimentally in the following section, when Type II hot corrosion is considered.

It is well established that Pt greatly increases scale adherence during thermal cycling [65]. It is very likely that this is part of the reason for the beneficial effect of Pt during Type I hot corrosion. However, this would mainly have an influence during thermal cycling, whereas in the current study, it was observed that the addition 5 at. % Pt to Ni-36Al resulted in greatly improved Type I hot corrosion resistance even after one 20 h isothermal cycle (Fig. 37). Therefore, it is deduced that the main beneficial role of Pt is to aid in the establishment of a

protective Al_2O_3 scale. This has indeed been shown to be true at higher temperatures than those of interest in this study by Gleeson et al. [71]. These investigators explained the enhanced Al_2O_3 establishment in Pt-containing NiAl alloys by pointing out that Pt primarily occupies Ni lattice sites in the B2 structure of NiAl, effectively increasing the Al/Ni ratio on a given lattice plane. This increase in effective Al content kinetically favors the establishment of Al_2O_3 over NiO during high temperature exposure. The rapid establishment of an Al_2O_3 scale is clearly favorable in the presence of a salt deposit, hence the enhanced hot corrosion resistance afforded by Pt addition.

5.3.3 Relationship Between Type I Hot Corrosion Resistance and Al_2O_3 Scale Healing

As discussed above, in order to exhibit hot-corrosion resistance, it is of utmost importance for an alloy to rapidly form an Al_2O_3 -rich surface scale at the beginning of exposure, and to heal this oxide if it is breached during exposure to Type I hot corrosion conditions so that Na_2SO_4 does not have direct contact with the underlying alloy. If Al is consumed via the formation of internal precipitates, this capability may be lost. It would therefore be expected, based on the results of the Type I hot corrosion exposures, that after a given amount of Type I exposure, the Ni-36Al-5Pt-5Co would be more capable than the Ni-36Al-5Pt at forming a protective Al_2O_3 layer if the oxide were to be penetrated. Furthermore, since the Ni-36Al-5Cr exhibited the best Type I hot corrosion resistance, it may be expected that this alloy is able to heal a damaged thermally grown Al_2O_3 scale the most effectively of the alloys studied.

In order to test this, Ni-36Al-5Pt, Ni-36Al-5Pt-5Co, and Ni-36Al-5Cr specimens were first exposed to Type I hot corrosion conditions for 100 h, after which each of the alloys was still within a period of protective scaling (Fig. 37). Subsequently, the specimens were

ultrasonically cleaned in water for 20 min to partially spall the Al_2O_3 grown during Type I exposure. Finally, the partially spalled specimens were dried and then oxidized in air at 900°C for 100 h with no salt deposit in order to test their abilities to re-form a protective oxide.

Surface SEM micrographs of the specimens after 100 h of Type I hot corrosion exposure followed by 20 min of ultrasonic cleaning in water are shown in Fig. 46. The regions that had spalled, revealing the oxide/metal interface, appear bright white in these backscattered SEM images. Sufficient spallation occurred so that the healing behavior of these alloys could be studied.

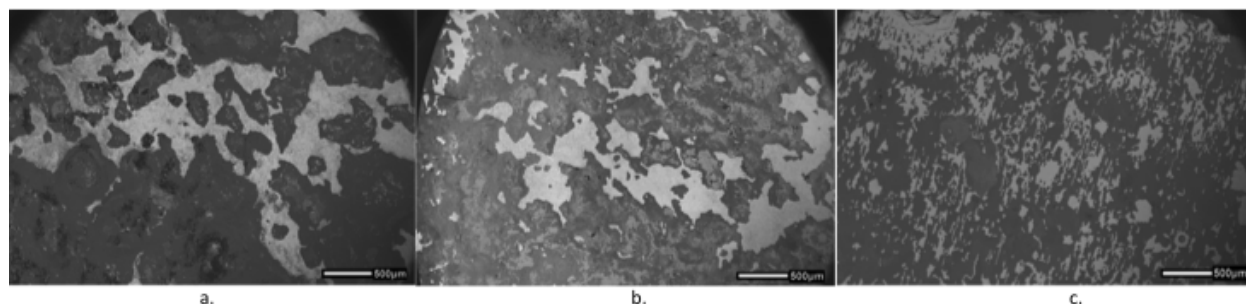


Figure 46. Surface SEM micrographs of the a) Ni-36Al-5Pt, b) Ni-36Al-5Pt-5Co, and c) Ni-36Al-5Cr after 100 h of Type I hot corrosion exposure followed by 20 min of ultrasonic cleaning in water

Higher magnification SEM micrographs of spalled areas on the Ni-36Al-5Pt and Ni-36Al-5Pt-5Co are shown in Fig. 47.

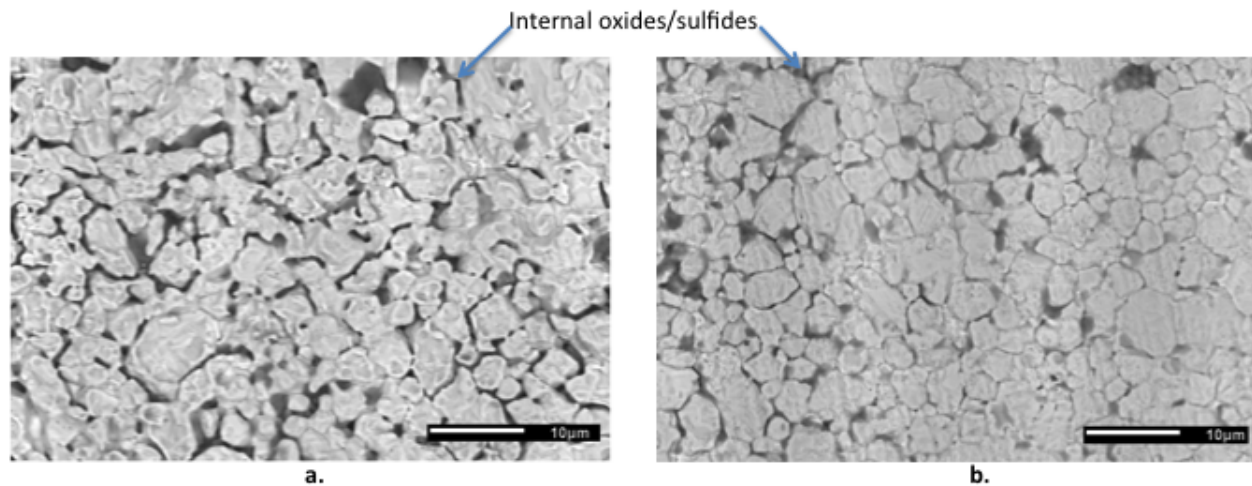


Figure 47. SEM micrographs of spalled areas on the a) Ni-36Al-5Pt and b) Ni-36Al-5Pt-5Co

It is clear that the internal sulfidation/oxidation occurs primarily at γ' grain boundaries. In addition, EDS analysis of these regions revealed that the majority of the internal precipitates located immediately below the external scale in the Ni-36Al-5Pt had been converted to oxide; many of these precipitates in the Ni-36Al-5Pt-5Co specimen were, however, Al-rich sulfides. This once again demonstrates the decrease in the rate of oxygen ingress in the Co-containing specimen. In addition, area fraction measurements conducted on images from these spalled regions using the ImageJ software package indicated that the areal coverage of the internal precipitates, whether oxide or sulfide, was approximately 15% in the Ni-36Al-5Pt but only 9% in the Ni-36Al-5Pt-5Co. Therefore, the extent of internal attack was considerably less in the presence of Co. Since this internal attack seems to occur preferentially along grain boundaries, the influence of Co on grain orientation and/or grain boundary transport in γ' should be investigated in the future.

Surface SEM micrographs of the spalled regions after an additional 100 h exposure at 900°C in air with no salt deposit are shown in Fig. 48.

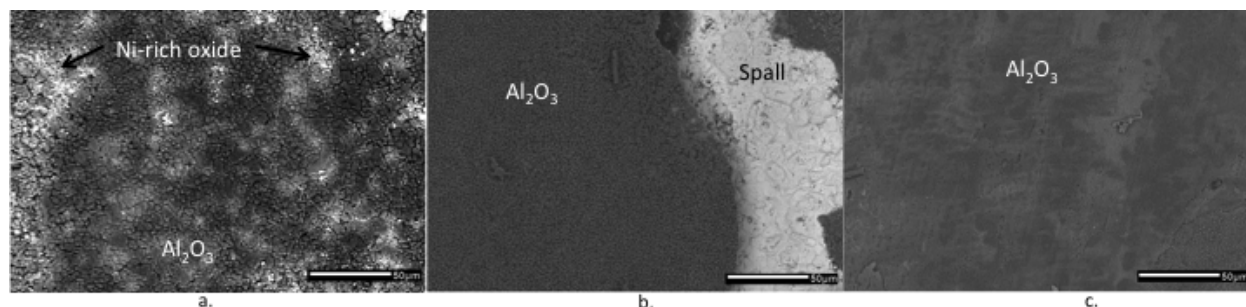


Figure 48. Surface SEM micrographs of the spalled regions on the a) Ni-36Al-5Pt, b) Ni-36Al-5Pt-5Co, and c) Ni-36Al-5Cr after an additional 100 h exposure at 900°C in air with no salt deposit

The Ni-36Al-5Pt formed a relatively coarse-grained Al₂O₃-rich scale; however, islands of Ni-rich oxide (NiO and/or NiAl₂O₄) were also frequently observed on the surface. This oxide was fairly coarse-grained, with a grain size similar to that of the underlying alloy (~5 μm).

Quite a different scale formed on the Ni-36Al-5Pt-5Co. As shown in Fig. 48 b., a very fine-grained, pure Al₂O₃ scale had grown on the previously spalled areas. Ni- or Co- rich oxides were not observed. This scale was clearly more desirable than that formed on the Ni-36Al-5Pt, although some spalling of the oxide was observed upon cooling, as can be seen in Fig. 48 b. Despite the spallation, the oxide formed on the Ni-36Al-5Pt-5Co was more pure (and as a result, presumably slower-growing, although these measurements were not made) than the oxide formed on the Ni-36Al-5Pt and should be more effective at preventing catastrophic corrosion should the original oxide scale be penetrated.

Finally, a fine-grained, adherent Al_2O_3 scale formed on the spalled regions of the Ni-36Al-5Cr specimen after oxidation exposure. No Ni-rich oxide was observed, and EDS measurements revealed that 2-3 at% Cr was present in the regions of the scale that appear slightly brighter. This Cr signal could at least partially be accounted for by the detection of Cr from the substrate.

Thus, the beneficial effects of Co, Cr, and Pt discussed in sections 5.3.1 and 5.3.2 ultimately result in an enhanced ability of the alloy to rapidly form a protective Al_2O_3 scale, and to heal this scale when it is penetrated during hot corrosion exposure.

5.4 CONCLUSIONS

Based on the results of this study, the increase in Type I hot corrosion resistance in the order Ni-36Al < Ni-36Al-5Co < Ni-36Al-5Pt < Ni-36Al-5Pt-5Co < Ni-36Al-5Cr can be attributed to a progressive increase in the ability of these alloys to rapidly form a protective oxide scale and to heal the scale when it sustains damage. The significance of this result is that regardless of the active mode of degradation, whether it is basic fluxing, sulfidation/oxidation, or simply cracking of the scale allowing the salt access to the bare alloy, the important factor from a coating design standpoint is the ability of the alloy to rapidly establish and even reform an Al_2O_3 scale. The addition of Co is effective, and this is partly due to Co imparting a hindrance on the internal oxidation of Al-rich sulfides. Type I hot corrosion and TGA experiments indicate that this is associated with an enhanced ability to rapidly form a pure Al_2O_3 scale with Co addition. This, along with internal oxidation experiments, indicates that the oxygen permeability may be

decreased with Co addition, although further experimentation is required. Also, Ni_3S_2 formation is inhibited by the presence of Co as a result of the positive thermodynamic interaction between Co and Al, and the negative interaction between Co and Ni. The addition of Pt to a binary nickel aluminide certainly aids with oxide adherence during thermal cycling, which should indeed enhance hot corrosion resistance, but the most important factor is the enhanced rate of Al_2O_3 establishment when Pt is present in solution in the B2 structure. Finally, Cr is the most effective element for imparting Type I hot corrosion resistance. This has been well established in past work, however the current results indicate that the traditional explanation for this effect, involving the salt buffering capability of Cr, is not the main effect in these systems. More importantly, Cr greatly aids in the rapid establishment of an Al_2O_3 scale at the onset of the exposure and after the scale formed during Type I hot corrosion is damaged.

6.0 COMPOSITIONAL EFFECTS ON THE TYPE II HOT CORROSION OF β -NiAl ALLOYS

Type II hot corrosion is currently extremely important from an industrial standpoint, as temperatures of modern gas turbine engines are increasing into a regime where the lower sections of the turbine blades, e.g., under the platform, are beginning to experience hot corrosion attack in the vicinity of 700°C [110]. These regions of the turbine blades are, in many cases, coated with diffusion aluminides. Most of the studies that have been conducted concerning Type II hot corrosion have focused on Co-base systems, e.g., CoCrAlY, as Type II hot corrosion was originally observed to be quite severe in these coatings [41]. In this chapter, the effect of Co, Cr, and Pt addition, both individually and in various combinations, on the Type II hot corrosion resistance of β -NiAl base alloys is investigated.

6.1 EXPERIMENTAL PROCEDURE

6.1.1 Alloy Preparation

Alloy specimens were prepared using the techniques described in section 5.1.1. The alloy compositions used in this portion of the study are the same as those detailed in Table 5, with the one exception that the Ni-36Al-5Co was replaced by Ni-36Al-5Pt-5Cr.

6.1.2 Type II Hot Corrosion Exposures

Specimens were exposed to Type II hot corrosion conditions isothermally for 100 h. Shorter exposures were conducted in select cases. The testing techniques used were the same as those described in section 4.1.2.

6.1.3 Oxidation Exposures

Oxidation exposures were carried out at 700°C in an O₂ + 1000 ppm SO₂ environment. The procedure for these experiments was the same as that described for Type II hot corrosion testing with the exception that, for the oxidation exposures, no Na₂SO₄ deposit was applied.

6.1.4 Analytical Techniques

The hot corrosion specimens were analyzed using weight change kinetic data, SEM/EDS, and XRD analysis. The scales formed on the specimens oxidized at 700°C in O₂ + 1000 ppm SO₂ were observed by surface SEM analysis, X-ray photoelectron spectroscopy (XPS), and time of flight secondary ion mass spectroscopy (TOF-SIMS) so that detailed composition profiles through the scales could be measured. For the XPS analysis, samples were sputtered at a rate of ~5 nm per cycle, and a spectrum was taken after each sputter cycle.

6.2 RESULTS

6.2.1 Type II Hot Corrosion

Plots of weight change per cm² after 100 h of Type II hot corrosion exposure are shown in Fig. 49. The base Ni-36Al alloy experienced the most rapid hot corrosion attack. The addition of 5 at. % Pt resulted in significantly greater resistance, as did the addition of 5 at. % Cr. The Ni-36Al-5Pt-5Co displayed fairly poor hot corrosion resistance, as did the Ni-36Al-5Pt-5Cr. Corresponding cross-sectional SEM micrographs of these specimens are presented in Fig. 50.

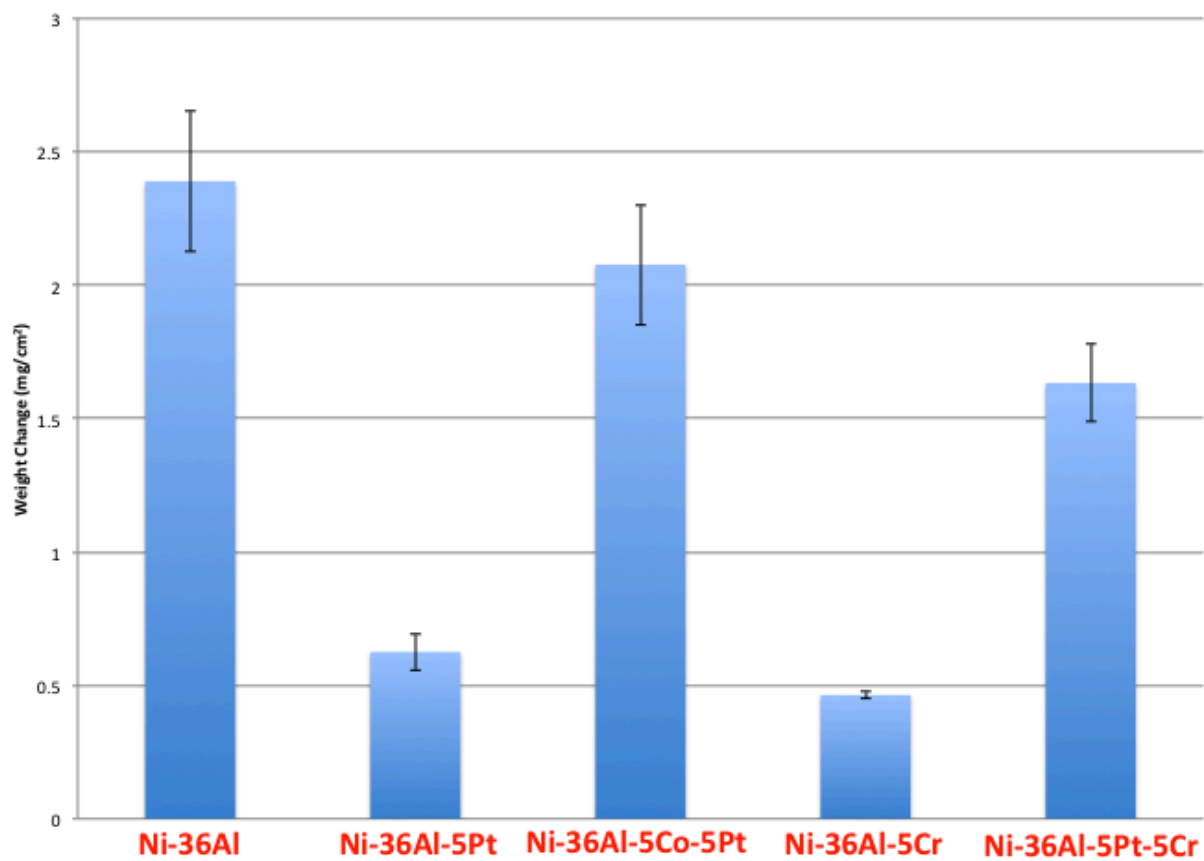


Figure 49. Plots of weight change per cm² of the β systems after 100 h of Type II hot corrosion exposure

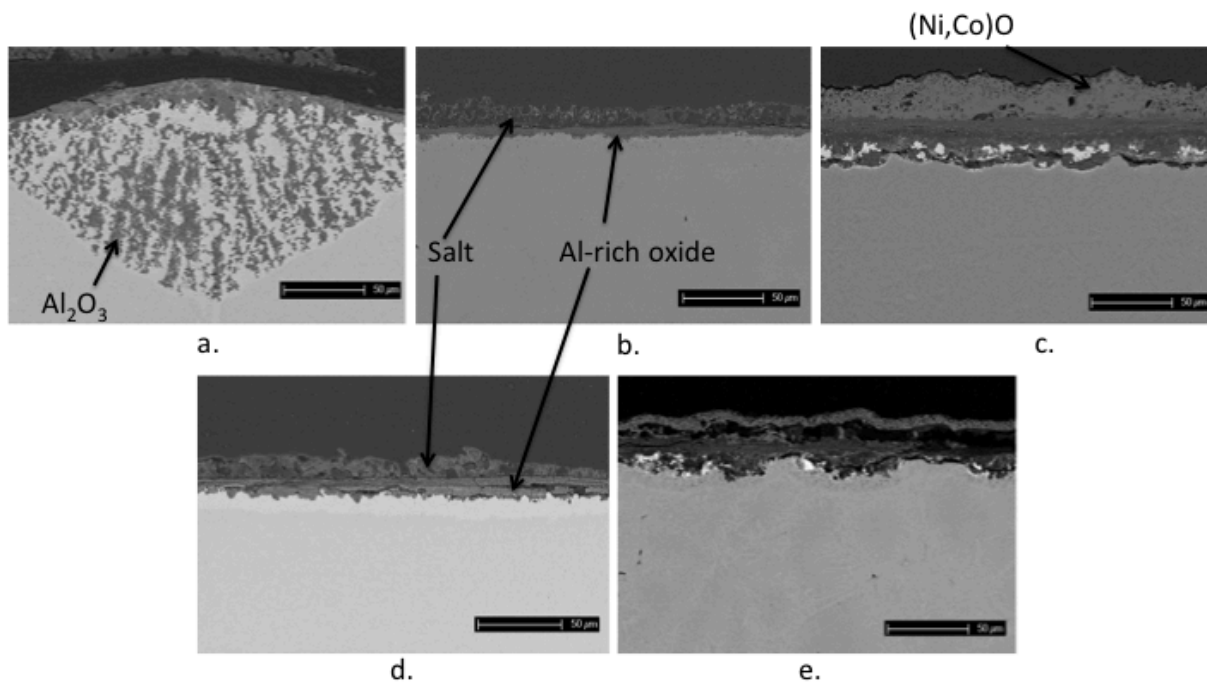


Figure 50. Cross sectional SEM micrographs of the a) Ni-36Al, b) Ni-36Al-5Pt, c) Ni-36Al-5Pt-5Co, d) Ni-36Al-5Cr, and e) Ni-36Al-5Pt-5Cr after a 100 h Type II hot corrosion exposure

The Ni-36Al developed a microstructure which is rather uncommon for Type II hot corrosion. The entire specimen experienced severe internal oxidation of Al, and locally the internal oxidation zone developed into large, cone-shaped regions comprised of finger-like Al_2O_3 precipitates (Fig. 50 a). The Ni-36Al-5Pt and Ni-36Al-5Cr specimens developed relatively thin, protective Al_2O_3 -rich scales that resulted in excellent hot corrosion resistance throughout the 100 h exposure. The Ni-36Al-5Pt-5Co and Ni-36Al-5Pt-5Cr specimens experienced rapid Type II hot corrosion degradation with broad, nearly uniform attack. Ahead of the corrosion front, the Ni-36Al-5Pt-5Cr developed a γ' - Ni_3Al zone approximately 10 μm deep due to selective Al depletion, within which internal Cr-rich sulfides had precipitated (Fig. 51).

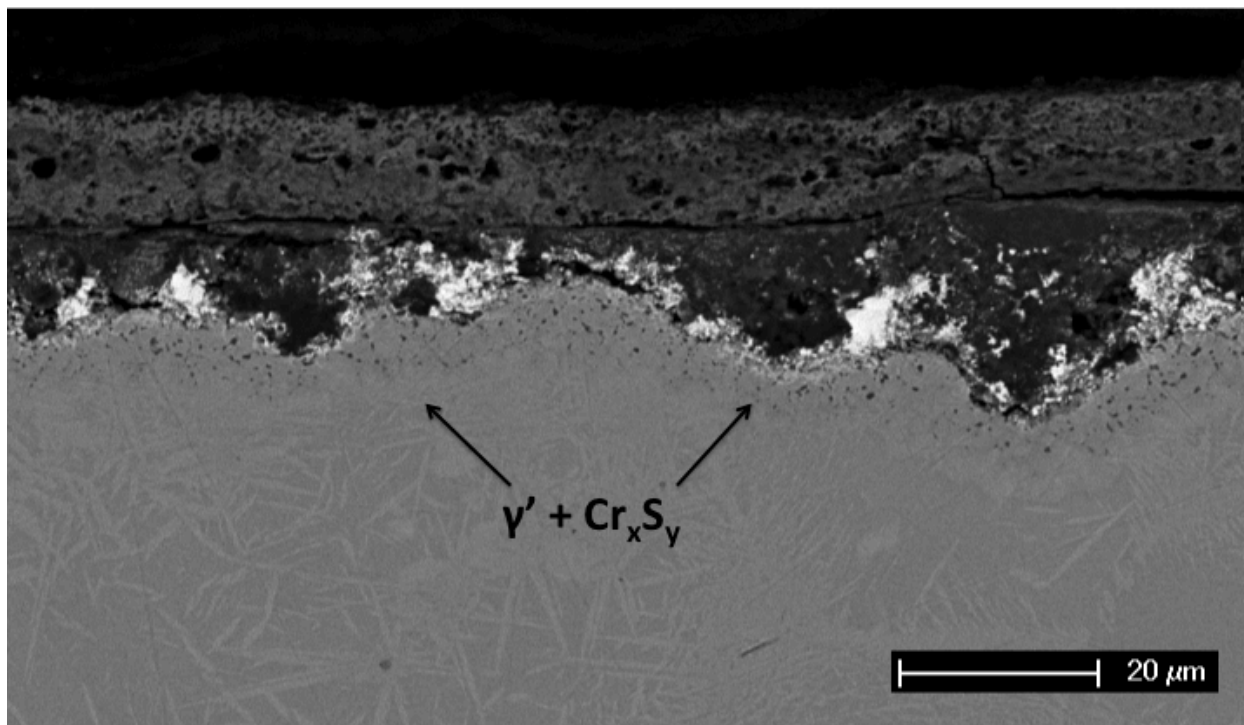


Figure 51. Cross sectional SEM micrograph of the Ni-36Al-5Pt-5Cr after a 100 h Type II hot corrosion exposure

It is difficult to ascertain the reasons for the observed differences in Type II hot corrosion behavior simply by observing the Type II degradation microstructures. In Chapter 5, the importance of the ability of a given alloy to rapidly form a protective scale and to reform that scale if it sustains damage under Type I hot corrosion conditions was demonstrated. In what follows, it is shown that similar considerations can be made in the case of Type II hot corrosion. However, as the temperature and gaseous atmosphere are different from what is found in Type I hot corrosion, the situation is unique and requires separate attention.

In order to determine the compositions of the scales that formed on each alloy, specimens were oxidized at 700°C for 100 h in O₂ + 1000 ppm SO₂, and the scales were investigated using surface SEM/EDS, XPS and TOF-SIMS.

6.2.2 700°C Oxidation in O₂ + 1000 ppm SO₂

Surface SEM revealed that each specimen formed a rather thin Al-rich oxide. The oxides were so thin, in fact, that the compositions could not be accurately determined using EDS analysis. In order to determine the compositions of these thin scales, XPS and TOF-SIMS analyses were performed. The XPS spectra for the Ni-36Al, Ni-36Al-5Pt, Ni-36Al-5Pt-5Co, Ni-36Al-5Cr, and Ni-36Al-5Pt-5Cr are shown in Figs. 52-56, respectively. In each figure, two plots are shown. The top plot shows the entire composition axis, while the bottom plot only shows concentrations from 0 to 5 at. %. The latter plots are shown so that elements that are present in the scales at fairly low concentrations can be easily seen.

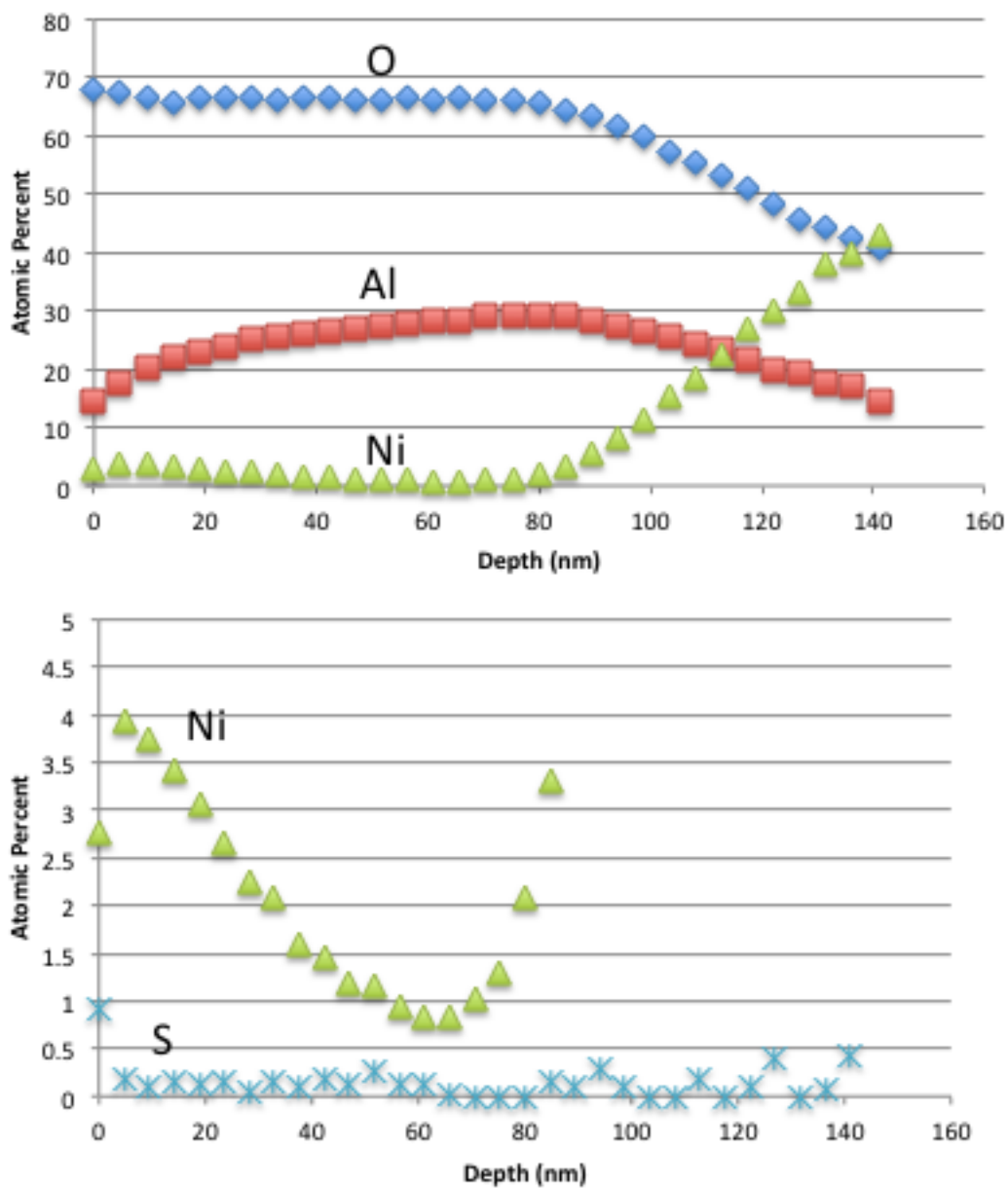


Figure 52. XPS depth profiles of the scale formed on the Ni-36Al alloy after 700°C oxidation for 100 h in O₂ + 1000 ppm SO₂

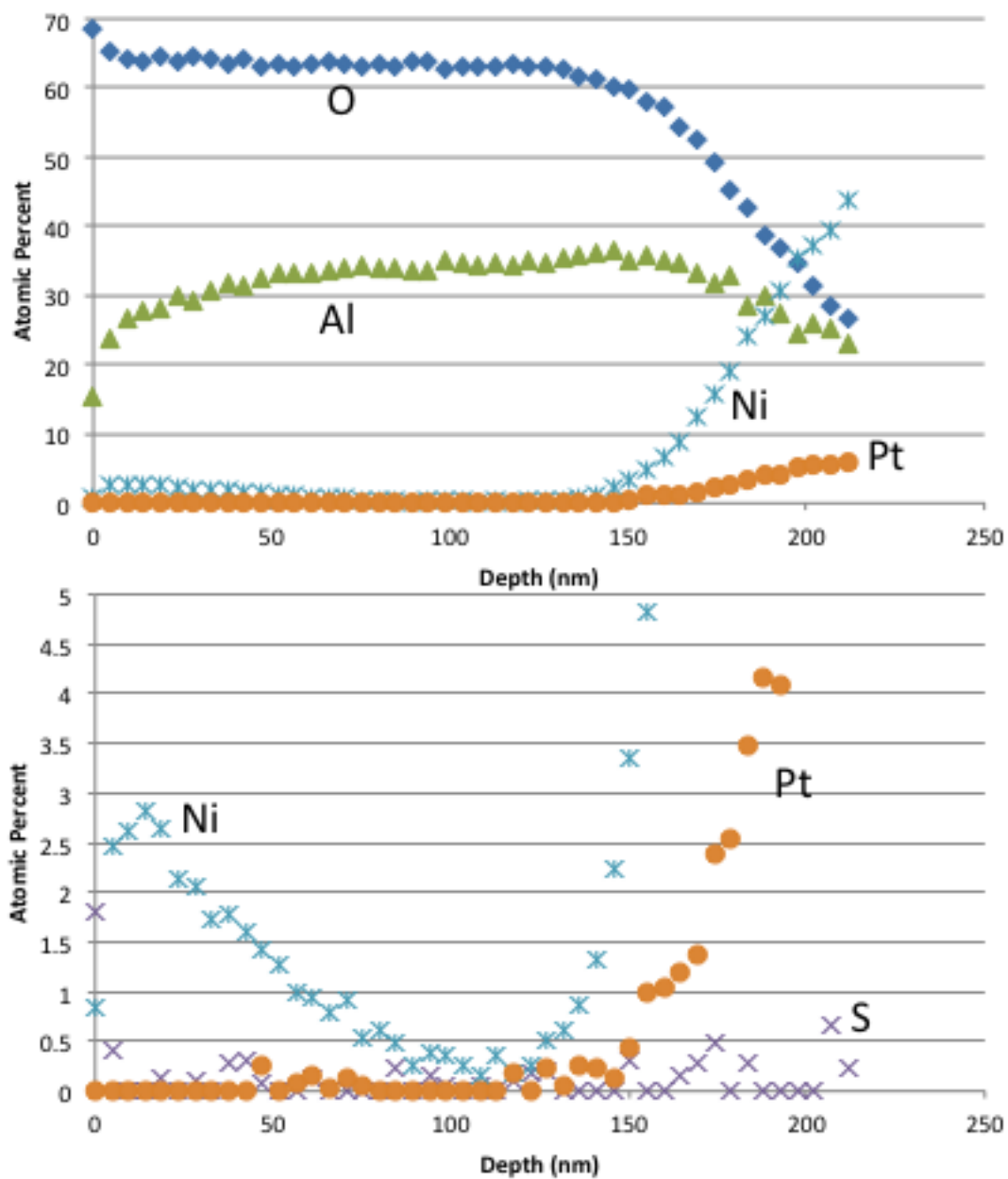


Figure 53. XPS depth profiles of the scale formed on the Ni-36Al-5Pt alloy after 700°C oxidation for 100 h in O₂ + 1000 ppm SO₂

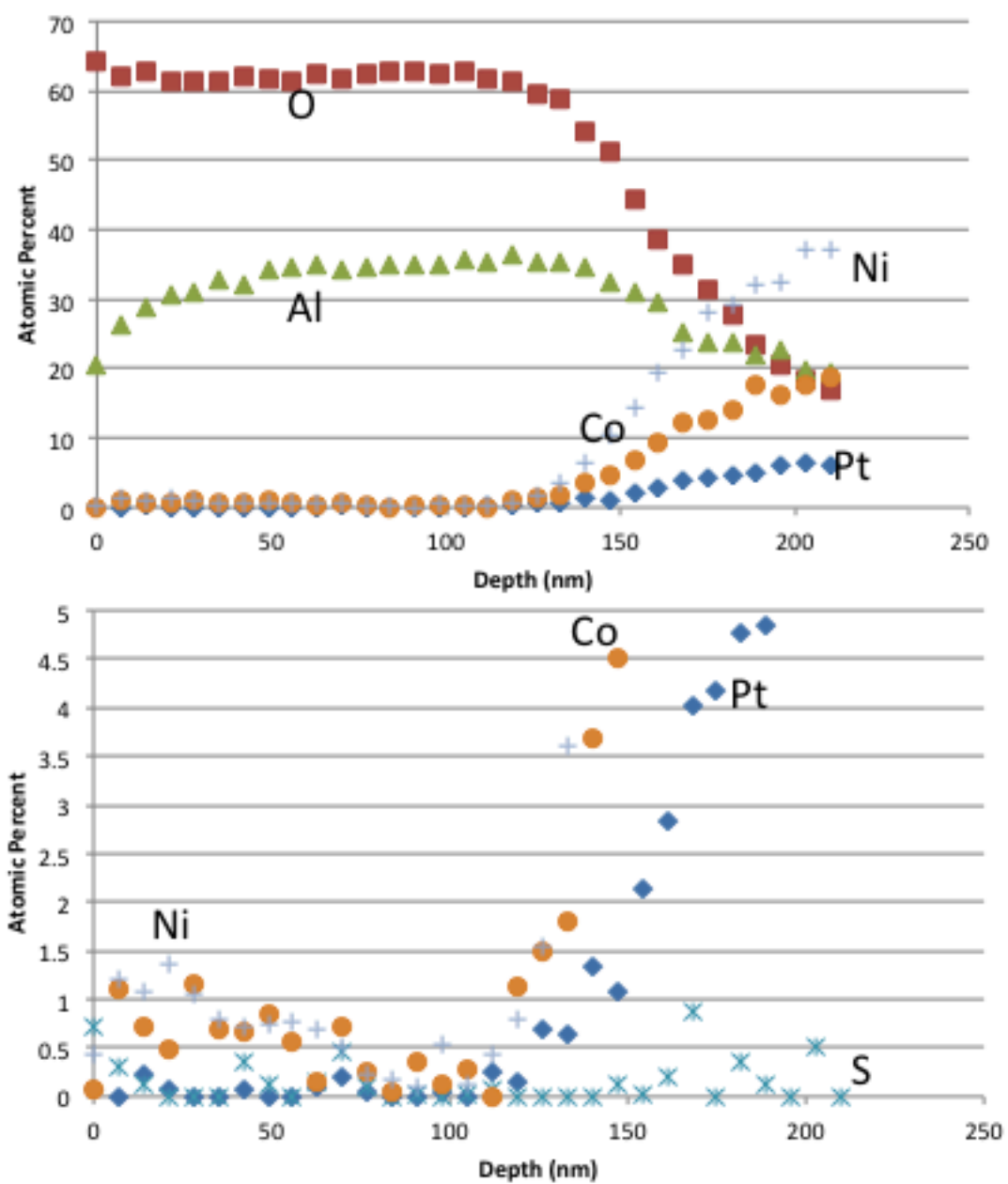


Figure 54. XPS depth profiles of the scale formed on the Ni-36Al-5Pt-5Co alloy after 700°C oxidation for 100 h in O₂ + 1000 ppm SO₂

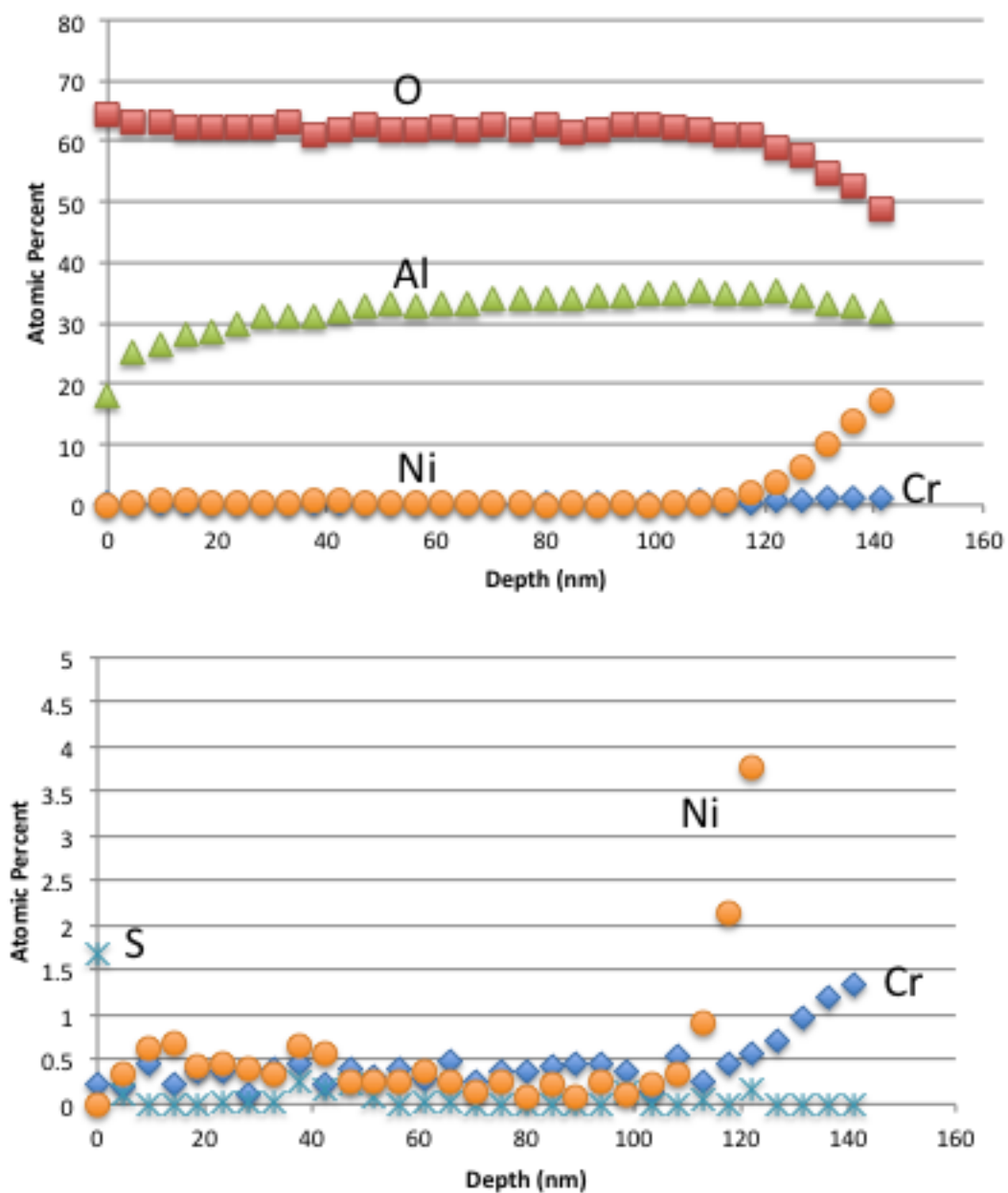


Figure 55. XPS depth profiles of the scale formed on the Ni-36Al-5Cr alloy after 700°C oxidation for 100 h in O₂ + 1000 ppm SO₂

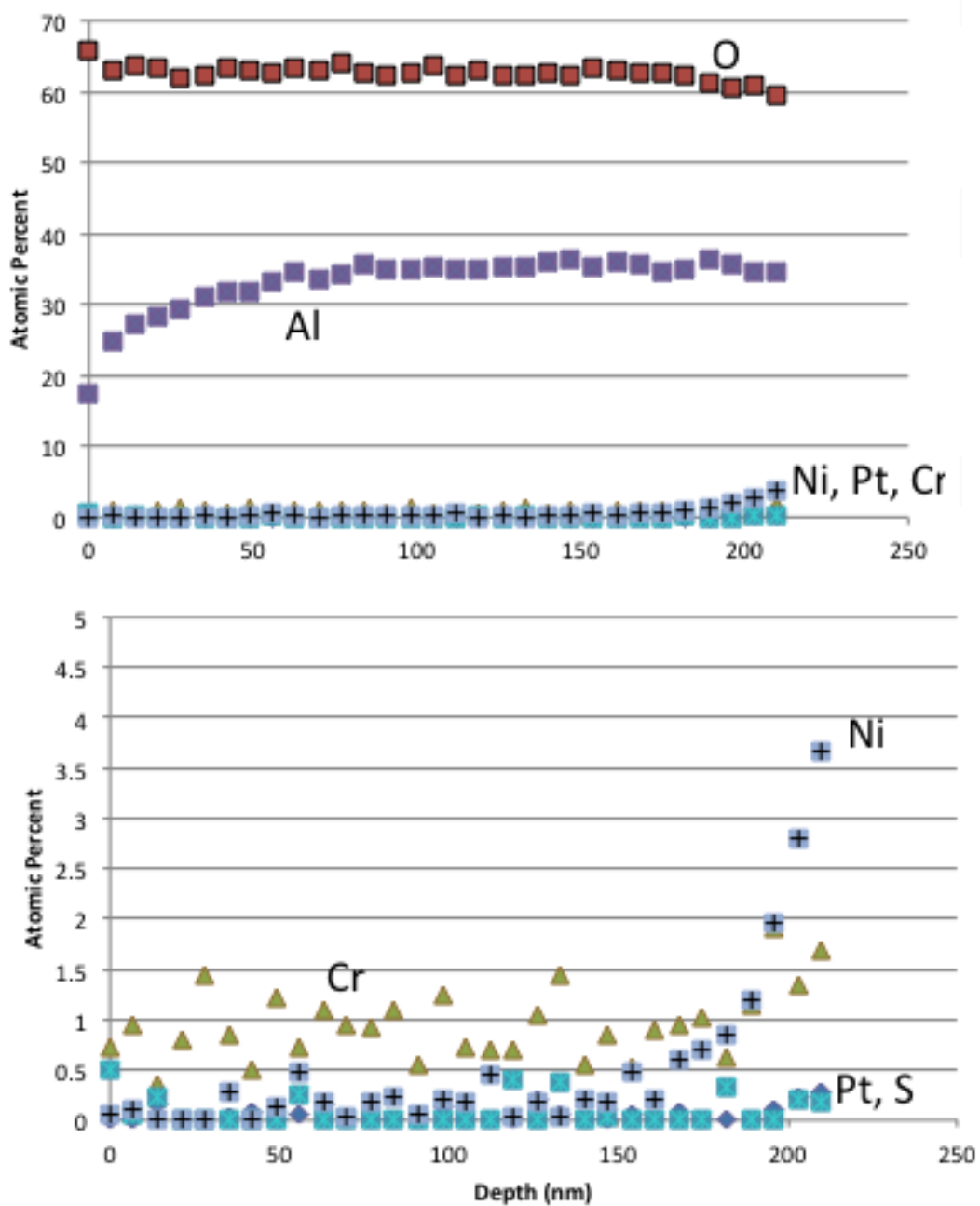


Figure 56. XPS depth profiles of the scale formed on the Ni-36Al-5Pt-5Cr alloy after 700°C oxidation for 100 h in O₂ + 1000 ppm SO₂

It should be noted that Si was present as an impurity in all of the scales. It tended to be concentrated at the surface and was more dilute at greater depths into the scale. An example, showing the XPS spectrum for the Ni-36Al specimen including the Si profile, is shown in Fig. 57. The Si profiles were omitted from the above figures for the sake of clarity. The quartz reaction chamber used for the oxidation exposures is assumed to be the source of the Si. Because the Si profiles were the same in each specimen, the contamination is assumed to be inconsequential.

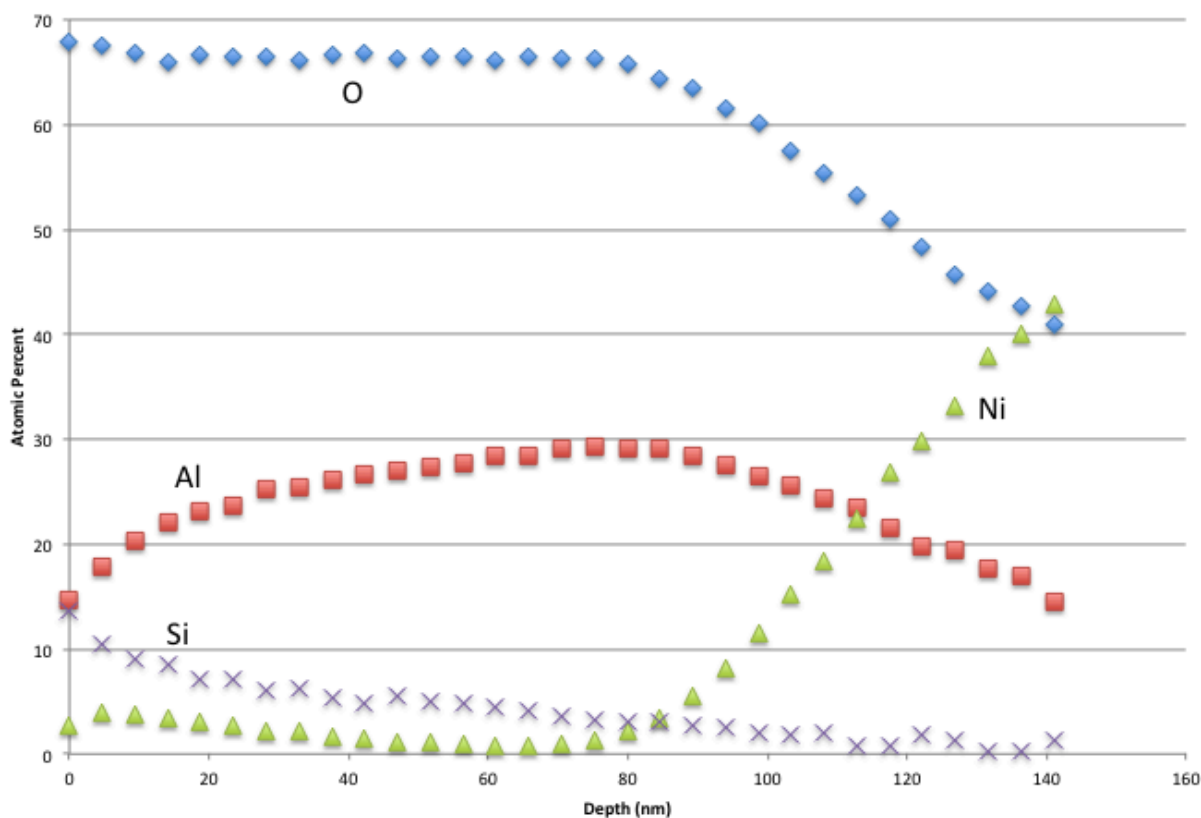


Figure 57. XPS depth profiles of the scale formed on the Ni-36Al alloy after 700°C oxidation for 100 h in O₂ + 1000 ppm SO₂, showing the Si contamination in the scale

Under these conditions, all alloys were primarily Al_2O_3 – formers, as indicated by the high levels of Al and O in the scales, present at a ratio of $X_{\text{O}}/X_{\text{Al}}$ approximately equal to 1.5. The polymorph of Al_2O_3 that was present on each specimen (see Chapter 7 for a thorough discussion of this topic) could not be ascertained based on the current analysis. All scales contained 0.5-2.0 at. % S at the surface of the scale, i.e., in the first few nanometers adjacent to the scale/gas interface. The source of this S is most likely adsorbed SO_x , or perhaps in some cases Ni or Co sulfates that formed via, e.g., Reaction 31.

Although Al_2O_3 scales were formed in all cases, the precise compositions of the scales varied significantly with alloy composition. The base Ni-36Al formed an Al_2O_3 scale which contained approximately 4 at. % Ni near the scale/gas interface, indicating that transient $\text{NiO}/\text{NiAl}_2\text{O}_4$ had formed during the early stages of exposure. The addition of 5 at. % Pt to the alloy resulted in a reduction of the Ni content in the scale to 2.5 at. %, while the addition of 5 at. % Cr resulted in exclusive Al_2O_3 formation with extremely small levels (<0.5 at. %) of Ni and Cr present in the scale. The scale formed on the Ni-36Al-5Pt-5Co alloy contained approximately 1 at. % each of Ni and Co. Finally the Ni-36Al-5Pt-5Cr alloy formed a scale containing essentially no Ni, but approximately 1 at. % Cr.

The XPS analysis provided very accurate quantitative compositional data; however, the spatial resolution of this technique is not extremely good (~200 x 200 μm spot size). Thus, TOF-SIMS analysis was also performed in order to determine the spatial distributions of the elements within the scale. In the following figures, the Al profiles are omitted, because Al is present throughout the scale. It is of interest to image the distributions of the other elements, i.e., Cr, Pt, Ni, and/or Co. It is to be noted that, as TOF-SIMS does not provide quantitative data, the brightness of a given color must not be taken as an accurate indication of concentration.

In Fig. 58, a lateral image (looking down at the surface of the oxide) of the Ni content is shown for the Ni-36Al and Ni-36Al-5Pt at depths of approximately 5 nm and 10 nm from the oxide/gas interface. For each specimen, the surface of the oxide contained a fairly even distribution of Ni, indicating that in the very early stages of exposure, both alloys formed a significant amount of transient Ni-rich oxide in addition to Al_2O_3 . 10 nm into the oxide, however, the Ni distribution was still uniform on the Ni-36Al, but at the same depth, Ni was present primarily at Al_2O_3 grain boundaries in the case of the Ni-36Al-5Pt.

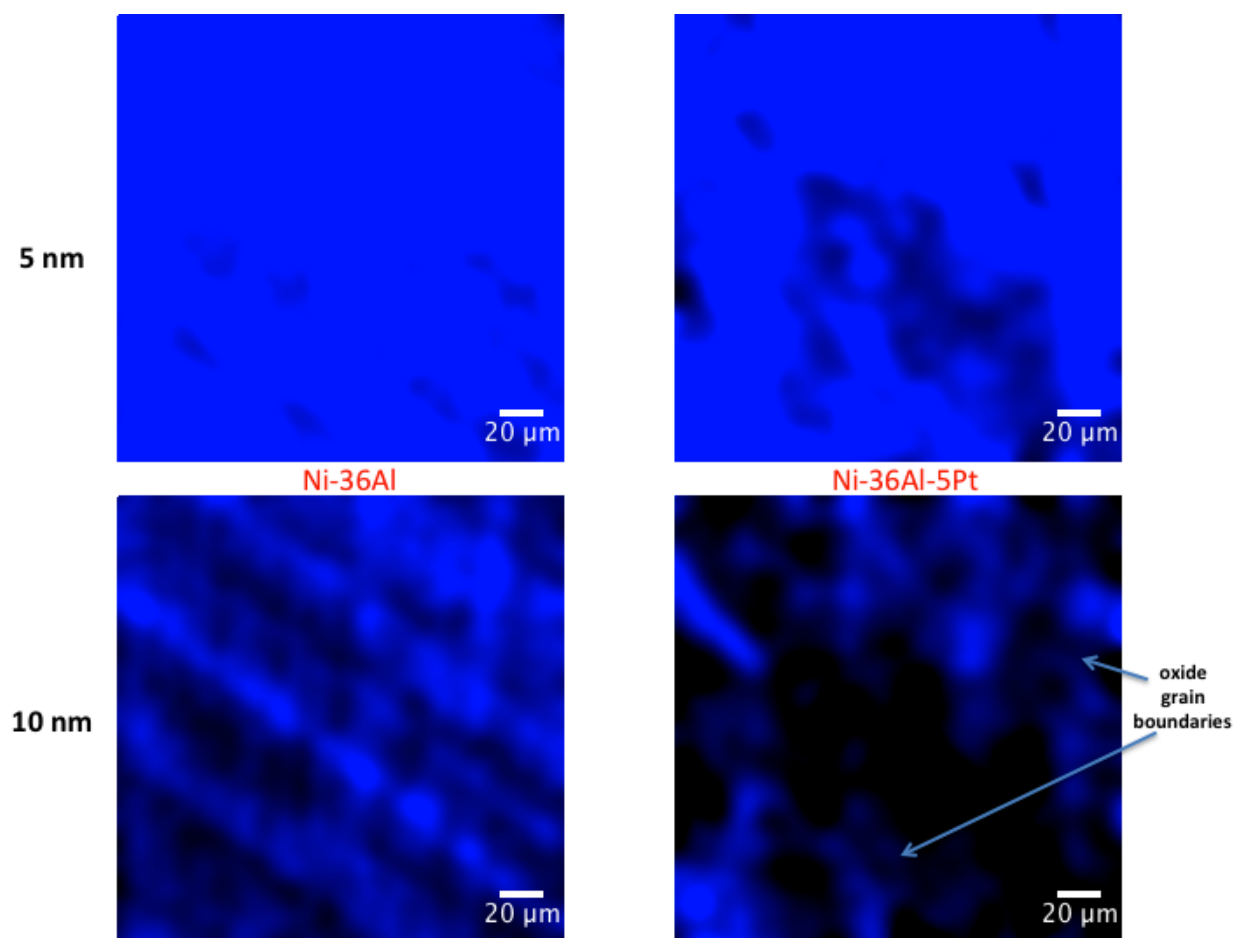


Figure 58. Lateral TOF-SIMS images of the Ni-36Al alloy showing the Ni distribution within the scale formed during 100 h oxidation at 700°C in O₂ + 1000 ppm SO₂ at a depth of 5 nm and 10 nm

In Fig. 59, the distributions of Ni and Cr within the scale formed on the Ni-36Al-5Cr specimen are shown. In this case, cross sectional images of the scale were generated. The ~0.6 at. % Ni enrichment at a depth of approximately 10 nm in Fig. 55 is visible at the surface. According to Fig. 55, the Cr concentration was constant throughout the thickness of the scale at ~0.3 – 0.4 at. %. The TOF-SIMS cross-section, however, reveals that the Cr was in fact distributed rather heterogeneously within the scale. There was a thin layer of Cr enrichment at the surface of the scale; within the bulk, however, Cr enrichment was localized (indicated by arrows), and very pure Al₂O₃ existed in between the Cr-rich regions. It is not completely obvious if these Cr-rich regions in the scale correlated with some microstructural feature in the underlying alloy; however, there were regions of γ -Ni at some β grain boundaries. The γ -Ni phase was found via EDS to have a higher Cr content than the surrounding β , and thus the Cr-rich regions in the scale may indeed have correlated with this phase.

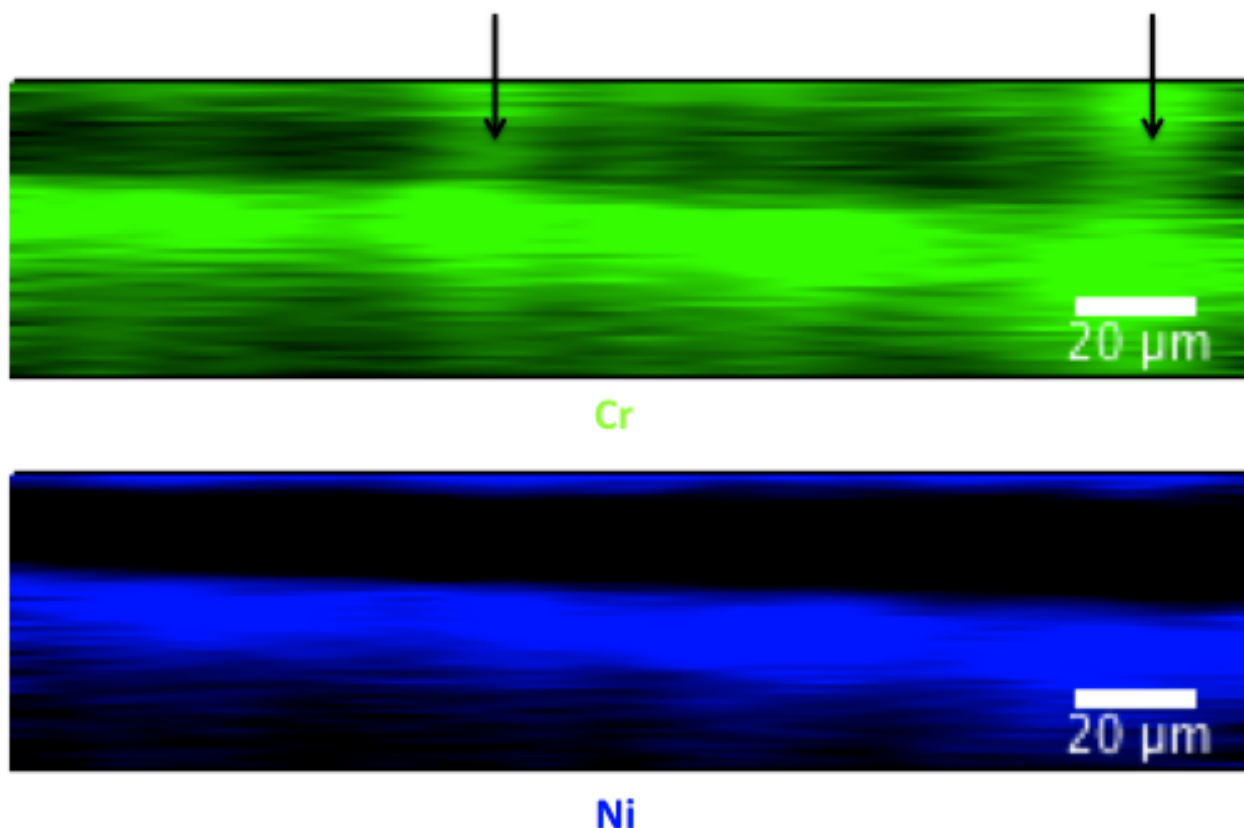


Figure 59. Cross-sectional TOF-SIMS images showing the Ni and Cr distributions within the scale formed on the Ni-36Al-5Cr alloy during 100 h oxidation at 700°C in O₂ + 1000 ppm SO₂

A lateral image of the oxide grown on the Ni-36Al-5Pt-5Co is presented in Fig. 60. Here it is shown that at the surface of the scale, Co and Ni were locally enriched in the scale. Deeper in the oxide, these elements were primarily located at scale grain boundaries, while the grain interiors consisted of fairly pure Al₂O₃.

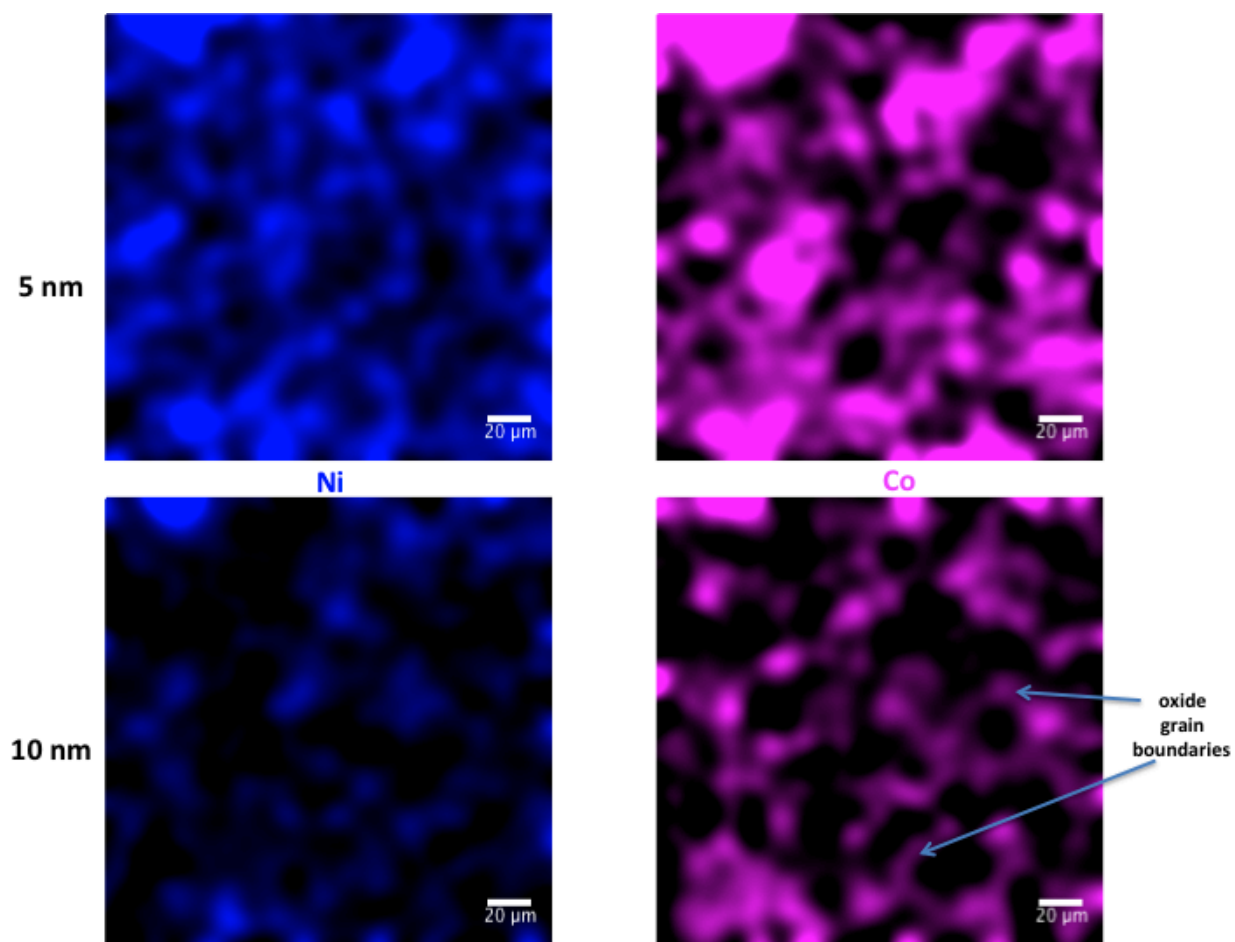


Figure 60. Lateral TOF-SIMS images showing the Ni and Co distributions within the scale formed on the Ni-36Al-5Pt-5Co alloy during 100 h oxidation at 700°C in O₂ + 1000 ppm SO₂ at a depth of 5 nm and 10 nm

Finally, a cross section of the oxide formed on the Ni-36Al-5Pt-5Cr is presented in Fig. 61, showing the Cr distribution in the scale. The ~1 at. % Cr detected within the scale was distributed heterogeneously, much like the Ni-36Al-5Cr. Aside from these Cr-rich regions, the scale consisted of pure Al_2O_3 , as indicated by XPS.

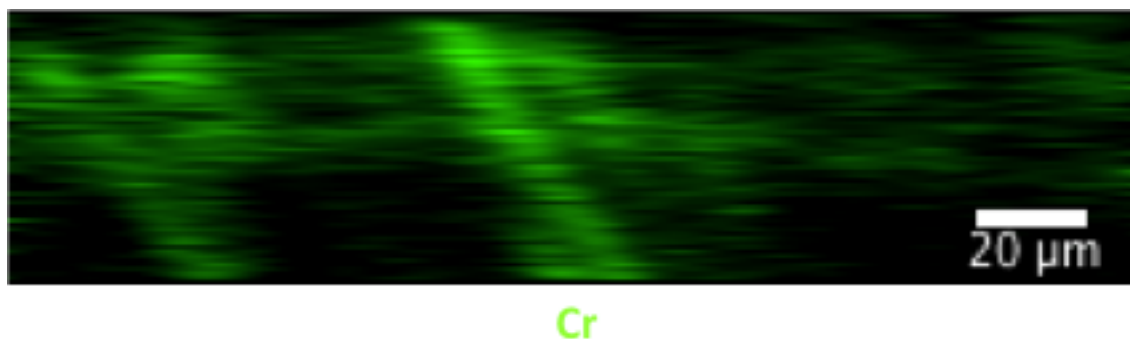


Figure 61. Cross-sectional TOF-SIMS image showing the Cr distribution within the scale formed on the Ni-36Al-5Pt-5Cr alloy during 100 h oxidation at 700°C in $\text{O}_2 + 1000 \text{ ppm SO}_2$

6.3 DISCUSSION

For most of the compositions studied, the 700°C oxidation results presented above greatly aid in understanding the observed Type II hot corrosion behavior. From the standpoint of providing hot corrosion resistance, it is desirable to rapidly form a pure Al_2O_3 scale. This statement is rather general, and applies during high temperature oxidation in the absence of a salt deposit, oxidation in multi-oxidant gases, hot corrosion, etc. Al_2O_3 , specifically $\alpha\text{-Al}_2\text{O}_3$, is the slowest-growing oxide that can form on modern coating systems. Slowly growing scales tend to offer the best protection due to a low rate of alloy depletion and metal consumption, and so the $\alpha\text{-Al}_2\text{O}_3$ phase is generally desired. There is an additional benefit of forming as pure of an Al_2O_3 scale as possible during Type II hot corrosion exposure. As discussed in Section 2.2.3, in order for a molten salt to develop during corrosion at 700°C, a $\text{Na}_2\text{SO}_4\text{-MSO}_4$ ($\text{M}=\text{Ni}$ and/or Co) eutectic must form by the sulfation of transient NiO and/or CoO to form NiSO_4 and/or CoSO_4 , respectively, and subsequent dissolution into the Na_2SO_4 . Therefore, if transient oxidation of Ni and Co can be prevented, a molten deposit may not develop and very mild corrosion will result. Further, the presence of Co in the scale is likely to be more deleterious than the presence of Ni , as CoSO_4 is significantly more stable than NiSO_4 with respect to the oxides CoO and NiO , respectively [111].

The 4 at. % Ni present in the scale formed on the Ni-36Al is, therefore, apt to be detrimental. The addition of 5 at. % Cr to this alloy resulted in a very pure Al_2O_3 scale containing less than 0.5 at. % Ni . As a result, the Ni-36Al-5Cr formed a rather protective scale

during hot corrosion exposure, and its resistance was quite good. The mechanism by which the Cr facilitated the formation of a pure Al_2O_3 scale can be ascribed to the well-known “third element effect” [112]. According to the proposed mechanism for this effect, a layer of transient Cr_2O_3 , formed during the early stages of exposure, lowered the p_{O_2} at the scale/alloy interface to the dissociation pressure of Cr_2O_3 , defined by equilibrium between the oxide and the alloy. At this low oxygen potential, only an oxide that is thermodynamically more stable than Cr_2O_3 can form, and thus pure Al_2O_3 , which forms the most stable oxide of the elements present in these alloys, formed as a healing layer beneath the transient oxide. If this is the mechanism by which Cr promoted the selective oxidation of Al, Cr should be detected near the surface of the scale during the early stages of oxidation. Indeed, ~0.2-0.3 at. % Cr was detected in the scale formed after 100 h oxidation (Fig. 55), and the TOF-SIMS analysis indicated that a thin layer of Cr-rich oxide was present at the surface of the scale in addition to the Cr-rich regions within it. Thus, the traditional third element effect seems to be a viable mechanism. Other contributing factors are also possible, such as a decrease in oxygen solubility in the alloy with Cr addition, as first suggested and quantified by Guan and Smeltzer [113].

The Ni-36Al-5Pt also demonstrated relatively good Type II hot corrosion resistance; this was slightly surprising, as the Ni content in the scale formed on this alloy at 700°C was substantial. It is true that the addition of Pt reduced the Ni content from 4 to 2.5 at. %; however, the difference in hot corrosion behavior between the Ni-36Al-5Pt and the Ni-36Al was striking. Upon closer observation of the XPS spectra presented in Figs. 52 and 53, however, a more distinct difference between the Pt-containing and Pt-free specimens becomes evident. In the Ni-36Al specimen, the entire scale was found to contain a significant amount of Ni, greater than 1 at. %. In the case of the Ni-36Al-5Pt specimen, however, the Ni-enriched region of the

scale extended from the surface to a depth of approximately 90 nm into the scale. From this depth to the oxide/alloy interface (at a depth of ~125 nm) the Ni content became constant at a very low level (~0.3 at. %). Therefore, it was found that the addition of Pt had indeed decreased the duration of the transient oxidation stage, and after 100 h of exposure, a pure Al_2O_3 had been established beneath the area of Ni enrichment. Once again, this decrease in the extent of transient oxidation, although not as dramatic as what was observed in the case of the Ni-36Al-5Cr, is expected to result in enhanced Type II hot corrosion performance, as observed. The reasons for this are twofold. Firstly, as mentioned above, transient oxides are ultimately responsible for the formation of a molten deposit at 700°C. Secondly, even in the presence of a molten salt, the underlying pure Al_2O_3 scale is required to provide protection against Type II hot corrosion.

XPS analyses were also conducted on the Ni-36Al-5Cr and Ni-36Al-5Pt after 20 h of oxidation at 700°C in $\text{O}_2 + 1000 \text{ ppm SO}_2$, and the results are shown in Fig. 62. Beneath the zone of slight Ni and Cr enrichment in the scale formed on the Ni-36Al-5Cr (Fig. 62 a.), starting at a depth of approximately 12 nm, a pure subscale of Al_2O_3 had formed, analogous to the scale formed on the Ni-36Al-5Pt after 100 h. In the case of the latter alloy after 20 h oxidation, however, no such pure Al_2O_3 layer was observed; as shown in Fig. 62 b., the entire scale formed on the Ni-36Al-5Pt contained from 1 – 2.5 at. % Ni, with no evidence of the establishment of a pure underlying Al_2O_3 scale.

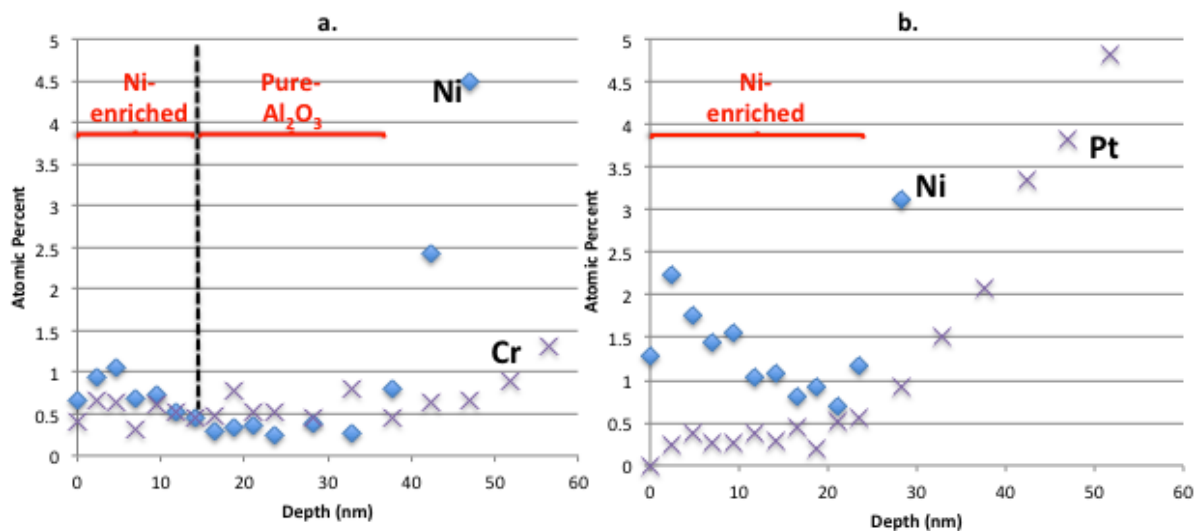


Figure 62. XPS depth profiles of the scale formed on the a) Ni-36Al-5Cr and b) Ni-36Al-5Pt alloys after 700°C oxidation for 20 h in O₂ + 1000 ppm SO₂

Thus, the results from the oxidation of the Ni-36Al, Ni-36Al-5Pt, and Ni-36Al-5Cr reveal a very important trend. The time required to establish a pure Al₂O₃ scale increases in the order of decreasing hot corrosion resistance, i.e., the more rapidly the alloy can establish a pure Al₂O₃ scale, the longer will be the protective incubation stage. This correlation is summarized in Table 6, which shows that the extent of Type II hot corrosion attack increased as the duration of the transient oxidation stage increased. The former is quantified by the weight change after 100 h of Type II exposure, with a smaller weight change indicating more protective behavior, and the latter is defined as the time elapsed from the beginning of the 700°C oxidation exposure to the time when a continuous subscale of pure Al₂O₃ was established.

Table 6. Correlation between Type II resistance and duration of transient oxidation stage

Alloy	100 h Type II Hot Corrosion Weight Change (mg/cm ²)	Duration of Transient Oxidation Stage (h)
Ni-36Al	2.39 ± 0.27	> 100
Ni-36Al-5Pt	0.63 ± 0.07	between 20 and 100
Ni-36Al-5Cr	0.46 ± 0.01	< 20

In Chapter 5, this same concept was also shown to explain the effect of composition on the Type I hot corrosion resistance of β alloys. In that work, the importance of not only rapidly forming an Al_2O_3 scale at the beginning of the exposure, but also reforming that scale if it is penetrated during exposure, was demonstrated. Although not explicitly shown in the current discussion, this scale healing is expected to be equally important during Type II hot corrosion exposure.

The addition of 5 at. % Co to the Ni-36Al-5Pt resulted in poor Type II hot corrosion performance. The XPS spectrum from this alloy after the oxidation exposure revealed that both Ni and Co were present in the outer portion of the scale. As mentioned above, CoSO_4 is significantly more stable than NiSO_4 , and as such Co is expected to be particularly detrimental to Type II hot corrosion resistance when present as a transient oxide. As a result, it was found that a relatively small amount of Co present in the scale, ~ 1 at. % in this case, can have a very large negative impact on hot corrosion resistance.

In Fig. 60, the TOF-SIMS analysis shows that the Co and Ni were highly localized into regions where their content was presumably significantly higher than the 1 at. % average value measured by XPS. These Ni/Co-rich regions of the scale very likely acted as initiation sites for eutectic salt formation and hence for hot corrosion.

The Type II hot corrosion performance of the Ni-36Al-5Pt-5Cr is difficult to explain based on the XPS/TOF-SIMS analyses. While 5 at. % additions of Cr or Pt individually resulted in quite good Type II resistance, the co-addition of the two elements in equal amounts resulted in significant hot corrosion attack. Further, the XPS and TOF-SIMS data gathered from the oxidized Ni-36Al-5Pt-5Cr show that the scale consisted solely of Al_2O_3 with localized Cr enrichment, which should be rather protective. Surface Ni-rich oxide is undetectable, and so even less transient oxidation of Ni occurred than in the case of the Ni-36Al-5Cr. The Type II degradation microstructure of this alloy after 100 h of exposure is shown once again in Fig. 63.

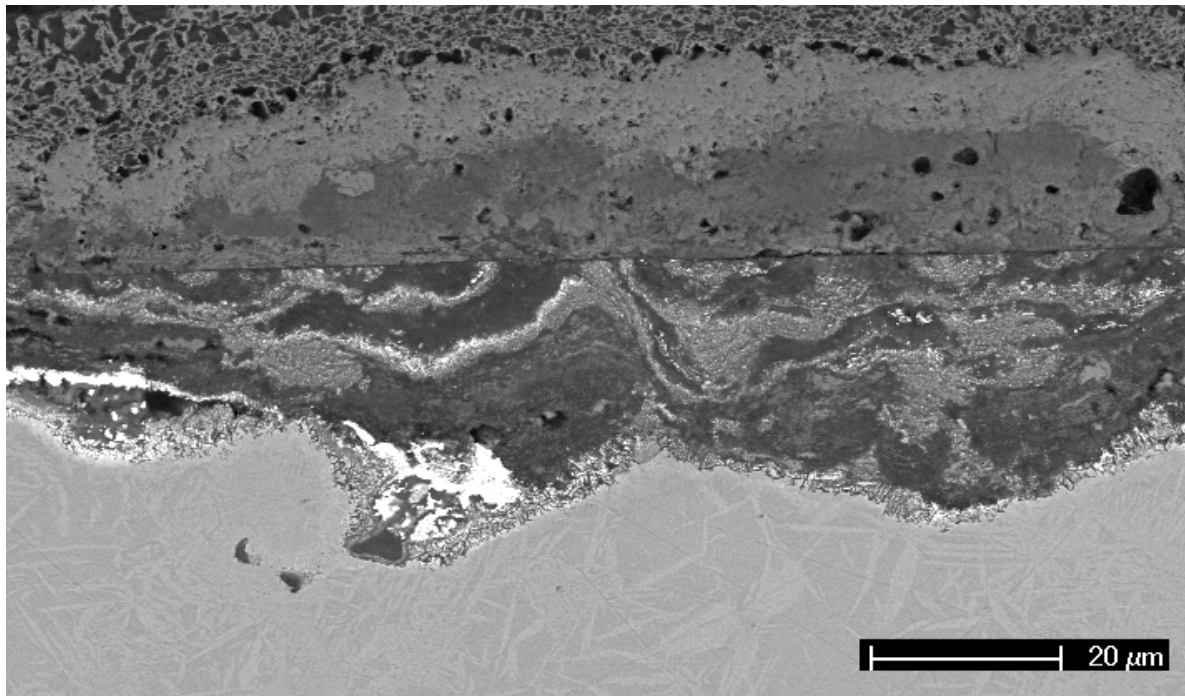


Figure 63. Cross sectional SEM micrograph of the Ni-36Al-5Pt-5Cr alloy after a 100 h Type II hot corrosion exposure

In this micrograph, a distinct layered structure is apparent within the corrosion product. In order to investigate the development of this corrosion product in its earlier stages, a 10 h Type II exposure was carried out. Images of the resulting microstructure taken at various magnifications in order to show all of the relevant features are shown in Fig. 64.

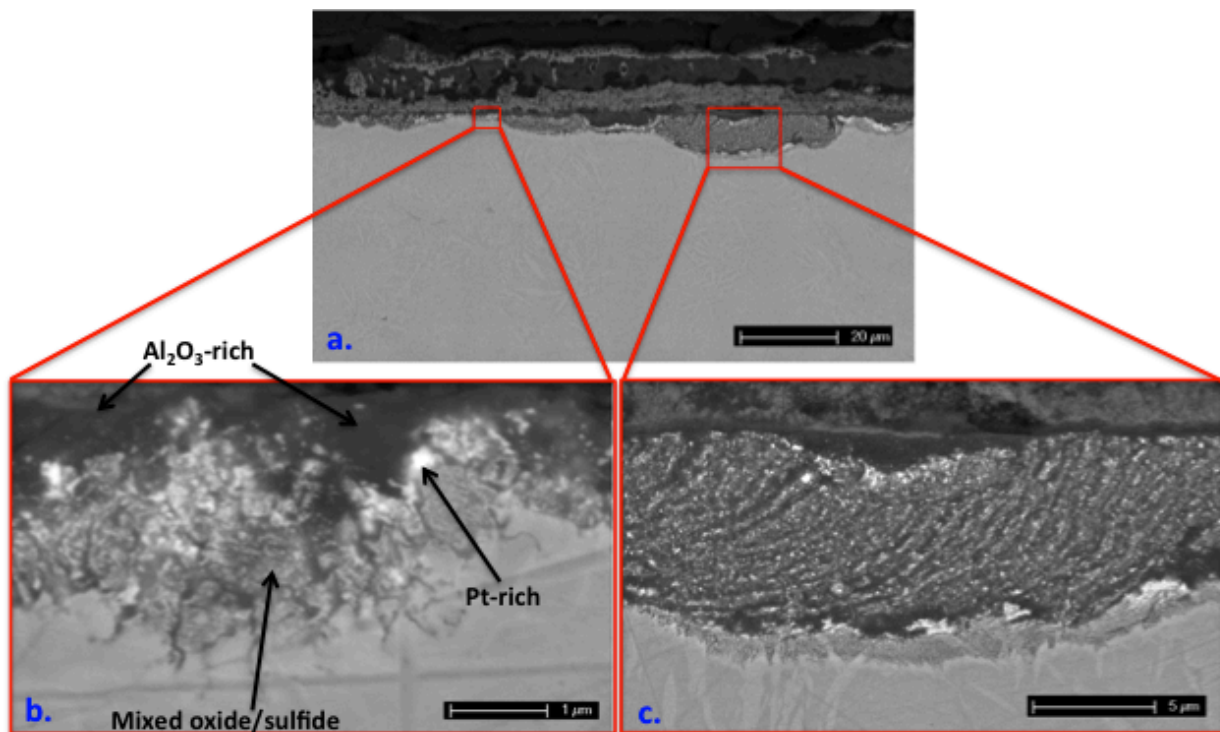


Figure 64. Cross-sectional SEM micrographs of the Ni-36Al-5Pt-5Cr after a 10 h Type II hot corrosion exposure

A high magnification micrograph of a region of the specimen that had not yet undergone rapid corrosion is shown in Fig. 64 b. Underneath the Al_2O_3 scale, precipitates rich in Pt were observed, amongst an internal zone of mixed oxide and sulfide. The Pt rich precipitates were, based on XRD, determined to be FCC Pt solid solution (henceforth referred to as γ). It is particularly clear that these precipitates do indeed form directly beneath the Al_2O_3 scale in the very early stages of attack in Fig. 65, which shows a cross-sectional SEM micrograph of this alloy after a 2 h Type II exposure.

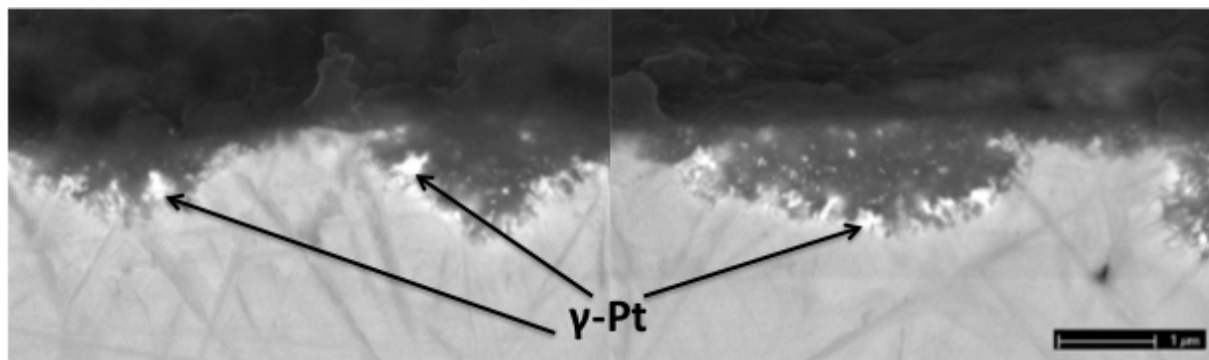


Figure 65. Cross-sectional SEM micrographs of the Ni-36Al-5Pt-5Cr after a 2 h Type II exposure, showing the precipitation of γ -Pt beneath the Al_2O_3 scale

In Fig. 64 c., the layered structure is observed to develop in the most rapidly attacked areas. A schematic representation of this layered corrosion product is shown in Fig. 66.

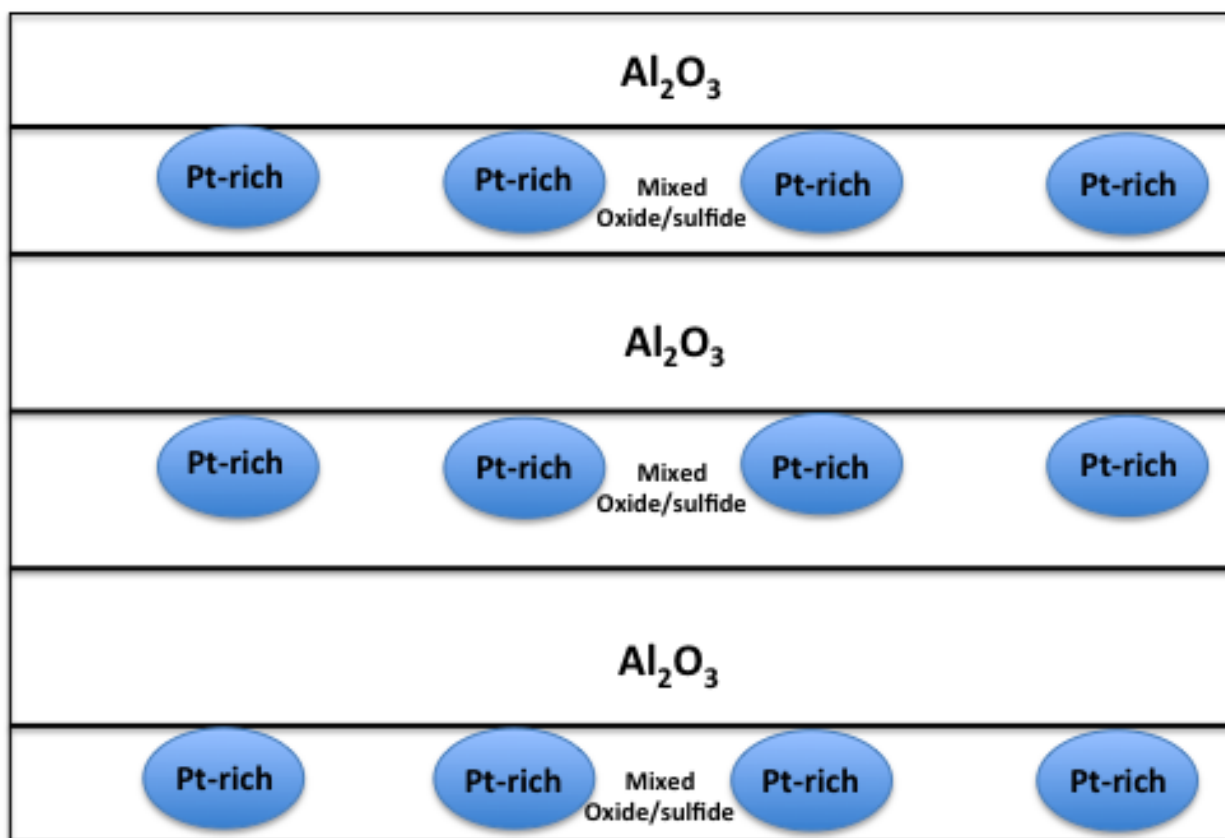


Figure 66. Schematic representation of the layered corrosion product formed during Type II hot corrosion attack of the Ni-36Al-5Pt-5Cr

The corrosion product consisted of alternating layers of Al_2O_3 and γ -Pt within and directly adjacent to an oxide/sulfide product.

The precipitation of the γ phase beneath the Al_2O_3 scale in the early stages of exposure is inferred to be responsible for the poor Type II hot corrosion performance of the Ni-36Al-5Pt-5Cr. The alloy very effectively formed an Al_2O_3 scale during 700°C oxidation (Fig. 56) and during the early stages of Type II hot corrosion (Fig. 65); however, the precipitation of the γ phase in the subsurface upon selective removal of Al prevented the alloy from maintaining the growth of the Al_2O_3 scale during exposure. This mechanism explains the layered structure that ultimately developed during Type II attack. Initially, a protective Al_2O_3 scale was formed, and in time the γ -Pt phase began to nucleate in the subsurface. This phase was disruptive to the maintenance of the scale and its reformation if penetrated during exposure, and hence internal sulfidation/oxidation attack proceeded. Eventually, a healing layer of Al_2O_3 formed beneath this non-protective product. As this scale thickened, the γ phase began to precipitate beneath it as a result of Al depletion. These precipitates disrupted the maintenance of the Al_2O_3 healing layer, which ceased to be protective as a result, and the process repeated.

Two important issues must be addressed: the appearance of the γ -Pt phase in the subsurface of the Ni-36Al-5Pt-5Cr alloy and not in the Ni-36Al-5Pt, and also the importance of temperature. Observation of the subsurface in Fig. 65 clearly reveals that the γ phase nucleated early in the exposure, directly beneath the Al_2O_3 scale. Thus, as Al was depleted from the alloy due to oxidation, a driving force developed for γ nucleation. Tin et. al. showed that, when 3.7 at. % Cr was added to a Ni-base superalloy at the expense of Ni, keeping the composition otherwise constant, the partition coefficient for Pt, $k_{\text{Pt}} = \frac{C_{\text{Pt}}^{\gamma}}{C_{\text{Pt}}^{\gamma'}}$ increased by a factor of approximately 2 [114].

In other words, the solubility of Pt in γ' decreased with Cr addition. In the current work, as Al was depleted from the subsurface of the Ni-36Al-5Pt-5Cr, Pt and Cr became enriched in these regions. Thus, the Pt content increased, while its solubility decreased due to Cr enrichment. Hence, the solubility limit of Pt in γ' was surpassed and γ -Pt precipitation resulted. The importance of the relatively low temperature of these exposures is that, at 700°C, back-diffusion of Pt and Cr towards the specimen bulk was rather slow, allowing for the accumulation of these species. In addition, the solubility of Pt in γ' decreases with decreasing temperature. During Type I (900°C) hot corrosion, for example, the precipitation of the γ phase is not observed as a result of the higher temperature, and the Ni-36Al-5Pt-5Cr is very resistant to this mode of attack [115].

6.4 CONCLUSIONS

The influence of composition on the Type II hot corrosion resistance of Ni-36Al base alloys has been investigated. It has been shown that, in many cases, the duration of the protective incubation stage of hot corrosion depends strongly on the ability of the alloy to rapidly form a pure Al_2O_3 scale. The faster this can be accomplished, i.e., the shorter the duration of the transient oxidation stage, the more highly resistant the alloy will be to Type II attack. For example, for the binary and ternary alloys, the hot corrosion resistance increased in the order Ni-36Al < Ni-36Al-5Pt < Ni-36Al-5Cr. XPS and TOF-SIMS analyses of the scales grown on these alloys during oxidation at 700°C clearly showed that, of the three alloys, the Ni-36Al-5Cr established a pure Al_2O_3 scale the most rapidly, followed by the Ni-36Al-5Pt, and finally the Ni-36Al. Addition of 5 at. % Co to the Ni-36Al-5Pt resulted in very poor Type II hot corrosion resistance, partially due to the local enrichment of Ni and Co in the scale, which helped to stabilize a liquid salt deposit.

The Ni-36Al-5Pt-5Cr alloy formed what appeared to be a rather protective scale during 700°C oxidation. However, during Type II hot corrosion exposure, the formation of Pt solid solution precipitates in the alloy subsurface prevented the maintenance of a protective Al_2O_3 scale, and rapid attack resulted. These precipitates formed in this system due to Al depletion coupled with a decrease in Pt solubility in the γ' - Ni_3Al phase with Cr addition. A similar mechanism may indeed have contributed to the poor Type II hot corrosion resistance of the Ni-36Al-5Pt-5Co; however, further experimentation is required.

7.0 ENVIRONMENTAL AND COMPOSITIONAL EFFECTS ON THE Al_2O_3 STABILITY AND ASSOCIATED HOT CORROSION BEHAVIOR OF β -NiAl ALLOYS

An important aspect of the oxidation of Al_2O_3 -forming alloys is the formation of metastable phases of Al_2O_3 , which form initially and transform isothermally to the protective, thermodynamically stable α - Al_2O_3 phase. The presence of metastable Al_2O_3 (δ , γ , θ) is fleeting during oxidation at temperatures above $\sim 1100^\circ\text{C}$, but these phases can persist for extended periods of time at lower temperatures [116]. The transformation of these metastable phases to α - Al_2O_3 is of interest from both a scientific and a practical standpoint, as the α phase is the slowest-growing and therefore most protective oxide of Al.

The metastable \rightarrow stable Al_2O_3 transformation during the oxidation of Ni-base alloys has been the focus of a number of studies [116-122]; however, very little work has been done to carefully characterize how various alloying additions influence the transformation during oxidation at relatively low temperatures. It has been shown that Cr [116] and Ti [122] accelerate the transformation, while larger species such as Y, Zr, La, and Hf have the opposite effect [122]. A widely accepted explanation for the accelerating effect of Cr is the “template effect”, which is based on the fact that Cr_2O_3 and α - Al_2O_3 are isostructural (corundum structure). During the initial stages of oxidation, transient Cr_2O_3 will form and act as a heterogeneous nucleation site for α - Al_2O_3 .

The accelerating effect of Cr has been verified for the oxidation of Fe-base alloys as well [123]. The latter study also demonstrated that Ti and Fe additions accelerate the $\theta \rightarrow \alpha$ transformation in scales grown on Fe-Al alloys, presumably by the same sympathetic nucleation mechanism that is thought to be active when Cr is present. Numerous other authors have studied the influence of various surface treatments on the transformation behavior in scales grown on Fe-base alloys as well [124-126].

At the temperatures at which Type I hot corrosion occurs ($\sim 900^\circ\text{C}$), metastable forms of Al_2O_3 can be present on β -NiAl alloys for a significant amount of time prior to transformation to α - Al_2O_3 . It is important, therefore, to determine if there is a correlation between the rate at which the $\theta \rightarrow \alpha$ transformation occurs and the resistance of NiAl-base alloys to Type I hot corrosion.

Due to the complex compositions of actual aluminide coatings, it is of interest to document the influence of various alloying additions on the kinetics of the $\theta \rightarrow \alpha$ transformation and subsequently on Type I hot corrosion resistance. In the current study, cast alloys of composition Ni-36Al, Ni-46Al, Ni-36Al-5X and Ni-46Al-5X (at%) with X being Cr, Co, or Pt, were oxidized at 900°C for various amounts of time and analyzed in terms of oxidation kinetics and oxide microstructure using thermo-gravimetric analysis (TGA) and scanning electron microscopy (SEM), respectively. The kinetics of the $\theta \rightarrow \alpha$ - Al_2O_3 transformation were studied using photo-stimulated luminescence spectroscopy (PSLS) and verified in select cases using x-ray diffraction (XRD). The model alloys were also oxidized in the presence of a Na_2SO_4 surface deposit (Type I hot corrosion conditions) and in a SO_2 -containing gas in order to determine the influence of the exposure environment on the Al_2O_3 phase stability and protective properties. Based on these and previous results obtained in our laboratory, the relative importance of the $\theta \rightarrow \alpha$ transformation kinetics during Type I hot corrosion was determined.

7.1 EXPERIMENTAL PROCEDURE

7.1.1 Alloy Preparation

The nominal compositions of the alloys used in this study are presented in Table 7. These alloys were prepared using the techniques described in Section 5.1.1. The Ni-36Al-5Cr, Ni-46Al, and Ni-46Al-5Pt are 100% β -NiAl at 900°C, the exposure temperature in this study. β is the primary phase in the Ni-36Al and Ni-36Al-5Co; however, they also contain a small amount of γ' -Ni₃Al.

Table 7. Nominal alloy compositions

	Ni	Al	Co	Cr	Pt
Ni-36Al	Balance	36	-	-	-
Ni-36Al-5Co	Balance	36	5	-	-
Ni-36Al-5Cr	Balance	36	-	5	-
Ni-46Al	Balance	46	-	-	-
Ni-46Al-5Pt	Balance	46	-	-	5

Circular coupons approximately 1.5 mm thick were cut from the alloy castings. The coupons were polished to a 1200-grit finish on all sides, cleaned ultrasonically in soap and water, and then degreased in acetone.

7.1.2 Exposures

Isothermal oxidation exposures were conducted at 900°C in air for 100 h in a Setaram TAG-1750 thermobalance. Shorter-term (50h) air oxidation experiments were conducted in a horizontal tube furnace. In addition, as will be explained in subsequent sections, the Ni-46Al-5Pt was exposed isothermally at 900°C in a gaseous environment of O₂ + 1000 ppm SO₂ for 100 h, also in a horizontal tube furnace.

Finally, Type I hot corrosion specimens were deposited with Na₂SO₄ using the techniques described in Section 4.1.2, and exposed at 900°C in air in a vertical tube furnace (Figure 36) for 10 h. Following this 10 h Type I exposure, the specimens were cleaned ultrasonically in water for 20 min to remove the salt and any loosely-adherent corrosion products.

Oxidation in the Setaram instrument allowed the continuous measurement of the mass changes of the specimens during 900°C oxidation. The morphology of the scales formed after the isothermal oxidation exposures were analyzed using surface SEM. The oxide phases present were determined using Photo-Stimulated Luminescence Spectroscopy on an Olympus BX62 upright motorized microscope (Olympus Corp.) coupled with an Acton 2300i 0.3 m spectrometer

(Princeton Instruments), and, in some cases, by glancing angle X-ray diffraction (XRD) on a Philips X'Pert diffractometer.

7.2 RESULTS

7.2.1 Compositional Effects on the $\theta \rightarrow \alpha$ Al_2O_3 Transformation Kinetics

7.2.1.1 Isothermal Oxidation Kinetics and Scale Microstructure The parabolic weight change plots after oxidation in dry air at 900°C for 100 h are shown in Fig. 67. A method developed by Zhao and Gleeson [127] was used to determine the instantaneous parabolic rate constants (k_p) as a function of time. The k_p values for each alloy at 3 different times are shown in Table 8. The column entitled “Corresponding Scaling Kinetics” indicates the phase of Al_2O_3 , either θ or α , most closely associated with the measured k_p value at a given time based on the literature values of $4.5 \times 10^{-13} \text{ g}^2/(\text{cm}^4\text{-sec})$ for θ and $9 \times 10^{-16} \text{ g}^2/(\text{cm}^4\text{-sec})$ for α [116]. In this column, “transition” indicates that the k_p value falls in between the literature values for θ and α , and thus the scale is in the process of transforming.

Table 8. Instantaneous parabolic rate constants as a function of time at 900°C

Specimen	Time (h)	k_p ($\text{g}^2/\text{cm}^4\text{-sec}$)	Corresponding Scaling Kinetics
Ni-36Al	5	4.0×10^{-13}	θ
Ni-36Al	50	4.6×10^{-13}	θ
Ni-36Al	100	4.5×10^{-13}	θ
Ni-36Al-5Co	5	4.3×10^{-13}	θ
Ni-36Al-5Co	50	3.0×10^{-13}	transition
Ni-36Al-5Co	100	1.6×10^{-13}	transition
Ni-36Al-5Cr	5	6.5×10^{-13}	$\sim\theta$
Ni-36Al-5Cr	50	5.0×10^{-14}	transition
Ni-36Al-5Cr	100	2.6×10^{-15}	$\sim\alpha$
Ni-46Al	5	3.4×10^{-13}	θ
Ni-46Al	50	1.5×10^{-13}	transition
Ni-46Al	100	1.0×10^{-13}	transition
Ni-46Al-5Pt	5	2.5×10^{-13}	transition
Ni-46Al-5Pt	50	2.0×10^{-13}	transition
Ni-46Al-5Pt	100	1.5×10^{-13}	transition

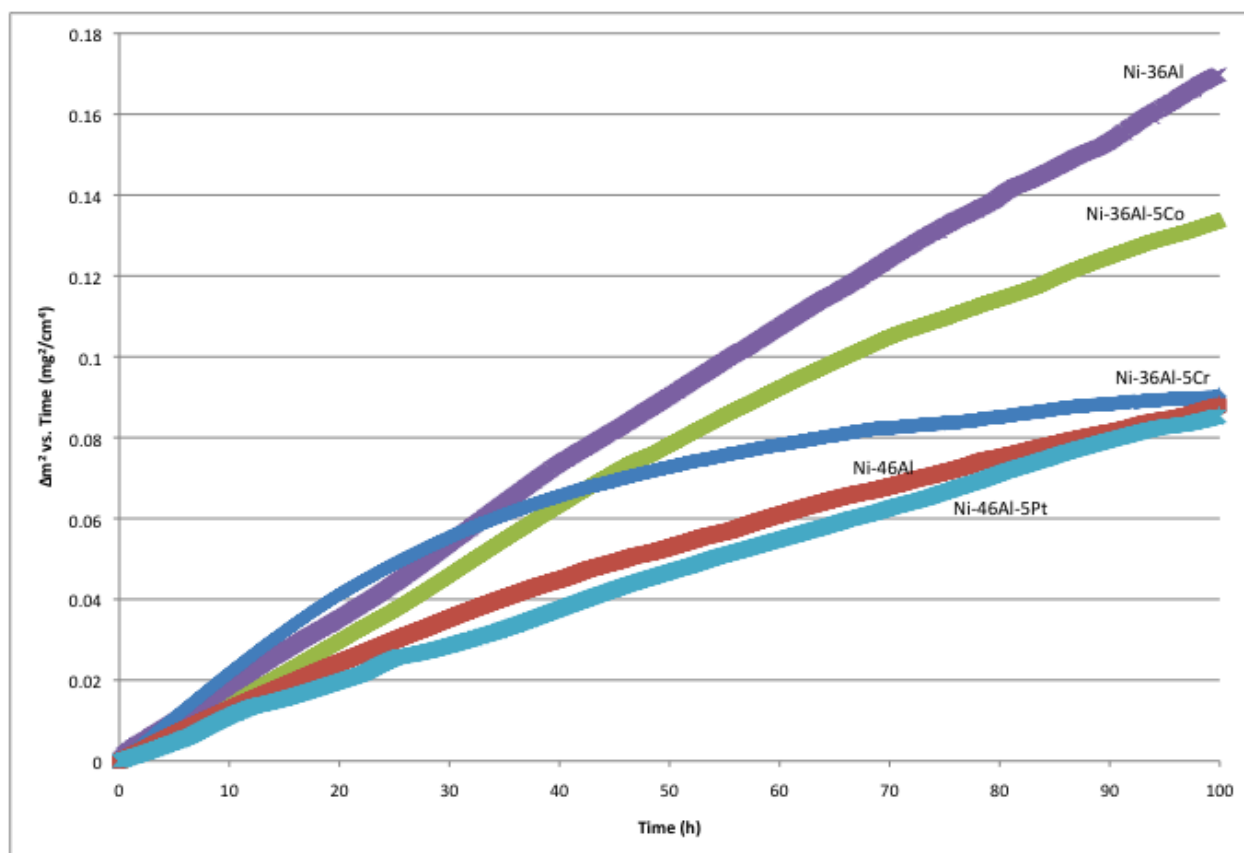


Figure 67. Parabolic weight changes plots for the oxidation of the β systems at 900°C

The measured k_p values serve as a starting point for analyzing the kinetics of the $\theta \rightarrow \alpha$ transformation and the influence of composition. The base Ni-36Al alloy oxidized with a k_p which was similar to the literature value for the formation of θ - Al_2O_3 throughout the 100 h exposure, with no clear indication of transformation to α . Addition of 5 at. % Co yielded a similar initial rate; however, beyond 50 h the k_p dropped to a transition value, indicating the partial transformation of the scale to the α phase. The Ni-36Al-5Cr oxidized at a rate that was initially higher than that of the binary Ni-36Al, but the rate decreased dramatically with continued oxidation, until the k_p reached a value characteristic of the thermal growth of α - Al_2O_3 . Increasing the Al content of the base alloy to 46 at. % resulted in scale transformation behavior similar to that of the Ni-36Al-5Co, although slightly lower rates were observed for the Ni-46Al. Finally, the initial k_p for the Ni-46Al-5Pt was slightly lower than that of the Ni-46Al; however, it did not change much throughout the course of the 100 h exposure, indicating that little transformation to α occurred.

Surface SEM micrographs of the scales formed on the β alloys after the 100 h isothermal oxidation exposure at 900°C in air are shown in Fig. 68.

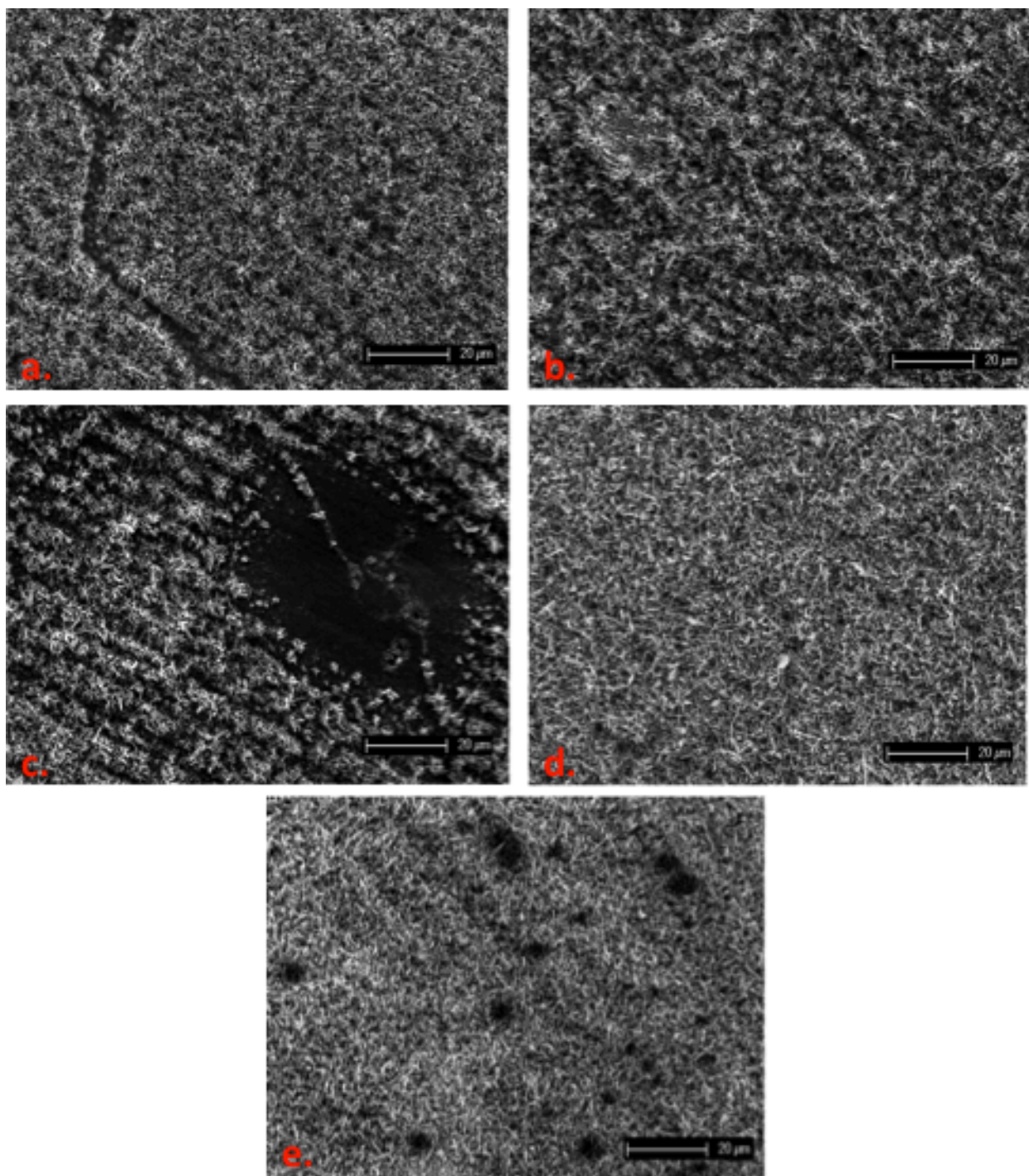


Figure 68. Surface SEM micrographs of the β systems after 100 h isothermal oxidation at 900°C: a) Ni-36Al, b) Ni-36Al-5Co, c) Ni-36Al-5Cr, d) Ni-46Al, and e) Ni-46Al-5Pt

From the surface micrographs, it was found that the scales grown on all compositions had the plate-like morphology characteristic of outward-growing θ - Al_2O_3 scales [128]. This was true even of the scales that had, based on the oxidation kinetics, transformed primarily to the α phase, e.g., Ni-36Al-5Cr. The circular patches of oxide that are thinner than the surrounding scale on the Ni-36Al-5Cr (Fig. 68 c.) were presumably areas that had transformed to the slower-growing α phase relatively early in the exposure, resulting in an overall thinner scale after 100 h.

All scales were thin and adherent. The differences in oxide thickness were difficult to quantify based on cross sectional SEM because the plate/whisker-like morphology of the scales made it difficult to define an oxide thickness. As an example, a cross sectional micrograph of the Ni-36Al after 100 h isothermal exposure at 900°C is shown in Fig. 69. The whisker morphology of the Al_2O_3 scale is clearly visible. In this case, a γ' layer $\sim 8\ \mu\text{m}$ thick formed beneath the scale as a result of Al depletion due to scaling.

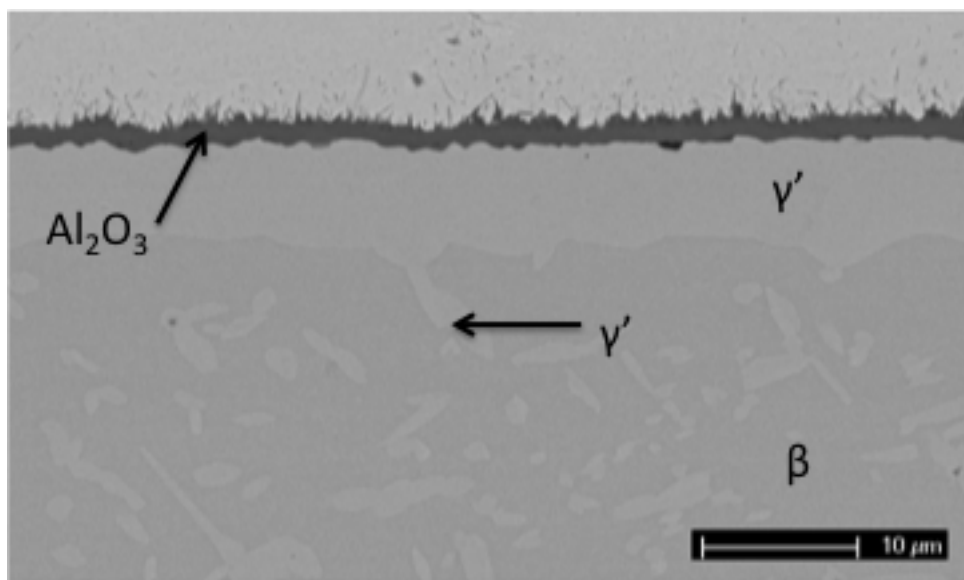


Figure 69. Cross sectional SEM micrograph of the Ni-36Al after 100 h isothermal oxidation at 900°C

7.2.1.2 PSLS Analysis In order to confirm the conclusions drawn from the oxidation kinetics, PSLS was performed on the scale surfaces after 50 and 100 h of exposure at 900°C in air. PSLS [129] is a technique which can be used to distinguish, among many other things, the θ from the α phase of Al_2O_3 . The fluorescence doublet, which arises due to Cr^{3+} impurities in the scale, for the θ phase is blue-shifted from that of α by approximately 10 nm, so the two can be easily distinguished. The luminescence spectra are shown in Fig. 70.

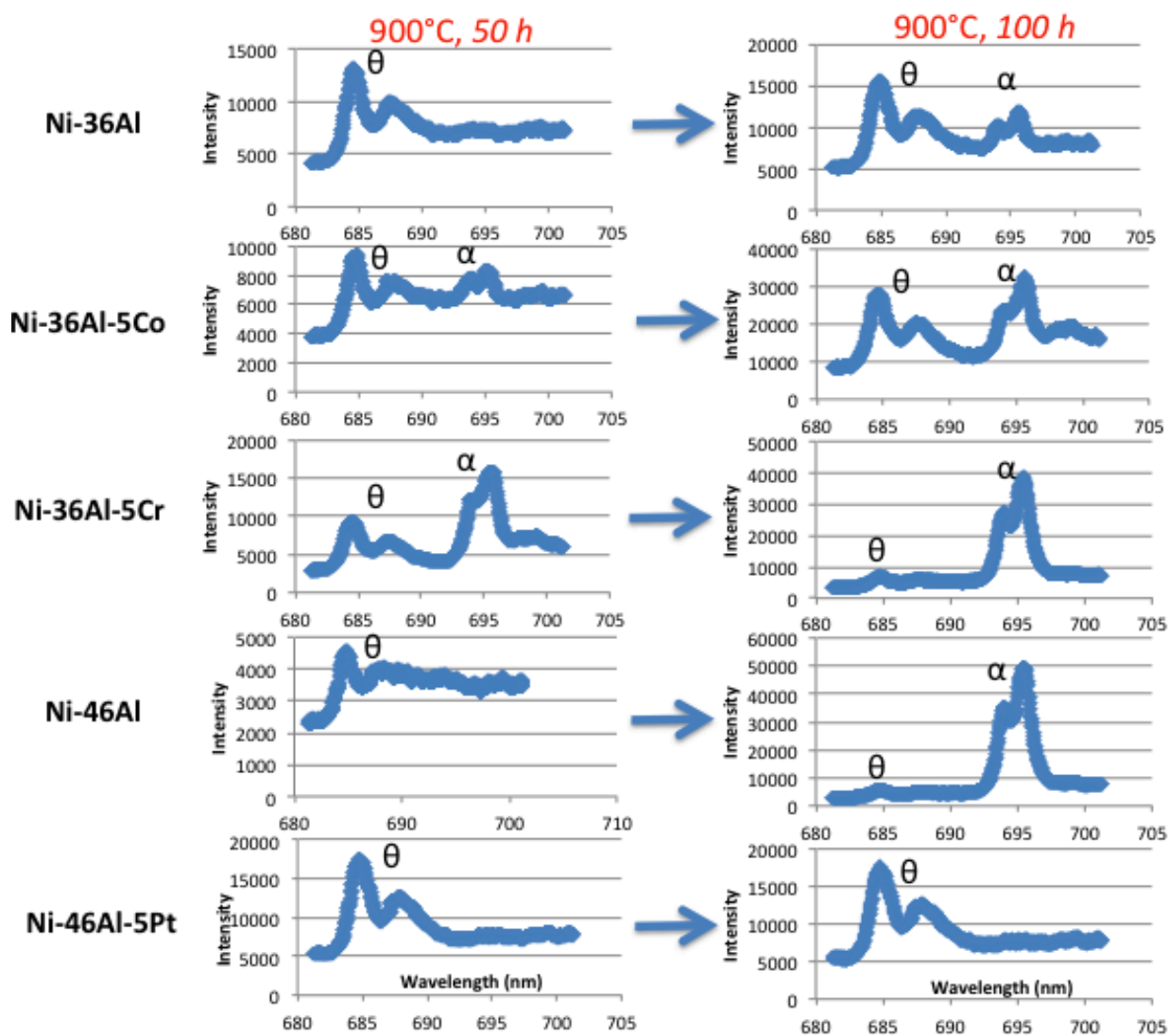


Figure 70. PSLS spectra from the scales formed during isothermal oxidation at 900°C for 50 and 100 h

The spectra in Fig. 70 confirm the conclusions drawn from the isothermal oxidation kinetics (Table 8). After 50 h oxidation of the Ni-36Al, primarily θ -Al₂O₃ was detected. After 100 h, a small amount of transformed α was found; however, the amount of transformed oxide was apparently not sufficient to significantly affect the growth kinetics. The addition of 5 at. % Co enhanced the rate of transformation. The scale grown on the Ni-36Al-5Co was partially α -Al₂O₃ after 50 h, in agreement with the 30% decrease in instantaneous k_p observed between 5 and 50 h of exposure. After 100 h, further transformation to α -Al₂O₃ was detected by PSLS, and correspondingly the k_p had decreased to approximately 37% of the 5 h value. PSLS showed that the scale formed on the Ni-36Al-5Cr was largely α -Al₂O₃ after 50 h, at which point the k_p had already decreased by an order of magnitude relative to the 5 h value. After 100 h, PSLS revealed a scale that was nearly 100% α -Al₂O₃, in accordance with the measured rate constant. After 50 h exposure, primarily θ -Al₂O₃ was detected on the Ni-46Al alloy; the high background signal at higher wavelengths is not entirely understood at this time. After 100 h, a scale of similar constitution to the Ni-36Al-5Cr, i.e., nearly 100% α -Al₂O₃, was detected. This is the only slightly surprising result, as the oxidation kinetics revealed that the k_p value for this specimen was still more than two orders of magnitude greater than the literature value for α -Al₂O₃ after 100 h [116], and just under two orders of magnitude greater than that measured for the Ni-36Al-5Cr. This perhaps indicates that while the scale had transformed to mostly α -Al₂O₃ after 100 h, the α had not yet formed a continuous layer, and thus the growth kinetics were still largely dictated by the rapid growth of θ -Al₂O₃. Finally, according to the PSLS analysis, the addition of 5 at. % Pt to the Ni-46Al resulted in the suppression of the transformation to α -Al₂O₃, which is consistent with the fairly constant k_p value measured for this composition from the oxidation kinetics. As this k_p is lower than the literature value for θ [116] and also lower than the initial k_p

for any of the other compositions in this study, it is concluded that Pt delays the transformation to α , but also decreases the growth rate for θ .

7.2.2 Environmental Effects on the $\theta \rightarrow \alpha$ -Al₂O₃ Transformation Kinetics

Surface SEM micrographs after 10 h of Type I hot corrosion exposure followed by ultrasonic cleaning in water are shown in Fig. 71.

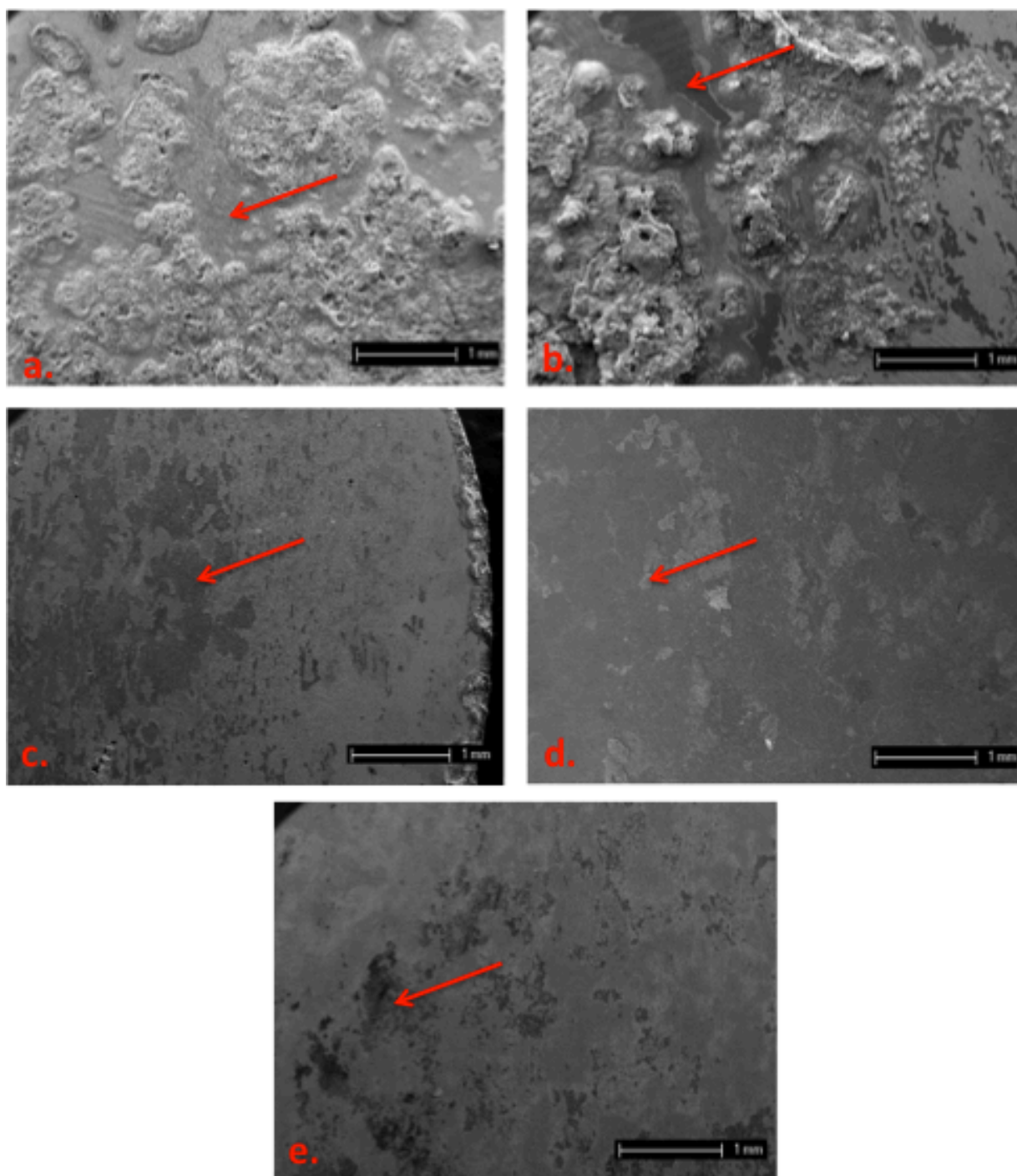


Figure 71. Surface SEM micrographs of the a) Ni-36Al, b) Ni-36Al-5Co, c) Ni-36Al-5Cr, d) Ni-46Al, and e) Ni-46Al-5Pt after 10 h of Type I hot corrosion exposure followed by ultrasonic cleaning in water. Select regions of adherent Al_2O_3 are identified with arrows.

The majority of the oxide had spalled as a result of the ultrasonic cleaning on the Ni-36Al-5Cr, Ni-46Al, and Ni-46Al-5Pt specimens. Isolated regions of Al_2O_3 remained adherent, as indicated by the red arrows in Fig. 71; these regions were most numerous on the Ni-36Al-5Cr. It is these regions of adherent oxide that were subsequently analyzed using PSLS. A large amount of the oxide remained adherent on the Ni-36Al and Ni-36Al-5Co; however, the majority of this oxide was NiO and NiAl_2O_4 , indicating that very rapid corrosion had already ensued after 10 h. In addition to these Ni-rich oxides, there were some areas in which adherent Al_2O_3 remained that were suitable for evaluation, also indicated by red arrows in Fig. 71.

The Al_2O_3 that remained adherent on each specimen was analyzed using PSLS. Approximately five equivalent locations were probed on each surface. The resulting spectra are shown in Fig. 72.

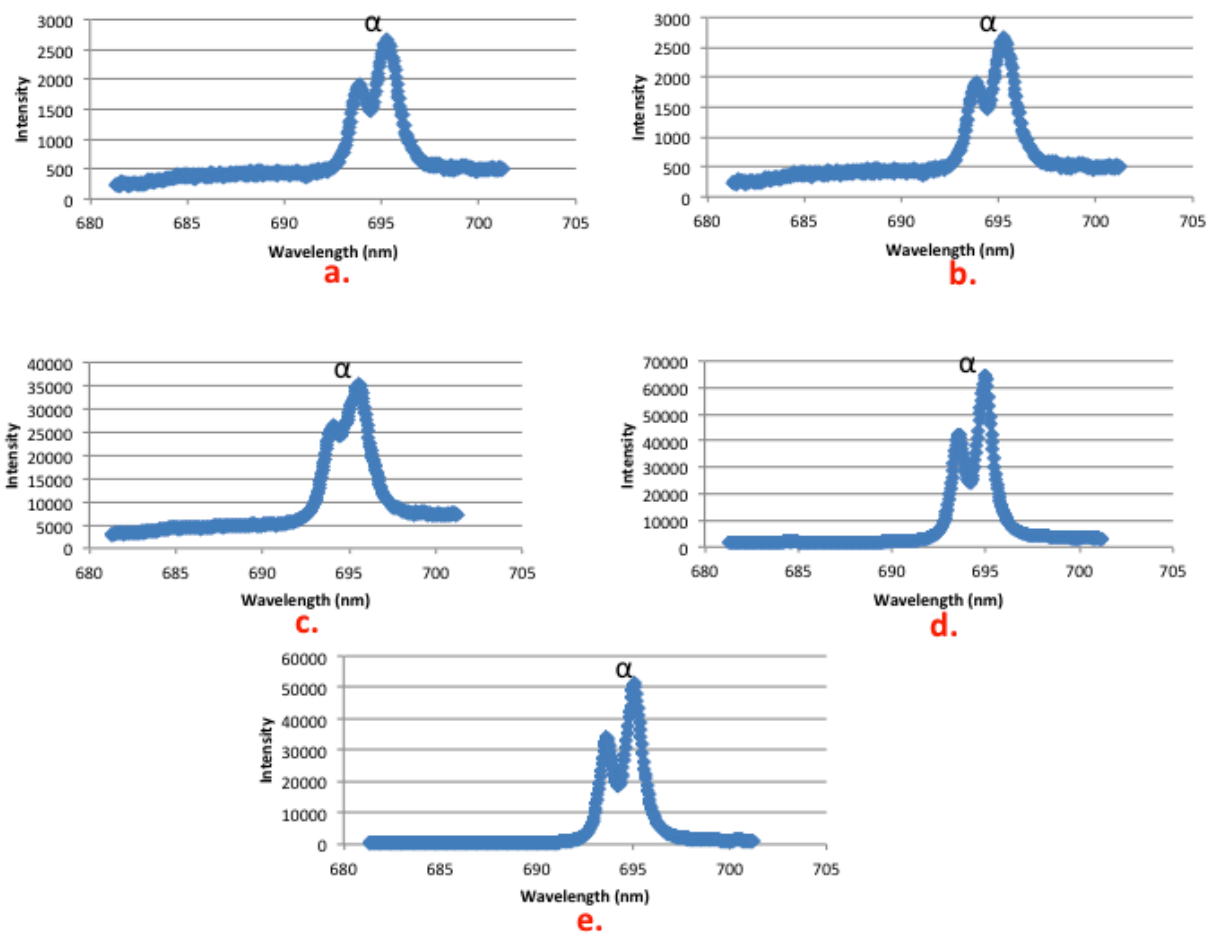


Figure 72. PLS spectra from the remaining adherent Al_2O_3 after a 10 h Type I hot corrosion exposure followed by ultrasonic cleaning in water for 10 h: a) Ni-36Al, b) Ni-36Al-5Co, c) Ni-36Al-5Cr, d) Ni-46Al, and e) Ni-46Al-5Pt

Only α - Al_2O_3 was detected on all specimens. This result clearly shows that the presence of an Na_2SO_4 deposit accelerates the transformation from θ to α . For example, after 100 h of 900°C oxidation with no salt deposit, only θ - Al_2O_3 was detected on the Ni-46Al-5Pt specimen. However, after only 10 h of oxidation in the presence of a Na_2SO_4 deposit, this alloy had formed a significant amount of the α phase.

There are a number of potential causes for this effect, e.g., the presence of Na, the presence of S, the salt acting as a preferential nucleation site for α , etc. The simplest of these to isolate and test is the presence of S. In order to do this, the Ni-46Al-5Pt was oxidized at 900°C for 100 h in a gaseous atmosphere of Pt-catalyzed $\text{O}_2 + 1000 \text{ ppm SO}_2$ (equilibrium $p_{\text{SO}_3} = 1.5 \times 10^{-4} \text{ atm}$) with no salt deposit. A surface SEM image of the specimen after this exposure is shown in Fig. 73.

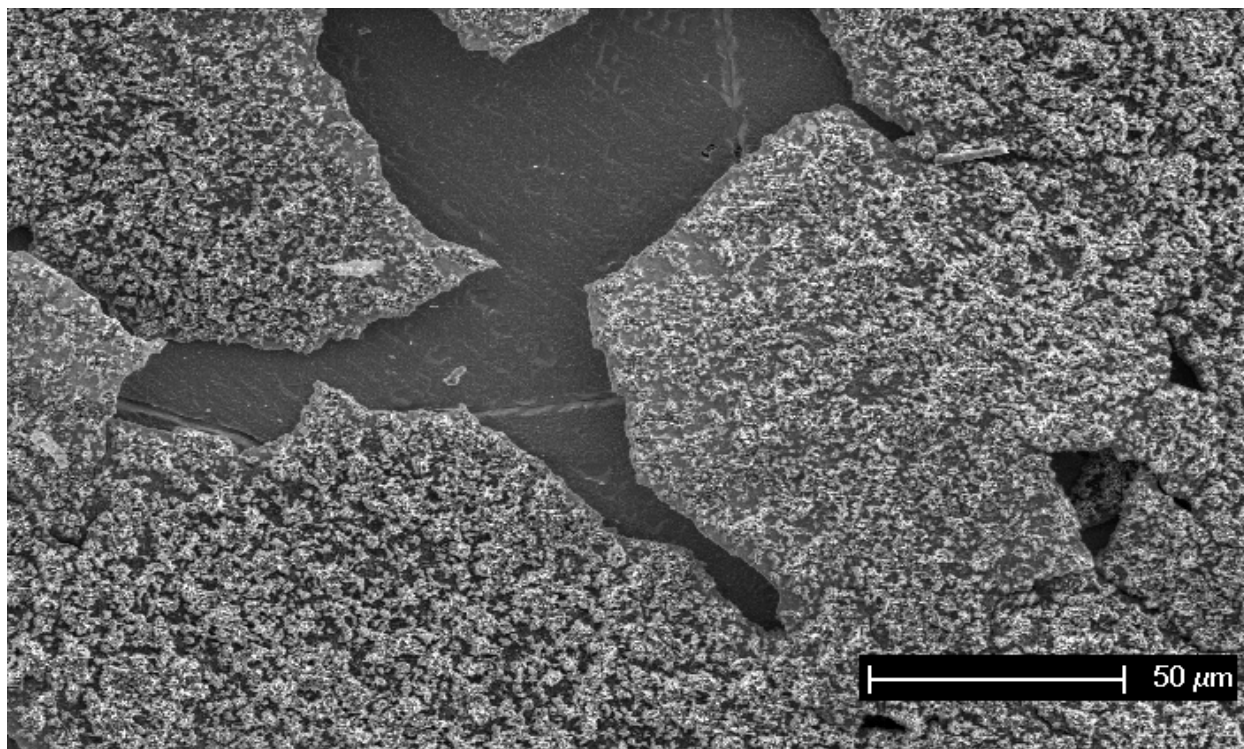


Figure 73. Surface SEM micrograph of the Ni-46Al-5Pt after a 100 h isothermal oxidation exposure in $O_2 + 1000 \text{ ppm } SO_2$

The oxide adherence decreased as a result of the presence of SO_2 , as can be seen by the large amount of scale cracking and spallation which occurred during cooling to room temperature. In spite of this spallation, a sufficient amount of oxide remained at least loosely adherent so that PSLS could be performed. The resulting spectrum is shown in Fig. 74.

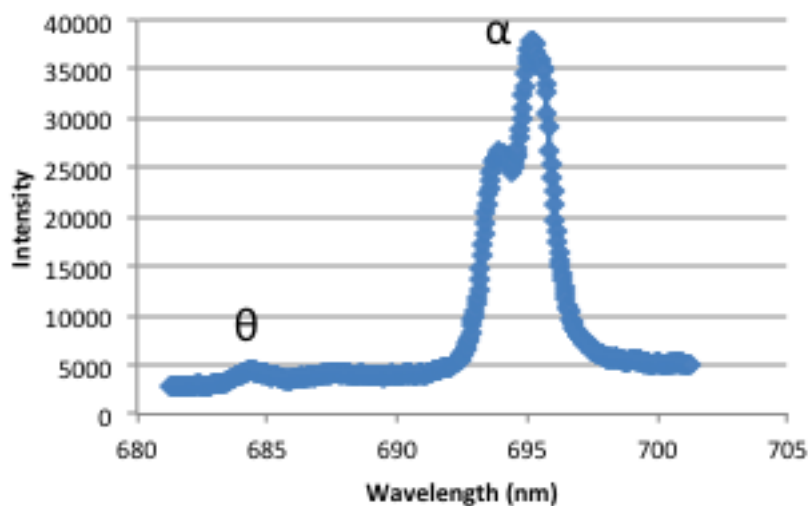


Figure 74. PLS spectrum from the oxide formed on the Ni-46Al-5Pt after 100 h isothermal oxidation at 900°C in $O_2 + 1000 \text{ ppm } SO_2$

The scale was nearly 100% α - Al_2O_3 after this exposure. This is in sharp contrast to the result for the Ni-46Al-5Pt in Fig. 70, which showed that the scale formed after 100 h oxidation at 900°C in air was 100% θ - Al_2O_3 . It is clear that the presence of S, whether in a salt deposit or in the gaseous atmosphere, accelerates the rate of transformation from θ to α - Al_2O_3 .

7.3 DISCUSSION

7.3.1 Compositional Effects on the $\theta \rightarrow \alpha$ Al_2O_3 Transformation Kinetics

Based on studies that have been conducted on bulk ceramics [130] and thermally grown scales [122], it has generally been concluded that larger cations, e.g., Zr^{4+} , Y^{3+} , and La^{3+} , decrease the rate of transformation from θ to α - Al_2O_3 , while smaller cations, e.g., Mg^{2+} and Ti^{4+} , increase the rate. A possible explanation for this comes from a simple strain energy argument. It has been found [118] that the transformation from θ to α - Al_2O_3 results in a volume decrease of $\sim 8\%$. Substitution of large cations into the θ lattice results in lattice expansion; the resulting strain energy acts to increase the barrier to nucleation of the denser α phase. The opposite argument can be made for smaller cations.

In the current study, it was found that the addition of Co or Cr, as well as an increase in the Al content, results in an increase in the rate of transformation to α - Al_2O_3 . The primary problem with the strain energy argument is that Co^{2+} , Co^{3+} , and Cr^{3+} ions are all larger than the Al^{3+} ion [131]. Thus, when these ions dissolve into θ - Al_2O_3 , the lattice resulting lattice expansion will hinder the transformation to α - Al_2O_3 . The inconsistency can be explained in the case of Cr based on the widely-accepted “template effect”, which was discussed briefly above [116]. A similar argument cannot, however, be made for Co, as the crystal structures of CoO and Co_3O_4 differ substantially from that of α - Al_2O_3 .

A basic schematic of the nucleation of α - Al_2O_3 from θ is shown in Fig. 75. Two scenarios are considered: one in which the α - Al_2O_3 nucleates at the scale/alloy interface, and one in which nucleation occurs at the free surface of the scale. Nucleation within the bulk of the scale has never been documented and seems to be highly unlikely; however, heterogeneous

nucleation at both the scale/alloy [132, 133] and scale/gas [120] interfaces has been observed using cross sectional TEM. The β systems studied were Y-doped in the former studies and Zr-doped in the latter, and so it is possible that the dopants affect not only the kinetics of the transformation but also the preferential nucleation site. Included in Fig. 75 are the relevant interfacial energies for each case, where the subscripts indicate the phases forming the interface and g stands for gas.

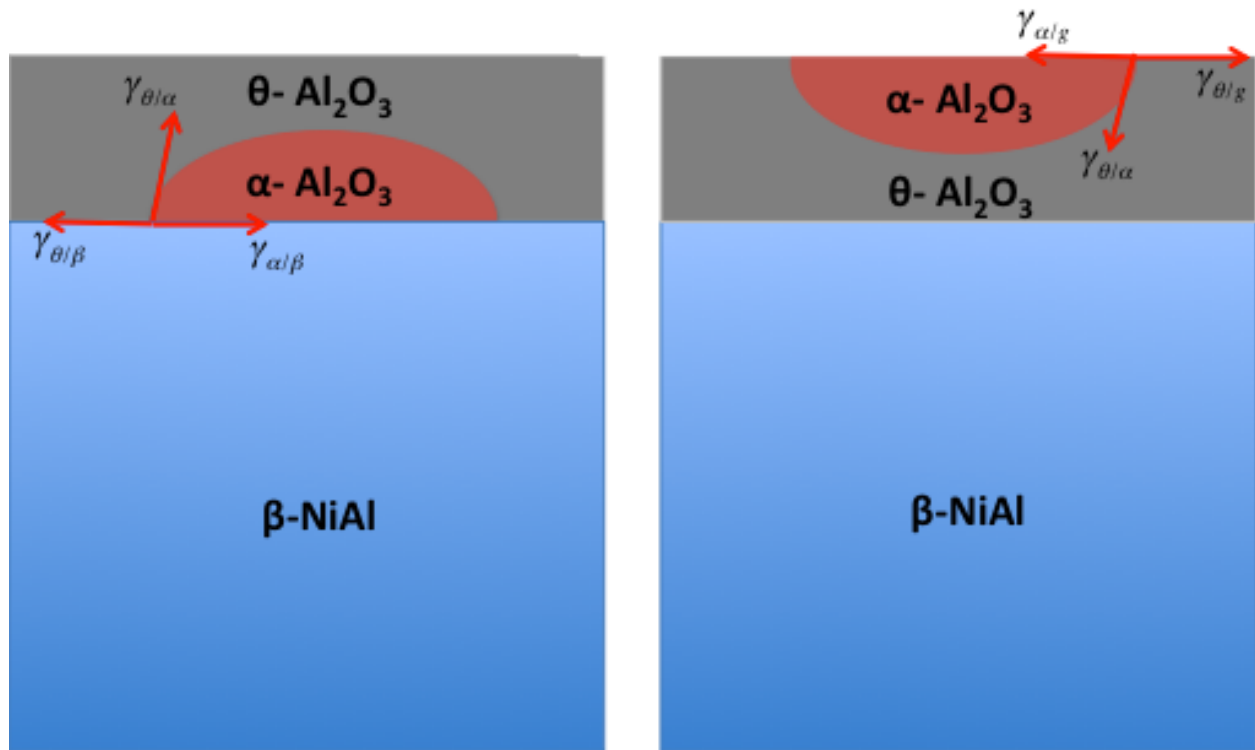


Figure 75. Schematic of the nucleation of α - Al_2O_3 from θ .

The free energy change due to nucleation can be expressed as:

$$\Delta G = -V(\Delta G_V - \Delta G_S) + A_{new}\gamma_{new} - A_{des}\gamma_{des} \quad (43)$$

where ΔG_V and ΔG_S are the volume free energy and strain energy, respectively, A is interfacial area, and γ is interfacial energy. Subscripts “new” and “des” are used to indicate that a term refers to interface which has been created and destroyed, respectively, as a result of nucleation of the new phase. In order to discuss the effects of various factors on the kinetics of the transformation from θ to α -Al₂O₃, one must identify the possible ways to influence the free energy barrier to nucleation, ΔG^* (the value obtained by taking the first derivative of Equation 43 with respect to r , the radius of the nucleus, and setting it equal to 0). A decrease in ΔG^* will result in an increase in the nucleation rate of α , and increasing ΔG^* will decrease the nucleation rate. For nucleation of α at the scale/alloy interface, ΔG^* can be decreased by decreasing $\gamma_{\theta/\alpha}$ or $\gamma_{\beta/\alpha}$, or by increasing $\gamma_{\beta/\theta}$. For nucleation of α at the scale/gas interface, ΔG^* can be decreased by decreasing $\gamma_{\theta/\alpha}$ or $\gamma_{\alpha/g}$, or by increasing $\gamma_{\theta/g}$. All of these factors could potentially be affected by alloying additions. Also, increasing the magnitude of ΔG_V , i.e., the thermodynamic stability of the α phase, or decreasing the magnitude of ΔG_S , will result in a decrease in ΔG^* and hence a faster nucleation rate.

Experimentally verifying mechanisms for the effects of alloying elements on the kinetics of the transformation from θ to α -Al₂O₃ is a highly involved undertaking that would require its own dedicated study. As the main purpose of the current work is to ascertain the factors that influence the hot corrosion process and how they do so, no attempt is made in what follows to prove a given mechanism. Rather, a number of scientifically viable mechanisms are discussed.

Two that have been published in the past will be very briefly mentioned; in addition, two novel explanations for the effects of Co and Pt will be proposed.

7.3.1.1 The Template Effect

As mentioned above, it has been proposed [116] that Cr accelerates the transformation to α by forming transient Cr_2O_3 , which is isostructural with α - Al_2O_3 , and hence acting as a heterogeneous nucleation site. Before the transformation occurs, it would be expected that the Cr_2O_3 would be present at the θ /gas interface, as Cr_2O_3 cannot be thermodynamically stable at an Al_2O_3 /alloy interface. A schematic of this situation is shown in Fig. 76, which shows α - Al_2O_3 nucleating at the Cr_2O_3 / θ - Al_2O_3 interface.

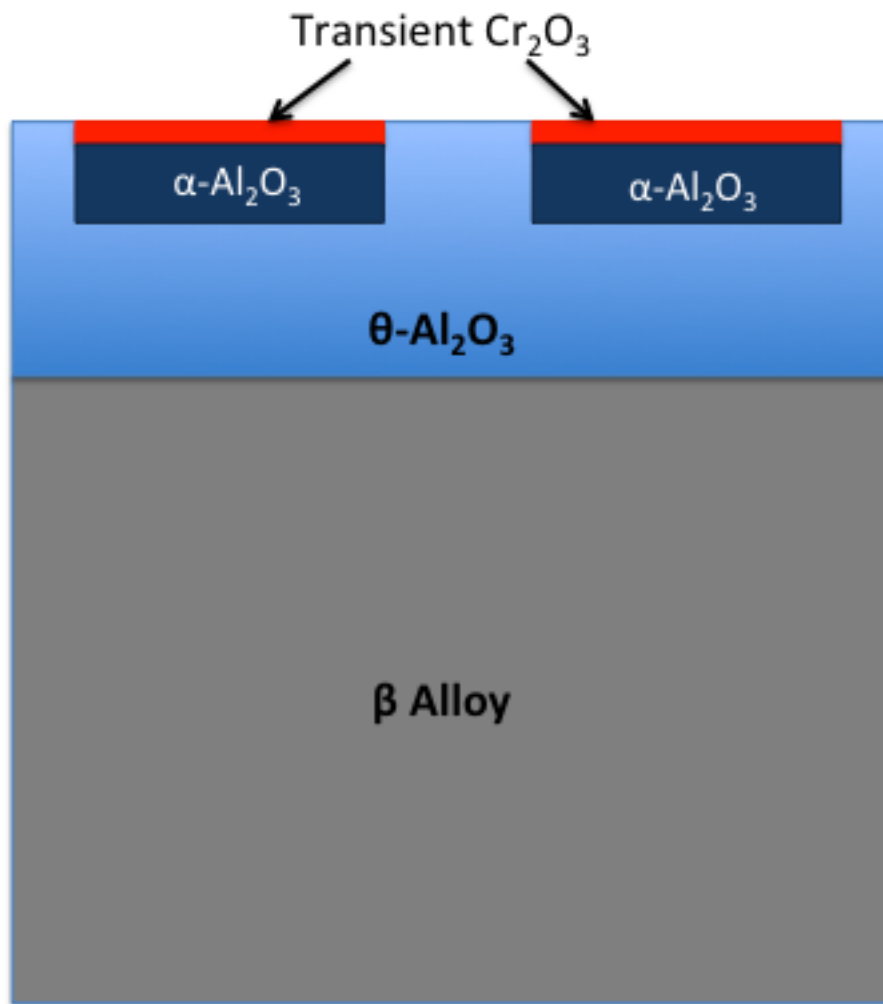
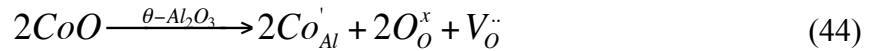


Figure 76. Schematic representation of the heterogeneous nucleation of α -Al₂O₃ on transient Cr₂O₃

In order for the nucleation of α at the $\theta/\text{Cr}_2\text{O}_3$ interface to be thermodynamically favorable over nucleation at the θ/gas boundary, $\gamma_{\alpha/g}$ must be greater than $\gamma_{\alpha/\text{Cr}_2\text{O}_3}$. Since Cr_2O_3 and $\alpha\text{-Al}_2\text{O}_3$ are isostructural, this is almost certainly the case. In addition, the coherency strain and resulting strain energy (ΔG_s) generated by the formation of the $\alpha/\text{Cr}_2\text{O}_3$ interface must not be large enough to outweigh the energy benefit afforded by the decrease in interfacial energy. This latter point has not been explicitly shown.

7.3.1.2 Ionic Size Effects It has already been discussed that large cations, such as Zr^{4+} , Y^{3+} , and La^{3+} , decrease the rate of transformation from θ to $\alpha\text{-Al}_2\text{O}_3$, while smaller cations, such as Mg^{2+} and Ti^{4+} , accelerate the transformation [122, 130]. This has been explained in the past based on a strain energy argument. The larger the volume misfit between the θ and α , the larger the strain energy, ΔG_s , associated with the transformation (ΔG_s increases with the square of the volume misfit [134]). Substitution of large cations into the θ lattice effectively increases the misfit and hence ΔG_s ; small substitutional cations have the opposite effect. This is very likely a viable mechanism for some of the larger ions; however, as mentioned above, the ionic size argument begins to break down when one considers the ions Mg^{2+} , Ti^{4+} , and (from the current study) Co^{2+} , which are found to accelerate the transformation. These cations, although categorized above as “small”, are actually larger than the Al^{3+} ion [131]. Hence, they cannot possibly provide the decrease in volume misfit required for the ionic size argument to be adequate. Clearly, alternative mechanisms are required in some cases.

7.3.1.3 The Influence of Co and the Importance of Defect Structure It is proposed that defect structure, and how it is influenced by foreign cations, should be considered when determining the effects of various alloying elements on the $\theta \rightarrow \alpha$ transformation kinetics. Assuming that the Co enters the θ - Al_2O_3 lattice substitutionally as Co^{2+} , the following is a possible defect reaction (using Kröger-Vink notation):

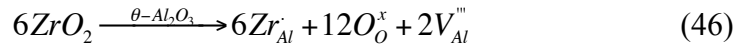
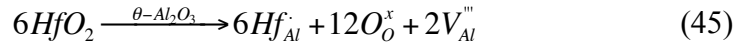


Substitution of the lower-valence Co^{2+} necessarily results in the formation of oxygen ion vacancies. The lattice contraction that results from these vacancies decreases the barrier to nucleation of α - Al_2O_3 by decreasing the magnitude of the $V\Delta G_s$ term in Equation (43), hence enhancing the transformation rate. It may be argued that the lattice expansion resulting from the substitution of the slightly larger Co^{2+} ion on Al^{3+} sites should counteract this effect; however, as the difference in ionic radius between these two species is relatively small ($\sim 36\%$, compared to 38% for Hf^{4+} , 42% for Zr^{4+} , 60% for Y^{3+} , and 73% for La^{3+} , the latter four of which have been shown to slow the transformation [122]), and the oxide ion vacancies are rather large (the ionic radius of O^{2-} is greater than that of Al^{3+} by a factor of 2.3 [131]) the contraction generated by the oxygen vacancies should be the dominant factor, and the transformation rate is enhanced.

It is important to note that, as Al_2O_3 is significantly more stable than CoO , the p_{O_2} at the Al_2O_3 /alloy interface cannot be high enough to oxidize Co. Thus, the incorporation of Co into the Al_2O_3 scale must occur either via the transient oxidation of Co to CoO and subsequent dissolution of the CoO into the θ - Al_2O_3 , or due to the development of non-equilibrium conditions at the Al_2O_3 /alloy interface, e.g., cracking of the scale, with the subsequent ingress of

O₂ providing a sufficiently high p_{O_2} to oxidize Co to Co²⁺. The solubility of CoO in α -Al₂O₃ is negligible at 900°C [135]; however, it is expected that the solubility in the more open-structured θ phase is greater.

It is appropriate, in light of the preceding explanation of the effect of Co, to comment on the results of Pint et. al. [122], who found that the rate of transformation to α -Al₂O₃ is slowed when thermally grown scales are doped by Hf⁴⁺, Zr⁴⁺, Y³⁺, and La³⁺ via oxide dispersions within a β -NiAl alloy. In the case of Hf⁴⁺ and Zr⁴⁺, the substitutional incorporation of these species into the θ -Al₂O₃ lattice would be expected to result in the formation of Al³⁺ vacancies:



As in the case of the O²⁻ vacancies in Equation (44), the Al³⁺ vacancies in (45) and (46) would create a contraction in the lattice which may be expected to result in an enhanced rate of transformation to the denser α -Al₂O₃. However, when comparing the effects of these elements to that of Co²⁺ (defect reaction (44)), fundamental differences arise. Firstly, as noted above, Hf⁴⁺ and Zr⁴⁺ are significantly larger than Co²⁺. In addition, the radius of the Al³⁺ ion, and hence the magnitude of the strain generated by its vacancy, is significantly smaller than that of the O²⁻ vacancy in reaction (44). Finally, for every mole of HfO₂ dissolved in the θ lattice, 1 mole of substitutional cations is generated, while only 1/3 of a mole of Al vacancies are created. Therefore, in the cases of Hf⁴⁺ and Zr⁴⁺, the dominant factor is the lattice expansion that arises

due to the larger ionic radius of these ions relative to Al^{3+} , and hence these ions retard the transformation from θ to α - Al_2O_3 .

Y^{3+} and La^{3+} have the same valence as Al^{3+} , and hence no vacancies are generated upon their incorporation into the θ - Al_2O_3 lattice. Therefore, the cationic radii are the main factors to consider. As noted above, Y^{3+} and La^{3+} are substantially larger than Al^{3+} . As such, substitutional Y^{3+} and La^{3+} ions generate significant lattice expansion, retarding the transformation to α - Al_2O_3 .

An additional factor to consider is that, as shown by Stiger et. al. [136] in the case of Zr^{4+} , large cations generally have a much greater solubility in θ than in α . Thus, upon transformation to α , these ions must be rejected from the lattice, which is inferred to further slow the transformation.

7.3.1.4 Influence of Pt: Preventing Sulfur Segregation

Pt does not form a stable

oxide under the current exposure conditions, and hence its incorporation into the Al_2O_3 scale is unlikely. Thus, whatever the mechanism by which Pt delays the $\theta \rightarrow \alpha$ transformation, it must be acting from within the alloy.

A detailed chemical analysis of the S content of the alloys used in the current study was not carried out. However, it is well known that a significant amount of impurity S is generally present and strongly segregates to the α - Al_2O_3 /Ni-rich β -NiAl interface, both at intact regions and at interfacial voids [137]. Further, it has been shown that Pt in the alloy prevents this interfacial S segregation [138]. It is unclear why this occurs, however it has been proposed that there is a competitive segregation process between Pt and S. In section 7.2.2, it was shown that S enhances the kinetics of the transformation from θ to α - Al_2O_3 . It is therefore proposed that the primary mechanism by which Pt slows the transformation to α is by preventing the segregation

of indigenous S in the alloy to the scale/alloy interface. This is reasonable considering that Pt slows the transformation when oxidation is conducted in air with no salt deposit, with the only source of S being that in the alloy (likely on the order of tens of ppm), but not when a significant source of S is continuously supplied to the external surface of the scale via an Na_2SO_4 deposit or SO_2 -containing gas.

In the work of Cadoret et. al. [139], it was observed that the presence of Pt in low-S cast β -NiAl alloys enhanced the growth rate of the transient θ - Al_2O_3 and lengthened the transition time from θ -controlled to α -controlled kinetics. The effect was diminished in alloys with higher S content. In the current study, the presence of Pt did not increase the growth rate of the θ - Al_2O_3 . In fact, the growth rate of the transient oxide was found to be *decreased* in the Ni-46Al-5Pt relative to the Ni-46Al after 5 h of oxidation at 900°C (Table 8). However, Pt was found to slow the transformation to α , and S was found to counteract this effect and increase the rate of transformation. Thus, the S segregation mechanism is consistent with both sets of experiments: Pt can effectively mitigate the effect of a small amount of S (the low-S alloy in [139], and the Ni-46Al-5Pt oxidized in air with no salt deposit in the current study) hence decreasing the transformation kinetics, but in the presence of relatively large quantities of S (the high-S alloy in [139], and the Ni-46Al-5Pt oxidized either in the O_2/SO_2 gas or with a Na_2SO_4 deposit in the current study), the S effect dominates and the kinetics of the transformation are accelerated.

7.3.2 The Influence of S on the $\theta \rightarrow \alpha$ Al_2O_3 Transformation Kinetics

Sulfur clearly accelerates the transformation to the stable α - Al_2O_3 . Similar to what was done in Section 7.3.1, in this section one likely explanation for this effect will be discussed, although no

attempt will be made to verify this mechanism experimentally, as this would be beyond the scope of the current work.

Impurity S is known to segregate to the α -Al₂O₃/alloy interface during oxidation of sub-stoichiometric β -NiAl alloys [103]. In order for there to be a thermodynamic driving force for this segregation to occur, S must lower the β/α interfacial energy, $\gamma_{\beta/\alpha}$ (see Fig. 75). From the discussion presented in Section 7.3.1, it is clear that this decrease in interfacial energy will decrease ΔG^* , and hence increase the nucleation rate of α . In order for this mechanism to be active, the transformation to α -Al₂O₃ must occur at the scale/alloy interface.

7.3.3 Influence of the $\theta \rightarrow \alpha$ Al₂O₃ transformation on Type I hot corrosion resistance

It has been shown that alloy composition has a profound effect on the kinetics of the $\theta \rightarrow \alpha$ Al₂O₃ transformation in scales grown on β -NiAl alloys. It is of interest to determine whether or not the kinetics of this transformation have any influence on hot corrosion resistance. It seems reasonable to postulate that there may be some correlation. Firstly, it has been shown in Chapters 5 and 6 that the ability of an alloy to reform an Al₂O₃ – rich scale when the scale sustains damage during exposure is important in determining its hot corrosion resistance. This scale healing capability is directly related to the subsurface alloy composition. One consequence of the presence of a θ -Al₂O₃ scale and its rapid growth rate (relative to α -Al₂O₃) is that a greater amount of Al depletion occurs, simply because more oxide is being formed in a given amount of time. Consequently, it could be argued that the scale healing capability of an alloy growing a θ scale should be less than that of an alloy forming an α scale.

In addition, it has been shown by Smialek and Rybicki [121] that during 1000°C oxidation of a Zr-modified NiAl alloy, the transformation from θ to α resulted in extensive

cracking of the scale, due to the $\sim 8\%$ volume decrease. An example, taken from ref. [121], is shown in Fig. 77.

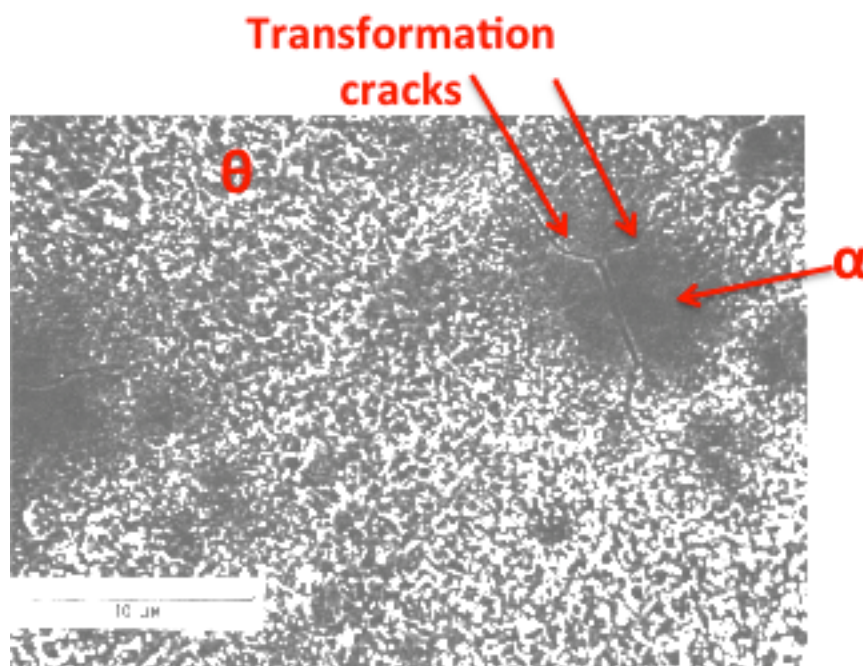


Figure 77. Surface SEM micrograph of an Al₂O₃ scale grown on a Zr-modified NiAl alloy, showing tensile cracks that form as a result of the volume decrease that occurs upon transformation from θ to α (from ref. [121])

During hot corrosion exposure, the presence of these transformation cracks would be expected to be quite detrimental, as they would presumably allow for the penetration of the molten salt to the scale/alloy interface.

Thus, if the $\theta \rightarrow \alpha$ transformation is indeed an important factor to consider when evaluating Type I hot corrosion resistance, it is expected that one of the following three scenarios will arise:

1. Elements that promote the rapid transformation to α are beneficial due to the decrease in subsurface Al depletion, and subsequent enhanced scale healing capability, when the slower-growing α phase is present,
2. Elements that delay the transformation to α are beneficial due to suppression of transformation cracks in the scale, or
3. Sulfur, from the Na_2SO_4 deposit, will enhance the rate of transformation in the scales grown on all alloy compositions, hence overriding the influence of alloy composition on the transformation kinetics.

As shown in Section 5.2, additions of Pt, Cr, and Co to Ni-36Al are all beneficial during Type I hot corrosion exposure. According to Fig. 70, these three elements can be classified into two categories, i.e., those that accelerate the $\theta \rightarrow \alpha$ transformation (Co, Cr), and those that retard it (Pt). Since the elements belonging to both of these categories improve Type I hot corrosion resistance, one of two conclusions must be made: either the $\theta \rightarrow \alpha$ transformation is not an extremely important factor to consider when evaluating the hot corrosion behavior of β -NiAl – base alloys, or scenario 3 above is correct, i.e., although the transformation kinetics may indeed be influential during Type I hot corrosion, S causes the rapid transformation to α regardless of alloy composition.

If the former conclusion is correct, it is of interest to determine why the kinetics of the transformation does not seem to have a first order effect. In scenario 1 above, Co and Cr would be expected to be beneficial during hot corrosion, as observed; however, Pt would be expected to have a detrimental effect since it slows the transformation to α . The latter effect is not observed; hence, it must be that the beneficial effects of Pt in promoting the rapid establishment of an Al_2O_3 scale (be it θ or α) and improving scale adherence are outweighing the negative effects of

having the faster-growing θ phase present for an extended period of time. In other words, it may be more beneficial to rapidly establish a θ - Al_2O_3 scale that remains untransformed for a long period of time (as in the case of the Ni-46Al-5Pt) than to more slowly establish an Al_2O_3 scale that, once formed, transforms more quickly to α (as in the case of the Ni-36Al).

If, however, the second scenario proposed above were correct, then Pt would be expected to be beneficial during hot corrosion, as observed; however, Co and Cr would be expected to have a detrimental effect since they accelerate the transformation to α , which should cause numerous tensile cracks to occur within the Al_2O_3 scale early in the exposure. Cobalt and Cr are, however, found to be quite beneficial during Type I exposure. The reason becomes apparent upon observation of Fig. 78, which shows a surface SEM micrograph of the scale grown on the Ni-36Al-5Co specimen after 100 h oxidation at 900°C.

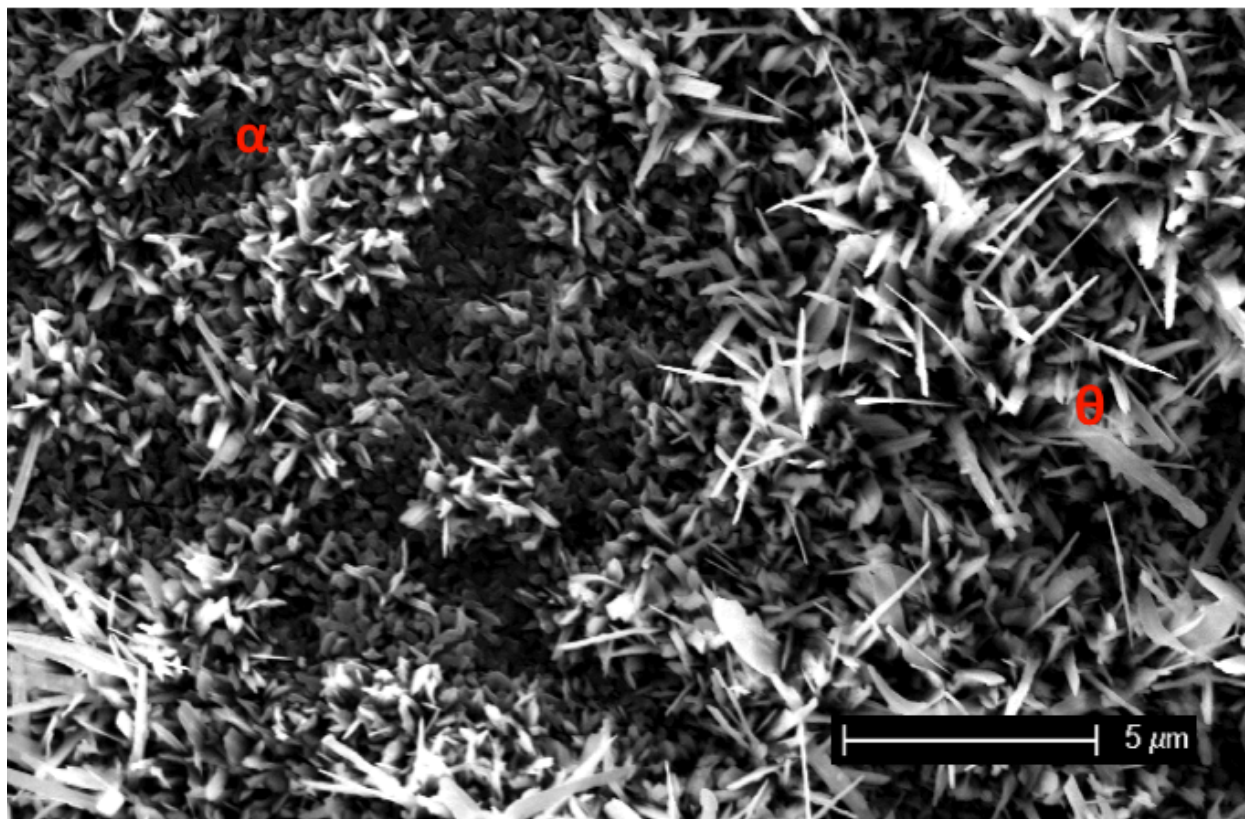


Figure 78. Surface SEM micrograph of the partially-transformed scale grown on the Ni-36Al-5Co specimen after 100 h oxidation at 900°C

In this micrograph, which shows a partially-transformed ($\theta + \alpha$) Al_2O_3 scale, it is clear that the transformation cracks found by Smialek and Rybicki [121] are not present. Since the volume contraction upon transformation to α does not, in the systems investigated in the current study, lead to tensile cracking, the transformation is innocuous from a Type I hot corrosion standpoint.

The primary difference between the experiments of Smialek and Rybicki [121] and those performed in the current study which explains why tensile cracks in the oxide are observed in the former and not in the latter seems to be alloy composition. Specifically, in the previous investigation, a Ni-47Al-0.05Zr (at. %) alloy was tested; this composition differs significantly from those used in the current study. The addition of Zr is of particular interest. It has been shown [140] that doping of Al_2O_3 with ZrO_2 results in a significant improvement in creep strength (the activation energies for creep of high-purity and ZrO_2 -doped Al_2O_3 were estimated to be ~ 430 and 650 kJ/mol, respectively). When a thermally grown scale is subjected to stress at high temperatures, it is possible to relieve this stress via creep deformation [141]. In this regard, higher creep strength can be detrimental, as it may preclude this stress relief mechanism from occurring. Thus, it is likely that the cracking observed by Smialek and Rybicki was indeed a result of the tensile strains introduced during transformation from θ to α - Al_2O_3 , but it is proposed that the strains introduced were sufficient to nucleate these cracks primarily due to the high creep strength of the Zr-doped oxide scales relative to the scales observed in this investigation. In the absence of any elements that are known to significantly improve the creep strength of Al_2O_3 , the scales formed on the alloys studied here were presumably able to relieve the transformation-induced tensile strains by creep deformation at temperature.

However, evidence in favor of the conclusion that the influence of the $\theta \rightarrow \alpha$ transformation kinetics should not be dismissed as inconsequential was presented in Fig. 71. After the 10 h Type I exposure followed by an ultrasonic water wash, only transformed α -Al₂O₃ remained adherent. All of the θ -Al₂O₃ that had presumably formed during the Type I exposure had been removed during the ultrasonic cleaning. Thus, it seems that in aggressive environments where the scales are exposed to high stresses, oxide adherence during hot corrosion exposure may indeed be affected by the transformation, with α -Al₂O₃ scales being more adherent than θ scales.

7.4 CONCLUSIONS

The kinetics of the transformation from the metastable θ to the thermodynamically stable α -Al₂O₃ during 900°C oxidation of Ni-36Al (at. %) base alloys was found to be highly dependent on alloy composition and exposure environment. Additions of 5% Co or Cr accelerated the transformation, with Cr being more effective. Conversely, alloying with 5% Pt slowed the transformation. The strong influence of Cr is likely a result of the template effect, whereby transient Cr₂O₃ acts as a heterogeneous nucleation site for α -Al₂O₃. Changes in the defect structure of the θ scale with Co addition have been used to explain its accelerating effect. This explanation requires either that transient CoO forms early in the exposure and is incorporated into the θ scale, or that CoO forms during exposure as a result of oxide cracking and subsequent ingress of O₂. Platinum addition likely slows the kinetics of the transformation by preventing impurity S from segregating to the scale/alloy interface and subsequently being

incorporated into the scale. Sulfur was shown to enhance the transformation rate when present in a Na_2SO_4 surface deposit or in the gas phase. Sulfur is known to segregate to the β/α interface, hence it is inferred to lower $\gamma_{\beta/\alpha}$. This decrease in interfacial free energy decreases the barrier to α nucleation and hence enhances the transformation rate.

There is no clear correlation between the influence of alloy composition on the $\theta \rightarrow \alpha$ transformation kinetics and Type I hot corrosion resistance during pseudo-isothermal exposures. The first potential explanation for this is that the influence of alloy composition on the transformation kinetics is truly irrelevant to Type I hot corrosion resistance. In this case, retarding the transformation to α by Pt addition is not detrimental because the positive effects of Pt on Al_2O_3 establishment and adhesion dominate. Accelerating the transformation by adding Co or Cr is also not detrimental, largely because the transformation cracks that have been reported in other systems do not form on the alloys in the current study upon transformation to α . The second potential explanation for the lack of a correlation between the influence of composition on the $\theta \rightarrow \alpha$ transformation kinetics and Type I hot corrosion resistance is that S, present in the Na_2SO_4 deposit, accelerates the transformation in the scales formed on all alloys, regardless of alloy composition. This could in effect supersede the influence of alloy composition on the transformation kinetics.

If during Type I hot corrosion exposure the scale is perturbed in some way, the kinetics of the transformation may indeed be quite significant. This is indicated by the fact that after a 10 h Type I hot corrosion exposure followed by an ultrasonic wash in water, only $\alpha\text{-Al}_2\text{O}_3$ remains adherent. Thus, the α phase is more adherent than the θ phase during Type I hot corrosion exposure.

8.0 CONCLUDING REMARKS

Many factors have been shown to have a profound influence on hot corrosion resistance, and all of these factors must be considered when designing coatings for applications in which hot corrosion is a concern. Bulk-alloy composition is obviously important; however, for a given bulk composition, hot corrosion resistance can vary drastically as a function of microstructure and phase composition, which can be changed by controlling processing parameters. In the case of MCrAlY alloys, microstructural refinement is generally beneficial for Type II hot corrosion resistance, but it has been shown that phase composition and distribution can be the overriding factors. Two examples of this were shown. For a given bulk Cr content, resistance to Type II attack was greatly decreased if a processing route was chosen which resulted in the precipitation of a large amount of α -Cr, and consequently a low Cr content in the surrounding matrix. In addition, the precipitation of coarse reactive-element-rich phases, which are incorporated as inclusions in the Al_2O_3 scale, can serve as initiation sites for Type II attack. The latter observation serves to stress the importance of not only reactive element content, but also distribution. Closely controlling the concentration of reactive element and its distribution can present difficult processing challenges which are inferred to be worthwhile addressing in order to optimize hot corrosion performance of MCrAlY coatings.

The compositions of β -NiAl diffusion coatings are dynamic, as they change dramatically during deposition and service. Although work has been done in the past to describe the effect of

composition on the oxidation and hot corrosion behavior of these systems, much of the focus has been placed on the influence of Pt. Furthermore, the majority of the mechanistic work that has been done in the field of hot corrosion has focused on the *propagation stage*, during which rapid degradation occurs. In this study, it has been shown that, in addition to Pt, elements such as Co and Cr, which are present in these coatings in relatively small amounts due to coating/substrate interdiffusion, have marked effects on the duration of the protective *incubation stage* during both Type I and Type II hot corrosion. Experiments were aimed at determining the mechanisms by which these elements affect, either positively or negatively, the duration of the incubation stage.

Investigation on the influence of Pt, Co, and Cr lead to the conclusion that the beneficial effects of these elements during Type I (900°C) hot corrosion exposure can be linked to an enhanced ability of the alloys to rapidly form an Al_2O_3 – rich scale and to heal this scale if it sustains damage. The mechanistic details of this enhanced scale forming and healing capability have been discussed, particularly in the case of Co. Although not entirely clear, results indicate that Co addition likely decreases the oxygen permeability in these alloys, which results in a decrease in the transient oxidation stage, i.e., promotes the rapid establishment of a protective Al_2O_3 scale. In addition, Co decreases the chemical activity of Ni while increasing that of Al, and hence reduces the tendency to form Ni_3S_2 , a product which is liquid at 900°C, and, as a consequence, generally leads to rapid attack if it is formed. Platinum and Cr have also been shown to greatly improve the rate of Al_2O_3 scale establishment and healing, and the validity of some traditional explanations for this has been discussed.

Under Type II (700°C) hot corrosion conditions, the beneficial effects of Pt and Cr on the duration of the incubation stage can, once again, be linked to an enhanced ability to rapidly form a protective Al_2O_3 -rich scale. This was shown by performing XPS and TOF-SIMS analyses to

probe the compositions of the scales formed on Ni-36Al base alloys containing Pt and Cr after 700°C oxidation in a gaseous atmosphere of O₂ + 1000 ppm SO₂. Cobalt, however, is found to be detrimental under these conditions. This can be partially linked to the rapid formation of transient Co-rich oxides on, e.g., the Ni-36Al-5Pt-5Co specimen during oxidation at 700°C in O₂ + 1000 ppm SO₂. This demonstrates yet another complexity that must be faced when designing coatings for hot corrosion resistance: certain elements may have different, even contrary effects in different temperature regimes.

In addition, two elements, which have beneficial effects when added separately, may be highly detrimental when present in the same alloy. The Ni-36Al-5Pt-5Cr alloy exposed to Type II hot corrosion conditions provides a clear example of this. While the composition of the scale formed on this alloy during 700°C oxidation strongly indicates that it should be protective, phase changes that occur in the subsurface, specifically the precipitation of a Pt-rich solid solution phase, inhibit the continued formation of a protective scale. A similar phenomenon may indeed occur in the Ni-36Al-5Pt-5Co. Thus, phase equilibria, including phase changes that may occur in the subsurface of an alloy or coating as a result of depletion and/or enrichment of various elements during exposure, must be considered. These phase changes can have a profound effect on the ability of an alloy to form and maintain a protective Al₂O₃ scale.

Finally, the influence of phase changes that occur in the scale itself, specifically the $\theta \rightarrow \alpha$ -Al₂O₃ transformation, was investigated in detail. The kinetics of this transformation can be greatly affected by relatively small alloying additions of Co, Cr, Pt, and Al, and also by changes in the exposure environment, e.g., the presence of S in the gas or surface deposit. Under pseudo-isothermal Type I hot corrosion conditions, where thermal cycles are relatively long and no external stress is applied, no correlation was found between the influence of composition on the

kinetics of the transformation and hot corrosion resistance. It seems as though either the kinetics of the $\theta \rightarrow \alpha$ -Al₂O₃ transformation are truly unimportant, or the presence of S enhances the rate of transformation in the scales grown on all alloys, obscuring the influence of alloy composition.

For specimens washed ultrasonically in water after a brief Type I hot corrosion exposure, only transformed α -Al₂O₃ remained adherent. Thus, if an external stress is applied to the scale (as is often the case in actual applications), the kinetics of the transformation to α may rather important. Scales that transform quickly to the thermodynamically stable α phase will provide superior protection. This is an important point, and presents an interesting opportunity for future research. A significant amount of work has been done, in this study and many others, on various aspects of the $\theta \rightarrow \alpha$ -Al₂O₃ transformation, e.g., the kinetics and mechanism of the transformation in bulk oxides and in thermally grown scales. However, the significance of this transformation in the context of high temperature corrosion has not been extensively discussed, with a few exceptions, including the effect of the transformation rate in scales grown on thin-walled FeCrAl components [125] and in TBC systems [136]. According to the current study, the kinetics of the transformation may, under certain conditions, play an important role during deposit-induced attack; there are very likely other instances that have yet to be explored in which this is also the case.

APPENDIX A

THE INFLUENCE OF Co ON THE FORMATION OF Ni₃S₂: A MODIFIED INTERACTION PARAMETER ANALYSIS

In what follows, thermodynamic measurements that have been made in the Ni-Al-Pt and Ni-Al-Co systems are used to quantify the effect of Co on the tendency to form Ni₃S₂ in the subsurface of the Ni-36Al-5Pt-5Co alloy during Type I hot corrosion exposure. Each set of measurements was made using γ' -Ni₃Al base alloys, which is appropriate as this is the matrix phase in the subsurfaces of the systems studied. The matrix compositions used for the Ni-36Al-5Pt and Ni-36Al-5Pt-5Co alloys are Ni-24Al-5Pt and Ni-24Al-5Pt-5Co, respectively, which are the approximate compositions of the subsurface γ' regions, as measured by EDS. The following calculations were performed at 1200°C rather than 900°C (the Type I hot corrosion temperature) because the necessary data were not available at the latter temperature. This approach eliminated the need to extrapolate measured values to lower temperatures; the trends observed should be equally valid at the temperature of interest for Type I hot corrosion. The limitations and sources of error associated with this calculation are discussed in detail in section 5.3.1.

It is reasonable to approximate the sulfides to be pure and thus present at unit activity. The equilibrium constant for Reaction (42) is then given by:

$$K^{eq} = \frac{a_{Al}^2}{a_{Ni}^{9/2}} \quad (47)$$

At 1200°C, $K^{eq} = 9.3 \times 10^{-9}$. In order to determine whether or not the formation of Ni_3S_2 is

favorable relative to Al_2S_3 , the non-equilibrium activity ratio $\frac{a_{Al}^2}{a_{Ni}^2}$ (from here on referred to as

Q), must be calculated from measured activity values. If Q is greater than K^{eq} , Ni_3S_2 formation is not thermodynamically favorable; conversely, if Q is less than K^{eq} , Ni_3S_2 can form, and rapid corrosion would be expected.

Copland [108] performed activity measurements on Ni-24Al-XPt alloys (at. %). Using his values for the composition Ni-24Al-5Pt, a Q value of 4.24×10^{-8} was calculated. This is found to be greater than K^{eq} , however the difference is less than an order of magnitude. Thus, it is reasonable to infer that Ni_3S_2 can form in the sub-surface zone of the Ni-36Al-5Pt, particularly with continued Al depletion, which was in fact observed.

At this juncture, it is necessary to determine if the addition of Co can increase the Q value substantially such that Ni_3S_2 formation is unfavorable. Pelton and Bale [106] developed a modified version of the interaction parameter formalism initially developed by Wagner [109], suitably adjusted for use with non-dilute solutions. The first-order interaction parameter is defined as [109]:

$$\varepsilon_{ij} = \left(\frac{\partial \ln \gamma_i}{\partial x_j} \right)_{x_{solvent}=1} \quad (48)$$

where γ is the activity coefficient, X is the mole fraction of a given component, and subscripts i and j represent components in the alloy. Thus, the interaction parameter describes the influence of a given species on the thermodynamic activity of another species, or on itself if $i = j$. If these

parameters are known for a given alloy, then the activity coefficient of any species in the alloy is given as:

$$\ln\left(\frac{\gamma_i}{\gamma_i^o}\right) = \varepsilon_{i1}X_1 + \varepsilon_{i2}X_2 + \dots\varepsilon_{iN}X_N \quad (49)$$

for components $i=1$ through N , where γ_i^o denotes the Henry's Law constant for component i .

Note in Equation (48) that, in its original form, this formulation is only suitable at infinite dilution, i.e., when $X_{\text{solvent}} = 1$. Pelton and Bale showed that, by making a fairly simple change to Equation (49), the interaction parameter can be utilized at finite concentrations. The resulting formula is given in Equation (50) [106].

$$\ln\left(\frac{\gamma_i}{\gamma_i^o}\right) = \ln\gamma_{\text{solvent}} + \varepsilon_{i1}X_1 + \varepsilon_{i2}X_2 + \dots\varepsilon_{iN}X_N \quad (50)$$

where

$$\ln\gamma_{\text{solvent}} = -\frac{1}{2} \sum_{j=1}^N \sum_{k=1}^N \varepsilon_{jk} X_j X_k \quad (51)$$

Utilizing this work, the following values are necessary in order to determine the influence of Co on the activities of Al and Ni and hence on the sulfide formation: $\gamma_{Al}^o, \epsilon_{AlAl}, \epsilon_{AlCo}, \epsilon_{AlPt}, \epsilon_{CoCo}, \epsilon_{PtPt}$ and ϵ_{CoPt} .

$\epsilon_{AlAl}, \epsilon_{CoAl}, \epsilon_{AlPt}$, and ϵ_{CoCo} can be approximated as the slopes of the plots of $\ln \gamma_i$ vs. X_j .

An example for ϵ_{CoAl} is shown in Fig. 79; the activity coefficient data were taken from Albers et. al. [107].

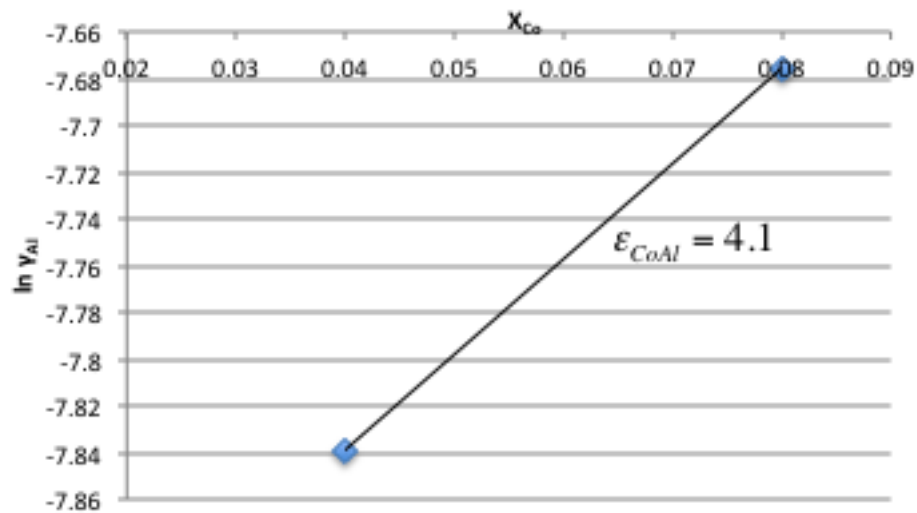


Figure 79. Plot of $\ln \gamma_{Al}$ vs. X_{Co} used to estimate ϵ_{CoAl}

The other three interaction parameters were obtained in a similar way, and the results are summarized in Table 9.

Table 9. Summary of the estimated interaction parameters ϵ_{AlAl} , ϵ_{CoAl} , ϵ_{AlPt} , and

ϵ_{CoCo}	
i-j	ϵ_{ij}
Co-Al	4.1
Al-Al	30.1
Al-Pt	-8.6
Co-Co	-3.9

ϵ_{PtPt} and ϵ_{CoPt} are also required, and yet no data is available in the literature to facilitate their direct graphical calculation. In order to approximate ϵ_{CoPt} , the Pandat© software package was used to generate a plot of $\ln \gamma_{Pt}$ vs. X_{Co} for $0.010 < X_{Co} < 0.027$. Pandat is a thermodynamic calculation software package based on the CALPHAD method (CALculation of PHase Diagrams). The slope of this plot resulted in an approximate ϵ_{CoPt} value of 7.5.

In order to calculate ϵ_{PtPt} , it is recognized that, as γ_{Al} and γ_{Ni} are known as a function of Pt content from the work of Copland [108], one can solve for γ_{Pt} as a function of X_{Pt} using the Gibbs-Duhem equation:

$$X_{Ni} d \ln \gamma_{Ni} + X_{Al} d \ln \gamma_{Al} + X_{Pt} d \ln \gamma_{Pt} = 0 \quad (52)$$

which can be rearranged to yield:

$$d \ln \gamma_{Pt} = -\frac{X_{Ni}}{X_{Pt}} d \ln \gamma_{Ni} - \frac{X_{Al}}{X_{Pt}} d \ln \gamma_{Al} \quad (53)$$

In order to calculate ε_{PtPt} , this equation must be integrated between two arbitrary values of X_{Pt} ,

here chosen to be 0.02 and 0.25, i.e.,

$$\int_{\ln \gamma_{Pt}|_{X_{Pt}=0.02}}^{\ln \gamma_{Pt}|_{X_{Pt}=0.25}} d \ln \gamma_{Pt} = - \int_{\ln \gamma_{Ni}|_{X_{Pt}=0.02}}^{\ln \gamma_{Ni}|_{X_{Pt}=0.25}} \frac{X_{Ni}}{X_{Pt}} d \ln \gamma_{Ni} - \int_{\ln \gamma_{Al}|_{X_{Pt}=0.02}}^{\ln \gamma_{Al}|_{X_{Pt}=0.25}} \frac{X_{Al}}{X_{Pt}} d \ln \gamma_{Al} \quad (54)$$

By numerically integrating plots of $\frac{X_{Ni}}{X_{Pt}}$ vs. $-\ln \gamma_{Ni}$ and $\frac{X_{Al}}{X_{Pt}}$ vs. $-\ln \gamma_{Al}$ between the integration

limits in the second and third terms of Equation (54), respectively, and summing the resulting

areas, one can solve for the value $\ln \gamma_{Pt}|_{X_{Pt}=0.25} - \ln \gamma_{Pt}|_{X_{Pt}=0.02}$; this value will henceforth be referred

to as Θ . These plots are shown in Fig. 80, in which the red lines indicate the areas defined by

the integrals on the right hand side of Equation (54).

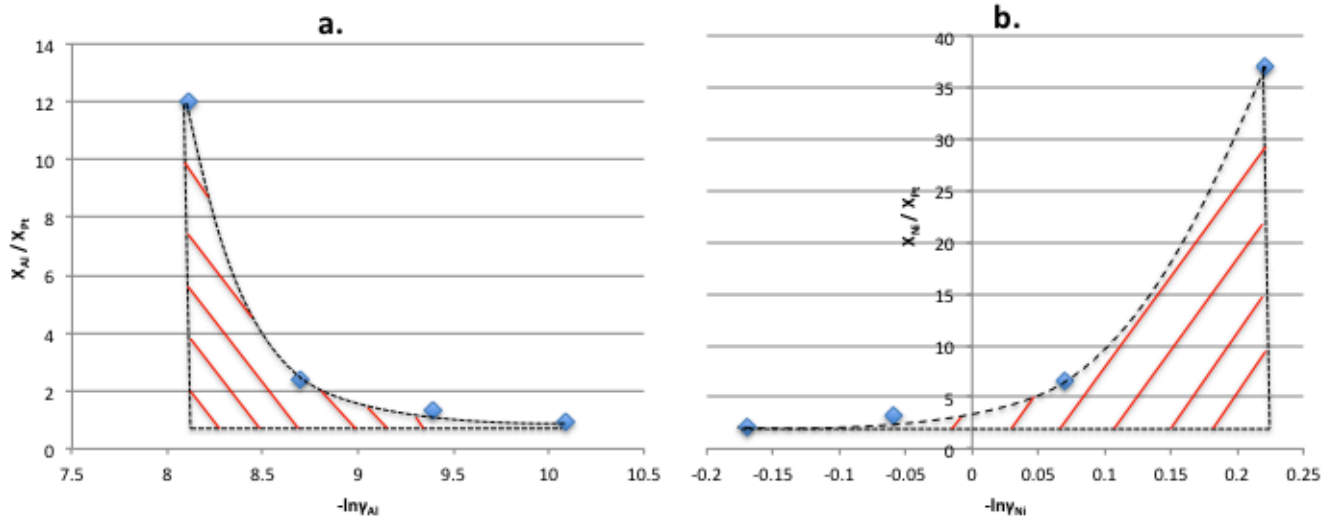


Figure 80. Plots of a) X_{Al}/X_{Pt} vs. $-\ln \gamma_{Al}$ and b) X_{Ni}/X_{Pt} vs. $-\ln \gamma_{Ni}$ which were numerically integrated in order to solve Equation (54). The relevant areas are indicated by red lines.

Assuming a linear relationship between $\ln \gamma_{Pt}$ and X_{Pt} , the interaction parameter ε_{PtPt} can be approximated as:

$$\varepsilon_{PtPt} \approx \frac{\Theta}{0.25 - 0.02} \quad (55)$$

From this analysis, it is found that $\varepsilon_{PtPt} = 45.7$.

In order to solve Equation (50) for γ_{Al} , one more value is required, namely γ_{Al}^o . This presents a difficult problem, as the Henry's law constant of Al in γ' -Ni-24Al-5Pt-5Co holds no physical meaning. The most accurate estimate that can be made for this parameter comes from the data of Copland [108]. From these data, a plot of a_{Al} vs X_{Al} in γ' was generated, and the slope

of this line was taken to be γ_{Al}^o . The value obtained, 4.3×10^{-3} , is not technically a Henry's law constant, but it is expected to be a reasonable order-of-magnitude approximation.

Finally, inserting each of these parameters into Equations (51) and (50) to calculate γ_{Ni} and γ_{Al} , respectively, in Ni-24Al-5Pt-5Co, a Q value for Reaction (42) of 75.1 is obtained. This value is approximately 9 orders of magnitude greater than both the K^{eq} and Q value for the Ni-24Al-5Pt alloy, indicating that the addition of Co very effectively decreases the thermodynamic tendency for Ni_3S_3 formation.

BIBLIOGRAPHY

1. Bornstein N.S., A., W.P., *The Chemistry of Sulfidation Corrosion-Revisited*. Mater. Sci. Forum, 1997. **127**: p. 127-134.
2. Sloof, W.G., Nijdam, T.J., *On the High-Temperature Oxidation of MCrAlY Coatings*. Int. J. Mat. Res., 2009. **100**: p. 1318-1330.
3. Birks, N., Meier, G.H., Pettit, F.S., *Introduction to the High Temperature Oxidation of Metals*. 2 ed2006, New York: Cambridge University Press.
4. Task, M.N., *The Effects of Composition and Microstructure on the Reaction Behavior of MCrAlY Alloys Under a Variety of Aggressive Environmental Conditions*, 2009, University of Pittsburgh: Pittsburgh, PA.
5. Das, D.K., Gleeson, B., Murphy, K.S., Ma, S., Pollock, T.M., *Formation of Secondary Reaction Zone in Ruthenium Bearing Nickel Based Single Crystal Superalloys with Diffusion Aluminide Coatings*. Mater. Sci. and Technol., 2009. **25**: p. 300-308.
6. McCreath, C.G., *Hot Corrosion Site Environment in Gas Turbines*. Mater. Sci. and Technol., 1987. **3**: p. 494-500.
7. DeCrescente, M.A., Bornstein, N.S., *Formation and Reactivity Thermodynamics of Sodium Sulfate with Gas Turbine Alloys*. Corrosion, 1968. **24**: p. 127-133.
8. Hanby, H.I., Beer, J.M., *Salt Deposition and Corrosion in Marine Gas Turbines*, 1969-1972.
9. Janz, G.J., *Molten Salts Handbook*1967, New York: Academic Press.
10. Giggins, C.S., Pettit, F.S. , *Hot Corrosion Degradation of Metals and Alloys - A Unified Theory*, 1979.
11. Deodshmukh, V., Gleeson, B. *Environmental and Compositional Effects on the Hot-Corrosion Behavior of Ni-Based Alloys and Coatings*. in *Corrosion 2008*. New Orleans, LA: NACE International.
12. Inman, D., Wrench, D.M., *Corrosion in Fused Salts*. Brit. Corr. J., 1966. **1**: p. 246-250.

13. Rapp, R.A., *Chemistry and Electrochemistry of the Hot Corrosion of Metals*. Corrosion, 1986. **42**: p. 568-577.
14. Gupta, D.K., Rapp, R.A., *The Solubilities of NiO, Co₃O₄, and Ternary Oxides in Fused Na₂SO₄ at 1200°K*. J. Electrochem. Soc., 1980. **127**: p. 2194-2202.
15. Jose, P.D., Gupta, D.K., Rapp, R.A., *The Solubility of α -Al₂O₃ in Fused Na₂SO₄ at 1200°K*. J. Electrochem. Soc., 1985. **132**: p. 735-737.
16. Shi, D.Z., Rapp, R.A., *The Solubility of SiO₂ in Fused Na₂SO₄ at 900°C*. J. Electrochem. Soc., 1986. **133**: p. 849-580.
17. Deanhardt, M.L., Stern, K.H., *Solubility Products of Metal Oxides in Molten Salts by Coulometric Titration of Oxide Ion Through Zirconia Electrodes*. J. Electrochem. Soc., 1982. **128**: p. 2577-2582.
18. Rapp, R.A., Otsuka, N., *The Role of Chromium in the Hot Corrosion of Metals*. ECS Trans., 2009. **16**: p. 271-282.
19. Zhang, Z.S., *Solubilities of Cr₂O₃ in Fused Na₂SO₄ at 1200K*. J. Electrochem. Soc., 1986. **133**: p. 655-657.
20. Zhang, Z.S., Rapp R.A., *Solubility of α -Fe₂O₃ in Fused Na₂SO₄ at 1200K*. J. Electrochem. Soc., 1985. **132**: p. 734-735.
21. Rapp, R.A., Goto, K.S. *The Hot Corrosion of Metals by Molten Salts*. in *The Second International Symposium on Molten Salts*. 1981.
22. Simons, E.L., Browning G.V., Liebhafsky, H.A., *Sodium Sulfate in Gas Turbines*. Corrosion, 1956. **11**: p. 63-64.
23. Quets, J.M., Drescher, W.H., *Thermochemistry of the Hot Corrosion of Superalloys*. J. Mater., 1969. **4**: p. 583-599.
24. Danek, G.J., *State-of-the-Art Survey on Hot Corrosion in Marine Gas Turbines*. Naval Engineers Journal, 1965. **77**: p. 859-869.
25. Seybolt, A.U., *Contribution to the Study of Hot Corrosion*. Trans. TMS AIME, 1968. **242**: p. 1955-1961.
26. Bornstein N.S., D., M.A., *The Relationship Between Compounds of Sodium and Sulfur and Sulfidation*. Trans. TMS AIME, 1969. **245**: p. 1947-1952.
27. Goebel, J.A., Pettit, F.S., *Na₂SO₄-Induced Accelerated Oxidation (Hot Corrosion) of Nickel*. Met. Trans., 1970. **1**(1970): p. 1943-1954.

28. Rapp, R.A., *Hot Corrosion of Materials: A Fluxing Mechanism?* Corrosion Sci., 2002. **44**: p. 209-221.
29. Shores, D.A., Fang, W.C., *Transport of Oxidant in Molten Na₂SO₄ in O₂-SO₂-SO₃ Environments.* J. Electrochem. Soc., 1981: p. 346.
30. Fang, W.C., Rapp, R.A., *Electrochemical Reactions in a Pure Na₂SO₄ Melt.* J. Electrochem. Soc., 1983. **130**: p. 2335.
31. Zheng, X., Rapp, R.A., *Electrochemical Impedance of a Platinum Electrode in Fused Na₂SO₄ Melts in SO₂-O₂ Environments.* J. Electrochem. Soc., 1993. **140**: p. 2857-2862.
32. Pettit, F.S., Goebel, J.A., Goward, G.W., *Thermodynamic Analysis of Simultaneous Attack of Some Metals and Alloys by Two Oxidants.* Corrosion Sci., 1969. **9**: p. 903-913.
33. Goebel, J.A., Pettit, F.S., *The Influence of Sulfides on the Oxidation Behavior of Nickel-Base Alloys.* Met. Trans., 1970. **1**: p. 3421-3429.
34. Bornstein N.S., D., M.A., *The Role of Sodium in the Accelerated Oxidation Phenomenon Termed Sulfidation.* Met. Trans., 1971. **2**: p. 2875-2883.
35. Goebel, J.A., Pettit, F.S., Goward, G.W., *Mechanisms for the Hot Corrosion of Nickel-Base Alloys.* Met. Trans., 1973. **4**: p. 261-278.
36. Meier, G.H., *A Review of Advances in High-Temperature Corrosion.* Mater. Sci. Eng., 1989. **A120**: p. 1-11.
37. Ross, E.W., Sims, C.T., ed. *Nickel-Base Alloys.* Superalloys II, ed. C.T. Sims, Stoloff, N.S., Hagel, W.C. 1987, John Wiley & Sons: New York.
38. Bornstein, N.S., DeCrescente, M.A., Roth, H.A. *Accelerated Corrosion in Gas Turbine Engines.* in *Gas Turbine Materials Conference.* 1972. Washington, D.C.
39. Conde, J.F.G., Wareham, G.C. *Aspects of the Mechanisms of Hot Corrosion in Marine Gas Turbines.* in *The 2nd Conference on Gas Turbine Materials in a Marine Environment.* 1974.
40. Wortman, D.J., Fryxell, R.E., Luthra, K.L., Bergman, P.A., *Mechanism of Low-Temperature Hot Corrosion: Burner Rig Studies.* Thin Solid Films, 1979. **64**: p. 281-288.
41. Luthra, K.L., Shores, D.A., *Mechanism of Na₂SO₄ Induced Corrosion at 600°-900°C.* J. Electrochem. Soc., 1980. **127**: p. 2202-2210.
42. Wortman, D.J., Fryxell, R.E., Bessen, I.I. *A Theory for Accelerated Turbine Corrosion at Intermediate Temperatures.* in *The 3rd Conference on Gas Turbine Materials in a Marine Environment.* 1976.

43. Luthra, K.L., *Low Temperature Hot Corrosion of Cobalt-Base Alloys: Part I. Morphology of the Reaction Product*. Met. Trans. A, 1982. **13A**: p. 1843-1852.
44. Barkalow, R.H., Goward, G.W., *Microstructural Features of Low Temperature Hot Corrosion in Nickel and Cobalt Base MCrAlY Coatings Alloys*, in *High Temperature Corrosion*, R.A. Rapp, Editor 1983, National Society of Corrosion Engineers: Houston. p. 502-506.
45. Chiang, K.T., Pettit, F.S., Meier, G.H., *Low Temperature Hot Corrosion*, in *High Temperature Corrosion*, R.A. Rapp, Editor 1983, National Society of Corrosion Engineers: Houston. p. 519-530.
46. Jones, R.L., *Cobalt Oxide-SO₂/SO₃ Reactions in Cobalt-Sodium Mixed Sulfate Formation and Low Temperature Hot Corrosion*, in *High Temperature Corrosion*, R.A. Rapp, Editor 1983, National Society of Corrosion Engineers: Houston. p. 513-518.
47. Luthra, K.L., Shores, D.A. *Morphology of Na₂SO₄ Induced Hot Corrosion at 600-750°C*. in *The 4th Conference on Gas Turbine Materials in a Marine Environment*. 1979.
48. Luthra, K.L., *Low Temperature Hot Corrosion of Cobalt-Base Alloys: Part 2. Reaction Mechanism*. Met. Trans. A, 1982. **13A**: p. 1853-1864.
49. Nicholls, J.R., *Advances in Coating Design for High-Performance Gas Turbines*. MRS Bulletin, 2003: p. 659-670.
50. Tatlock, G.J., Hurd, T.J., Punni, J.S., *High Temperature Degradation of Nickel Based Alloys: A Consideration of the Role of Platinum*. Platinum Metals Rev., 1987. **31**: p. 26-31.
51. Batzner, C., *Aluminum-Nickel-Platinum*, in *Phase Diagrams of Ternary Nickel Alloys* 1990, VCH. p. 449.
52. Jackson, M.R., and Rairden, J.R., *The Aluminization of Platinum and Platinum-Coated IN-738*. Met. Mater. Trans. A, 1977. **8A**: p. 1697-1707.
53. Gleeson, B.W., W., Hayashi, S., Sordélet, D., *Effects of Platinum on the Interdiffusion and Oxidation Behavior of Ni-Al-Based alloys*. Mater. Sci. Forum, 2004. **461**: p. 213-222.
54. Hayashi, S., Ford, S.I., Young, D.J., Sordélet, D.J., Besser, M.F., Gleeson, B., *Alpha-NiPt(Al) and Phase Equilibria in the Ni-Al-Pt System at 1150C*. Acta Mater., 2005. **53**: p. 3319-3328.
55. Smialek, J.L., Hehemann, R.F., *Transformation Temperatures of Martensite in Beta-Phase Nickel Aluminide*. Met. Trans., 1973. **4**: p. 1571-1575.

56. Kainuma, R., Ohtani, H., Ishida, K., *Effect of Alloying Elements on Martensitic Transformation in the Binary NiAl (Beta) Phase Alloys*. Met. Mater. Trans. A, 1996. **27A**: p. 2445-2453.
57. Pan, D., Chen, M.W., Wright, P.K., Hemker, K.J., *Evolution of a Diffusion Aluminide Bond Coat for Thermal Barrier Coatings During Thermal Cycling*. Acta Mater., 2003. **51**: p. 2205-2217.
58. Chen, M.W., Livi, K.J.T., Wright, P.K., Hemker, K.J., *Microstructural Characterization of a Platinum-Modified Diffusion Aluminide Bond Coat for Thermal Barrier Coatings*. Met. Mater. Trans. A, 2003. **34A**: p. 2289-2299.
59. Chen, M.W., Glynn, M.L., Ott, R.T., Hufnagel, T.C., Hemker, K.J., *Characterization and Modeling of a Martensitic Transformation in a Platinum Modified Diffusion Aluminide Bond Coat for Thermal Barrier Coatings*. Acta Mater., 2003. **51**: p. 4279-4294.
60. Sordellet, D.J., Besser, M.F., Ott, R.T., Zimmerman, B.J., Porter, W.D., Gleeson, B., *Isothermal Nature of Martensite Formation in Pt-Modified Beta-NiAl Alloys*. Acta Mater., 2007. **55**: p. 2433-2441.
61. Goward, G.W., Boone, D.H., *Mechanisms of Formation of Diffusion Aluminide Coatings on Nickel-Base Superalloys*. Oxid. Met., 1971. **3**: p. 475-495.
62. Levine, S.R., Caves, R.M., *Thermodynamics and Kinetics of Pack Aluminide Coating Formation on IN-100*. J. Electrochem. Soc., 1974. **121**: p. 1051-1064.
63. Wing, R.G., McGill, I.R., *The Protection of Gas Turbine Blades: A Platinum Aluminide Diffusion Coating*. Platinum Metals Rev., 1981. **25**: p. 94-105.
64. Krishna, G.R., Das, D.K., Singh, V., Joshi, S.V., *Role of Pt Content in the Microstructural Development and Oxidation Performance of Pt-Aluminide Coatings Produced Using a High-Activity Aluminizing Process*. Mater. Sci. Eng., 1998. **A251**(40-47).
65. Felten, E.J., Pettit, F.S., *Development, Growth, and Adhesion of Al₂O₃ on Platinum-Aluminum Alloys*. Oxid. Met., 1976. **10**: p. 189-223.
66. Schaeffer, J., Kim, G.M., Meier, G.H., Pettit, F.S., ed. *The Effects of Precious Metals on the Oxidation and Hot Corrosion of Coatings*. The Role of Active Elements in the Oxidation Behavior of High Temperature Metals and Alloys, ed. E. Lang 1989, Elsevier: Amsterdam. 231-267.
67. Zhang, Y., Haynes, J.A., Lee, W.Y., Wright, I.G., Pint, B.A., Cooley, K.M., Liaw, P.K., *Effects of Pt Incorporation on the Isothermal Oxidation Behavior of Chemical Vapor Deposition Aluminide Coatings*. Met. Mater. Trans. A, 2001. **32A**: p. 1727-1741.

68. Haynes, J.A., Pint, B.A., More, K.L., Zhang, Y., Wright, I.G., *Influence of Sulfur, Platinum, and Hafnium on the Oxidation Behavior of CVD NiAl Bond Coatings*. Oxid. Met., 2002. **58**: p. 513-544.
69. Svensson, H., Knutsson, P., Stiller, K., *Formation and Healing of Voids at the Metal-Oxide Interface in NiAl Alloys*. Oxid. Met., 2009. **71**: p. 143-156.
70. Rivoaland, L., Maurice, V., Josso, P., Bacos, M.-P., Marcus, P., *The Effect of Sulfur Segregation on the Adherence of the Thermally-Grown Oxide on NiAl-II. The Oxidation Behavior at 900C of Standard, Desulfurized or Sulfur-Doped NiAl(001) Single-Crystals*. Oxid. Met., 2003. **60**: p. 159-178.
71. Gleeson, B., Mu, N., Hayashi, S., *Compositional Factors Affecting the Establishment and Maintenance of Al₂O₃ Scales on Ni-Al-Pt Systems*. J. Mater. Sci., 2009. **44**: p. 1704-1710.
72. Jiang, C., Besser, M.F., Sordellet, D.J., Gleeson, B., *A Combined First-Principles and Experimental Study of the Lattice Site Preference of Pt in B2 NiAl*. Acta Mater., 2005. **53**: p. 2101-2109.
73. Marino, K.A., Carter, E.A., *The Effect of Platinum on Al Diffusion Kinetics in Beta-NiAl: Implications for Thermal Barrier Coating Lifetime*. Acta Mater., 2010. **58**: p. 2726-2737.
74. Leyens, C., Pint, B.A., Wright, I.G., *Effect of Composition on the Oxidation and Hot Corrosion Resistance of NiAl Doped with Precious Metals*. Surf. Coatings Tech., 2000. **133-134**: p. 15-22.
75. Wu, W.T., Rahmel, A., Schorr, M., *Role of Platinum in the Na₂SO₄-Induced Hot Corrosion Resistnce of Aluminum Duffusion (sic) Coatings*. Oxid. Met., 1984. **22**: p. 59-81.
76. Gleeson, B., Cheung, W.H., Da Costa, W., Young, D.J., *The Hot-Corrosion Behavior of Novel CO-Deposited Chromium-Modified Aluminide Coatings*. Oxid. Met., 1992. **38**: p. 407-424.
77. Murakami, H., Kuroda, S., Wu, Y.N., Yamaguchi, A., *Role of Iridium in Hot Corrosion Resistance of Pt-Ir Modified Aluminide Coatings with Na₂SO₄-NaCl Salt at 1173K*. Mater. Trans., 2006. **47**(1918-1921).
78. Raghavan, V., *Al-Cr-Ni (Aluminum-Chromium-Nickel)*. J. Phase Equil. and Diff., 2008. **29**: p. 175.
79. Task, M.N., Kim, D.E., Liu, Z., Gleeson, B., Pettit, F.S., Meier, G.H., *Phase Stability and Oxidation Behavior of an Alumina Scale-Forming NiCrAlY Alloy*. Oxid. Met., 2010. **74**: p. 179-191.

80. Randhawa, H., *Cathodic Arc Plasma Deposition Technology*. Thin Solid Films, 1988. **167**: p. 175-185.
81. Nijdam, T.J., Jeurgens, L.P.H., Chen, J.H., Sloof, W.G., *On the Microstructure of the Initial Oxide Grown by Controlled Annealing and Oxidation on a NiCoCrAlY Bond Coating*. Oxid. Met., 2005. **64**: p. 355-377.
82. Nijdam, T.J., Kwakernaak, C., Sloof, W.G., *The Effects of Alloy Microstructure Refinement on the Short-Term Thermal Oxidation of NiCoCrAlY Alloys*. Met. Mater. Trans. A, 2006. **37A**: p. 683-693.
83. Goedjen, J.G., Shores, D. A., *The Effect of Alloy Grain Size on the Transient Oxidation Behavior of an Alumina-Forming Alloy*. Oxid. Met., 1992. **37**: p. 125-142.
84. Levi, C.G., Sommer, E., Terry, S.G., Catanoiu, A., Ruhle, M., *Alumina Grown During Deposition of Thermal Barrier Coatings on NiCrAlY*. J. Am. Ceram. Soc., 2003. **86**: p. 676-685.
85. Nijdam, T.J., Sloof, W.G., *Effect of Y Distribution on the Oxidation Kinetics of NiCoCrAlY Bond Coat Alloys*. Oxid. Met., 2008. **69**: p. 1-12.
86. Quadakkers, W.J., Huczowski, P., Naumenko, D., Zurek, J., Meier, G.H., Niewolak, L., Singheiser, L., *Why the Growth Rates of Alumina and Chromia Scales on Thin Specimens Differ from those on Thick Specimens*. Mater. Sci. Forum, 2008. **595**: p. 1111-1118.
87. Evans, A.G., Mumm, D.R., Hutchinson, J.W., Meier, G.H., Pettit, F.S., *Mechanisms Controlling the Durability of Thermal Barrier Coatings*. Prog. Mater. Sci., 2001. **46**: p. 505-553.
88. Meier-Jackson, E.M., Yanar, N. M., Maris-Jakubowski, M. C., Onal-Hance, K., Meier, G.H., Pettit, F. S., *Effect of Surface Preparation on the Durability of NiCoCrAlY Coatings for Oxidation Protection and Bond Coats for Thermal Barrier Coatings*. Mater. and Corr., 2008. **59**: p. 494-500.
89. Toscano, J., Vasen, R., Gil, A., Subanovic, M., Naumenko, D., Singheiser, L., Quadakkers, W.J., *Parameters Affecting TGO Growth and Adherence on MCrAlY Bond Coats for TBCs*. Surf. Coatings Tech., 2006. **201**: p. 3906-3910.
90. Vande Put, A., Oquab, D., Pere, E., Raffaitin, A., Monceau, D., *Beneficial Effect of Pt and of Pre-Oxidation on the Oxidation Behavior of an NiCoCrAlYTaN Bond-Coating for Thermal Barrier Coating Systems*. Oxid. Met., 2011. **75**: p. 247-279.
91. Nijdam, T.J., Marijnissen, G.H., Vergeldt, E., Kloosterman, A.B., Sloof, W.G., *Development of a Pre-Oxidation Treatment to Improve the Adhesion Between Thermal Barrier Coatings and NiCoCrAlY Bond Coatings*. Oxid. Met., 2006. **66**: p. 269-294.

92. Yanar, N.M., Meier, G.H., Pettit, F.S., *The Influence of Platinum on the Failure of EBPVD YSZ TBCs on NiCoCrAlY Bond Coats*. Scripta Mat., 2002. **46**: p. 325-330.
93. Gil, A., Shemet, V., Vassen, R., Subanovic, M., Toscano, J., Naumenko, D., Singheiser, L., Quadakkers, W.J., *Effect of Surface Condition on the Oxidation Behaviour of MCrAlY Coatings*. Surf. Coatings Tech., 2006. **201**: p. 3824-3828.
94. Lowell, C.E., Garlick, R.G., Henry, B., *Thermal Expansion in the Ni-Cr-Al and Co-Cr-Al Systems to 1200C Determined by High-Temperature X-Ray Diffraction*. Met. Trans. A, 1976. **7A**: p. 655-660.
95. Gurrappa, I., *Identification of Hot Corrosion Resistant MCrAlY Based Bond Coatings for Gas Turbine Engine Applications*. Surf. Coatings Tech., 2001. **139**: p. 272-283.
96. Materials Preparation Center, A.L.U., Ames, IA, USA. <http://www.mpc.ameslab.gov>.
97. Achar, D.R.G., Munoz-Arroyo, R., Singheiser, L., Quadakkers, W.J., *Modeling of Phase Equilibria in MCrAlY Coating Systems*. Surf. Coatings Tech., 2004. **187**: p. 272-283.
98. Gleeson, B., *Thermodynamics and Theory of External and Internal Oxidation of Alloys*. Shreir's Corrosion, ed. T.R.e. al. Vol. 1: Basic Concepts, High Temperature Corrosion. 2010: Elsevier.
99. Gilmer, G.H., Farrel, H.H., *Grain-boundary Diffusion in Thin Films. I. The Isolated Grain Boundary*. J. Appl. Phys., 1976. **47**: p. 3792-3798.
100. Gesmundo, F., Gleeson, B., *Oxidation of Multicomponent Two-Phase Alloys*. Oxid. Met., 1995. **44**: p. 211-247.
101. Meijering, J.L. *Advances in Materials Research* 51971, New York: Wiley-Interscience.
102. Young, D.J., Gleeson, B., *Alloy Phase Transformations Driven by High Temperature Corrosion Processes*. Corr. Sci., 2002. **44**: p. 345-357.
103. Hou, P.Y., *Oxidation of Metals and Alloys*, in *Shreir's Corrosion, Fourth Edition* 2010. p. 195-239.
104. Stott, F.H., Wood, G.C., Whittle, D.P., Bastow, B.D., Shida, Y., Martinez-Villafane, A., *The Transport of Oxygen to the Advancing Internal Oxide Front During Internal Oxidation of Nickel-Base Alloys at High Temperature*. Solid State Ionics, 1984. **12**: p. 365-374.
105. Deodeshmukh, V., Gleeson, B., *Effects of Platinum on the Hot Corrosion Behavior of Hf-Modified Gamma'-Ni₃Al + Gamma-Ni - Based Alloys*. Oxid. Met., 2011. **76**: p. 43-55.

106. Pelton, A.D., Bale, C.W., *A Modified Interaction Parameter Formalism for Non-Dilute Solutions*. Met. Trans. A, 1986. **17A**: p. 1211-1215.
107. Albers, M., Kath, D., Hilpert, K., *Thermodynamic Activities and Phase Boundaries for the Alloys of the Solid Solution of Co in Ni₃Al*. Met. Mater. Trans. A, 1997. **28A**: p. 2183-2188.
108. Copland, E., *Partial Thermodynamic Properties of Gamma'-(Ni,Pt)₃Al in the Ni-Al-Pt System*. J. Phase Equil. and Diff., 2006. **28**: p. 38-48.
109. Wagner, C., *Thermodynamics of Alloys* 1962, Reading, MA: Addison-Wesley.
110. Nagaraj, B., *Personal Communication*, 2011.
111. Luthra, K.L., Shores, D.A., *Mechanism of Na₂SO₄ Induced Hot Corrosion at 600-900C*. J. Electrochem. Soc., 1980. **127**: p. 2202-2210.
112. Wagner, C., *Passivity and Inhibition During the Oxidation of Metals at Elevated Temperatures*. Corr. Sci., 1965. **5**: p. 751-764.
113. Guan, S.W., Smeltzer, W.W., *Oxygen Solubility and a Criterion for the Transition from Internal to External Oxidation of Ternary Alloys*. Oxid. Met., 1994. **42**: p. 375-391.
114. Tin, S., Zhang, L., Brewster, G., Miller, M.K., *Investigation of Oxidation Characteristics and Atomic Partitioning in Platinum and Ruthenium Bearing Single-Crystal Ni-Based Superalloys*. Met. Mater. Trans. , 2006. **37A**: p. 1389-1396.
115. Task, M.N., Gleeson, B., Pettit, F.S., Meier, G.H., *Unpublished research*.
116. Brumm, M.W., Grabke, H.J., *The Oxidation Behavior of NiAl-I. Phase Transformations in the Alumina Scale During Oxidation of NiAl and NiAl-Cr Alloys*. Corr. Sci., 1992. **33**: p. 1677-1690.
117. Tolpygo, V.K., Clarke, D.R., *Microstructural Study of the Theta-Alpha Transformation in Alumina Scales Formed on Nickel-Aluminides*. Mater. High. Temp., 2000. **17**: p. 59-70.
118. Doychak, J., Smialek, J.L., Mitchell, T.E., *Transient Oxidation of Single-Crystal Beta-NiAl*. Met. Trans. A, 1989. **20A**: p. 499-518.
119. Prescott, R., Mitchell, D.F., Graham, M.J., Doychak, J., *Oxidation Mechanisms of Beta-NiAl+Zr Determined by SIMS*. Corr. Sci., 1995. **37**: p. 1341-1364.
120. Doychak, J., Ruhle, M., *TEM Studies of Oxidized NiAl and Ni₃Al Cross Sections*. Oxid. Met., 1988. **31**: p. 431-452.

121. Rybicki, G.C., Smialek, J.L., *Effect of the theta-alpha-Al₂O₃ Transformation on the Oxidation Behavior of Beta-NiAl + Zr*. Oxid. Met., 1989. **31**: p. 275-304.
122. Pint, B.A., Treska, M., Hobbs, L.W., *The Effect of Various Oxide Dispersions on the Phase Composition and Morphology of Al₂O₃ Scales Grown on Beta-NiAl*. Oxid. Met., 1997. **47**: p. 1-20.
123. Kitajima, Y., Hayashi, S., Nishimoto, T., Narita, T., Ukai, S., *Rapid Formation of Alpha-Al₂O₃ Scale on an Fe-Al Alloy by Pure-Metal Coatings at 900C*. Oxid. Met., 2010. **73**: p. 375-388.
124. Fei, W., Kuiry, S.C., Seal, S., *Inhibition of Metastable Alumina Formation on Fe-Cr-Al-Y Alloy Fibers at High Temperatures using Titania Coating*. Oxid. Met., 2004. **62**: p. 29-44.
125. N'Dah, E., Galerie, A., Wouters, Y., Goossens, D., Naumenko, D., Kochubey, V., Quadackers, W.J., *Metastable Alumina Formation During Oxidation of FeCrAl and its Suppression by Surface Treatments*. Mater. and Corr., 2005. **56**: p. 843-847.
126. Galerie, A., N'Dah, E., Wouters, Y., Roussel-Dherbey, F., *Influence of a TiO₂ Surface Treatment on the Growth and Adhesion of Alumina Scales on FeCrAl Alloys*. Mater. and Corr., 2008. **59**: p. 423-428.
127. Zhao, W., Gleeson, B., *Unpublished research*.
128. Pint, B.A., Martin, J.R., Hobbs, L.W., *The Oxidation Mechanism of Theta-Al₂O₃ Scales*. Solid. State Ionics, 1995. **78**: p. 99-107.
129. Hovis, D.B., Heuer, A.H., *The Use of Laser Scanning Confocal Microscopy (LSCM) in Materials Science*. J. of Micros., 2010. **240**: p. 173-180.
130. Burtin, P., Brunelle, J.P., Pijolat, M., Soustelle, M., *Influence of Surface Area and Additives on the Thermal Stability of Transition Alumina Catalyst Supports. I: Kinetic Data*. App. Cat., 1987. **34**: p. 225-238.
131. Shackelford, J.F., Alexander, W., *CRC Materials Science and Engineering Handbook, 2nd Ed.* 2001, New York: CRC Press.
132. Yang, J.C., Schumann, E., Levin, I., Ruhle, M., *Transient Oxidation of NiAl*. Acta Mater., 1998. **46**: p. 2195-2201.
133. Schumann, E., *The Effect of Y-Ion Implantation on the Oxidation of Beta-NiAl*. Oxid. Met., 1995. **43**: p. 157-172.
134. Porter, D.A., Easterling, K.E., *Phase Transformations in Metals and Alloys, Second Edition* 2004, Boca Raton, FL: CRC Press.

135. Mori, T., *Phase Diagram of the System CoO-Al₂O₃*. J. Ceram. Soc. Jap., 1982. **90**: p. 58-59.
136. Stiger, M.J., Yanar, N.M., Jackson, R.W., Laney, S.J., Pettit, F.S., Meier, G.H., Gandhi, A.S., Levi, C.G., *Development of Intermixed Zones of Alumina/Zirconia in Thermal Barrier Coating Systems*. Met. Mater. Trans. A, 2007. **38**: p. 848-857.
137. Hou, P.Y., *Segregation Phenomena at Thermally Grown Al₂O₃/Alloy Interfaces*. Ann. Rev. Mater. Res., 2008. **38**: p. 275-298.
138. hou, P.Y., McCarty, K.F., *Surface and Interface Segregation in Beta-NiAl with and without Pt Addition*. Scripta Mat., 2006. **54**: p. 937-941.
139. Cadoret, Y., Monceau, D., Bacos, M.P., Josso, P., Maurice, V., Marcus, P., *Effect of Platinum on the Growth Rate of the Oxide Scale Formed on Cast Nickel Aluminide Intermetallic Alloys*. Oxid. Met., 2005. **64**: p. 185-205.
140. Yoshida, H., Okada, K., Ikuhara, Y., Sakuma, T., *Improvement of High-Temperature Creep Resistance in Fine-Grained Al₂O₃ by Zr⁴⁺ Segregation in Grain Boundaries*. Phil. Mag. Let., 1997. **76**: p. 9-14.
141. Schutze, M., *Plasticity of Protective Oxide Scales*. Mater. Sci. and Technol., 1990. **6**: p. 32-38.